UNIVERSITAT POLITÈCNICA DE CATALUNYA

DOCTORAL THESIS

Structural and Functional Studies of AT-Rich DNA Ligands and Their Effect on *Trypanosoma brucei*

Author:

Cinthia Raquel

MILLAN ELIAS

Supervisors:

Dr. J. Lourdes CAMPOS

Dr. Núria SAPERAS

A thesis submitted for the degree of Doctor of Philosophy

at the Universitat Politècnica de Catalunya

Doctoral Program: Polymers and Biopolymers

Department of Chemical Engineering

MACROM Group

ETSEIB

Barcelona, July 2017

Dedicated to my sisters,

from whom I have learned to fight for my big dreams.

"Almost all aspects of life are engineered at the molecular level, and without understanding molecules we can only have a very sketchy understanding of life itself."

Francis Crick

ACKNOWLEDGEMENTS

First of all, I would like to thank my supervisors, Dr. Lourdes Campos for all the guidance, unlimited support and patience, encouragement and advice she has always been able to provide throughout my time as her student; and to Dr. Núria Saperas, for her invaluable guidance and immense support every day, she always encouraged me to do it better. I can affirm that I have been very lucky to have two supervisors who always cared and showed their interest in my research and work, and who have been available to provide their guidance in every stage of the development of this thesis, making it possible for me to achieve my goals.

I would also like to thank Dr. Juan Antonio Subirana and all the members of the MACROM group: David, Sonia and Fabiola. A special recognition to Raquel and Paco, for sharing with me their knowledge and experience in protein purification and crystallography. I want to thank them both for the support they provided every time I needed it, their helpful advises, but also their friendship. It was a pleasure to work with you both. I admire you so much.

I want to express my gratitude to Dr. Harry de Koning for giving me the opportunity to be a part of his group at the University of Glasgow and for introducing me to the world of parasites. I want to thank him for the valuable suggestions and his thoughtful guidance that made my stay in Glasgow so remarkable and successful. This thesis would not have been possible without his help. I would like to acknowledge the members of Dr. de Koning's research lab: Anne, Jane, Manal, Amani, Lauren, Gordon, and Daniel, and a very special thanks to my dear friends Gustavo and Khalid, for sharing their knowledge with me, for being patient and for their support during my experiments. I am so grateful to all them who have contributed to make my experience in Glasgow unforgettable and fulfilling.

I would like to thank our thoughtful collaborators. To Dr. Christophe Dardonville, as his continuous interest helped me enormously during the development of Chapter 4. I would like to thank him for his valuable help during my short stay in Madrid and

during the last two years, having always a prompt response to my numerous questions. To Laura Lagartera, for the time she dedicated me, and her invaluable support with the SPR experiments. To Dr. Leandro Lemgruber for performing amazing TEM images and providing all those useful insights.

Thanks to all the generous and kind people I have met in the Chemical Engineering Department of the ETSEIB and EEBE: Dr. Juan Jesús Pérez, Dr. Ma. Teresa Casas, Dr. Lourdes Franco, Dr. Alfonso Rodríguez, Dr. Luis J. del Valle, Dr. Jordi Puiggali, Manolo, Neudys, Ana, Silvana, Angélica and Georgina. To the great international group of students we have formed during the last year: Jordi, Guillem, Hamidreza, Reza, Amir, Anna, Maricruz, Brenda, with a special mention to Ina, for me, the best leader this group could have, and Max, for his special and kind way to see this life.

Thanks to the best friends I could have: Grey and Dany, you are the best partners for the most unforgettable adventures I can have; to my favourite Catalans Mary and Pablo; to my old-school friends Melissa, Anilú, Paulina and Polette; to Fátima and Claudia; to my dear Daniel; to my mother from Barcelona, Lilia; to Luz, for being always there for me, for showing me your support and for having the right words; and to my best friend José Angel, for everything he has done for me, for his trust and support, for making me laugh no matter what, and for being next to me through this years. I love you all very much. I would also like to thank Chris, for changing my life.

And finally, I want to show my infinite gratitude to my amazing family, the most important part of my life. To my parents Rosy and Edgardo, for the unconditional love and the enormous support they have always given me throughout my life, for giving me the freedom and courage to pursue my ambitions, for making me who I am. I will always carry a part of you everywhere I go. To Rosiel and Riza, for being the best sisters I could have had, for always pushing me to be a better person, for being my mentors, my role models, and my inspiration to be better every day, thank you very much. To my wonderful, amazing and funny nephews, Ruben and Leonardo, for giving me the chance to feel love in ways I didn't know existed. Life is continuous research.

ABSTRACT

Adenine (A) and thymine (T) rich sequences confer unique properties to DNA, such as high polymorphism and flexibility. The abundance of AT-rich DNA in several pathogens' genomes and the ability of specific molecules to selectively target AT base pairs have prompted studies on ligands that interact with the minor groove of high AT content DNA. Of special interest are kinetoplastid parasites, such as *Trypanosoma brucei*, the causative agent of sleeping sickness, which are distinguished by the presence of a very AT-rich mitochondrial DNA structure called kinetoplast.

Minor groove binding ligands have offered critical information on DNA molecular recognition, providing clinically useful strategies against diseases. Thus, the binding affinity and structural characteristics of AT-rich oligonucleotides in complex with different ligands, specifically with HMG proteins and bisimidazolinium compounds, has been chosen as the object of study.

The 'High Mobility Group' (HMG) is a family of architectural proteins that bind to DNA and influence a myriad of essential cellular processes. This research work has focused in two HMG subfamilies: HMGA and HMGB. They bind to the minor groove of the DNA by means of different binding motifs: AT-hook (HMGA) and HMG-box (HMGB). An HMGA1a fragment containing AT-hook II and III, HMGB1 box B and HMGB1 box AB have been expressed and purified. High and similar binding affinity to an AT-rich DNA sequence containing [AATAAT_ATTATT] has been found by surface plasmon resonance (SPR)–biosensor experiments for both proteins. A complex of the HMGB1 box B with d[CCAATAATCGCGATTATTGG]$_2$ was crystallized. The diffraction patterns of the crystal at 2.68 Å resolution presented well-defined spots revealing two diffraction orientations.

On the other hand, a series of diphenyl-based bis(2-iminoimidazolidine) derivatives of FR60 [4-((4,5-dihydro-1*H*-imidazol-2-yl)amino)-*N*-(4-((4,5-dihydro-1*H*-imidazol-2-yl) amino)phenyl)benzamide] have been proved to be high affinity DNA binders with a preference for AT over GC-rich DNA, showing slight selectivity towards sequences containing [AATT] versus [(AT)$_4$] or [AATAAT_ATTATT]. Furthermore, competition assays

have demonstrated that JNI18 competes with HMGA1a and HMGB1 for binding to DNA and it is able to displace the proteins from their DNA binding sites. This last interaction is of prime importance, as related proteins have been found to be essential in kinetoplastid parasites.

The structure of the bis(2-aminoimidazoline) compound CDIV32 [4,4'-bis(1-hydroxy imidazolinylamino)diphenylamine] with the oligonucleotide d[AAATTT]$_2$ partially solved at 3.10 Å resolution, displays DNA columns of stacked oligonucleotides forming a pseudo-continuous helix packed in a crossed column configuration of DNA helices that are at ~90° to each other. The presence of the drug CDIV32 modulates the organization of duplexes.

The crystal structure of the complex of the oligonucleotide d[AAATTT]$_2$ with the lead compound FR60, solved at atomic resolution of 1.25 Å (PDB-ID: **5LIT**) by X-ray crystallography, is constituted of stacked oligonucleotides organized as infinite continuous parallel columns, packed in a pseudo-tetragonal configuration. The structure revealed that the drug interacts with the central [AATT] region, covers the minor groove of DNA, displaces bound water and interacts with neighboring DNA molecules as a cross-linking agent.

Finally, a functional analysis has been performed on the effect of different bis(2-aminoimidazolines) on *Trypanosoma brucei*, which has a kDNA with higher than 70% AT base pair content. The main objective was to assess whether parasite DNA was a target for these compounds inside the cell. The *in vitro* effect of these drugs against *T. brucei* was evaluated. By a combination of flow cytometry and imaging techniques such as fluorescence microscopy and transmission electron microscopy, it was demonstrated that these compounds have a clear effect on the S-phase of *T. brucei* cell cycle by inflicting specific damage on the kinetoplast. It can be concluded that the studied DNA binding bis(2-aminoimidazoline) compounds FR60 and JNI18 are powerful trypanocides that act directly on the kinetoplast DNA. As the compounds show 100% curative activity in a mouse model of *T. b. rhodesiense* infection, they are potentially an effective chemotherapeutic agent for the treatment of sleeping sickness.

RESUMEN

Las secuencias ricas en adeninas (A) y timinas (T) le confieren al ADN propiedades únicas como un alto polimorfismo y flexibilidad. La abundancia de ADN rico en AT en el genoma de varios patógenos y la selectividad de unión a secuencias AT que presentan ciertas moléculas, han llevado al estudio de ligandos que interactúan con el surco estrecho de DNA con alto contenido en AT. De especial interés son los parásitos kinetoplástidos, como el *Trypanosoma brucei*, agente causante de la enfermedad del sueño, los cuales se distinguen por la presencia de una estructura de ADN mitocondrial muy rica en AT llamada kinetoplasto.

Los ligandos de unión al surco estrecho han ofrecido información primordial sobre el reconocimiento molecular del ADN, proporcionando estrategias clínicamente útiles para combatir enfermedades. Por ello, se ha elegido como objeto de estudio la afinidad de unión y las características estructurales de complejos de oligonucleótidos ricos en AT con diferentes ligandos, específicamente con proteínas HMG y con compuestos bisimidazolinio.

Las HMG (*High Mobility Group*) son una familia de proteínas arquitectónicas que se unen al ADN e influyen en numerosos procesos celulares esenciales. Este trabajo de investigación se ha centrado en dos subfamilias de las HMG: las HMGA y las HMGB. Ambas se unen al surco estrecho del ADN pero mediante diferentes motivos de unión: *AT-hook* (HMGA) y *HMG-box* (HMGB). Se ha expresado y purificado un fragmento de HMGA1a que contiene los *AT-hook* II y III, así como la HMGB1 box B y la HMGB1 box AB. Por medio de experimentos de resonancia de plasmón superficial (SPR), se ha encontrado para ambas proteínas una afinidad de unión alta y similar hacia un oligonucleótido rico en AT conteniendo la secuencia [AATAAT_ATTATT]. Se cristalizó un complejo de la HMGB1 box B con el oligonucleótido d[CCAATAATCGCGATTATTGG]$_2$. Los diagramas de difracción del cristal a una resolución de 2.68 Å presentaban reflexiones bien definidas que indicaban dos orientaciones preferenciales en el cristal.

Por otra parte, una serie de derivados difenilo bisimidazolinio basados en el compuesto FR60 [4-((4,5-dihidro-1*H*-imidazol-2-il)amino)-*N*-(4-((4,5-dihidro-1*H*-imidazol-2-il) amino)fenil)benzamida] han demostrado ser ligandos de alta afinidad por secuencias AT con respecto a GC, mostrando cierta preferencia hacia secuencias que contienen [AATT] comparado con $[(AT)_4]$ o [AATAAT_ATTATT]. Además, los ensayos de competencia han demostrado que el JNI18 compite con la HMGA1a y la HMGB1 en su unión al ADN y es capaz de desplazar a dichas proteínas de sus sitios de unión al ADN. Esta última interacción es de especial relevancia, ya que se han encontrado proteínas relacionadas que son esenciales en parásitos kinetoplástidos.

La estructura del compuesto de bis(2-aminoimidazolinio) CDIV32 [4,4'-bis (1-hidroxi imidazolinilaminio)difenilamina] con el oligonucleótido $d[AAATTT]_2$ ha sido parcialmente resuelta a una resolución de 3.10 Å. Se encontraron columnas de oligonucleótidos apilados formando una hélice pseudo-continua, empaquetada en una configuración de columnas cruzadas perpendicularmente. La presencia del fármaco CDIV32 modula la organización de las hélices de ADN.

Por medio de cristalografía de rayos X se ha resuelto la estructura del complejo formado por el oligonucleótido $d[AAATTT]_2$ y el compuesto líder FR60 a resolución atómica de 1.25 Å (PDB-ID: **5LIT**). Se encontraron los oligonucleótidos apilados organizados en columnas infinitas y paralelas en una configuración pseudo-tetragonal. La estructura reveló que el fármaco interacciona con la región central [AATT], ocupa el surco estrecho del ADN, desplaza las moléculas de agua presentes e interactúa con moléculas de ADN vecinas como un agente entrecruzador.

Finalmente, se ha realizado un análisis funcional del efecto de diferentes compuestos bis(2-aminoimidazolinio) en *Trypanosoma brucei*, el cual posee un kDNA con un contenido de AT superior al 70%. El objetivo principal ha sido evaluar si el ADN del parásito es una diana para estos compuestos dentro de la célula. Para ello se ha estudiado su efecto *in vitro* mediante una combinación de citometría de flujo y técnicas como microscopía de fluorescencia y microscopía electrónica de transmisión. Los resultados permitieron demostrar que estos compuestos tienen un efecto claro

sobre la fase S del ciclo celular de *T. brucei* al dañar específicamente el kinetoplasto. Se ha podido concluir que los compuestos bis(2-aminoimidazolinio) FR60 y JNI18 son potentes tripanocidas que actúan directamente sobre el ADN del kinetoplasto. Ya que los compuestos muestran una actividad curativa del 100% en un modelo de ratón infectado por *T. b. rhodesiense*, representan un agente quimioterapéutico potencialmente eficaz para el tratamiento de la enfermedad del sueño.

CONTENTS

LIST OF FIGURES

LIST OF TABLES

ABBREVIATIONS

A	**A**denine
AAC	**A**TP–**A**DP **C**arrier
ADP	**A**denosine **D**i**p**hosphate
Ak	Akinetoplastidy
amp^R	**Amp**icillin resistance gene
APS	**A**mmonium **P**ersulfate
ATP	**A**denosine **T**ri**p**hosphate
AU	**A**symmetric **U**nit
AU-PAGE	**A**cetic Acid – **U**rea **P**oly**a**crylamide **G**el **E**lectrophoresis
BBB	**B**lood-**B**rain **B**arrier
BF	**B**loodstream **F**orm
bp	**B**ase **P**air
C	**C**ytosine
CC	**C**orrelation **C**oeffcient
CC_{50}	Half-Maximal Cytotoxic Concentration (**C**ytotoxic **C**oncentration **50**%)
CCP4	**C**ollaborative **C**omputational **P**roject **N**umber **4**
CD27	4,4'-bis(imidazolinylamino)diphenylamine
CDIV32	4,4'-bis(1-hydroxyimidazolinylamino)diphenylamine
CHUD	**Ch**romatin **U**nfolding **D**omain
CNS	**C**entral **N**ervous **S**ystem
CSIC	The Spanish National Research Council (Spanish: **C**onsejo Superior de **I**nvestigaciones **C**ientíficas)
DAMP	**D**amage-**A**ssociated **M**olecular **P**atterns
DAPI	4′,6-**d**i**a**midino-2-**p**heny**l**indole

Dk	**D**yskinetoplastidy
DMSO	**D**i**m**ethyl**s**ulf**o**xide
DNA	**D**eoxyribo**n**ucleic **A**cid
dsDNA	**d**ouble-**s**tranded **DNA**
dsRNA	**d**ouble-**s**tranded **RNA**
EC_{50}	Half-Maximal Effective Concentration (**E**ffective **C**oncentration **50%**)
EDTA	**E**thylene**d**iamine**t**etraacetic **A**cid
EMSA	**E**lectrophoretic **M**obility **S**hift **A**ssay
FBS	**F**etal **B**ovine **S**erum
FR60	4-((4,5-dihydro-1*H*-imidazol-2-yl)amino)-*N*-(4-((4,5-dihydro-1*H*-imidazol-2-yl)amino)phenyl)benzamide dihydrochloride
G	**G**uanine
gRNA	Small **G**uide **RNA**
GST	**G**lutathione **S**-**t**ransferase
HASO	**H**elical **A**rrangement of **S**tacked **O**ligonucleotides
HAT	**H**uman **A**frican **T**rypanosomiasis
HBSS	**H**anks' **B**alanced **S**alt **S**olution
HEK	**H**uman **E**mbryonic **K**idney
HEPES	(4-(2-**H**ydroxy**e**thyl)-1-**p**iperazine**e**thane**s**ulfonic Acid
HMG	**H**igh **M**obility **G**roup
IBMB	**M**olecular **B**iology **I**nstitute of **B**arcelona
IC_{50}	Half-Maximal Inhibitory Concentration (**I**nhibitory **C**oncentration **50**%)
IDP	**I**ntrinsically **D**isordered **P**roteins
IFN-ß	**I**nter**f**eron **ß**
IM	**I**nner **M**embrane

IMS	**I**nter**M**embrane **S**pace
IP	**I**ntra**p**eritoneal
IPTG	**I**so**p**ropyl β-d-1-**t**hio**g**alactopyranoside
ISM	**I**so**m**etamidium
JNI18	3-chloro-4-((4,5-dihydro-1*H*-imidazol-2-yl)amino)-*N*-(4-((4,5-dihydro-1*H*-imidazol-2-yl)amino)phenyl)benzamide
K	**K**inetoplast
KAP	**K**inetoplast-**A**ssociated **P**rotein
kDNA	**K**inetoplast **DNA**, **K**inetoplast
MAD	**M**ulti-wavelength **A**nomalous **D**iffraction
MAR	**M**atrix-**a**ssociated **R**egion
MGBD	**M**inor **G**roove **B**inding **D**rugs
MIR	**M**ultiple **I**somorphous **R**eplacement
MPD	2-**M**ethyl-2,4-**p**entane**d**iol (hexylene glycol)
MR	**M**olecular **R**eplacement
Mr	**M**olecular Weight **R**ange
mRNA	Ribosomal **RNA**
mtDNA	**M**i**t**ochondrial **DNA**
MW	**M**olecular **W**eight
N	**N**ucleus/**N**uclei
NBD	**N**ucleosomal **B**inding **D**omain
NCS	**N**on **C**rystallographic **S**ymmetry
NECT	**N**ifurtimox-**E**flornithine **C**ombination **T**reatment
NMR	**N**uclear **M**agnetic **R**esonance
OC	**O**pen **C**ircular DNA
OM	**O**uter **M**embrane

PAGE	**P**oly**a**crylamide **G**el **E**lectrophoresis
PAO	**P**henyl**a**rsine **O**xide
PAO	**P**henyl**a**rsine **O**xide
PCR	**P**olymerase **C**hain **R**eaction
PDB	**P**rotein **D**ata **B**ank
PEG	**P**oly**e**thylene **G**lycol
PI	**P**ropidium **I**odide
PTM	**P**ost-**T**ranslational **M**odifications
r.m.s.d.	**R**oot **M**ean **S**quare **D**eviation
RAGE	**R**eceptor for **A**dvanced **G**lycation **E**nd-products
RNA	**R**ibo**n**ucleic **A**cid
RU	**R**esonance **U**nit (binding response)
SAD	**S**ingle-wavelength **A**nomalous **D**iffraction
SAR	**S**caffold-**a**ssociated **R**egion
SC	**S**uper**c**oiled DNA
SDS	**S**odium **D**odecyl **S**ulfate
SI	**S**electivity **I**ndex
SP	**S**ulpho**p**ropyl
spp.	Latin abbreviation for multiple species (**S**pecies **P**luralis)
SPR	**S**urface **P**lasmon **R**esonance
ssDNA	**S**ingle-**s**tranded **DNA**
T	**T**hymine
TAC	**T**ripartite **A**ttachment **C**omplex
TBP	**T**ATA **B**inding **P**rotein
TCA	**T**ri**c**hloroacetic **A**cid
TEMED	N,N,N',N-**Te**tra**m**ethyl**e**thylene**d**iamine

TF	**T**ranscription **F**actors
TFA	**T**rif**f**luoro**a**cetate
TFAM	**M**itochondrial **T**ranscription **F**actor **A**
TMRE	**T**etra**m**ethylrhodamine **E**thyl **E**ster
VDG	**V**ariable **S**urface **G**lycoprotein
WC	**W**atson-Crick (Basepairing)
WHO	**W**orld **H**ealth **O**rganization
WT	**W**ild **T**ype

CHAPTER 1

INTRODUCTION

1.1 The DNA

Nucleic acids are biomolecules essential to all known forms of life. DNA (deoxyribonucleic acid) carries the genetic information used in all vital processes of every living organism, and transfers it from one generation to the next.

The discovery of the DNA structure led to a revolution in biological science and to the foundation of molecular biology. The explanation of the structure of the DNA contributed dramatically to establish the interrelationship of its biological and chemical properties and functions, such as the elucidation of the genetic code (Crick et al., 1961), and thus establishing it as the key molecule of heredity, developmental biology and evolution.

Structural determination of macromolecules has evolved to reach atomic resolution with the use of crystallography and single crystal diffraction, which has contributed significantly to increase the knowledge of properties and functions of nucleic acids over the last 60 years.

1.2 DNA Structure

In molecular biology, DNA duplex, double-stranded DNA and double helix are used to describe the structure of the deoxyribonucleic acid molecule. DNA structure was first published by James Watson and Francis Crick (Watson & Crick, 1953) based upon the crucial X-ray diffraction patterns of DNA obtained by Rosalind Franklin and Maurice Wilkins. They described the double helix as two intertwined helical phosphate-sugar backbones, with the heterocyclic DNA bases projecting inwards from each of the two strands. The two chains are antiparallel (running in opposite directions) and are held together by hydrogen bonds formed between complementary nitrogen base pairs.

DNA is the most important biopolymer for life and consists of repetitive units, called nucleotides (deoxyribonucleotides). Nucleotides are composed of a phosphate group linked by a phosphoester bond to a pentose (specifically a 2'-deoxyribose) that in turn

is linked to a nitrogenous base (Figure 1-1a). DNA encodes information through the order, or sequence, of the short segments of nucleotides called genes, along each strand. Four nitrogenous bases or nucleobases establish the DNA sequence: adenine (A), guanine (G), cytosine (C) and thymine (T).

A DNA strand is a string of nucleotides joined together. Nevertheless, DNA does not usually exist naturally as a single strand molecule. Instead, two strands running in opposite directions are coupled in a double helix structure creating generally very large polynucleotide chains (Figure 1-1b).

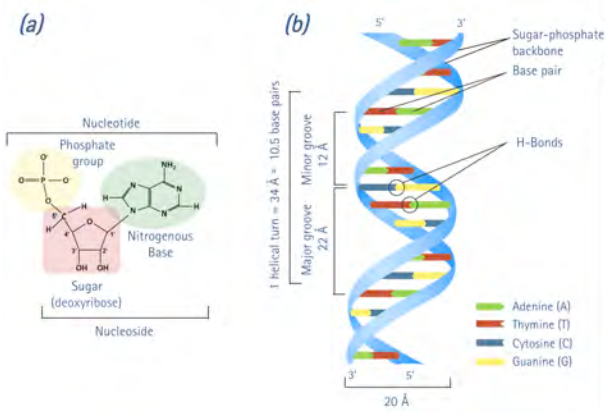

Figure 1-1. Schemes of *(a)* the three elements of a nucleotide and *(b)* the DNA double helix.

DNA is well-suited to perform its biological function because of its molecular structure. DNA geometric properties and configuration determine the base paring interaction, the helix conformation with a major and a minor groove, and the backbone charge distribution, among others (as presented in following sections).

The acidic character of nucleotides is due to the presence of the phosphates, which dissociates at the pH found inside cells, freeing hydrogen ions and leaving the phosphate negatively charged. In the cell, the negative charge of DNA is shielded by its association with positive proteins. It also allows the interaction with other ligands, such as small molecules that bind the DNA helix.

1.2.1 Base Paring and Stacking

The reasons behind the stability of the three-dimensional structure of DNA double helix are mainly the base pairing between complementary strands and the stacking between adjacent bases (Yakovchuk et al., 2006).

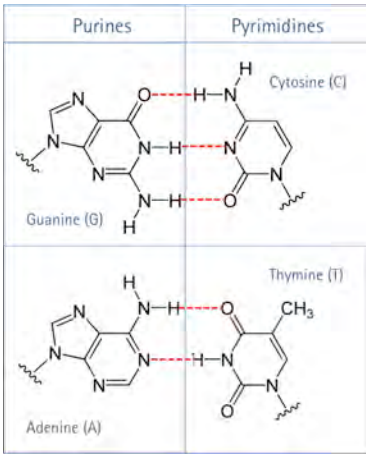

Figure 1-2. Chemical structures and classification of the DNA nucleobases. Red dotted lines show the hydrogen bonds between adenine and thymine (AT) and guanine and cytosine (GC).

DNA base pair complementarity is achieved by interactions between nucleobases. These bases are heterocyclic compounds with the rings containing nitrogen and carbon (Figure 1-2). Adenine and guanine belong to the purine group, while thymine and cytosine are pyrimidines. Both types of molecules complement each other with the opposing type of nucleobase, held together by hydrogen bonding. For an H-bond to occur there must be a donor group (-NH_2 or –NH) and an acceptor group with at least one lone pair of electrons (C=O or N). Thus, the base complement adenine and thymine (AT) shares two hydrogen bonds, while the base pair guanine and cytosine (CG) has three hydrogen bonds (Yakovchuk et al., 2006) (Figure 1-2).

DNA denaturation occurs when hydrogen bonding between nucleotides is disrupted by applying mechanical force, high temperature, or chemical treatment, among other factors. This results in the separation of previously annealed strands into two single strands. This permits the DNA strands to unzip for biologically important mechanisms

such as DNA replication, transcription and DNA repair (Sicard et al., 2016). However, this process is reversible. DNA can be recovered as the fully base-paired duplex.

Figure 1-2 shows the Watson-Crick (WC) base pairing, which is the most common base pairing configuration. Nevertheless, there are different types of base pairing dictated by specific hydrogen bonding patterns, such as the Hoogsteen base pair (Hoogsteen, 1963; Abrescia, 2002; Abrescia, 2004; Acosta-Reyes et al., 2015) and Wobble (Crick, 1966; Varani & McClain 2000), which can be formed under specific circumstances.

The base stacking is due to pi bonding (π-π), which involves interactions between delocalized electrons in p-orbitals of the aromatic rings of the nucleobases. This includes a combination of van der Waals and dipole-dipole interactions between the bases. These hydrophobic, electrostatic interactions in which two or more bases are positioned with the planes of their rings parallel are the other essential mode of collaboration between bases in DNA. Undoubtedly, base stacking interactions are important contributors to duplex stability and also significantly contribute to the dependence of the duplex stability on its sequence, as well as its flexibility (Travers, 2004).

Pi stacking plays an important role in DNA crystal structures, stabilizing the typical configuration of columns in a helical arrangement of stacked oligonucleotides (HASO) (Campos et al., 2006). Base stacking interactions also contribute to the interactions between small-molecules and proteins. As a result, pi-pi and cation-pi interactions are important factors in rational drug design (Babine et al., 1997).

1.2.2 Minor and Major Groove

In the duplex structure, the bases of one strand are paired with the complementary ones and are localized in the cavity left between the two backbones. In the common conformation of DNA, the backbones of the two strands exhibit two helical grooves because of their antiparallel arrangement. They are closer together on one side of the helix than on the other due to the glycosidic bond formed between the ribose group

and a nitrogen base group in both nucleobases of the base pair, exposing different parts of the nitrogenous bases.

The major and minor grooves are opposite to each other, and each runs continuously along the entire length of the DNA molecule. The major groove has 22 Å of width while the minor groove has12 Å. In B-DNA, the height of one helical turn measures 34 Å, equivalent to 10.5 base pairs (see Figure 1-1b).

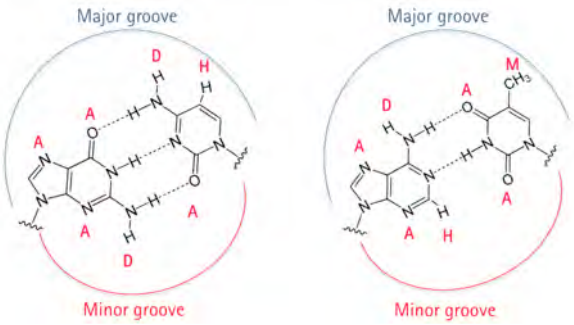

Figure 1-3. The minor and major grooves for B-form DNA for the base pairs GC (left) and AT (right). A, acceptor; D, donor; H, hydrogen; and M, methyl.

The sides of each base pair are exposed so the minor and the major grooves generate patterns of donors and acceptors for hydrogen bonds and van der Waals interactions specific to each base pair (Figure 1-3). The codes of chemical groups A-A-D-H and its reverse pattern, H-D-A-A in the major groove specify the identity of the GC and CG pairs of bases respectively. Similarly, the patterns A-D-A-M and M-A-D-A uniquely identify AT and TA base pairs, respectively. This allows DNA binding proteins involved in biological processes to unequivocally recognize a DNA sequence. However, the minor groove's codes A-D-A and A-H-A don't display such explicit information. Nevertheless, it appears that minor groove electronegative potential may contribute significantly in guiding proteins to their binding sites in the genome (Lindemose et al., 2011).

The grooves' parameters change in every DNA type (see section 1.2.3). However, changes are also function of the base paring and sequence composition. These sequence specific variations and parameters of the DNA grooves play a vital role in DNA-ligand identification.

DNA-ligand interactions through the major groove mainly tend to associate with proteins and through the minor groove with small molecules; since the minor groove is assumed too narrow to accommodate protein structures without energetically costly distortions. While the major groove dimensions remain very similar in free and bound DNA, the minor groove is particularly variable in complexes (Oguey et al., 2010). However, the importance of the minor groove in DNA-protein complexes has risen by the increasing number of X-ray structures found (Morávek et al., 2002).

1.2.3 DNA Parameters

In DNA, the 2-deoxirybose is a five-carbon sugar linked to the phosphate group by phosphodiester bond to the third and fifth carbons of the adjacent sugars. This irregular bonding to C3' and C5' confers specific orientation of the bases on each DNA strand. Thus, a 5'-end of a strand means that only a phosphate group is attached to the fifth carbon atom of the pentose sugar of that nucleotide. On the other hand, 3'-end of a strand is when the third carbon atom of the pentose sugar of the terminal nucleotide ends with a hydroxyl group. The antiparallel disposition between the two strands of the DNA duplex confers its directionality: one strand runs 5' to 3' while the other one runs 3' to 5'. DNA can only be synthesized *in vivo* in the 5' to 3' direction.

DNA folding and structural conformation is determined by a set of backbone parameters, including the six main chain torsion angles (α, β, γ, δ, ε, and ζ) around the covalent bonds and one more (χ) related to the glycosidic bond (Figure 1-4a). The five endocyclic torsion angles for the bonds of the sugar pucker are denoted by the symbols ν_0, ν_1, ν_2, ν_3, and ν_4, (Figure 1-4b). All these torsional angles confer a large number of degrees of freedom to the DNA single strand, which are limited when the double helix takes place. The permissible values depend on the adopted conformation (Schneider et al., 1997; see section 1.2.4). The backbone torsion angles are defined in Table 1-1.

The sugar group occupies a crucial position in the nucleotide unit because it forms part of both the backbone and the side chain. Since the sugar ring is non-planar and

flexible, it can adopt different configurations, being the C3'-endo for A-DNA and the C2'-endo for B-DNA the most common ones.

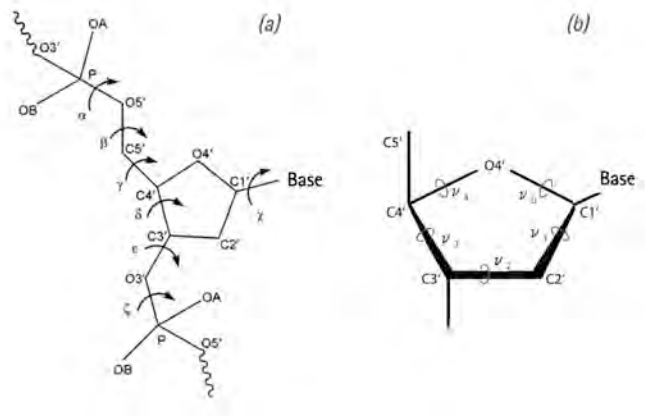

Figure 1-4. ***(a)*** **Torsion angles for backbone conformations of the *i* th nucleotide in polynucleotide chains.** ***(b)*** **DNA sugar group and its torsion angles ν_0, ν_1, ν_2, ν_3, and ν_4.**

The intrinsic flexibility of the DNA allows it to bend on local scales to facilitate genome-based processes such as transcription, DNA repair and replication (Garcia et al., 2007). Besides, in the highly packed state, genomic DNA is bent substantially to fit into the volume of a cell or cell nucleus, employing small architectural proteins that bend the DNA to compact the genome (Luijsterburg et al., 2008).

The mechanical properties that give DNA its flexibility are sequence dependent (Sarai, et al., 1989). The physical and chemical properties of each nucleotide will define the base step interactions with torsional and bending specific parameters.

Table 1-1. Atoms involved in the backbone and sugar torsion angles.

α : $O3'_{(i-1)} - P - O5' - C5'$	β : $P - O5' - C5' - C4'$
γ : $O5' - C5' - C4' - C3'$	δ : $C5' - C4' - C3' - O3'$
ε : $C4' - C3' - O3' - P_{(i+1)}$	ζ : $C3' - O3' - P_{(i+1)} - O5'_{(i+1)}$
$\chi_{pyrimidines}$: $O4' - C1' - N1 - C2$	$\chi_{purines}$: $O4' - C1' - N9 - C4$
ν_0 : C2' – C1' – O4' – C4'	ν_1 : C3' – C2' – C1' – O4'
ν_2 : C4' – C3' – C2' – C1'	ν_3 : O4' – C4' – C3' – C2'
ν_4 : C1' – O4' – C4' – C3'	

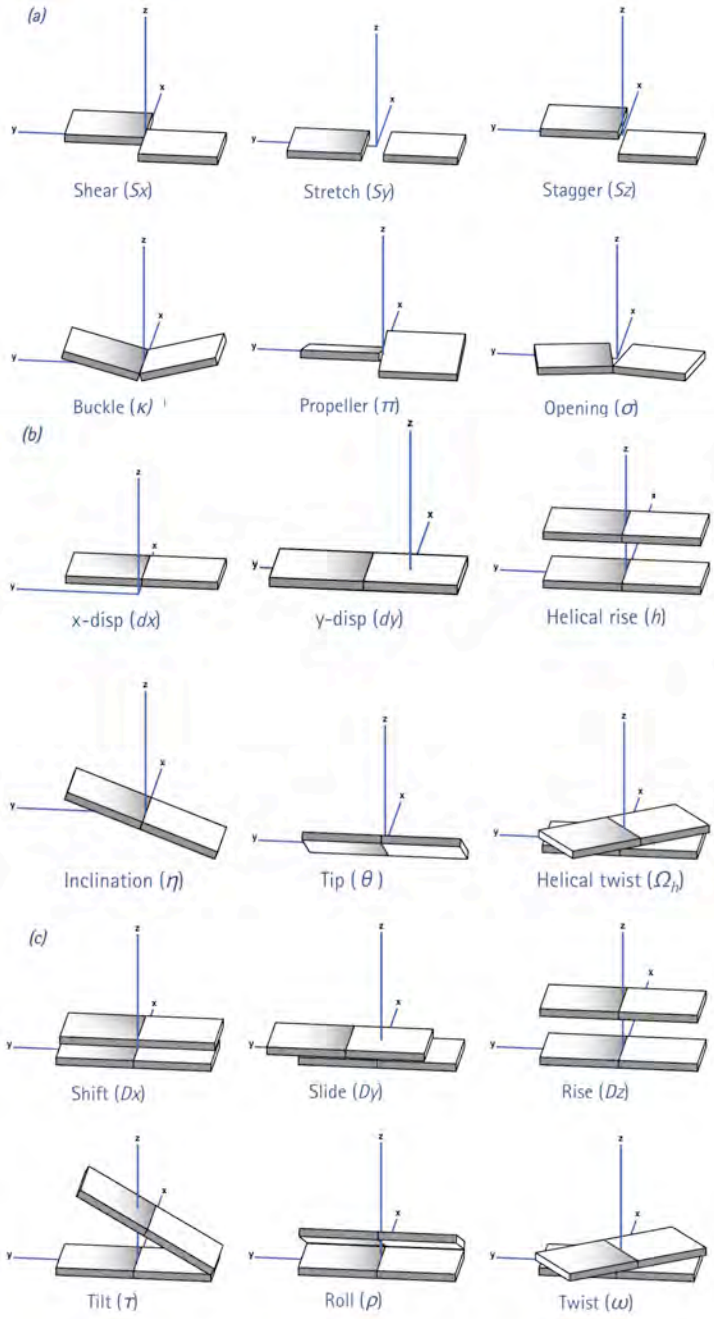

Figure 1-5. Base pair parameters classification by rotations and translations. *(a)* Local base pair parameters, *(b)* local base pair helical parameters, and *(c)* local base pair step parameters.

DNA capacity to adopt a particular conformation entails important biological consequences (Travers, 2004). The formation of a DNA-protein complex not only can be achieved by the recognition of a particular sequence, but also by the identification of specific configurations of torsion and bending when nonspecific binding proteins have preference for certain DNA structural features (Heddi et al., 2010).

DNA molecules do not have a perfect double helix. There are various structural variations of the strands and helices according to every individual base pair, as well as the neighboring base pairs along the duplex. The study of the morphology of the bases allows the knowledge and identification of many features and deformations of nucleic acids structures related to the sequence. In order to standardize those variations, a set of parameters was defined according to the Cambridge convention (Dickerson, 1989; Lu & Olson, 2003):

- Parameters for individual base pairs:
  - Local (or complementary) base pair parameters: the relative position and orientation between bases of a base pair (Figure 1-5a).
  - Local base pair helical parameters: the position and orientation of a rigid body formed by one base pair (Figure 1-5b).
- Parameters for local base pair step: the relative position and orientation from one base pair to its adjacent (Figure 1-5c).

1.2.4 DNA Double Helix Forms

Previous sections have described the most common DNA-form described by Watson and Crick, called B-form. Nevertheless, there are other theoretical DNA conformations such as A, C, D, Z. However, only forms A, B and Z exist within the cells of living organisms (Figure 1-6).

The helical structure of DNA is variable and depends, among other factors, on the nucleotide sequence, hydration, chemical modifications and superhelical tension. Furthermore, the ionic character of the backbone makes the DNA especially sensitive to

local environment, with DNA-ligand interactions that often lead to a change of conformational state (Lu & Olson, 2003).

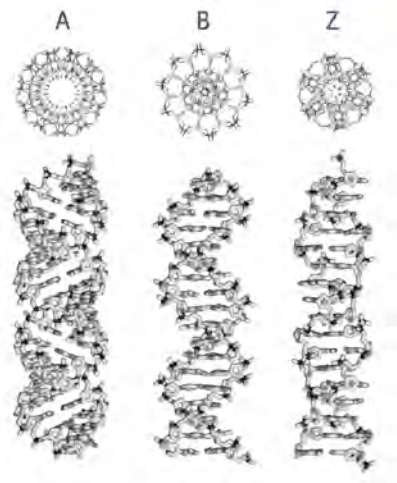

Figure 1-6. Top and side views illustrating the characteristic features of regular helical structures of DNA forms A, B and Z. Generated by parameters reported in (Lu & Olson, 2003).

Table 1-2 lists the structural parameters for the three structural families of DNA helical conformations. B-DNA is the term given for the canonical DNA helix and consists, as mentioned before, in a double helix made of two antiparallel strands that are held together via hydrogen bonding in the AT and GC base pairs. In B-DNA the distance between the bases (rise) is 3.4 Å and the diameter of the helix is 20 Å (Figure 1-1b). However, crystallographic studies of oligonucleotides had shown significant sequence-dependent flexibility of the parameters on B-DNA helix listed in Table 1-2. The A- and B-DNA families are right-handed (dextrorotatory) helices, while the Z-DNA family has a left-handed orientation of the helix (levorotatory).

The A-DNA form has eleven base pairs per helical turn, a tilt of about 20 Å with respect to the helical axis and an average rise of 2.55 Å, resulting in a shorter and more compact helix where the base pairs are not perpendicular to the helix-axis as in B-DNA. The major groove of A-DNA is narrower and deeper, while the minor groove is wide and slightly shallower. The sugar pucker is C3' endo compared to C2' endo for B-

DNA and the base pairs are shifted to the helix edge, which generate a 9 Å hole in the centre of the helix.

In 1952, Rosalind Franklin discovered and named the A and B form, and she also established that A-DNA conformation occurs in non-physiological dehydrating conditions (Franklin & Gosling, 1953). This explains the incidence of A-DNA structures found by X-ray crystallography; as such conditions are commonly used to form crystals. However, A-DNA form has been identified as the most biologically active non-B-DNA conformation.

Table 1-2. Structural parameters of DNA configurations.

Structural Parameter	A-DNA	B-DNA	Z-DNA
Direction of helix rotation	Right handed	Right handed	Left handed
Residue per helical turn	11	10.5	12
Axial rise per residue	2.55 Å	3.4 Å	3.7 Å
Pitch (length) of the helix	28 Å	33.2 Å	44.6 Å
Base pair tilt	20°	-6°	7°
Rotation per residue	32.7°	34.3°	-30°
Diameter of helix	23 Å	20 Å	18 Å
Configuration dA, dT, dC	anti	anti	anti
of glycosidic bond dG	anti	anti	syn
Sugar Pucker dA, dT, dC	C3' endo	C2' endo	C2' endo
dG	C3' endo	C2' endo	C3' endo

Values from Potaman & Sinden, 2013.

The B- to A-DNA conformational transition *in vivo* is reversible, cooperative and comes from many different aspects including the sequence, the hydration level and the interactions with enzymes, ions and ligands involved in biologically relevant reactions (Whelan et al., 2014). This helical conformation occurs in double-stranded **r**ibo**n**ucleic **a**cids (dsRNAs), and in DNA-RNA hybrid double helices. Specific sequence repeats such as 5'-CC-3' and 5-'ACT-3', that present predisposition to adopt an A-DNA have been found (Feig & Pettitt, 1998). Other authors found preference for CG-rich sequences to assume A-form most easily, attributed to the ability of cytosine to switch to C3' endo and have been confirmed by quantum mechanics calculations and nuclear magnetic resonance study of 11-mer duplex (Tolstorukov et al., 2001). Added to this,

experimental and theoretical studies have confirmed that some sequences as the A-tracts can generate intermediate DNA conformations with specific structural parameters like the *B-DNA (Hud & Plavec, 2003).

The third active form of duplex DNA has an outstandingly different, left-handed helical structure with a pronounced zig-zag pattern in the phosphate-sugar backbone (Wang et al., 1979). Z-DNA is formed by short stretches of alternating purines and pyrimidines, particularly poly(dG-dC)$_2$, in negatively supercoiled DNA, or at high salt concentrations. The sugar of the G nucleotide is in the C3' endo conformation, but the guanine base is in the *syn* conformation, positioned the guanine back over the sugar ring; while in A- and B-DNA guanine adopts the common and most favoured *anti* orientation (Figure 1-7). This *syn* conformation is the responsible for the laevorotatory structure. Z-DNA has twelve bases per turn with a rise of 3.8 Å; the grooves, unlike A- and B-DNA, show little difference in size.

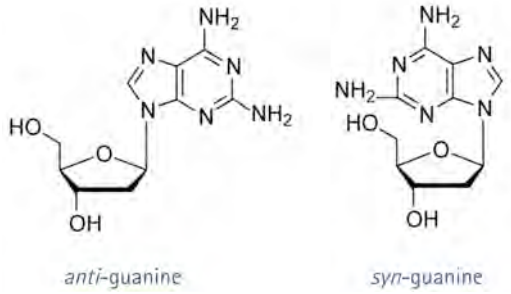

Figure 1-7. Structures of *anti* and *syn* guanine nucleoside conformations.

Z-DNA only exists in a small amount of the DNA, and is difficult to study due to its instability. Although its biological role has not been fully elucidated, proteins involved in transcriptional activity that recognize and bind Z-DNA with great specificity have been found (Oh et al, 2002).

The transition from B- to Z-DNA occurs, despite it is a higher energy conformation, under physiological salt conditions when cytosine is methylated (Behe & Felsenfeld, 1981). This transition can also form an intermediate called B-to-Z junction box, which is involved in the base pair extrusion (De Rosa et al., 2010; Martinez de Ilarduya et al., 2010).

1.2.5 DNA Structural Scales

The elaborate three-dimensional shape of biomolecules can be explained at any of several organization levels starting from the level of individual atoms until complex organizations between two or more biopolymers. The DNA structural scale classification is expressed in four levels: primary, secondary, tertiary and quaternary (Figure 1-8).

Primary Structure

The primary structure of a nucleic acid describes the detailed atomic composition and the chemical bonds connecting those atoms. Hence, DNA primary structure refers to the exact sequence of nucleotides and the phosphodiester bonds that comprise the chain starting from the 5' end to the 3' end.

Secondary Structure

The secondary structure defines the pattern of hydrogen bonds in a biomolecule. In DNA, it is determined by the intramolecular H-bonds between the nucleobases of one strand with its complementary one. This structural level described the double helix of the DNA molecule formed by two strands of nucleotides in antiparallel position, held together by the formation of the hydrogen bonds between nucleobases associated to both strands, where the base pairing geometry and helical parameters variations can create different arrangement of DNA as A, B, Z, and others (see section 1.2.4).

These interactions between bases occur only when a purine pairs a pyrimidine (see section 1.2.1). Besides the canonical Watson-Crick base pairing, where CG base pairs are bound by three hydrogen bonds whilst AT base pair forms two H-bonds, variations between the base pairing conformation can generate alternate hydrogen bonding patterns, such as the Wobble base pair and Hoogsteen base pair. Moreover, DNA can adopt other secondary structures by the presence of mismatches or changes in the complementarity between bases such as bulges, internal loops, hairpin loops and junctions.

Tertiary Structure

The tertiary structure of a DNA molecule comprehends its three-dimensional structure, as defined by the atomic coordinates in space. The ability of DNA to fold into highly compact and extremely ordered 3D forms leads to this structural scale.

Both linear and circular DNA molecules can rotate, twisting around each other, to adjust to changes of various dynamic processes in the cell triggering supercoiled DNA, which is the tertiary structure of DNA (Figure 1-8). Supercoiling, specifically the negative one, can cause B-DNA to adopt a four-armed, cruciform structure that resembles a Holliday junction, or stabilize three-stranded triplex DNA (Bochman et al., 2012). Macro helices and other non-canonical structures like triplexes and quadruplexes formed in telomeres are also included in the tertiary level of structure.

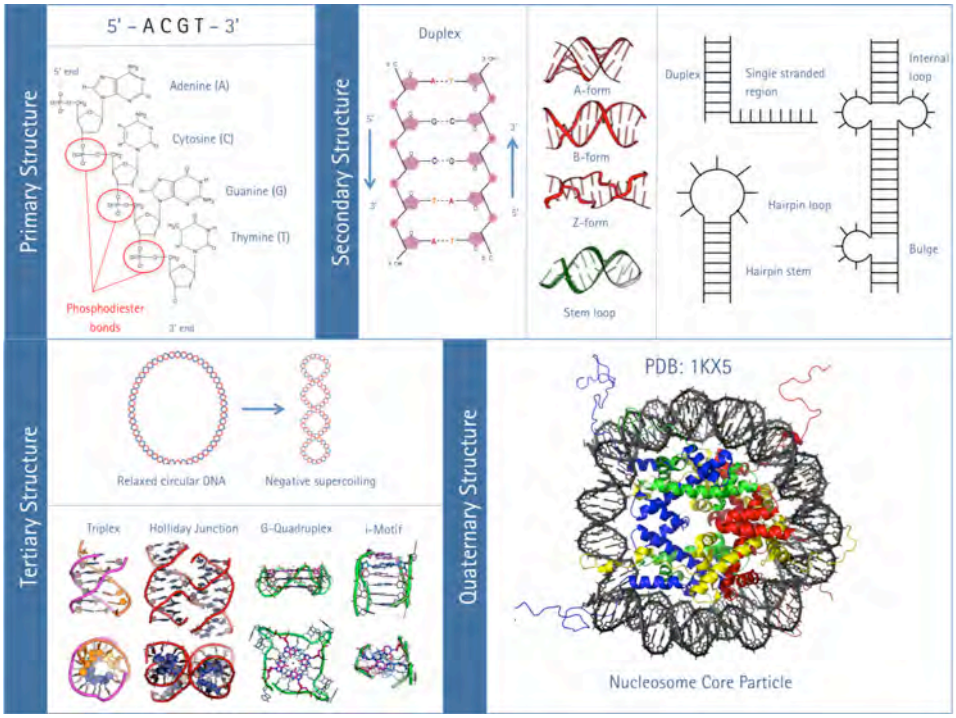

Figure 1-8. The four structural scales in DNA.

The Quaternary Structure

The quaternary structure is the higher level of organization and it refers to the interactions between two or more nucleic acid molecules, or between nucleic acid molecules and proteins. The most commonly seen form of this DNA structural scale is the interaction with the nuclear proteins histones to create nucleosomes when DNA packing in eukaryotic chromatin takes place (Figure 1-8). DNA quaternary structures change constantly according to the regions of genes needed to be transcript or during DNA replication.

1.3 AT-Rich DNA

High AT-content in the range of 70% or more is called AT-rich DNA. AT-rich sequences can form motifs located strategically in the genome to perform a particular function. These repeated sequences are present in the sites for DNA replication initiation in both eukaryotic and prokaryotic replicons, as binding places or regulatory factors for the appropriate replication initiation protein. The AT-rich fragment of the replication origin represents the most ubiquitous conserved structural element identified in all replicons (Rajewska et al., 2012). This AT-rich sequence contains the DNA unwinding element (DUE), where the initial DNA helix destabilization (unwinding) occurs during the process of replication initiation (Kowalski & Eddy, 1989; Carr & Kaguni, 2001).

The AT-rich regions constantly play an important role in the regulation of gene transcription through the ability to influence transcription factors (TFs) and chromatin proteins. The TATA box is an AT-rich DNA sequence found in the promoter region of genes that facilitates easy unwinding and bending of the DNA double helix during the process of transcription by the TATA binding protein (TBP; Roeder, 1996). The matrix attachment regions (MARs) are AT-rich DNA sequences that could facilitate dynamic processes in chromatin structure allowing accessibility to transcription factors at their binding sites (Hart & Laemmli, 1998; Petersen el al., 2002), such as the transcriptional regulation protein SATB1, which recognizes and binds specific regions of MARs in order to fold chromatin into loop domains (Yasui et al., 2002; De Belle et al., 1998).

H1 histone preferentially binds AT-rich DNA to repress their transcription and therewith to contribute to chromatin condensation (Roque el al., 2004, Flickinger, 2015). The chromatin proteins called HMGA (High mobility group A) are able to bind DNA in AT-rich regions and regulate gene expression by acting as architectural proteins (see section 1.5.1.1; Baldassarre et al., 2005).

In spite of the identification of many AT-rich motifs, the fully knowledge about the AT-rich regions is limited. Nevertheless, it is important to emphasize the strong relationship between the two main functions of the AT-rich sequences in the genome: the protein recognition and the structural peculiarities. These structural distinctions have been specially studied within the A-tracts. Formed by four adenine and/or thymine nucleotides, the A-tracts are a universal DNA element in regulatory regions of many organisms (Haran & Mohanty, 2009). When they are inserted in phase with the helical periodicity, these motifs present a narrow minor groove and an unusual DNA form due to its flexibility, giving rise to a global curvature of the DNA double helix and increasing stability of the DNA complexes with architectural proteins (Hizver et al., 2001; Tolstorukov et al., 2005).

1.3.1 Non-coding DNA

Firstly called "junk DNA" because its supposed lack of biological functions for the organism, the non-coding DNA are sequences in the genome that do not encode protein sequences. Although the functions of the non-coding sequences are not completely clear yet, researchers have shown that a large fraction of this DNA is transcribed and plays an important role in the regulation of differential gene expression by the transcription of non-coding RNAs (Mattick, 2009). Other sections of non-coding DNA provide regulatory sites (i.e., binding sites where transcriptional proteins can bind to enhance or inhibit transcription), or act as structural elements involved with chromatin and other architectural DNA components (Narlikar & Ovcharenko, 2009).

Non-coding DNA corresponds to the vast majority of the entire genome and is composed by repeated sequences, usually regions that contain an above average number of adenine and thymine bases (Campos et al., 2006).

The distinctive features of AT-rich DNA are based on its structural and mechanical properties. The low thermodynamic stability of AT-rich regions causes the relatively easy melting of the double helix, but provides also flexibility and high degree of polymorphism.

1.3.2 AT-Rich Organisms

The ratio between the four nucleotides in organism genomes is not equal and the shifts to very high AT or CG content levels can occur in many different proportions for every living system. Hence, *Dictyostelium discoideum* is an example of AT-biased genome with 78% of AT content, while *Streptomyces ceolicolor A3(2)* with only 28% of AT content is an example of a CG-rich genome. Shifts to very high AT or GC levels can occur in several distinct branches of the tree of life. The underlying reasons for these shifts therefore may be of different origin (Szafranski at al., 2005).

The singular properties of the AT-rich DNA and the necessity to understand the unknown biological functions of certain AT-rich sequences encourage our interest on organisms with high AT content. This includes various parasites, like the human malaria parasite *Plasmodium falciparum*, which has a genome with extremely high AT content (80%) and numerous repetitive sequences (Gardner et al., 2002). Another example are species of kinetoplastid parasites, such as the genus *Trypanosoma* present a kinetoplast (see section 1.7.2) with high content of adenines and thymines (around 70%).

The reason why the DNA of these organisms is constituted mainly by AT is not clear. Comparison of the genomes of *P. falciparum* and *D. discoideum* shows that the slightly higher AT content of *P. falciparum* genome compared to *D. discoideum* (80.1 versus 77.4%) is not achieved by increased AT richness in intergenic regions. Instead, both the shift of the nucleotide usage in coding regions to AT-rich codons and the longer

intergenic regions make an equal contribution to the higher AT content in this organism (Szafranski at al., 2005).

1.3.3 Importance of AT-Rich Regions in Target Site Recognition

Previous sections have listed several AT-rich regions that are implicated in gene regulation and DNA folding processes. Those regions act as specific binding sites for certain proteins and their accessibility is crucial to achieve the protein-DNA binding and thus, the right performance of DNA functions. Therefore, the ability to disrupt or to direct changes in gene activity and replication functions can be performed by other molecules such as drugs that specifically target these sequences.

An example is the nucleosome disruption by the DNA binding drug DAPI (Fitzgerald & Anderson, 1999). DAPI specificity for AT sites creates a DNA-drug interaction that prevents the nucleosome from forming on the DNA bending, leading to a histone-free DNA during the assembly reaction. Opposite structural changes in the chromatin structure are caused by distamycin A, a drug that preferentially binds to AT-rich DNA (Radic, Lundgren, & Hamkalo, 1987). In this case, the drug distamycin A induces the compaction of the chromatin by two mechanisms: linker DNA bending and internucleosomal angle contraction. Changes in chromatin packing may directly affect protein binding, altering the recognition of genes towards transcription factors (Majumder & Dasgupta, 2011).

Some other AT-rich DNA-protein interactions could be not favourable for the cell health. This research works focuses on the subfamily of proteins HMGA, which binds preferentially to AT-rich DNA regions of the chromatin and their overexpression is a hallmark of several metastatic cancers (Hock et al., 2007) (explained in detail in section 1.5.1.1). Studies on the use of drugs to directly interfere with the DNA-HMGA binding have found that the drugs distamycin (Smith & Buchmueller, 2011) and netropsin (Miao et al., 2008) cause a displacement of HMGA protein motifs from the DNA, acting as competitors for the same binding site. Furthermore, the DNA-

intercalator drug cisplastin seems to enhance sensitivity in mouse embryonic stem cells with high expression levels of HMGA1 proteins (Baldassarre et al., 2005).

One of the main focuses of this research work is the study of the DNA as a biological target for antiparasitic drugs, particularly against *Trypanosoma brucei*, the causative agent of African sleeping sickness. The kinetoplast of this parasite is particularly AT-rich, with about 73% of AT content (Chen & Donelson, 1980) and thus, presents a likely target for diamidines who bind the minor groove of parasitic DNA (Scott et al., 2016). DNA-binders with preference for AT sequences as the aromatic dications pentamidine, diminazene, furamidine and several derivatives are being used against different strains of *T. brucei*, showing high efficiency but, in some cases, toxic side effects (Wilson et al., 2008; Scott et al., 2016).

1.4 DNA-Ligand Binding

In DNA-ligand binding studies, the ligand can be a drug (small molecule), an ion or a protein, which binds to the DNA duplex. The interaction between the DNA and the ligand may be function of charge, hydrophobicity or structural features, and occurs generally by intermolecular forces, such as ionic bonds, hydrogen bonds and van der Waals forces. When the DNA-ligand binding occurs, it may induce conformational changes in the DNA, the ligand or both.

The tendency or strength of a ligand to interact with its binding sites can be measured in terms of a binding affinity. In addition to the DNA and the ligand, the solvent plays a very important role in binding recognition and affinity since it provides the environment to drive or reject the binding (Baron, et al., 2010).

1.5 DNA-Protein Interactions

DNA-protein interactions control a number of important cellular processes: transcription factors modulate the process of transcription; various enzymes including polymerases and topoisomerases are present during replication and transcription; and

chromosomal proteins such as histones or HMG proteins are involved in chromosome packaging.

Some DNA-protein interactions are mediated by DNA flexibility, particularly when architectural proteins are involved. Factors like temperature and nucleotide sequence contribute in the DNA intrinsic flexibility (Driessen et al., 2014; Geggier & Vologodskii, 2010).

The binding can occur to specific sequences or through non-specific DNA-binding proteins, and they could present affinity for either single or double stranded DNA. Nevertheless, all DNA-binding proteins are composed of domains where the binding takes place. Most of the binding proteins interact with the major groove of the DNA helix. However, the HMG proteins bind to the minor groove of the double helix. Basically every biological function of DNA depends on site-specific DNA-binding proteins finding their targets (Halford & Marko, 2004).

1.5.1 HMG proteins

The 'High Mobility Group' (HMG) is a family of ubiquitous and abundant non-histone nuclear proteins. The main function of HMG proteins is to coordinate and facilitate DNA-directed nuclear processes by producing structural changes in the structure of DNA and in the organization of the chromatin fiber (Bustin, 1999; Reeves, 2010).

Discovered in the early 1970s, the HMG proteins receive their name according to their electrophoretic mobility in polyacrylamide gels. They were characterized by having low molecular weight and high content of positively charged amino acids (Goodwin, 1973). According to their DNA binding motifs, HMG proteins are classified into three families (Table 1-3): HMGA, HMGB and HMGN, previously called HMG-I/Y, HMG-1/2 and HMG-14/17 respectively. The members of each family are ubiquitously and abundantly expressed in most eukaryotic cells. Although they display different binding domains and structures, all of them act as architectural factors (Štros, 2010).

The execution of vital cellular processes involves multiple changes in gene expression where the structure of the nucleosome and the chromatin play a central role. Therefore proteins like the HMG family, which contribute in remodeling the assembly of chromatin, are crucial mediators of proper or abnormal cellular development (Hock et al., 2007).

HMG proteins are involved in many biological processes such as cellular differentiation, embryonic development, transcription regulation and DNA repair modulation. However, each HMG family influences different sets of those processes.

Table 1-3. The three HMG protein families and their main characteristics.

Family	Motifs & Diagram	N· residues	Interactions with DNA
HMGA	AT-hook 	95-178	Bind AT-rich DNA stretches in the minor groove
HMGB	HMG-Box 	199-214	Bind into the minor groove of DNA with limited or no sequence specificity
HMGN	Nucleosomal Binding Domain 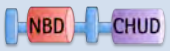	98-406	Bind inside Nucleosomes, between DNA spires and the histone octamer

The main structural features, size and DNA binding specificities of HMGs are shown in the table. HMGAs contain three AT-hooks (green) and HMGB have two HMG-boxes (orange), both contain an acidic C-terminal end (purple). HMGN includes a Nucleosomal Binding Domain (NBD, red) and a negatively charged C-terminal region named chromatin unfolding domain (CHUD, purple).

The HMGA family is constituted by four members: HMGA1a, HMGA1b, HMGA1c and HMGA2. All of them contain three AT-hook motifs, except the HMGA1c which contains only two. The AT-hooks are segments of seven to nine amino acids unstructured in solution, which bind to the minor groove of AT-rich DNA regions. In mammalians, the members of the HMGB family are: HMGB1, HMGB2, HMGB3 and HMGB4. Each of them contains two HMG-boxes and an extended acidic C-terminus. The HMG-box domain presents about 75 amino acids and binds also to the minor groove of DNA but, in this case with limited or no sequence specificity. The third and last family is the HMGN composed by six members: HMGN1, HMGN2, HMGN3a, HMGN3b, HMGN4 and HMGN5 (previously called NSBP1). The HMGN proteins are characterized by the

presence of a positively charged nucleosomal binding domain (NBD) with 30 amino acids through which they bind specifically to the nucleosome core.

HMG proteins interactions with DNA and other proteins are highly regulated by extensive post-translational modifications (PTMs). Essential participants in the performance of nuclear functions, PTMs in HMG proteins include phosphorylation, acetylation, methylation, glycosylation and ADP-ribosylation (Zhang & Wang, 2010).

The mechanisms by which HMG proteins alter the chromatin structure vary according to each member of the family. HMGAs and HMGBs can facilitate the binding of additional proteins (as TFs) by DNA bending activity (Reeves, 2001; Bianchi & Agresti, 2005). On the other hand, the DNA-HMGN complex is able to either prevent or assist the access of modulating factors to chromatin (Lim et al., 2005). HMGA proteins as HMGNs, bind to nucleosomes and as part of regulatory multiprotein complexes can modulate the nucleosome flexibility, compacting or unfolding the chromatin. HMGA competes with histone H1 for binding sites in the chromatin. The interactions HMGA-H1-nucleosome provide flexibility to the chromatin structure affecting its functions (Bianchi & Agresti, 2005).

As specific modulators of chromatin, HMG proteins impact various cellular functions and affect the development and diseases. HMGs are present during embryonic development and most of them are gradually down-regulated until their absence or low expression in adult tissues (Fusco & Fedele, 2007). Overexpression of HMG proteins alters the cellular phenotype and may lead to anomalies such as developmental defects, diseases and cancer. Hence, high levels of expression of some HMGAs and HMGBs represent a feature (biomarker) of malignant tumours and are strongly related to neoplastic cell transformation (Fusco & Fedele, 2007; Shah & Resar, 2012).

1.5.1.1 HMGA

The human high mobility group A (HMGA) proteins comprise two types of proteins (HMGA1 and HMGA2) produced by different genes. The first group includes three proteins encoded by alternative splicing of the same gen: the two abundant variants

HMGA1a and HMGA1b, and one unusual variant, the HMGA1c. The HMGA2 protein is encoded by a different gene (Figure 1-9).

The HMGA1a protein is composed of 107 amino acids, HMGA1b has 96, HMGA1c 179 and HMGA2 comprises 109 residues. All HMGAs have a similar structure and are conserved during evolution. Each protein contains three domains named AT-hooks (except HMGA1c which only has two), through which they bind the minor groove of DNA, and an acidic carboxy-terminal tail which role is still unknown although it may be important in modulating protein-protein interactions (Cleynen & van de Ven, 2008) (Figure 1-9). AT-hook motifs bind AT-rich sequences but, rather than be sequence-specific DNA binding proteins, the HMGA proteins recognize particular structures of the DNA helix.

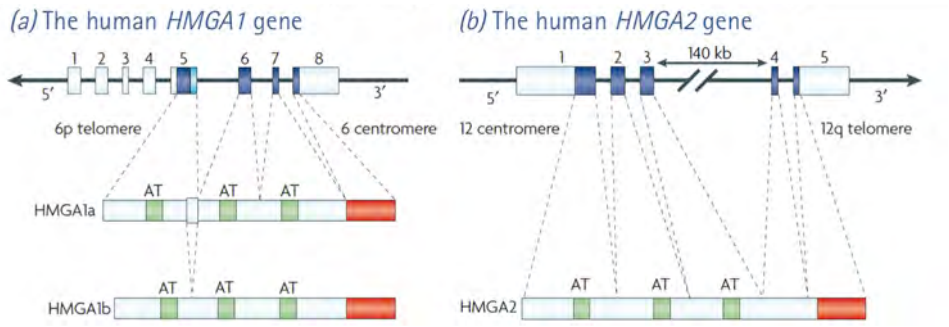

Figure 1-9. Schematic representation of the HMGA human protein-coding gens. Black arrows indicate the direction of the gene in the chromosome and their boxes illustrate their respective exons. Dark blue boxes represent the exons transcribed in mRNA and code for HMGA proteins. AT-hooks are shown in green and acidic C-terminal region in red. Adapted from Fusco & Fedele, 2007.

Figure 1-10 shows the primary structure of the HMGA proteins. The AT-hook motif is a positively charged nine amino acid tract with a central repeat Pro-Arg-Gly-Arg-Pro (AT-hook I contains a glycine instead of the first proline), flanked by flexible and positively charged residues. Furthermore, at their C-terminal end, the HMGA proteins, except for HMGA1c, have a high content of negatively charged acidic residues. Secondary and tertiary structures of HMGAs in solution are not defined since they belong to the intrinsically disordered proteins (IDP) group, that is to say, they lack a

fixed or ordered three-dimensional structure. However, the central element of the AT-hook induces structure formation upon binding with DNA (Slama-Schwok et al., 2000). In reality, the structural changes are induced in both, protein and DNA when the interaction occurs (Dunker et al, 2008).

Figure 1-10. Amino acid alignment of human HMGA proteins. Unique sequences are indicated by lowercase letters. AT-hook central invariant repeat R-G-R-P is shown in green boxes and C-terminal acid tail in purple boxes. BLAST [http://blast.ncbi.nlm.nih.gov/Blast.cgi#].

Hence, the study of DNA-HMGA interactions through structural studies has been challenging. A couple of decades ago, NMR studies have revealed the structure of a complex between a truncated form of HMGA protein (from the residue 51 to the 90), containing the II and III AT-hook motifs with the DNA dodecamer GGGAAATTCCTC (Figure 1-11a). There, it was shown how the central fragment RGR (Arg-Gly-Arg) of the AT-hook adopts an ordered and well-defined conformation that adapts perfectly to the minor groove of the oligonucleotide (Geierstanger et al., 1994; Huth et al., 1997). For a better understanding of the complex stabilization, the AT-hook motif structure can be divided into three segments: the central RGR core with an extended conformation deep in the minor groove, the residues lysine and arginine at either end of the central core provide electrostatic and hydrophobic interactions with the DNA backbone, and in the II (but not the III) domain, the six C-terminal residues next to the core interact with the backbone on the edge of the minor groove (Huth et al., 1997).

However, it was not until 2012 when a member of our research group (MACROM), could crystallize and solve the first crystal structure of an AT-hook (Fonfría-Subirós et

al., 2012). The structure shows the III AT-hook peptide in complex with the AT-rich oligonucleotide CGAATTAATTCG and exhibits in detail the interaction of the AT-hook domain in the minor groove of the double helix (Figure 1-11b). The inner PRGRP sequence of the AT-hook peptide interacts with one of the AATT regions of the DNA dodecamer and fully occupies its minor groove. In the binding region, the minor groove is 4 -5 Å wider than the free minor groove.

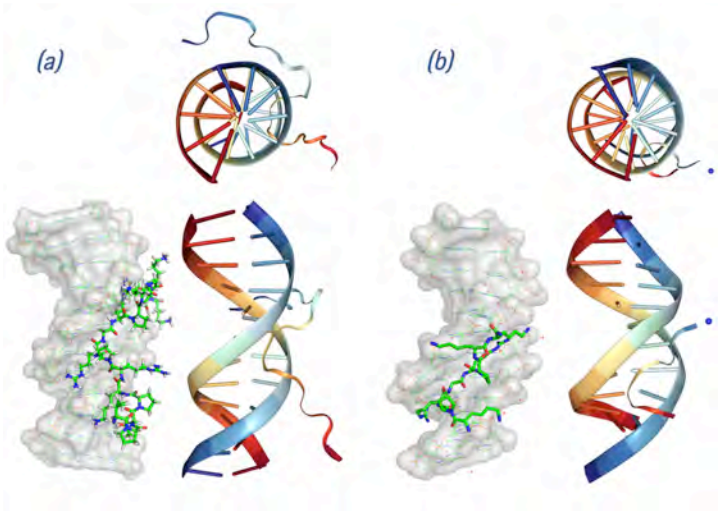

Figure 1-11. Top and front views of AT-hook interactions with DNA. *(a)* NMR structure of the complex of DNA dodecamer and the II AT-hook (PDB ID: 2EZD). *(b)* Crystal structure of a complex of AT-rich oligonucleotide with the III AT-hook of HMGA (PDB ID: 3UXW). The DNA dodecamers *(a)* GGGAAATTCCTC and *(b)* CGAATTAATTCG shown as partially transparent objects are drawn with *Pymol*.

HMGA proteins act as architectural elements positively and negatively regulating the transcription of a variety of genes by changing the DNA conformation or by interacting with several transcription factors (Ozturk et al, 2014). In this way, they are involved in multiple nuclear processes including cell growth, proliferation, differentiation and induction of apoptosis (Fujikane et al., 2016). The mechanism of action of the HMGA proteins according to the substrates with which they interact, can be summarized in the following list:

- *HMGAs direct interactions with DNA*. They can bind to specific structures in preferably AT-rich sequences of DNA, changing its conformation and

consequently facilitating the binding of transcription factors, giving rise to multiprotein stereospecific complexes bound to DNA (Figure 1-12a).

- *HMGAs direct interactions with TFs.* They can bind to a variety of transcription factors, changing its conformation and thus enhancing its DNA binding affinity (Figure 1-12b).
- *HMGAs interactions with chromatin.* They can be associated with specific segments of genomic AT-rich DNA that have affinity for nuclear MAR and SAR (matrix- and scaffold-associated regions), and de-represses transcription by displacement of histone H1 from the chromatin structure (Figure 1-12c).
- *HMGAs as co-factor in virus integration and expression.* They can facilitate the integration of the double-stranded linear cDNA copies of virus genomes into host cell chromosomes (Li et al., 2000).

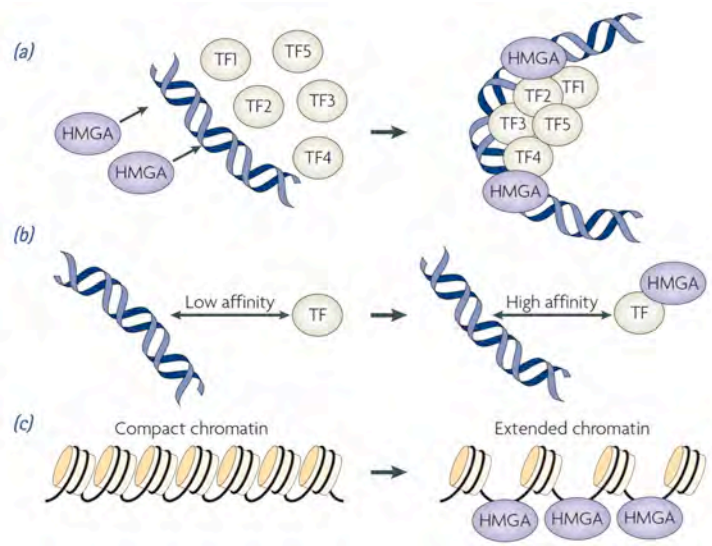

Figure 1-12. HMGA proteins interactions with *(a)* DNA, *(b)* other proteins such as transcription factors (TF), and *(c)* the chromatin structure. Fusco & Fedele, 2007.

The first example of HMGA interactions was described with the interferonß (IFN-ß) promoter. HMGA1 stimulates the binding of a specific isoform of the activating transcription factor 2 [ATF-2(195)] but also inhibits the binding of ATF-2(192) to the IFN- ß gene promoter (Du & Maniatis, 1994). The activation of the ATF-2(195) is stimulated by the bending of the DNA caused by the HMGA.

Another kind of interactions with DNA occurs when HMGA proteins alter the chromatin structure by forming a higher order transcriptional complex "enhanceosome". After binding DNA, the HMGA is able to coordinate the assembly of additional TFs, altering the expression of specific target genes (Shah & Resar, 2012).

Both HMGA1 and HMGA2 genes are highly and ubiquitously expressed during embryogenesis in undifferentiated or rapidly proliferating cells, and very low expressed or non-expressed in normal adult tissues (Reeves, 2001; Macrì et al., 2016).

HMGA proteins may play a significant role in human disorders, particularly in tumorogenesis. After the embryogenesis, there is a generalized de-repression of HMGA1 and frequently HMGA2 expression in tumor cells. Overexpression of HMGA1 has been found in various types of malignant epithelial tumors in organs such as prostate, colorectum, lung, breast, pancreatic, gastric, cervical and thyroid (Shah & Resar, 2012). In every instance, a correlation between the concentration of HMGA1 and the degree of malignancy or metastatic potential has been found (Fedele & Fusco, 2010). HMGA2 overexpression is also observed in breast cancer, sarcomas, pancreatic neoplasms, oral squamous cell carcinomas, and non-small cell lung cancer (Cleynen & van de Ven, 2008). The strong and consistent association between levels of expression of HMGA proteins and human cancers arising from diverse tissues suggests them as potential biomarkers for neoplastic transformations (Shah & Resar, 2012).

Aberrant expression of HMGA proteins is related to other human pathologies besides cancer. Examples of serious diseases where HMGA proteins play important roles are type 2 diabetes mellitus (Chiefari et al., 2011), obesity (Anand & Chada, 2000) and idiopathic pulmonary fibrosis (Pandit et al., 2010). Moreover, HMGA1 proteins are critical cellular factors required for the formation of functional HIV-1 preintegration complexes, its integration in the host genome and the viral gene transcription (Slama-Schwok et al., 2000).

The canonical HMGA proteins are not only expressed in mammalians, but also in other vertebrates such as the African clawed frog *Xenopus laevis*. This species has two allelic isoforms, α and β, of the Xlhmga2 protein, homologous to human HMGA2 (Benini et

al., 2006; Macrì et al., 2016), and the gene *Xhmgax*, which encodes a highly divergent HMGA with eight AT-hooks (Vignali et al., 2008). Most plants and invertebrates also express variants of HMGAs. An example is the fly *Drosophila melanogaster* that expresses the D1 protein, orthologue of HMGA, presenting ten repeated AT-hook motifs (Aulner et al., 2002).

In fact, studies have reported on the existence of more than 100 proteins from different species containing the AT-hook DNA-binding domain, including *Aspergillus nidulans*, *Arabidopsis thaliana*, Gallid herpesvirus 1, *Saccharomyces cerevisiae* (Aulner et al., 2002; Aravind & Landsman, 1998), as well as many species of *Leishmania* (Kelly et al., 2011).

1.5.1.2 HMGB

The mammalian high mobility group B (HMGB) comprises four types of proteins encoded by distinct genes: HMGB1 with 215 amino acids, HMGB2 with 209, HMGB3 contains 200 amino acids, and the recently discovered HMGB4 is composed of 186 residues. The canonical HMGB1-3 proteins share more than 80% identity. HMGB4 presents a lower molecular mass and lacks the C-terminal tail (Štros, 2010). Nevertheless, all members of the HMGB family contain two DNA-binding domains called HMG-boxes A and B (Figure 1-13). The two boxes are structurally similar, and their motions are completely independent (Bianchi & Agresti, 2005).

HMGB proteins exhibit not only high mobility in polyacrylamide gels like the rest of the HMGs, but they also show it in the nucleus, being the most dynamic nuclear proteins in cells (Scaffidi, et al., 2002).

All members of the HMGB family share a great similarity in the primary structure as shown in the amino acid sequence alignment of the HMGB proteins in Figure 1-13. The distinction is basically the acidic C-terminal tail length and in the case of the HMGB4, the lack of it. In contrast to the HMGAs, the two tandem highly homologous HMGB group motifs, HMG-boxes A and B, have a well-defined secondary and tertiary structure, while the acidic tail seems to be unstructured (Bianchi & Agresti, 2005).

Each HMG-box domain contains approximately 75 amino acids and is composed of three α-helices folded up into a typical wedge shape (Weir et al., 1993). This characteristic L-shape architecture from the tripartite structure of the HMG-box forms a concave surface that can delve into the minor groove of DNA with little or null apparent sequence specificity.

Figure 1-13. Amino acid alignment of human HMGB proteins. Residues contained in HMG-boxes are highlighted in brownish and C-terminal acid tail in purple. [*] Residues identical in all sequences in the alignment; [:] conserved substitutions; and [.] semi-conserved substitutions. Alignment created by UniProt [http://www.uniprot.org/align/].

The HMG-box motif has been identified in more than 150 different proteins in a large variety of organisms including human, bovine, rat, mouse, chicken, *Drosophila*, *Arabidopsis*, *Xenopus*, *Saccharomyces cerevisiae*, *Trypanosoma brucei* (see section 1.7.2.1), among others (Baxevanis & Landsman, 1995). According to the evolutionary and functional conservation, abundance, and DNA specificity, the HMG-box-containing proteins are grouped into two families. The first one, the most abundant, has little or no DNA sequence specificity and can present either a single motif such the *Drosophila* proteins HMGD/Z and the *S. cerevisiae* proteins Nhp6A/B; two in tandem like the human HMGB proteins and the mitochondrial transcription factor A (TFAM; Ngo, et al., 2011); or more than two DNA binding domains like the *Xenopus laevls* transcription factor xUBF with 5 tandemly repeated HMG-boxes (Bachvarov & Moss, 1991). The second family of HMG-box-containing proteins is able to recognize and bind specific DNA sequences and includes a few sequence-specific transcription factors such as the sex-determining factor SRY and SOX proteins (Ohe, et al., 2002).

The structures of the mammalian HMG-boxes A and B have previously been determined individually by NMR structural studies (Figure 1-14) (Hardman, et al. 1995; Weir et al., 1993). The conserved fold structure of the three α-helices in the HMG-box forms an L-shape with an angle of approximately 80° between the long and the short arms. Helix III and the extended N-terminal part create the long arm, while the short arm is composed of helices I and II (Štros, 2010).

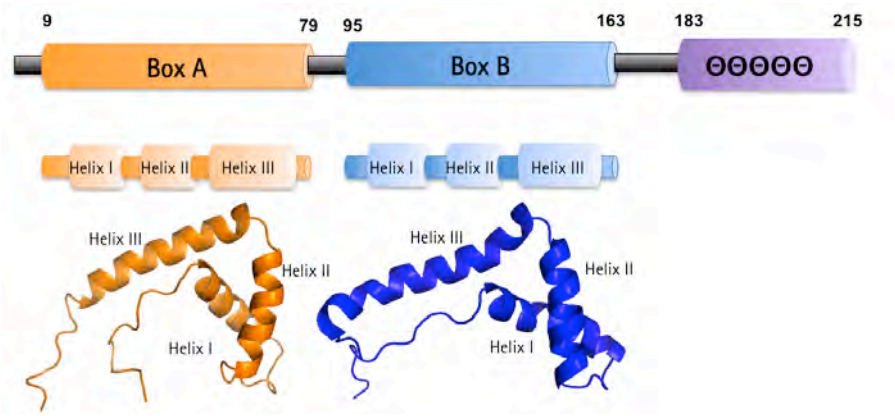

Figure 1-14. Domain structures of HMGB1 protein. Schematic representation of the HMGB proteins and the α-helices within the HMG-boxes A (orange; PDB ID: 1AAB) and B (blue; PDB ID: 1HME) as determined by NMR microscopy (Hardman, et al. 1995; Weir et al., 1993).

The tertiary structure of the HMGB1-3 proteins shows the conserved Cys23 located at the centre of helix I and Cys45 at helix II, opposing each other and at a distance capable to form a disulphide bond under appropriate oxidative conditions. HMGB4 lacks the Cys23 (Barreiro-Alonso et al., 2016).

NMR structures of the HMG-boxes of HMGD (*Drosophila* HMGB1-like protein), Nhp6A (yeast HMGB1-like), the transcriptional activators SOX-2, SOX-4 and SOX-17, and the human UBF HMG-boxes are also published in the PBD (Protein Data Bank). SOX-17 (Gao et al., 2013), the human mitochondrial transcription factor A box B (PDB ID: 3FGH; Gangelhoff et al., 2009) and UBF HMG-box 5 (PDB IDL: 2HDZ; Rong et al., 2007) has also been determined by X-ray crystallography.

The homologous structures of the HMG-boxes A and B in mammalians differ slightly. Box A presents a shorter and straighter helix I, has a longer length of the loop between helices I and II, and more positive charge in the helices I and II as compared to box B (see Figure 1-13 & Figure 1-14). This distribution of charged surface residues of box A gives it significantly greater affinity for unusual or distorted DNA configurations such as four-way junctions (Teo et al., 1995).

Significant age-dependent changes of HMGBs expression have been identified in many organisms. In mice for example, HMGB1-3 proteins are expressed in early embryos, but HMGB2 and HMGB3 are down regulated during embryogenesis (except for the HMGB2, which remains highly expressed in lymphoid organs and testes). On the other hand, HMGB1 is expressed during embryogenesis and continues in adult cells (Hock et al., 2007).

The evolutionarily highly conserved HMGB proteins participate in divergent biological tasks by means of two different roles: intracellular and extracellular. In the nuclear role, they may act as architectural factors through the following mechanisms:

- Acting as a DNA chaperon protein, binding the chromatin, altering the DNA configuration while:
  - Enhancing accessibility to transcriptional protein assemblies (Tang et al., 2010; Bianchi & Agresti, 2005) on specific DNA targets (Figure 1-15a).
  - Stabilizing a partner protein on its target and in some cases, augmenting the affinity of other DNA binding proteins (Figure 1-15b; Hock et al., 2007), e.g. the interactions with the TBP (TATA-binding protein)/TATA-box complex affect the recruitment of other transcription factors (Štros, 2010).
- Relaxing the structure of the nucleosome by inducing a shift between core histones and remodeling the chromatin (Figure 1-15c)
- Interacting with specific nuclear elements by protein-protein interactions, and promoting the formation of complex nucleoprotein structures (Figure 1-15d)

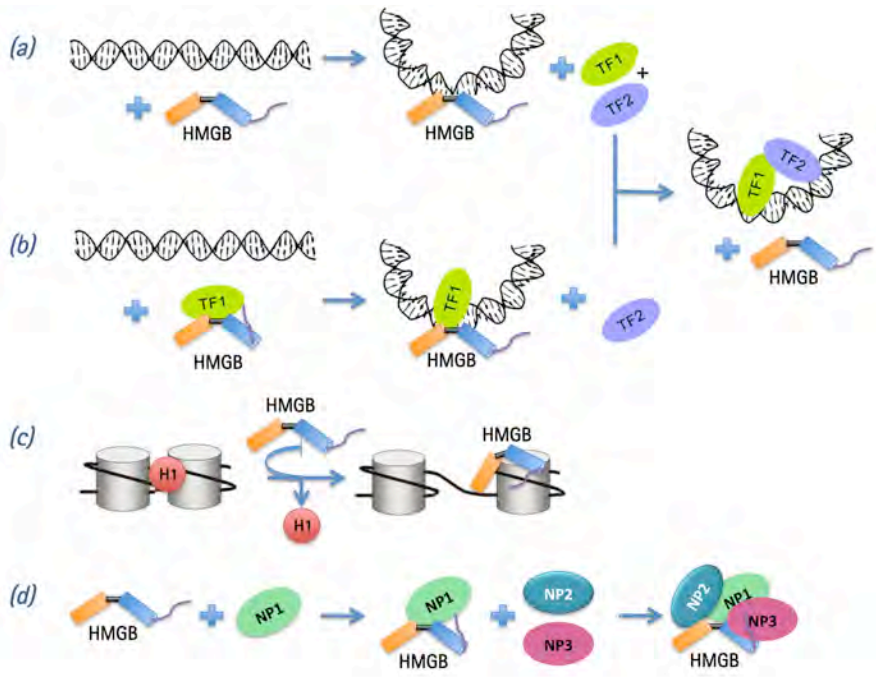

Figure 1-15. HMGBs intranuclear activity. *(a)* HMGB bends DNA and enhances the binding of specific transcription factors. *(b)* HMGB-TF1 complex binds and bends DNA and HMGB-TF1-DNA may promote the binding with other TFs. *(c)* HMGB induces chromatin unfolding by displacing histone H1. *(d)* HMGB promotes formation of complex nucleoprotein structures. Nucleosome structures are illustrated in grey cylinders. TF1/TF2 are examples of transcription factors (green and purple), NP1-3 are nuclear proteins (mint, aqua and pink). H1 in red simulate a histone.

In this way, the HMGB proteins are involved in numerous activities, including transcription, recombination, replication, telomere maintenance and a series of mechanisms of DNA repair (Barreiro-Alonso et al., 2016; Hock et al., 2007). Allosteric transitions of DNA such as DNA bending, kinking and unwinding can be promoted by binding of the HMG-boxes, causing greater distortions than AT-hooks (Bianchi & Agresti, 2005). All HMGBs are able to bend the DNA from 60° to 110° by binding to the minor groove in a number of different DNA structures. Besides supercoiled, single-stranded DNA and B- and Z- forms, it binds preferentially DNA minicircles and other non-canonical structures like four-way junctions, loops, hemicatenated DNA and triplex (Tang et al., 2010). HMG-box B presents superior ability than box A to bend linear DNA (Štros, 2010; Sánchez-Giraldo et al., 2015).

Although HMGB boxes A and B can bind DNA individually, the binding affinity improves when both domains remain attached. The major characteristic of the HMG-box/DNA interaction is the DNA dramatic distortion and bending. The basis of this DNA bending, demonstrated in published HMG-box/DNA structures (Sánchez-Giraldo et al., 2015; Ngo et al., 2014; Stott et al., 2006), is the intercalation of bulky hydrophobic amino acid residues of the HMG-box between consecutive base pairs within the minor groove of the DNA, complemented with a partial unwinding of the minor groove and bending towards the major groove. The box B first intercalated residue Phe102 is located in the helix I and the second intercalated amino acid Ile121 in the helix II; both flanked by conserved basic residues that bind to the phosphodiester bond of DNA and stabilize the complex. Box A only contains one intercalating residue, Phe37, in the helix II (Štros, 2010).

The structure of HMGB1 protein with both HMG-box domains in complex with DNA has not been solved so far. Yet, the crystal structure of the HMG box A binding a previously distorted DNA (distortion caused by the drug cisplatin) has been determined, producing a bend of 60° on the DNA (Ohndorf et al., 1999).

Moreover, structures of the human mitochondrial transcription factor TFAM in complex with different DNA sequences have been solved (Ngo et al., 2014; Ngo et al., 2011; Rubio-Cosials et al., 2011). Although TFAM differs in amino acid sequence from HMGB1 protein, it also has two tandem HMG-box domains (A and B). Crystal structures show two sharp ~90° kinks, each caused by one HMG-box, generating an overall U-turn of ~180° (Figure 1-16a).

Recently, the crystal structure of the HMG-box A bound to a linear AT-rich DNA has been solved by a member of the MACROM research group (Sánchez-Giraldo et al., 2015). The 2 Å resolution structure comprises in the asymmetric unit two oligonucleotides $d[ATATCGATAT]_2$: one unbound straight DNA duplex and one bent DNA duplex bound by two boxes A acting together. These two domains enclose, unwind and bend the DNA by approximately 85° (Figure 1-16b).

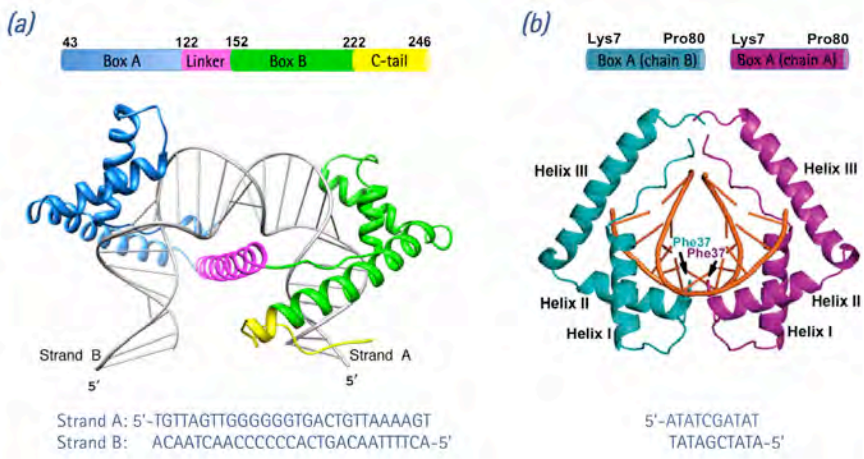

Figure 1-16. Crystal structures of HMG-box bound to DNA. ***(a)*** **The domain structure of mature TFAM in complex with a mitochondrial DNA fragment. HMG-box motifs, shown in blue and green, are forming a complex with the 28 base pair DNA (grey), and bending the DNA into a U-turn (Ngo et al., 2011; PDB ID: 3TMM).** ***(b)*** **The two near-symmetric box A domains (purple and cyan) of HMGB1 protein collaborate to bend the AT-rich DNA decamer (orange) (Sánchez-Giraldo et al., 2015; PDB ID: 1CKT). DNA sequences are given below each structure.**

HMGB proteins are extensively modified after translation. Post-translational modifications such as phosphorylation of HMGB1 are required for proper folding and stability, as well as to influence the transcription factor activity and acquire DNA-binding affinity. Besides, acetylation within the HMG-boxes is crucial for DNA binding and histone interaction. Several studies have shown that phosphorylation, acetylation and methylation modifications of the HMGB1 are involved in nucleo-cytoplasmic translocation and subcellular localization. Besides, the acetylation of certain lysine residues prevents a re-entry to the nucleus and participates in extracellular secretion (Erlandsson Harris & Andersson, 2004; Štros, 2010). The regulation of the HMGB1 translocation, release, and activity in diseases are also triggered by redox modifications (Kang et al., 2013).

After these post-translational modifications, some members of the HMGB family can be transported from the nucleus to the cell surface membranes, cytosol and mitochondria, and be released into the extracellular space. HMGB1 and HMGB2 shuttle frequently form the nucleus to the cytoplasm by passive diffusion across the nuclear

pores due to their relative small size, or by active transport mechanisms including direct binding to β–related nuclear transport receptors (Štros, 2010).

The levels of expression in nuclei and cytoplasm correlate with the organism's tissue and with the differentiation stage of cells (Erlandsson Harris & Andersson, 2004). High levels of HMGB proteins are found in undifferentiated cells as well as in the cytoplasm of most tumor cells.

HMGB1, the most studied member of the HMGB family, develops numerous biological functions inside as well as outside the cell. It also plays pathological effects in inflammatory diseases including sepsis and arthritis, in several cancers (Lotze & Tracey, 2005), and in human epilepsy (Maroso et al., 2010).

In the extracellular role, HMGB1 (and possibly HMGB2) acts as a signaling molecule during inflammation, cell differentiation, cell migration, tissue degeneration, metastasis and apoptosis (Banerjee et al., 2011). HMGB1 is released to the cytoplasm from necrotic, inflammatory or apoptotic cells. It is then secreted to the extracellular medium by macrophages, natural killer cells and dendritic cells alone, interacting with diverse proteins including the receptor for advanced glycation end-products (RAGE), TLR-2/4, CD24 and others DAMP (Damage-associated molecular patterns) receptors, or forming heterocomplexes with other immune coactivators (Kang et al., 2013; Barreiro-Alonso et al., 2016; Tang et al., 2010).

Alterations in HMGB1 location, abundance, and levels are associated with the principal cancer hallmarks and linked to poor prognosis in several tumors. The released HMGB1 indicates tumor cell stress or death and a warning of danger over the cells in the microenvironment. In cancer cells, this alert contributes to tumor cell survival by inhibition of apoptosis and the development of metastasis (Tang et al., 2010). Also, HMGB1 can act as pro-apoptotic protein by activating the apoptotic response to genotoxic stress caused by anticancer drugs (Štros, 2010). However, the role of HMGB1 in many types of cancer such as colon, prostate, breast, gastric, and other tumors is clearly related to both nuclear and extracellular performing of the protein (Hock et al., 2007; Tang et al., 2010; Barreiro-Alonso et al., 2016; Štros, 2010).

1.6 DNA-Drug Interactions

The distinctive structural features characteristic of DNA such as the regular helical grooves and the arrays of hydrogen bond donors and acceptors specific to each individual base pair (Figure 1-3), set it as an interesting target for drug design where small molecule ligands can recognize specific sequences and/or structures, and produce a predetermined biochemical response (Wemmer & Dervan, 1997).

Small molecules that bind to DNA generally alter the normal transcription and replication dynamics of the cell. Thus, the design of drugs targeting DNA has become an attractive strategy to obtain novel potent molecules for modulating gene expression (Fitzgerald & Anderson, 1999; Waring et al., 2005). For this reason, in the last few decades, remarkable effort has been devoted to studying DNA-drugs interactions and describing mechanisms by how small molecules promote these changes in the cell.

Hence, DNA is the molecular presumed target for diseases treatment of many clinical anticancer, antibacterial, antiviral and antiparasitic agents due to the inhibition of a series of downstream biological processes including not only transcription and replication but also cell cycle arrest and DNA repair mechanisms, leading eventually to cell death (Sheng et al., 2013).

However, modern drug discovery is complex and requires integrated understanding of the biological, biochemical and structural properties of the target, the ligand, the binding site and the complex. In this way, advances in structural biology (nucleic acid crystallography and NMR) are required to provide detailed 3D information of the drug target and the interactions between the target and the small molecule ligand, offering models to rationally design DNA-binging molecules. Subsequently, optimized compounds with better properties can be developed (Gurova, 2009; Bailly, 2003).

1.6.1 Types of DNA-Binding Drugs

By understanding the different chemical and structural modes of interaction between small molecules and DNA, it is possible to predict the potential biological

consequences of such interactions in the cell, and consequently in the organism to be treated. DNA-binding agents can be classified into three groups according to the general type of binding: intercalators, groove binders (minor or major) and covalent binders (Gurova, 2009). DNA intercalators may present covalent or non-covalent mode of DNA binding.

Small molecules forming covalent bonds with DNA can produce direct damage on the double strand by forming various types of DNA crosslinks capable of altering DNA conformation and stopping interactions with related proteins, thereby blocking biological processes such as replication or transcription (Wang et al., 2016; Hofr et al., 2001). This category includes many chemotherapeutic anticancer agents like various platinum-containing compounds (Sheng at al. 2013), such as cisplatin or *cis*-diamminedichloroplatinum (II), the most widely used and effective anticancer drug. However, because cisplatin acts on both cancer and normal cells, it is associated to substantial side effects (Dasari & Tchounwou, 2014). Cisplatin produces a direct and rigid kink into the major groove of DNA, which promotes recognition by HMG domain proteins (Hofr et al., 2001). In addition to Pt-containing compounds, other small molecules have been discovered to covalently bind DNA duplex, including nitrogen mustard drugs, mitomycin C and psoralen, which are used as anticancer drugs due to their high cytotoxic activity, mainly caused by the non-specific DNA cross-linking (Sheng et al., 2013).

Non-covalent DNA-drug interactions are generally stabilized by a combination of hydrogen bonds and other electrostatic interactions such as van der Waals forces. These bonds may change the conformation of DNA and/or cause indirect DNA damage by altering the normal activity of the DNA-binding enzymes. In any case, non-covalent binding is a reversible process beneficial for applications that require a controlled binding such as in gene regulation (Almaqwashi et al., 2016). There are two main modes of non-covalent DNA interactions:

- DNA–intercalator: a planar aromatic moiety is non-covalently inserted between adjacent DNA base pairs. Intercalation preferentially occurs at GC-rich

sequences (Paul & Bhattacharya, 2012) and is usually stabilized by the formation of strong stacking bonds between the aromatic chromophores of the ligand and the nucleobase (Berman & Young, 1981). Typical examples are ethidium bromide; the antimalarial drug quinacrine; and the natural antitumour and antiviral compound variolin B (Canals et al., 2017).

- DNA- groove binder: small molecules interacting with both the major or minor groove of double-stranded DNA by H-bonds between their functional groups and the adjacent base pairs. Due to the grooves' dimensional difference (see section 1.2.2), targeting them requires enormous dissimilar sized and shaped molecules. Major groove binders are necessarily much larger molecules. Thereby, it is the binding site of most of the DNA-interacting proteins. Added to this, there are also various carbohydrate compounds including neocarzinostatin, nogalamycin, and neomycin that interact with the major groove due to their size and distribution of hydrophobic and hydrophilic moieties (Sheng et al., 2013). Natural compounds such as pluramycins, aflatoxins, azinomycins and leinamycin also bind the DNA major groove, although they target DNA primarily by intercalation between DNA base pairs (Hamilton & Arya, 2012). Specific DNA-drug interactions through the major groove can alter recognition and binding of proteins with DNA. On the other hand, an extensive variety of small molecules can bind within the minor groove of DNA, preferentially at AT-rich regions (Wemmer & Dervan, 1997). Netropsin, Hoescht 33258, diminacyn, pentamidine and DAPI are typical examples of minor groove binding drugs (MGBD).

1.6.1.1 Minor Groove Binding Drugs (MGBD)

Specific recognition of DNA sequences by small organic molecules is important not only for the targeting of specific genes in a genome, but also for chemotherapeutic purposes as antibacterial, antiprotozoal, antiviral and antitumor agents (Bailly, 2003; Sheng et al., 2013). A large variety of such compounds have been developed, emphasizing the study of compounds that bind the minor groove of the DNA.

The molecular recognition elements of the minor groove binders are the electrostatic interactions with the negative potential in the groove, specific hydrogen bonds of functional groups in the ligand (donor) with the atoms of the nucleobases (acceptor), and van der Waals contacts and other hydrophobic interactions within the minor groove (Rentzeperis et al., 1995). MGBD display a degree of sequence specificity, preferentially to high AT-content sequences due to the higher electrostatic potential in AT-rich grooves than CG-rich grooves, and the formation of greater van der Waals interactions by small molecules with the narrower, deeper and easy to fit minor groove at AT sites (Tidwell & Boykin, 2003).

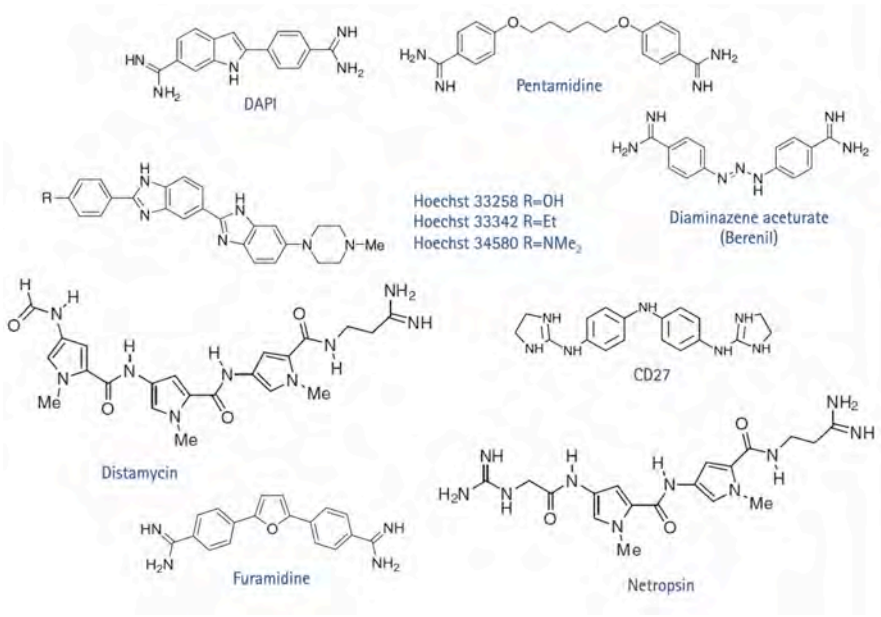

Figure 1-17. Diverse structures of minor groove binding drugs.

Although neutral, mono- or multi-charged ligands have been found, the electronegativity of the DNA minor groove makes it more appropriate target for cationic molecules. In addition, MGBD share several structural features to fit and follow the narrow groove, including aromatic rings and relative flexibility to let it form an overall curvature that matches with the DNA twist (Wemmer & Dervan, 1997). Therefore, minor groove binders are commonly polyamides and heterocyclic dications like pentamidine, Hoechst 33258 and DAPI (Figure 1-17).

A series of structural studies of small molecules in complex with various oligonucleotide duplexes containing stretches of AT base pairs via minor groove have been reported. Examples of these studies determined by X-ray crystallography include Hoechst 33258 in complex with DNA d[CGCGAATTCGCG]$_2$ (Pjura et al., 1987; PDB ID: 8BNA); the complex between netropsin and the DNA dodecamer d[CGCGATATCGCG]$_2$ (Coll et al., 1989; PDB ID: 1VTJ); the complex with d[GTATATAC]$_2$ and distamycin A (Mitra et al., 1999; PDB ID: 378D); among others.

The special interest of the MACROM research group for a better understanding of DNA-drug interactions through the minor groove of AT-rich oligonucleotides has also rendered two crystal structures at atomic resolution of DNA-MGBD complexes. First, a new mode of interaction of the drug pentamidine with the DNA duplex d[ATATATATAT]$_2$ was demonstrated (Figure 1-18a) containing a mixed structure Watson-Crick and Hoogsteen base pairs and interacting with neighboring molecules in the crystal to stabilize the coiled-coil structure of the stacked duplexes (Moreno et al., 2010). Lately, the crystal structure of the complex of the DNA duplex d[AAAATTTT]$_2$ with the dicationic drug 4,4′-bis(imidazolinylamino)diphenylamine (CD27) has been presented (Figure 1-18b; Acosta-Reyes et al., 2014). The CD27 molecules cover completely the minor groove of the oligonucleotide and act as a cross-linking agent by the interaction with neighboring molecules.

The amenability of the minor groove to bind with drugs is not only related to the narrowness and more attractive dimensions of the groove for small molecules, but also minor-groove binding generally involves greater binding affinity and higher sequence specificity than intercalator or major-groove binding (Paul & Bhattacharya, 2012). Hence, MGBD are extensively studied and are considered great promises for treating diseases at the DNA level.

There are only a few minor groove binders approved for treatment due to the initial significant toxicities they presented. Nevertheless, there has been renewed interest in MGBD over the past years through the development of new improved compounds (Cai et al., 2009). The major contributions of minor groove binders have been in the

discovery and development of anticancer agents. Nevertheless, they have demonstrated a wide range of applications such as antiviral, antiparasitic, antifungal and antibacterial. This research work has focused on MGBD as antiprotozoal agents.

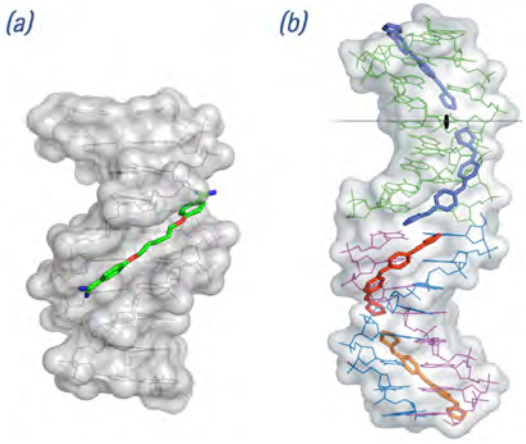

Figure 1-18. Crystal structures of MGBD with all-AT DNA. ***(a)*** **Asymmetric unit of the crystal containing pentamidine-d[ATATATATAT]$_2$ complex. The drug interacts through the minor groove at the centre of the sequence. (Moreno et al., 2010; PDB ID: 3EY0).** ***(b)*** **The different crystallographic units of the CD27-d[AAAATTTT]$_2$ complex . The black lozenge indicates one of the dyad axes (Acosta-Reyes et al., 2014; PDB ID: 4OCD).**

1.6.2 Structure-Based DNA-Targeting Strategies for Drug Discovery

Nucleic acids have usually been less attractive as drug targets in structure-based drug design as compared with proteins. This is mainly due to the limited structural information existing on nucleic acids complexed with potential drugs (Sheng et al., 2013). However, over the past years, a number of structures of diverse complexities have been determined and more than 300 structures with small molecules binding nucleic acids have been deposited in the Protein Data Bank (PDB; www.rcsb.org) since 2004.

DNA is the primary molecular target of some clinical drugs, including anticancer and antiprotozoal agents (Cai et al., 2009). For rational development of novel small

molecules targeting DNA, scientists have developed different strategies including virtual screening, molecular modeling, and structure-based drug design (Sheng et al., 2013). These techniques depend mainly on the availability of the DNA-drug complex 3D structure, especially the high-resolution crystal structure. By extracting the key features from this structural information it is possible to define the optimum geometry and distance for binding site recognition, or to identify the right position of the functional groups in the ligand for better interaction. Moreover, structure-based approaches are also applied to integrate properties into compounds to create alternative molecules less likely to show resistance mechanisms (Hol, 2015).

Due to the high toxicity and side effects that unspecific DNA-targeted therapies have faced during the past decade, new approaches are being investigated for individualized therapies that target specific genes and/or displace key proteins interacting with DNA in determined regions of the genome causing pathogenic effects. These approaches have progressed immensely thanks to the advances in nucleic acid chemistry, molecular biology and structural biology.

In the complex process of drug discovery, the challenge is to identify the right DNA ligand for a given pharmacological action. That is, a balance of affinity, selectivity, specificity, effectiveness and minimum side effects. Selective targeting of a specific sequence is a major challenge when designing nucleic acid ligands. Models to enhance specificity of DNA binding agents have been developed and thereby, the design of compounds that can minimize the off-target effects by the recognition of particular regions, specific genes or certain configurations of DNA has allowed new therapeutics and gene-specific probes (Paul et al., 2015).

Currently available structural information has enriched enormously the understanding and knowledge of the molecular binding mechanisms, specific DNA-ligand interactions, particular configurational changes, and topological deformations of DNA caused by binding with small molecules (Smith & Buchmueller, 2011). Nevertheless, more research and information on DNA-drug interactions is needed to help rationalized drug design.

1.6.3 DNA-Binders Targeting Parasitic Diseases

Infectious diseases caused by protozoan pathogens represent a global health, social and economic problem which rank among the top leading causes of mortality, resulting in more than one million deaths world-wide every year and threaten the health of millions more (Andrews, et al., 2014; WHO, 2015). This enormous burden has been aggravated by the lack of preventive chemotherapy and suitable treatments for many of the diseases these parasites cause, added to the already existing challenge of controlling the growing threat of drug resistance. In addition, the low economic status of the majority of people living in the endemic countries aggravates the situation, making the pharmaceutical market for the development of new drugs financially unattractive to the private-research sector (Ndjonka, 2013).

Discovering and developing safe and affordable treatments to respond the neglected tropical diseases is an urgent need. Notable progress in the development of new antiparasitic drugs has been made in the last two decades using rational drug design including new targets or the use of natural sources (Ndjonka, 2013; Scott et al., 2016). Furthermore, many efforts have been devoted on creating chemotherapeutic treatments targeting parasitic DNA as a safe, selective, and effective antiparasitic strategy.

The DNA of protozoan organisms differs tremendously between species. However, common trends such as a high AT content are observed in species such as *P. falciparum*, (80% overall at content) (Carlton et al., 2002) or *Trypanosoma brucei* [about 73% AT content in its mitochondrial DNA (mtDNA)]. Due to these AT rich genomes, parasites' DNA appears as a suitable target for minor groove binders, particularly for aromatic diamidines (Barrett et al., 2013).

Minor groove binding drugs (MGBD) have been extensively used as antiprotozoal agents to fight diseases like American trypanosomiasis (Chagas disease) caused by *Trypanosoma cruzi*; human African trypanosomiasis (HAT or sleeping sickness) caused by two subspecies of *Trypanosoma brucei*; malaria, caused by *Plasmodium falciparum*;

leishmaniasis caused by several species of *Leishmania*; and trichomoniasis caused by *Trichomonas vaginalis* (Montalvo-Quirós et al., 2015; Soeiro et al., 2013; Scott et al., 2016; Wilson et al., 2008; Acosta-Reyes et al., 2014).

Although widely studied, the precise mechanisms by which the minor groove binders act in protozoa remains unclear and seems to differ between different species (Scott et al., 2016). Still, high intracellular concentrations of dicationic drugs such as pentamidine, have been found in treated trypanosome and plasmodia cells. It was demonstrated that these compounds bind preferentially to AT-rich regions through the minor groove of DNA (see section 1.6.1.1). Then, the specific parasitic DNA-drug binding has been suggested as a potential mode of action of MGBD. This interaction would trigger a particular trypanocidal or trypanostatic activity (Barrett et al., 2013).

Well-studied antiprotozoal compounds like pentamidine, diminazene, furamidine, berenil and others are MDBG have been used for years against *Plasmodium* spp., *Leishmania* spp., *Trypanosoma* spp., *Toxoplasma gondii*, *Trichomonas vaginalis*, *Acanthamoeba* spp., *Balamuthia mandrillaris*, *Babesia microti*, *Cryptosporidium parvum* and *Crithidia fasciculata* (Soeiro et al., 2013). Nevertheless, new antiprotozoal drugs are urgently required due to the appearance of drug resistant parasite strains. The high toxicity and significant side effects of current drugs, added to the complexity of treatment regimens (e.g. lack of oral bioavailability), the high cost, or the lack of supply are some of the main drawbacks that available antiparasitic treatments face.

The search for efficient novel antiparasitic agents has led to the design and synthesis of small molecules that strongly bind to the minor groove of DNA, such as the diamidines (Soeiro et al., 2013; Scott et al., 2016). Among them, bis(2-aminoimidazoline) compounds are considered promising due to the DNA sequence specificity to AT-rich sites and their *in vitro* and *in vivo* antimalarial and antitrypanosomal activity (Rodríguez et al., 2008; Nieto Garrido et al., 2011; Ríos Martínez et al., 2014).

1.7 Human African Trypanosomiasis

Also known as sleeping sickness, human African trypanosomiasis (HAT) is a neglected tropical disease caused by infection with protozoan parasites belonging to the species *Trypanosoma brucei.* There are two forms of the disease in humans: the subspecies *Trypanosoma brucei gambiense* is found in West and Central Africa and causes the chronic form of HAT (98% of reported cases; WHO, 2017), whereas the less common form is an acute, rapidly progressive and mortal disease caused by *Trypanosma brucei rhodesiense* and is spread through East and South Africa (Figure 1-19). Both forms of HAT are transmitted to human by the tsetse fly vector (Franco et al., 2014). Approximately 55 million people distributed over a surface of 340,000 km^2 in 33 sub-Saharan African countries are estimated to be at different levels of risk of contracting sleeping sickness (WHO, 2016). Most of the affected populations live in remote rural areas with limited access to health services, which complicates the diagnosis and treatment of cases in Africa's poorest countries.

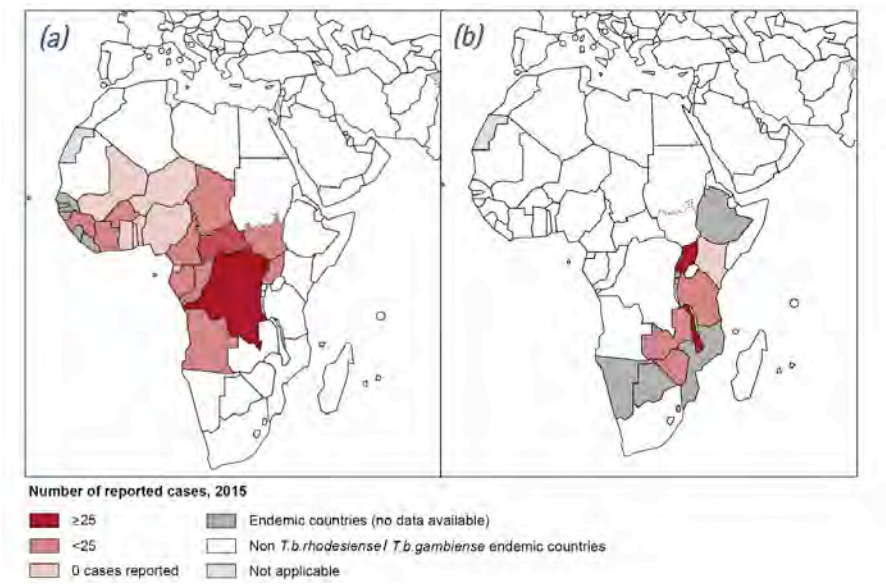

Figure 1-19. Distribution of human African trypanosomiasis worldwide in 2015. Number of reported cases caused by *(a) Trypanosoma brucei gambiense* and *(b) Trypanosoma brucei rhodesiense*. Data source: World Health Organization.

The epidemiology of the disease is mediated by a painful bite of an infected blood-feeding tsetse fly (genus *Glossina*) to humans, where metacyclic trypomastigotes present in the salivary fluid of the fly produce a primary lesion in the skin of the human host, called "trypanosomal chancre" that appears from 5 to 15 days after the bite (Nagle et al., 2014). Then, the clinical progression of sleeping sickness depends on the type of trypanosome infection. The incubation period for Rhodesian sleeping sickness is two to three weeks, and if left untreated, death generally occurs within a year. Gambian sleeping sickness (gambiense HAT) has an incubation period of several days to some weeks (Markell et al., 2006). During the incubation period, the parasites proliferate and spread to the blood where they start to disseminate throughout the body.

In general, HAT clinically evolves in two stages. Initially, in the first or early hemolymphatic stage, the parasites dwell in the lymphatic system and bloodstream. At this point, patients experience nonspecific symptoms of intermittent fevers, malaise, arthralgias, and headaches (Franco et al., 2014). Besides the common symptoms, lymphadenopathy, the swelling of lymph nodes (especially in the posterior cervical nodes along the back of the neck) is exclusive and main sign of gambiense HAT and is termed Winterbottom's sign (Nagle et al., 2014; Markell et al., 2006).

The second stage of the disease begins when parasites penetrate the Central Nervous System (CNS), crossing the blood-brain barrier (BBB) from capillary vasculature in the brain. In rhodesiense HAT, this occurs a few weeks after infection, while in gambiense HAT, it can take several months or even years before evolving into a late period of the disease. In the late (meningoencephalitic) stage, symptoms include psychiatric, motor, and sensory disturbances, severe headaches, personality changes, apathy, and, for approximately three-quarters of patients, profound disorder of the sleep patterns which includes nocturnal insomnia and daytime somnolence, symptoms from which the disease name arises: sleeping sickness. Without treatment, patients eventually progress to a deepening coma and death (Lamb, 2012; Barrett et al., 2003).

1.7.1 *Trypanosoma brucei*

Trypanosoma brucei is a species of parasitic kinetoplastid belonging to the genus *Trypanosoma* and the class Kinetoplastida. There are three morphologically indistinguishable subspecies of *Trypanosoma brucei*: *T. b. gambiense*, *T. b. rhodesiense*, and *T. b. brucei*. In humans, *T. brucei* causes human African trypanosomiasis (sleeping sickness) and in cattle, horses, lions, antelopes, buffaloes, and others, it causes animal trypanosomiasis (nagana).

Cell Structure

T. brucei is a eukaryotic unicellular organism. Besides the typical eukaryotic organelles, i.e. nucleus, mitochondrion, endoplasmic reticulum, Golgi apparatus, lysosomes, and cell membrane, it has an unusual organelle called the kinetoplast composed of a mass of catenated DNA (kDNA) (Figure 1-20). Kinetoplast is localed within a specialized region of the mitochondrion, a single elongated organelle that extends from the posterior to the anterior end of the cell (Matthews, 2005).

The trypanosome cell is asymmetric in shape, approximately 10 to 20 µm long, with clearly dissimilar anterior and posterior ends (Figure 1-20). It has a long slender shape with a single flagellum surrounded by its own membrane, which origins from the basal body near the posterior end of the cell. The flagellum exits the cytoplasm from a small invagination of the plasma membrane called flagellar pocket. This specialized compartment also participates in many cellular processes (Ralston & Hill, 2008; Field & Carrington, 2009). The flagellum is attached to the cell body along most of its length, holding together a thin layer known as flagellum attachment zone (a network of cytoskeletal and membranous connections) and drawing a left-handed helical path from posterior to anterior (Ralston & Hill, 2008). The movement of the cell body is strongly linked to flagellar wave propagation, giving the appearance of an "undulating membrane" (Hill, 2003).

The cell membrane, called pellicle, consists of phospholipids, proteins, cholesterol, and glycolipids. In the bloodstream, a dense coat of variable surface glycoproteins (VSG)

covers the trypanosome surface to protect it from the mammalian immune response (Franco et al., 2014).

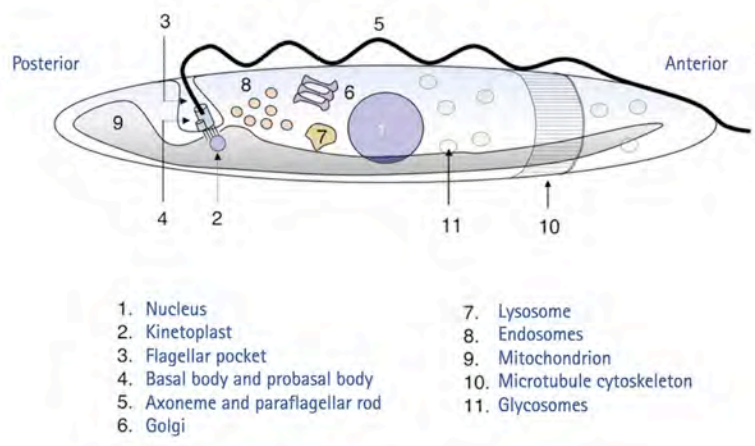

Figure 1-20. Trypanosome cell architecture. A simplified schematic representation of the location of the major organelles of the trypanosome cell. Adapted from Matthews, 2005.

The characteristic cell body shape is defined by a stable and highly cross-linked subpellicular microtubule cytoskeleton, beneath the cell membrane. The single-copy organelles (flagellar pocket, flagellum, kinetoplast, mitochondrion and nucleus) are positioned specifically within the cytoskeletal corset and are concentrated between the center and the posterior end of the cell (Figure 1-20; Matthews, 2005).

The kinetoplast and basal body are physically connected via a high-order transmembrane structure termed tripartite attachment complex (TAC) that must cross both the cell and the mitochondrial membranes (Figure 1-24). TAC includes a series of filaments providing guide ropes through which mitochondrial genome segregation is linked to replication and division of the basal body and flagellum (Ogbadoyi et al., 2003)

Life Cycle

The organization of cell structure is fundamental to the trypanosome throughout its life cycle. Trypanosomes pass through five distinct forms: metacyclic trypanosomes,

long slender bloodstream form, short stumpy bloodstream form, procyclic trypomastigotes and epimastigotes (Figure 1-21). The trypomastigote is the only form to be observed in the mammalian host, whereas the epimastigote form occurs during the development phase in the tsetse fly. The metacyclic form is the only stage that is infective to vertebrates.

Trypanosomes undergo dramatic morphological and biochemical adaptions over their life cycle. Life-cycle stages alternates between bloodstream-form and insect-form to adapt and survive in the mammalian host and the insect vector, respectively (Ralston & Hill, 2008). They proliferate in the midgut of the fly as a procyclic trypomastigote form. After migration to the salivary glands, they progress into proliferative epimastigote forms and then to the non-proliferative metacyclic form that are ready for transmission to the next mammalian host (Akiyoshi & Gull, 2013).

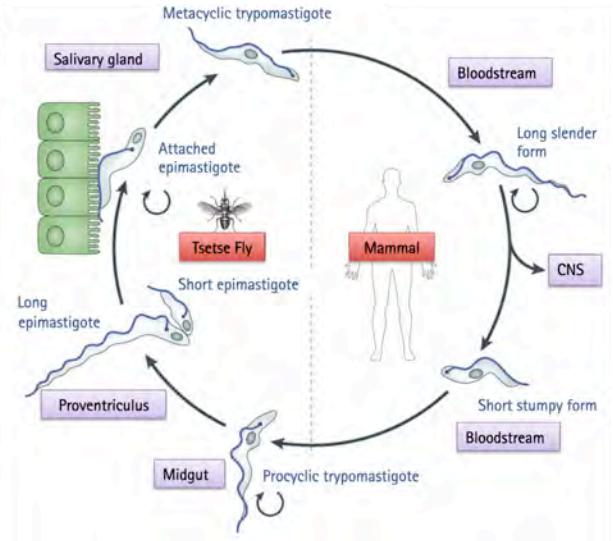

Figure 1-21. A generalized life cycle of *Trypanosoma brucei*. CNS: central nervous system. Adapted from Langousis & Hill, 2014.

Infection of the mammalian host starts when the bite of an infected tsetse fly introduces the metacyclic trypomastigote into skin tissue. The trypanosomes first multiply locally at the site of the bite before invading the lymphatic system, the blood stream, and later, other tissues and organs including the central nervous system (CNS;

Kennedy, 2004). Two different trypomastigote forms can be observed in the mammalian host: a long, slender proliferative (actively-dividing) form and a short, stumpy non-dividing form. Both trypomastigote forms can infect tsetse flies, but only the latter is able to develop into the proliferative procyclic trypomastigote form, completing the life cycle (Chappuis, 2005).

Cell Cycle

Like other eukaryotic organisms, the cell cycle of trypanosomes consists of distinct G1, S, G2 and M phases (Hammarton, 2007). The presence of single-copy organelles and the detailed morphology of the trypanosomes cells require a highly ordered process of organelle duplication and segregation at cell division (Woodward & Gull, 1990).

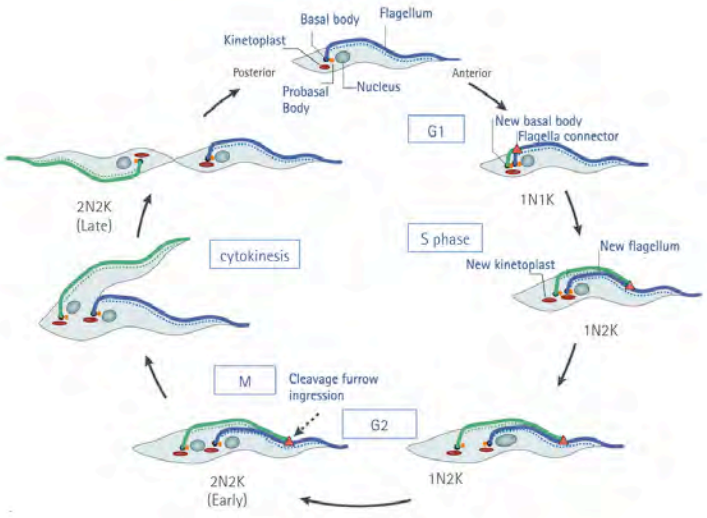

Figure 1-22. Cell cycle regulation in *Trypanosoma brucei*. Duplication of the major organelles and structures during the cell cycle is illustrated, indicating the stages G1, S phase, G2 and M (mitosis). Kinetoplast (K) is shown in red ovals and nucleus (N) in blue sphere.

During the first gap phase G1 in procyclic form *T. brucei*, the cell prepares for entry into a new round of replication and cell division. The earliest detectable cytological events during this stage are the basal body and flagellum duplication: the probasal body (lying adjacent to the flagellar basal body) matures, daughter flagellum outgrowth starts, and new probasal bodies for each mature basal body are formed

(Figure 1-22; Gluenz et al., 2011). Duplication of the Golgi apparatus commences just after basal body duplication (Hammarton, 2007).

S phase separates two gap phases, G1 and G2, which are followed by mitosis (M phase). DNA is replicated during S phase. However, as mentioned before, trypanosomes have two DNA-containing organelles: a nuclear genome and an unusual mitochondrial genome that constitutes the kinetoplast (both of which must be replicated and segregated coordinated) (Gluenz et al., 2011). Kinetoplast S phase is much shorter than nuclear S phase and begins just prior to nuclear S phase (Woodward & Gull, 1990).

The segregation of the two genomes takes place in a specific chronological order. Early in G2 phase, the replicated kinetoplast segregates, followed by nuclear mitosis and finally cytokinesis (Figure 1-22), resulting in the formation of two daughter cells that contain one kinetoplast and one nucleus. It has been suggested that entry to cytokinesis may be more dependent on kinetoplast division and segregation than on mitosis (Hammarton et al., 2003). However, it remains unknown how these temporal orders are established and regulated. Strictly controlled regulation of DNA replication, and kinetoplast and chromosome segregation is essential for maintenance of genome stability.

1.7.2 The Kinetoplast

The mitochondrial DNA of *Trypanosoma brucei* is organized in a unique and complex structure called kinetoplast. The kinetoplast constitutes about the 5% of the trypanosome's DNA and consists of an interlocked network of tens maxicircles (23 kb each) and several thousand minicircles (1 kb each). These circles are intercatenated into a single huge planar disk-shaped network that resides within a specialized region of the mitochondrial matrix near the flagellar basal body (Roy Chowdhury, 2010) (Figure 1-23).

Maxicircles encode ribosomal RNAs and a few proteins involved in energy transduction, such as subunits of NADH dehydrogenase, cytochrome oxidase complexes I, II and III, cytochrome b and A6 subunit of the F_1F_0-ATPase (Shapiro & Englund, 1995). Most of

the maxicircle precursor mRNAs (pre-mRNAs) would need to be modified post-transcriptionally by a process called RNA editing in order to produce complete open reading frames. Minicircles encode small guide RNAs (gRNAs), templates for editing of maxicircle transcripts, which decode the encrypted information, specifying the site and number of uridine residues added or deleted during the RNA editing (Klingbeil & Englund, 2004; Szempruch et al, 2005). While maxicircles are homogeneous in sequence, minicircles are highly heterogeneous and different minicircles are required for editing different maxicircle transcripts (Beck et al., 2013). Therefore, both minicircles and maxicircles are essential for mitochondrial physiology.

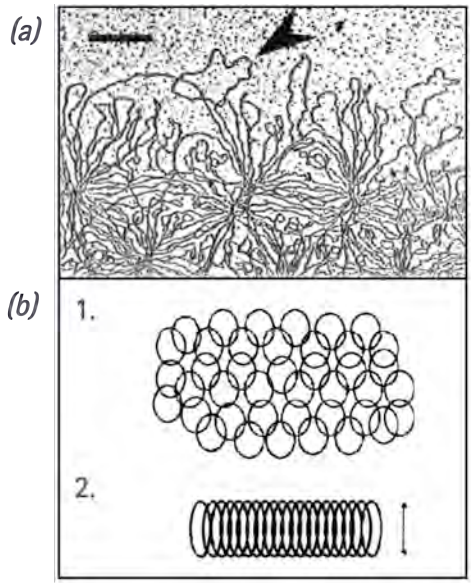

Figure 1-23. Kinetoplast DNA network structure. ***(a)*** **Electron micrograph of the periphery of an isolated kDNA network. Loops represent interlocked minicircles (arrowhead indicates a clear example). Scale bar 500 nm.** ***(b)*** **Schematic representation of the minicircles' organization. 1. Segment of an isolated network showing interlocked minicircles in a planar array. 2. Section through a condensed network disk-shaped *in vivo* showing stretched-out minicircles. The double-headed arrow indicates the thickness of the disk, which is about half the perimeter of a minicircle. Adapted from Lukes et al., 2002.**

The replication of the kinetoplast occurs simultaneously to the duplication of the adjacent flagellum and just prior to the nuclear DNA replication. It is catalyzed by an enzymatic machinery located at defined sites flanking the kDNA disk (antipodal sites) (Figure 1-24) and consisting of at least six DNA polymerases, six helicases, two

primasas, two ligases (Bruhn et al. 2011, Beck et al., 2013) and two topoisomerases: a topoisomerase II (Wang & Englund, 2001) and a topoisomerase 1A (Scocca & Shapiro, 2008).

Covalent closed minicircles are released from the network by a topoisomerase II before replication, so that they could be copied as free circular molecules (Szempruch et al, 2005). The free detached minicircles replicate first as theta-structures. Then, the progeny minicircles, which contain nicks or gaps, are reattached to the network periphery (Figure 1-24). Maxicircles also replicate as theta-structures, but they remain linked to the network. However, exact mechanisms for maxicircle replication have yet to be determined in the same detail as minicircles'. When the network has doubled the size, the minicircles mismatches are repaired, and networks are segregated into two daughter kinetoplasts.

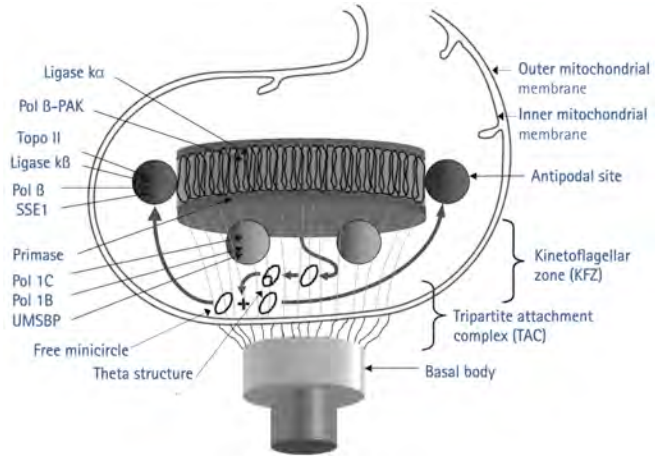

Figure 1-24. The kDNA replication model of *Trypanosoma brucei* showing the location of replication proteins and minicircle replication intermediates. Pol, DNA polymerase; PAK, proline, alanine and lysine-rich; Topo, topoisomerase; SSE1, structure-specific endonuclease 1; UMSBP, universal minicircle sequence-binding protein. Adapted from Englund et al., 2005.

Minicircles make up over 90% of the mass of the network (Shapiro & Englund, 1995). *T. brucei* contains approximately 300 different minicircle sequences in different number of copies, as many maxicircle transcripts are extensively edited (Feagin, 2000). Besides this extensive sequence heterogeneity, apart from the coding region, minicircles have a

conserved region containing the origin of replication, which is virtually identical in all minicircles of the network (Ray, 1989). They also have a single region of bent helix, composed of short A-tracts (4 to 6 residues each) spaced in phase about every 10 base pairs (Shapiro & Englund, 1995). The flexibility of A-tracts (see section 1.3) results in a substantial curvature of the DNA double helix. Moreover, *T. brucei* minicircles include up to 73% of AT-content.

ATP production (through oxidative phosphorylation) is the most well-known function of mitochondria. Nevertheless, it has key roles in many other metabolic and cellular processes. The vast majority of mitochondrial proteins are encoded on nuclear genes and need to be imported from the cytosol and sorted to the mitochondrial outer membrane (OM), inner membrane (IM), intermembrane space (IMS) or matrix (Jensen *et al*, 2008). Mitochondrial enzymes, but also metabolites and other small molecules import, depend upon a membrane potential ($\Delta\Psi$) across the IM. To generate $\Delta\Psi$, *T. brucei* procyclic form uses the proton-pumping electron transport chain and bloodstream form uses the ATP synthase to hydrolyze ATP and thus pumping protons from the matrix to the IMS (Figure 1-25).

The partial loss (dyskinetoplastidy, Dk) or complete loss (akinetoplastidy, Ak) of kinetoplast means that mitochondria cannot fully function due to a deficiency in maxicircles (Jensen et al., 2008). They can propagate only as bloodstream form. The tsetse fly is therefore eliminated from the life cycle and transmission between individual hosts becomes via mechanical or sexual means, allowing the parasite to spread outside the African tsetse belt (Lai et al., 2008). It was found that kDNA-deficient *T. brucei* and several strains of *T. equiperdum* (dyskinetoplastid) and *T. evansi* (akinetoplastid) need a mutation in the nuclear gene encoding the γ-subunit of the F_1 portion of the F_1F_0-ATPase to survive the loss of their kinetoplast (Eze et al., 2016; Lai *et al*, 2008). The loss of proton-pumping membrane component (F_o) of the ATP synthase in the Dk and/or Ak trypanosomes leads to a release of the soluble, catalytically active domain of the synthase (F_1) into the matrix. ATP hydrolysis by F_1 produces ADP, and the exchange of the ADP-3 for cytosolic ATP-4 via IM ADP-ATP

carrier, re-establishes the mitochondrial membrane potential ($\Delta\Psi$) (Figure 1-25; Jensen et al, 2008).

Pentamidine, diminazene and other trypanocidal diamidine-type compounds have been shown to collapse the mitochondrial membrane potential, but the mechanism through which these drugs exert their activity is still not entirely known (Lanteri et al., 2008). However, and just as MGBD (see section 1.6.1.1), they are expected to interact with parasitic DNA, both nuclear and kinetoplastid; nevertheless the rapid accumulation of these drugs within the mitochondrion of treated trypanosomes suggests the kDNA as the potential cellular target (Scott et al., 2016).

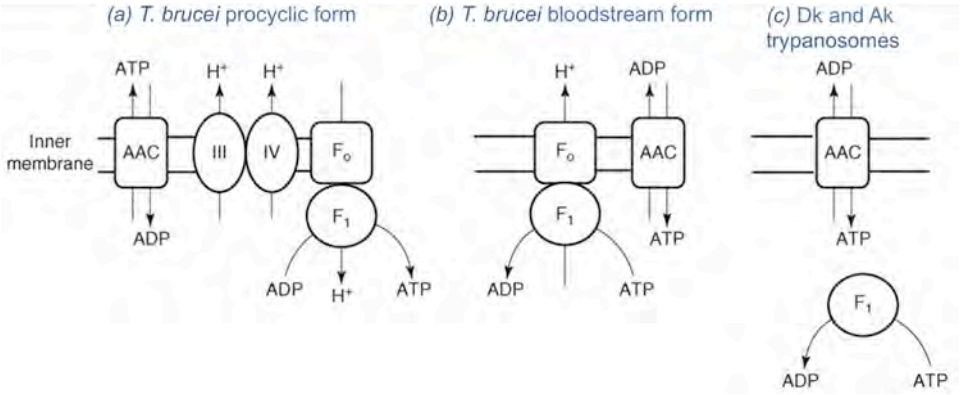

Figure 1-25. Mitochondrial inner-membrane potential in *T. brucei*. The ATP synthase is composed of F_o, which is embedded in the IM and translocates protons, and F_1, which can either synthesize or hydrolyze ATP. The ATP–ADP carrier (AAC) mediates the exchange of ATP and ADP across the IM. *(a)* In the procyclic form, the electron transport machinery generates $\Delta\Psi$ to drive ATP synthesis, in addition to protein import and metabolite transport (not shown). *(b)* In the bloodstream form, the ATP synthase runs backwards and uses ATP hydrolysis to pump protons across the IM to generate $\Delta\Psi$. *(c)* In Dk or Ak trypanosomes, the F_o portion of the ATP synthase is missing (e.g. owing to a lack of the kDNA encoded subunit, A6), but the F_1 portion hydrolyzes ATP to ADP in the matrix. The exchange of ADP–3 with ATP–4 from the cytosol establishes $\Delta\Psi$. Adapted from Jensen et al, 2008.

The unusual structural features of kinetoplast, its particular location, its unique functions, its DNA composition and its sophisticated mode of replication, division and segregation, make this system an attractive target for antitrypanosomal drugs (Sela et al., 2008).

1.7.2.1 *HMG-box proteins in* Trypanosoma brucei

The proper synthesis and function of kinetoplast are largely based on its structure integrity. This highly condensed network demands proteins or protein complexes in order to stabilize the disk architecture. Nevertheless, no information about such proteins was discovered in the kinetoplastid protozoan *Trypanosoma brucei* until 2014, when Wang and co-workers found the first trypanosomatid kinetoplast-associated protein (KAP) called TbKAP6 (Wang et al., 2014).

Various KAP proteins had been previously identified in *Crithidia fasciculate* as small, basic and nucleus-encoded histone H1-like proteins, which were able to condense the isolated kDNA networks *in vitro* and colocalize with the kinetoplast disk *in vivo* (Xu et al., 1996). Moreover, they may also play a role in regulating kDNA gene expression (Avliyakulov et al., 2004). *Trypanosoma cruzi* also has TcKAP proteins characterized. They are similar to KAP proteins of *C. fasciculata*, implicated in kDNA packaging and architectural rearrangement (Cavalcanti et al., 2009).

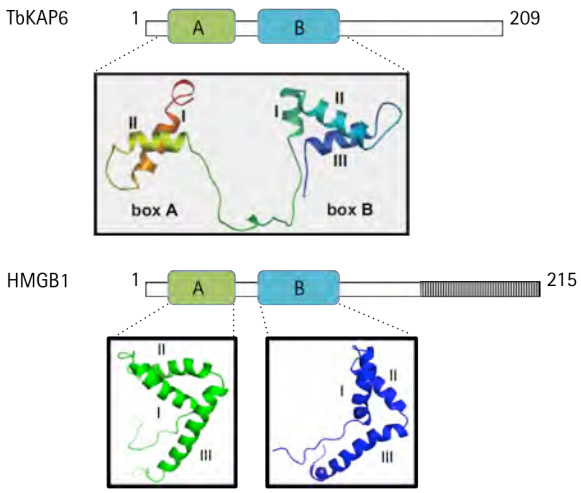

Figure 1-26. The HMG box-containing proteins TbKAP6 and HMGB1. Schematic comparison of two tandem HMG-boxes in TbKAP6 with those of human HMGB1. HMG-box A: green box; HMG-box B: blue box; C-terminal acidic tails: hatched lines. Structure comparison (below each diagram) of the HMG boxes A and B of TbKAP6 constructed by SWISS-MODEL workspace [http://swissmodel.expasy.org/] (Wang, et al., 2014); and HMGB1 box A (green; PDB ID: 1AAB) and box B (blue; PDB ID: 1HME) as determined by NMR microscopy (Hardman, et al. 1995; Weir et al., 1993).

The *T. brucei* TbKAP6 protein, which is homologous to CfKAP4 and TcKAP6, is involved in stabilizing the kDNA disk structure. It belongs to the HMG-box-containing proteins (see section 1.5.1.2) and presents two tandem HMG-boxes: a corrupt and shorter box A and a conserved box B (Figure 1-26). It lacks the acidic C-tail and binds directly to minicircles in the kDNA (Wang, et al., 2014).

```
TbKAP6-Box A  .............LAVSPFTLFMMDQKNN.............PALKGCAISKR...GKLLSKM.............YKELSQNQRR... 44
TbKAP6-Box B  ...ELNMRAARHPNLGKRSKTEI.............TDEKRSSRRKSKGTFATFV.............KNNYASVRGLN 50
HMGB1-Box B   PNAPKRPPSAFFLFCSEYRPKIKGEHPGLSIGDVAKKLGEMWNNTAADDKQPYEKKAAKL 60

TbKAP6-Box A  .............ELNMRAAR---------- 52
TbKAP6-Box B  .............YRKRFAALSKLYNLSRPQME 70
HMGB1-Box B   KEKYEKDIAAYRAKG-------- 75
```

Figure 1-27. Amino acid alignment of the two HMG-boxes of TbKAP6 and the box B of HMGB1. Adapted from Wang, et al., 2014.

Both the knockdown of TbKAP6 and its overexpression alter the normal kDNA organization and segregation, triggering kDNA loss. Therefore, TbKAP6 is essential for kDNA replication and maintenance (Wang, et al., 2014).

1.7.3 Current Treatment

Five drugs are currently approved for the treatment of HAT, depending on the causative trypanosome subspecies and on the disease stage (see Table 1-4 and Figure 1-28; Nagle et al., 2014). Drugs for the treatment of late (CNS) stage trypanosomiasis are those that are able to cross the blood-brain barrier (BBB) to kill the parasites in the cerebrospinal fluid and brain parenchyma (Fèvre et al., 2006). They include melarsoprol, effective against both *T. b. rhodesiense* and *T. b. gambiense*; and eflornithine only useful against *T. b. gambiense*. Pentamidine and suramin are limited by their effectiveness only to the early stage of gambiense and rhodesiense HAT, respectively (Babokhov et al., 2013). Nifurtimox has been used in the past for patients suffering from eflornithine- or melarsoprol-resistant trypanosomiasis (Fairlamb, 2003) but was never licensed as monotherapy for HAT due to the severity of its side-effects. In fact, the action of the mentioned clinically-approved drugs for HAT is marred by a range of severe side-effects that are sometimes life-threatening.

An important advance in HAT chemotherapy occurred in 2009 with the introduction of nifurtimox-eflornithine combination treatment (NECT). NECT was compared in efficiency to eflornithine monotherapy in the treatment of second-stage *T. gambiense* infection (Priotto et al., 2009). In addition, it was found to be safer since it proved to be half as toxic as the standard eflornithine monotherapy, being able to cure HAT in a shorter period of administration than the monotherapy, and showing lower propensity for resistance by trypanosomes (Priotto et al., 2009). Despite this positive progress, the necessity of intravenous treatment, together with the high costs of distribution, place NECT far from being optimal chemotherapy for treating HAT.

Table 1-4. Approval drugs for treating HAT.

Disease	Stage	Drug	Year introduced	Route of admin.	Disadvantages
Gambiense HAT	1 (Early)	Pentamidine	1941	IM or IV	No oral formulation
		Eflornithine	1981	IV	Expensive Every 6 h dosing
		Melarsoprol	1949	IV	Arsenical (toxic encephalopathy)
	2 (Late)	NECT [a]	2009	IV + PO	Expensive, IV for eflornithine part
Rhodesiense HAT	1 (Early)	Suramin	1922	IV	No oral formulation
	2 (Late)	Melarsoprol	1949	IV	Arsenical (toxic encephalopathy)

[a]NECT: nufurtimox-eflornithine combination therapy. IV: intravenous; IM: intramuscular; PO: oral administration. From Nagle et al., 2014.

Due to the limits of currently used HAT therapies, greater emphasis should be placed on the research and development of the ideal HAT drug. This should be effective for both early and late disease, orally administered over relatively short periods, economic and the most important characteristic, it should be safe for all patients (Nagle et al., 2014).

Recent discoveries had suggested fexinidazole and oxaborole SCXY-7158 as drug candidates for HAT. Both cure the acute and the chronic mouse models of HAT infections, have oral bioavailability in mice (41% and 55% respectively), and progressed to the phase II/III studies in 2012 (Nagle et al., 2014). Furthermore, a wide variety of minor groove binding drugs, in particular amidines and imidazolines, have

been synthesized, and have been strong and extensively evaluated against trypanosomiasis (Scott et al., 2016).

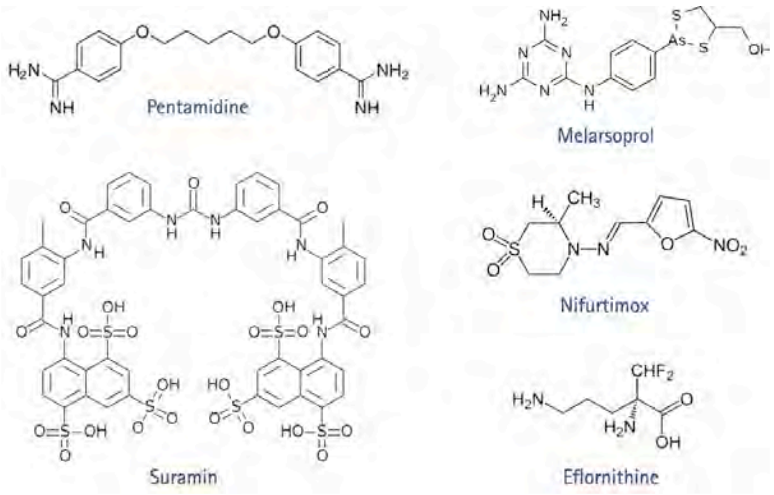

Figure 1-28. Chemical structures of the established drugs used in chemotherapy of HAT. Pentamidine and suramin are effective at early stage, while melarsoprol, nifurtimox and eflornithine are used as at late stage of HAT.

1.7.4 Dicationic MGBD as Antitrypanosomal Agents

Diamidine-like derivatives are potent trypanocides. These dicationic aromatic compounds are DNA minor groove binders that have been used clinically against trypanosomes since the 1930s, starting with the diamidines pentamidine and diminazene (Scott et al., 2016). For years, scientists have synthesized and extensively screened *in vitro* and *in vivo* series of diamidines patterned after pentamidine, in order to improve their selectivity and properties such as bioavailability, efficiency, therapeutic index, and ability to cross the blood-brain barrier (BBB) (Paine et al., 2010; Mathis et al., 2006). The latter is of outmost importance to cure the late-stage of sleeping sickness when the parasites have invaded the central nervous system (CNS).

It has been previously described that these dicationic compounds are selectively cytotoxic to *T. brucei* cells over mammalian cells due to differences in the active

transport mechanism that aids in the accumulation of drug into parasites at levels ~1000-fold higher than in mammalian cells (Nagle et al., 2014).

The effectiveness of diamidine-like derivatives including bisguanidines and bis(2-aminoimidazolines) in recognizing the minor groove of AT-rich sequences of DNA has guided to design of novel potential antiparasitic agents (Tidwell & Boykin, 2003; Wilson et al., 2008; Soeiro et al., 2013; Dardonville & Nué Martínez, 2017). The compounds usually show a preference for binding to AT sequences of at least four consecutive AT base pairs in the binding site (Wilson et al., 2008). This selectivity is particularly relevant for the Kinetoplastid protozoa, like *Trypananosma brucei*, whose mitochondrial genome contains a high proportion of AT-containing DNA sequences (Ríos Martínez et al., 2014, Ríos Martínez et al., 2015a; Ríos Martínez et al., 2015b).

The mechanism of antiparasitic action of dicationic compounds is surprisingly unclear notwithstanding many years of study by a number of laboratories. Both the mitochondrial and nuclear DNA are well established as targets of the diamidines. The strongest evidence indicates that DNA functional destruction is related to their antiparasitic activity (Soeiro et al., 2013; Scott et al., 2016).

The necessity of new, more effective antiparasitic drugs with the lowest possible side effects has inspired Dr. Christophe Dardonville's group to design and develop dicationic compounds like the bis(2-aminoimidazoline) derivatives over the last decade (Dardonville & Brun, 2004; Dardonville et al., 2006; Ríos Martínez et al., 2014; Ríos Martínez et al., 2015a; Ríos Martínez et al., 2015b).

Bis(2-aminoimidazoline) derivatives display excellent antiprotozoal activity against *T. brucei* and *P. falciparum* and are generally safer than their bisguanidine counterparts (Rodríguez et al., 2008). These bis(2-aminoimidazoline) derivatives are excellent minor groove binders of AT rich DNA (Dardonville et al., 2006; Ríos Martínez et al., 2015a). This has prompted the study of the sequence affinity and selectivity with motifs like AATT, TTAA and ATAT (Nagle et al., 2010; Nagle et al., 2012; Glass et al., 2009; Ríos Martínez et al., 2015a).

A good example is the bis(2-aminoimidazoline) derivative 4,4'-bis(imidazolinylamino) diphenylamine (CD27) (see Figure 1-18b) that is a potent inhibitor of *Trypanosma brucei rhodesiense* growth *in vitro* and *in vivo* (Dardonville & Brun, 2004; Dardonville et al., 2006). This compound shows curative activity in a mouse model of early stage HAT but results inactive against the late stage of the disease (Dardonville et al., 2006).

The dicationic compound FR60 [4-((4,5-dihydro-1*H*-imidazol-2-yl)amino)-*N*-(4-((4,5-dihydro-1*H*-imidazol-2-yl)amino)phenyl)benzamide dihydrochloride] is a very promising compound that has demonstrated submicromolar to nanomolar trypanocidal activity *in vitro* against *Trypanosoma brucei brucei* s427-WT and *T. b. rhodesiense* (Rodríguez et al., 2008; Ríos Martínez et al., 2015b). It exhibits no major cross-resistance with the pentamidine-resistant cell line of *Trypanosoma brucei brucei* B48, and relatively low cytotoxicity (CC_{50}>200 µM) for human embryonic kidney cells (HEK). As a result, FR60 shows a high selectivity for the parasite (SI>240), where SI=[CC_{50}/EC_{50}(s427)] (Ríos Martínez et al., 2015b). In addition, FR60 is 100% curative *in vivo* in the STIB900 mouse model of acute rhodesiense trypanosomiasis (i.e. early stage HAT) (Rodríguez et al., 2008; Ríos Martínez et al., 2015a). However, this compound proved to be inactive in the mouse model of late (CNS) stage disease (Ríos Martínez et al., 2015a). This could be due to the high polarity shown by this dibasic compound that holds two cationic charges at physiological pH, which possibly decreases its BBB penetration (Ríos Martínez et al., 2015b).

A successful attempt to reduce the pK_a of this compound was carried out through the incorporation of a fluorine, chlorine, or nitrogen atom in the structure of the lead drug FR60. In this approach, the electronegative halogen atoms decrease the electron density of the adjacent 2-iminoimidazolidine groups, reducing their basicity and hence their charge at physiological pH. Such substitution also increased favorably the lipophilicity of the molecule, both effects being potentially favorable to increase the BBB permeability of the compound (Ríos Martínez et al., 2015b).

Ríos Martínez et al. measured *in vitro* the drug sensitivity of the FR60 derivative compounds on *T. b. brucei*. They reported a slow-acting effect of most compounds on

the trypanosomes compared with the fast killing cytotoxic drug phenylarsine oxide (PAO) used as reference in the assay (Ríos Martínez et al., 2015b). Nevertheless, the introduction of one halogen atom on the diphenyl scaffold led to an increase in antitrypanosomal activity for four compounds: JNI18, CRMV49, CRMV50 and CDMV65 (half maximal effective concentration [EC_{50}] < [EC_{50}]FR60). JNI18 showed to be the drug that most modified the dynamics of action of the compounds, increasing the speed of trypanocidal action (see Table 1-5 and Table 2-9).

None of the FR60 derivatives exhibit major cross-resistance with the pentamidine-resistant cell line of *T. b. brucei* B48. Moreover, compounds 1-10 present relatively low cytotoxicity (CC_{50}>200 µM) for human embryonic kidney cells (HEK).

Table 1-5. *In vitro* activity of FR60 and derivatives against *T. brucei* s427 (wild type) and B48 (resistant) strains.

Ref	Compound	*T. b. brucei* 427WT[a] EC_{50} (µM) ± SEM[b]	*T. b. brucei* AT1-B48[c] EC_{50}(µM) ± SEM	RF[d]	HEK[e] CC_{50}[f] (µM)	SI[g]
1	FR60	0.83 ± 0.08	0.87 ± 0.20	1.1	>200	>240
2	CRMV60	1.58 ± 0.31	2.16 ± 0.11	1.4	>200	>120
3	JNI33	4.22 ± 0.14	4.35 ± 1.16	1.0	>200	>45
4	CRMV65	0.58 ± 0.14	0.79 ± 0.21	1.4	>200	>340
5	JNI18	0.220 ± 0.002	0.36 ± 0.02	1.7	>200	>900
6	CRMV49	0.47 ± 0.05	0.65 ± 0.04	1.4	>200	>420
7	JNI17	1.32 ± 0.03	2.44 ± 0.15	1.8	>200	>150
8	CRMV50	0.53 ± 0.20	0.69 ± 0.07	1.3	>200	>370
9	CRMV45	0.97 ± 0.01	0.83 ± 0.08	0.9	>200	>200
10	JNI32	1.04 ± 0.02	3.23 ± 0.94	3.1	>200	>190
	Pentamidine	0.00011 ± 0.0004	0.55 ± 0.003	3349		
	Diminazene	0.012 ± 0.002	0.78 ± 0.04	42		
	PAO[h]				0.32 ± 0.03	

[a]Bloodstream form trypomastigotes of *T. b. brucei* s427 wild type. [b]Standard error of the mean.[c]*T. b. brucei* strain resistant to diminazene, pentamidine, and melaminophenyl arsenicals.[d]Resistance factor compared to WT. [e]Human embryonic kidney cells. [f]Half maximal cytotoxic concentration [g]Selectivity index (SI) = CC_{50}/EC_{50}(s427).[h]Phenylarsine oxide. Data taken from Ríos Martínez et al., 2015b.

As FR60, compound CD27 is curative for early stage HAT. However, it also results inactive against late (CNS) stage sleeping sickness (Dardonville & Brun, 2004;

Dardonville et al., 2006). To improve the BBB permeability of the CD27, Nieto Garrido et al. synthesized the 1-hydroxy analogue CDIV32 [4,4'-bis(1-hydroxyimidazolinyl amino)diphenylamine] (Table 2-9) (Nieto Garrido et al. 2011). CDIV32 was screened *in vitro* against *Trypanosoma brucei rhodesiense* and three other related parasites: *Trypanosoma cruzi*, *Leishmania donovani* and *Plasmodium falciparum*. CDIV32 demonstrated submicromolar trypanocidal activity *in vitro* against *T. b. rhodesiense* and nanomolar trypanocidal activity against *P. falciparum* (Table 1-6).

Table 1-6. *In vitro* antiprotozoal activity of CDIV32.

Cell	EC_{50} (µM)
T. b. rhodesiense[a] (SI)[b]	0.37 (236)
T. cruzi[c] (SI)	>204
L. donovani[d] (SI)	58
P. falciparum[e] (SI)	0.055 (1673)
Cytotox L6-cells[f]	92

[a] *T. brucei rhodesiense* STIB900 strain. Control: melarsoprol, EC_{50}=12.6 nM. [b] Selectivity index=[EC_{50}(L6-cells)/EC_{50}(parasite)]. [c] Amastigotes of *T. cruzi* Tulahuen C4 strain. Control: benznidazole, EC_{50}=1.64 µM. [d] *L. donovani* strain MHOM/ET/67/L82 axenically grown amastigotes. Control: miltefosine, EC_{50}=0.275 µM. [e] *P. falciparum* K1 erythrocytic stages. Control: chloroquine, EC_{50}=0.169 µM. [f] Rat skeletal myoblast L-6 cells. Data taken from Nieto Garrido et al. 2011.

Nieto Garrido et al. 2011 also proved that CDIV32 is active *in vivo* in the STIB900 mouse model after intraperitoneal (IP) administration and it showed significant higher permeability than compound CD27 (nearly 3-fold). These results show that N-substitution of the imidazolylamino group with OH enhances the *in vitro* BBB permeability of the CD27.

Nevertheless, the drug target and mechanism of action of these bis(2-aminoimidazolinium) compounds into the parasites' cells is still not clear.

Therefore, a functional and structural analysis of this bis(2-aminoimidazoline) series of FR60 derivatives, and a CD27-derivative compound, CDIV32, is presented here, in order to understand how these compounds affect trypanosomes.

1.8 Objective of the Work

The present research work has two main objectives:

- To contribute to the study of the structural and binding analysis of AT-rich DNA-ligand complexes, specifically with HMG proteins (HMGA1a and HMGB1) and minor groove binding drugs bis(2-aminoimidazoline) derivatives.
- To perform the *in vitro* study of the effect of bis(2-aminoimidazolines) derivatives on *Trypanosoma brucei*, in order to identify the mode of action of novel antitrypanosomal drug candidates.

To achieve the first objective several different approaches were followed:

- Expression and purification of the recombinant HMG protein: HMGA1a(Δ50-91), HMGB1(Δ93-165) and HMGB1(Δ8-165).
- Crystallographic assays with the HMG proteins and several different AT-rich oligonucleotide sequences.
- Crystallographic assays with different AT-rich oligonucleotide sequences and a series of diphenyl-based bis(2-iminoimidazolidine) compounds.
- X-ray diffraction of the crystals obtained from these complexes, analysis of the diffraction data and structural resolution of the molecules by computational methods.
- Binding and kinetic analysis of the HMG proteins and the bisimidazolinium compounds to AT-rich DNA by surface plasmon resonance (SPR) experiments.
- Study of the ability of the bisimidazolinium compounds to displace the HMG proteins from their DNA binding site by SPR experiments.
- Studies of the effect on the DNA topology induced by the HMGA1a protein in circular DNA containing fragments of alternating AT sequences by supercoiling assays.

Likewise, to accomplish the second objective different approaches were also followed:

- *In vitro* study of drug sensitivity in different cell lines of bloodstream form *Trypanosoma brucei*.
- Determination of the effect of the bis(2-iminoimidazolidine) compounds on *T. brucei* growth rate.
- Study of the cell cycle progression of *T. brucei* exposed to the bis(2-iminoimidazolidine) compounds by flow cytometry.
- Determination of the DNA content of drug-exposed *T. brucei* by fluorescence microscopy.
- Study of the mitochondrial membrane potential of treated *T. brucei* by flow cytometry.
- Study of treated *T. brucei* ultrastructure by transmission electron microscopy (TEM).

CHAPTER 2

MATERIALS AND METHODS

2.1 Production and Purification of Recombinant HMG Proteins in *E. coli*

For X-ray crystallography and surface plasmon resonance (SPR) assays protein samples with the maximum level of purity achievable are required. During the research work, the proteins HMGA1a(Δ50-91), HMGB1(Δ93-165) and HMGB1(Δ8-165) have been expressed and purified. Table 2-2 lists the sequence, molecular mass and other characteristics of these proteins.

Table 2-1. Relevant specification of HMG proteins studied.

Protein name	MW [Da]	Extinction coefficient (ε)	Amino acids	Amino acid sequence
HMGA1a (Δ50-91)	4,781.6	7.99· mL·mg^{-1}·cm^{-1} (at 220 nm) [a]	42	EVPTPKRPRG RPKGSKNKGA AKTRKTTTTP GRKPRGRPKK LE
HMGB1 Box B (Δ93-165)	8,430	10,930 cm^{-1}·M^{-1} (at 280 nm)	73 +2[b]	GSNAPKRPPS AFFLFCSEYR PKIKGEHPGL SIGDVAKKLG EMWNNTAADD KQPYEKKAAK LKEKYEKDIA AYRAK
HMGB1 Box AB (Δ8-165)	18,848	20,700 cm^{-1}·M^{-1} (at 280 nm)	158 +2[b]	GSKPRGKMSS YAFFVQTCRE EHKKKHPDAS VNFSEFSKKC SERWKTMSAK EKGKFEDMAK ADKARYEREM KTYIPPKGET KKKFKDPNAP KRPPSAFFLF CSEYRPKIKG EHPGLSIGDV AKKLGEMWNN TAADDKQPYE KKAAKLKEKY EKDIAAYRAK

HMGB1 extinction coefficients have been calculated using *Peptide Calculator, Northwestern University.* [a]Data from Reeves & Nissen, 1999.[b]The two additional N-terminal residues highlighted are derived from the cloning process.

Obtaining HMG proteins directly from human cells has many limitations. Thus, the proteins of interest have expressed in the bacterium *Escherichia coli*, using different strains and expression vectors (plasmids) in each case. The plasmid pET-3a containing the human HMGA1a(Δ50-91) was kindly provided by Dr. R. Reeves (Washington State University, USA) and the two plasmids pGEX-2T containing the genes encoding each of the HMGB1 mutant proteins were provided by Dr. M. E. A. Churchill (Department of Pharmacology at the University of Colorado).

A multi-stage purification strategy adapted to each protein has been followed. Table 2-2 includes the strain and type of plasmid used for protein expression, and

summarizes the techniques followed during each purification step (capture phase, intermediate purification and polishing).

The capture phase reduces the amount of unwanted proteins and concentrates the target protein. Intermediate purification removes most contaminant closely related to the target protein. Polishing removes specific contaminant and unwanted forms of the target protein that may have formed during isolation and purification.

Table 2-2. HMG proteins production main stages.

Protein	Expression		Purification Steps			
	E. coli strain	Plasmid	Capture	Intermediate		Polishing
HMGA1a (Δ50-91)	Rosetta (DE3) pLysS	pET-3a	Acid extraction	Cation-exchange chromatography		Size-exclusion chromatography
HMGB1 Box B	Rosetta (DE3) pLysS	pGEX-2T	Sonication	Affinity chromatography (Purification GST)	Cation-exchange chromatography	Size-exclusion chromatography
HMGB1 Box AB	Rosetta (DE3) pLysS	pGEX-2T	Sonication	Affinity chromatography (Purification GST)	Cation-exchange chromatography	Size-exclusion chromatography

2.1.1 Expression of HMGA1a(Δ50-91)

The research work has studied the HMGA1a protein fragment from the amino acid 50 to the 91, containing two of the three DNA binding domains: the II and the III AT-hook (Figure 2-1). This fraction does not include the acidic C-terminal tail to facilitate its crystallization.

Figure 2-1. Scheme of HMGA1a(Δ50-91) compared to the full-length protein HMGA1a. The AT-hook DNA-binding domains are shown in green.

E. coli Rosetta (DE3) pLysS strain (Novagen) has been transformed with the plasmid pET-3a containing the human HMGA1a(Δ50-91) gene (Figure 2-2). This plasmid also contains a gene that confers resistance to the antibiotic ampicillin (amp^R), in order for bacteria carrying the plasmids can be selected.

Through the T7 promoter system present in the pET vectors, the expression of the recombinant protein is much more specific and can be induced by isopropyl β-d-1-thiogalactopyranoside (IPTG) (see Appendix A). Induction will be done at the exponential growth phase of the cells to optimize the expression of the desired protein.

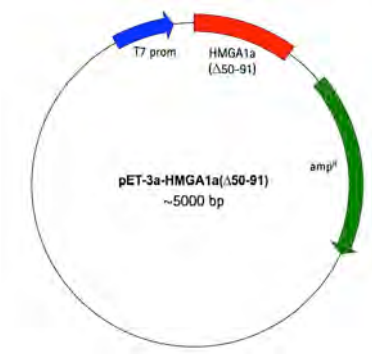

Figure 2-2. Scheme of the plasmid used to expressed HMGA1a(Δ50-91). Figure created by Savvy SVG plasmid map generating program [http://www.bioinformatics.org/savvy/].

The protocols followed for the transformation, transformed cell selection, induction and expression of HMGA1a(Δ50-91) are described next. In order to prevent contamination, all steps of the process were carried out under sterile conditions. Appendix B describes the protocol for preparing the culture media and buffers used for this process.

Transformation

0.5 µL of the pET-3a plasmid DNA solution (approximately 100 ng/µL) were added to ~100 µL of competent cells of *Escherichia coli* Rosetta (DE3) pLysS strain. A negative control with only competent cells was also prepared. Cells were placed on ice for 15 min. They were heat shocked in a 37°C water bath for 5 min and then transferred

to ice immediately for 2 min. This heat shock facilitates the entry of plasmid DNA into the competent cells. The cells were then added to 1 mL of LB medium and incubated for 1 hour at 37°C in a water bath, followed by centrifugation at 4,000 rpm for 3 min (microfuge). About 1 mL of supernatant was removed. The pellet was resuspended and plated directly onto LB agar plates containing the appropriate antibiotics: ampicillin (50 µg/mL) and chloramphenicol (25 µg/mL). Plates were incubated overnight at 37°C.

On the next day, some colonies must be observed on the transformed cells plate, whereas no colonies should appear in the control plate as the untransformed cells are not resistant to the ampicillin.

Growing transformed E. coli *in liquid media*

One single colony was picked from the transformed cells plate using a sterilized loop and inoculated into 3 mL LB medium containing 50 µg/mL ampicillin. Culture was grown for about 6 hours at 37°C with shaking at 250 rpm until medium turned turbid. Then, the culture was poured into 50 mL LB with 50 µg/mL ampicillin and incubated overnight at 37°C with shaking at 250 rpm.

HMGA1a(50-91) protein induction

The required volume of the overnight culture to reach a OD_{600} = 0.1-0.2 was diluted with 1 L of LB containing 50 µg/mL ampicillin. The culture was incubated at 37°C with shaking at 250 rpm until the OD_{600} of 0.6 to 0.7 was achieved. 1 mL of 1 M IPTG was added to the culture, followed by incubation at 37°C with shaking at 250 rpm for 3 hours. Culture was centrifuged at 4,000 rpm for 10 min at 4°C (*SLA* 3000 rotor) and the supernatant was removed. The pellet (bacteria) was stored at -80°C until needed.

Un-induced and induced samples (induction time: 0, 1.5 h and 3 h) were analyzed by measuring the absorbance and by SDS-PAGE to check protein expression levels. An aliquot of 125 µL was taken every time point and centrifuged at 4,000 rpm for 5 min (microfuge). The pellet was resuspended in 30 µL of 1× SDS sample buffer. 1 mL of culture was taken every time point to measure its absorbance. Samples were stored at -20°C until the electrophoresis was performed (see section 2.2.1).

Pellet preparation

As the recombinant HMGA1a(Δ50-91) protein is expressed intracellularly in *E. coli*, cell disruption is necessary. Preparation of the bacterial lysate is a critical step. Optimal conditions maximize the fraction of the recombinant protein extracted. The protocol followed is detailed next (adapted from Reeves & Nissen, 1999).

For bacterial pellet obtained from 1 L of starting culture, 100 mL of 5% $HClO_4$/0.5% Triton X-100 (cold) were used to resuspend the pellet by pipetting continuously to obtain a good dispersion of cells. Samples were incubated on ice for at least 15 min with occasional shaking. Cells were centrifuged at 10,000 rpm for 10 min at 4°C (*GSA* rotor, Sorvall) and the supernatant were collected. Recombinant HMGA1a(Δ50-91) protein was precipitated from the supernatant by adding trichloroacetic acid (TCA) to a 25% final concentration (add 33.3 mL). Samples were placed on ice for 1 h or more with occasional agitation. At this point, samples could be stored at 4°C overnight.

Samples were centrifuged at 10,000 rpm for 20 min at 4°C (*GSA* rotor, Sorvall) and the supernatant was discarded very carefully. The protein pellet often appears to be "oily" and fluid, thus care should be taken not to lose it while decanting the supernatant. Pellet was resuspended in 60 mL H_2O. 20 mL of TCA were added to get a final concentration of 25%. Samples were placed on ice with occasional shaking, followed by centrifugation at 10,000 rpm for 10 min at 4°C (*GSA* rotor, Sorvall). Supernatant was discarded carefully and the pellet was washed with 60 mL of acetone with 10 mM cold HCl (-20°C). Samples were centrifuged at 10,000 rpm for 10 min at 4°C (*GSA* rotor, Sorvall), the supernatant was discarded carefully right after centrifugation and the pellet was washed with 60 mL of cold acetone (-20°C). This step was repeated twice. The pellet was dried under vacuum and stored at -20°C.

The pellet obtained is enriched in HMGA1a(Δ5-91) but the protein needs to be purified.

2.1.2 Purification of HMGA1a(Δ50-91)

In order to achieve the required level of purity of the HMGA1a(Δ50-91), the chromatographic techniques described below have been performed.

Cation-exchange chromatography

Chromatography is one of the most widely used methods of protein purification. Proteins can be purified based on characteristics such as size and shape, charge, hydrophobic groups present on the surface, and binding capacity with the stationary phase.

Ion-exchange chromatography is based on electrostatic interactions between charged protein groups, and a solid support material called matrix. Matrix has an ion load opposite to that of the protein to be separated, and the affinity of the protein to the column is achieved with ionic bonds.

Proteins are separated from the column either by changing pH, concentration of ion salts or ionic strength of the buffer solution. Positively charged ion exchange matrices are called anion-exchange matrices, and adsorb negatively charged proteins, while matrices bound with negatively charged groups are known as cation-exchange matrices, and adsorb positively charged proteins. The latter have been used as the first purification step for the HMGA1a(Δ50-91) protein due to the net positive charge this protein has.

Cation-exchange chromatography consists of three phases:

- *Equilibration*. At this stage the matrix is adjusted to the initial saline and pH conditions required for the experiment by contacting the stationary phase with the counterion.
- *Application of protein sample*. The sample, in the same buffer used to equilibrate, is applied to the stationary phase. It is necessary to centrifuge the sample before loading it in the column to eliminate possible insoluble residues. Proteins carrying a charge opposite to the stationary phase displace

the counterion and bind to the matrix of the column. Proteins with the same charge as the matrix or no charge do not bind and are washed out during this stage.

- *Elution*. By changing the buffer conditions (in this case the counterion concentration) to proteins that have bound to the stationary phase, ions replace the bound protein. Proteins with weaker ion interactions are released at lower counterion concentrations, whereas proteins with stronger charges have a higher affinity for the stationary phase and remain bound to the column longer. The matrix needs to re-equilibrate after elution with at least 10 column volumes of equilibration buffer to reuse it.

For HMGA1a(Δ50-91) protein purification, a matrix (stationary phase) of carboxymethyl cellulose (CM52, Whatman) has been used, with sodium as counterion. Equilibration buffer solution was 50 mM NaCl, 25 mM Tris-HCl, pH 7 and elution was achieved by gradually increasing NaCl concentration from 50 mM to 600 mM, in 25 mM Tris-HCl, pH 7.

Eluted fractions were collected and their absorbance at 220 nm was measured. Selected fractions were analyzed by electrophoresis (see section 2.2). Fractions containing the HMGA1a(Δ50-91) are then submitted to the next purification step or can be conserved at -20°C until processing.

Size-exclusion chromatography

Also known as gel-filtration chromatography, the size-exclusion chromatography has been used for the final "polishing" step of HMGA1a(Δ50-91) protein purification. In this chromatographic method, molecules in solution are separated by their size.

The column matrix or stationary phase is a gel composed of a large number of microscopic porous spherical beads. These spheres are constituted of highly hydrophilic polymers linked together by chemical bonds to form a three-dimensional network. Separation occurs when molecules of different sizes are included or excluded from the different pore size distribution of the network. Thus, small molecules diffuse into the

pores and their flow through the column is retarded according to their size, while large molecules cannot enter the pores and are eluted in the column's void volume. Therefore, molecules are separated based on their size as they pass through the column and are eluted in order of decreasing molecular weight. The entire separation process takes place as one total column volume (equivalent to the volume of the packed bed) of buffer passes through the gel filtration medium.

In this case, unlike the ion-exchange columns, proteins do not bind to the matrix and therefore the buffer composition does not directly affect the resolution. The factors that indeed affect the resolution and thus good separation between the target protein and the impurities are mainly the sample volume, the particle and pore size, column dimensions, column packing, flow rate and sample viscosity.

To address fast and efficient HMGA1a(Δ50-91) protein polishing the *ÄKTA Purifier 10* system (GE Healthcare) has been used. The separating column was the *Superdex™ Peptide 10/300 GL* (GE Healthcare), with an optimum molecular weight range (Mr) from 100 to 7,000. Column matrix is composed of spherical composite of cross-linked agarose and dextran within a column volume of 24 mL. Protein samples were concentrated prior to loading onto the column by ultrafiltration using a *Vivaspin*® (GE Healthcare).

The buffer used for both column equilibration and elution was 25 mM Tris-HCl, pH 7.5 containing 100 mM NaCl. The flow rate was 0.5 mL/min, equilibration of the column was done with at least 2 column volumes and elution with 1.5 column volumes.

The *ÄKTA purifier 10* automatically collects fractions during elution and measures their absorbance at 220, 260 and 280 nm. Fractions absorbing at 220 were collected, and HMGA1a(Δ50-91) purity verification was achieved by electrophoretic analysis (section 2.2). The absorbance at 260 and 280 nm is monitored to evidence possible contamination of DNA or proteins containing aromatic residues, respectively.

For crystallography assays, pure samples were concentrated to at least 10 mg/mL by ultrafiltration using a *Vivaspin*® (GE Healthcare).

2.1.3 Expression of HMGB1 proteins

In this work two deletion mutants of the HMGB1 protein have been studied, one from the amino acid 8 to the 165, containing both HMG boxes, and the second from amino acid 93 to 165, containing only the second DNA binding domain, the HMG box B (Figure 2-3). Both lack the acidic C-terminal tail to facilitate crystallization.

As with HMGA1a(50-91), HMGB1 proteins production was performed in bacterial cultures. Plasmids pGEX2T containing GST-tagged rat HMGB1 proteins Boxes A+B and Box B were expressed in *E. coli* Rosetta (DE3) pLysS strain (Novagen). HMGB1 proteins were obtained by the Glutathione S-transferase (GST) Gene Fusion System, which is a versatile system for the expression, purification, and detection of GST-tagged proteins produced in *Escherichia coli*.

This technique involves expressing the protein of interest fused to the known protein glutathione S-transferase (GST) to facilitate its purification by affinity chromatography. The pGEX2T vectors are designed for inducible, high-level intracellular expression of genes or gene fragments as fusions with *Schistosoma japonicum* GST. Expression in *E. coli* yields tagged proteins with the GST moiety at the amino terminus and the protein of interest at the carboxyl terminus. Once purified, cleavage of the protein from GST is done to obtain pure sample of the target protein.

Figure 2-3 shows the scheme of the plasmid used to express the two fragments of the protein HMGB1. This expression vector also contains the genes Ptac promoter (Ptac), lacI repressor (lac I^q) and ampicillin resistance (amp^R). Recombinant HMGB1 protein expression can be induced by adding IPTG (Appendix A).

The protocols followed for the transformation, induction and expression of the HMGB1s are described next. In order to prevent possible contamination, all stages of the work were carried out under sterile conditions. Appendix B describes the protocol for preparing the culture media and buffers used in this section.

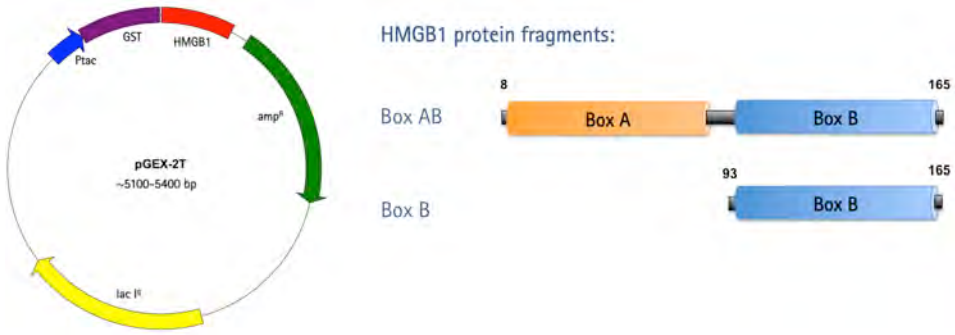

Figure 2-3. Scheme of the plasmid pGEX-2T encoding the GST-fusion protein HMGB1 (left). Figure created by Savvy SVG plasmid map generating program [http://www.bioinformatics.org/savvy/]. Schematic representation of the HMGB1 proteins studied (right): Box AB and Box B.

Transformation

0.5 µL of the pGEX-2T plasmid DNA solution (typically 1-20 ng/mL) were added to ~100 µL of competent cells of *Escherichia coli* Rosetta (DE3) pLysS strain. A negative control with only competent cells was also prepared. Cells were placed on ice for 10-20 min. They were heat shocked in a 37°C water bath for 5 min then transferred to ice immediately for 2 min. The cells were then added to 1 mL of room temperature LB medium and incubated for 1 hour at 37°C in a water bath, followed by centrifugation at 4,000 rpm for 2 min at 4°C (microfuge). About 1 mL of supernatant was removed and the pellet was resuspended and plated directly onto LB agar plates containing the appropriate antibiotics: ampicillin (50 µg/mL) and chloramphenicol (34 µg/mL). Plates were incubated overnight at 37°C.

Growing transformed E. coli *in liquid media*

One single colony was picked from the transformed cells plate using a sterilized loop and inoculated into 3 mL LB containing 50 µg/mL ampicillin and 34 µg/mL chloramphenicol. Culture was grown for about 6 hours at 37°C with shaking at 250 rpm until medium turned turbid. The culture was then diluted with 150 mL LB containing 50 µg/mL ampicillin and 34 µg/mL chloramphenicol and incubated overnight at 37°C with shaking at 250 rpm.

HMGB1 proteins induction

The required volume of culture to reach a OD_{600} = 0.1 (usually about 60 mL) was inoculated into 1 L of LB with 50 µg/mL ampicillin and 34 µg/mL chloramphenicol. Culture was incubated at 37°C with vigorous shaking at 250 rpm until OD_{600} of 0.8 was achieved. HMGB1 protein induction was then performed by adding 0.5 mM IPTG. The culture was incubated at 37°C with shaking at 250 rpm for 3 hours, followed by centrifugation at 5,000 rpm for 10 min at 4°C (*SLA* 3000 rotor). The supernatant was removed and the pellet (bacteria) was flash-frozen in liquid nitrogen and store at -80°C until needed.

As in the HMGA1a(Δ50-91) protein expression, aliquots were taken during induction at time 0, 1.5 and 3 h to measure the absorbance and to make electrophoretic controls of the process on SDS-PAGE gels (section 2.2.1).

50 µL aliquot was taken every time point and centrifuged at 4,000 rpm for 5 min (microfuge). The pellet was resuspended in 15 µL of 1× SDS sample buffer. Additionally, 1 mL of culture was taken every time point to measure its absorbance. Samples were stored at -20°C until the electrophoresis was performed.

Pellet preparation

HMGB1 protein fractions are expressed intracellularly in recombinant *E. coli*. Thus, cell disruption is necessary to extract the recombinant protein. Cell lysis is produced by sonication.

In a falcon siliconized tube, the bacterial pellet obtained from 1 L of starting culture was resuspended in 25 mL of affinity column equilibration buffer (0.5 M NaCl, 10 mM EDTA, 1 mM DTT, 10% glycerol, 20 mM Tris-HCl, pH 7.9) with protease inhibitors (1/2 *cOmplete Protease Inhibitor Cocktail tablet*, Roche) and a spatula tip of DNase by pipetting continuously to obtain a good dispersion of cells. Cell lysis was performed by sonication on *Bandelin SONOPULS Ultrasonic Homogenizer HD 2200* twice for 2 min with 50% of output. It is very important to keep the samples cool (on ice) during sonication to avoid heating. Samples were then centrifuged at 15,000 rpm for 30 min

at 4°C (*GSA* rotor, Sorvall) and the supernatant was decanted into a clean 50 mL centrifuge tube. Supernatant was ready for loading onto the affinity column.

2.1.4 Purification of the HMGB1 proteins

At this point, the recombinant protein mixed with bacterial proteins and other impurities is available. In order to achieve the required level of purity, a multi-step chromatographic strategy for optimizing purification of the HMGB proteins is carried out. The purification process begins with an affinity chromatography (also called affinity purification), which makes use of the specific binding interactions between the tails of the GST fusion protein. Subsequently, a cation-exchange chromatography and size-exclusion chromatography are performed.

Affinity chromatography

Purification of proteins can be easier and simpler if the protein of interest is tagged with a known sequence commonly referred to as a tag. Here, GST affinity tag to aid in the purification of the HMGB1 recombinant proteins was used.

The clarified lysate is incubated with *Glutathione Sepharose™ 4B matrix* (GE Healthcare). Hence, the GST moiety binds with high affinity to the glutathione coupled to the Sepharose beads. This binding is reversible and the protein can be eluted by the addition of reduced glutathione to the elution buffer. A specific protease site engineered between the GST moiety and the protein of interest allows removal of the GST moiety from the target recombinant protein. In our case, the pGEX-2T plasmid contains a protease cleavage site for thrombin, which cuts specifically the amino acid sequence LVPR/ /GS, between the GST moiety and the HMGB1 protein fragment, which is collected during the elution step. Finally, the glutathione Sepharose beads are regenerated by exposing to guanidine chloride, which denaturates the GST tag that remains bound to the column.

The matrix used is packed in a glass Bio-Rad column but unlike the chromatography system previously described (section 2.1.2), this is a semi-batch chromatography,

where the sample is incubated for a certain time with the column matrix and eluted by gravity flow. The protocol detailed for a clarified lysate obtained from 1 L of starting culture is presented next.

The *Glutathione Sepharose™ 4B* matrix (about 2.5 mL resin per 1 L of culture) was thoroughly equilibrated by passing 3 times 10 bed volumes of equilibration buffer: 0.5 M NaCl, 10 mM EDTA, 1 mM DTT, 10% glycerol, 20 mM Tris-HCl, pH 7.9. Then, the clarified lysate (supernatant from sonication) was loaded on the matrix and incubated by rotating gently for 2 h at 4°C. The flow through (FT) was eluted. 5 column volumes (one at a time) were washed with wash buffer: 1 M NaCl, 10 mM EDTA, 1 mM DTT, 20 mM Tris-HCl, pH 7.9. The eluent (W) was collected. 3 column volumes of thrombin buffer: 100 mM NaCl, 2,5 mM $CaCl_2$, 1 mM DTT, 20 mM Tris-HCl, pH 7.9 was passed through the column, eluted and collected (ThW). 200 U of thrombin (Fisher Bioreagents) in 1 mL of thrombin buffer was added to the column to remove the GST tag and incubated by rotating overnight at 4°C. To inactivate the enzyme, enough 0.5 mM EDTA was added to get to a final concentration of 10 mM. The flow through (FTc) was eluted and collected. The elution of the HMGB1 protein was performed using 3 volumes of elution buffer: 100 mM NaCl, 10 mM EDTA, 1 mM DTT, 10 mM Tris-HCl, pH 7.9. Each elution was collected separately (E1, E2, E3). Column matrix regeneration was achieved by passing 3 volumes of water, 3 volumes of 6 M guanidine chloride and rinse with 3 volumes of water. Column can be stored in ethanol to prevent any microbial growth once 3 volumes of ethanol have passed through it.

All samples eluted by SDS-PAGE were analyzed to verify the resolution of the purification process (section 2.2). The fractions eluted after the GST tag removal (FTc E1, E2, E3) are pooled in one sample ready to load into the cation exchange column as described below.

Cation-exchange chromatography

The protein was further purified using a 5 mL *HiTrap SP FF* cation-exchange column (GE Healthcare) to separate the enzyme thrombin and other minor impurities from the HMGB1 protein. SP Sepharose Fast Flow is composed of cross-linked, 6% agarose

particles, with sulphopropyl (SP) strong cation exchange groups. Cation-exchange chromatography technique has been described in section 2.1.2. The chromatography was performed in an *ÄKTA purifier 10* system. Equilibration buffer solution was 100 mM NaCl, 1 mM EDTA, 1 mM DTT, 10 mM Tris-HCl, pH 7.9 and the protein was eluted with a linear gradient to a final concentration of 1 M NaCl in the same buffer. The flow rate used is 2 mL/min, equilibration of the column is done with 10 column volumes.

Absorbance of each collected fraction was measured at 220, 260 and 280 nm. Fractions absorbing at 280 nm were separated (unlike the HMGA, HMGB protein does present aromatic residues), and their protein purity was verified by SDS-PAGE (section 2.2). The most pure fractions were pooled and concentrated for final purification via size-exclusion chromatography.

Size-exclusion chromatography

Size-exclusion chromatography technique is described in section 2.1.2. For HMGB1 protein polishing, a *HiLoad Superdex™ 75* (GE Healthcare) column was used, with an optimum molecular weight range (Mr) from 3,000 to 70,000 Da.

The buffer used for both column equilibration and elution was 150 mM NaCl, 1 mM DTT, 50 mM HEPES, pH 7.4. The flow rate used was 0.5 mL/min, equilibration of the column was done with at least 2 column volumes and the elution with 1 column volumes. Pure fractions, based on analysis by SDS–PAGE (section 2.2), were pooled and dialyzed to decrease the salt concentration in buffer containing in 50 mM NaCl, 1 mM DTT in 25 mM HEPES, pH 7.4 at 4°C. Finally, pure samples were concentrated to at least 10 mg/mL for crystallography assays using a *Vivaspin®* (GE Healthcare) ultra-concentration device. Samples were submitted to flash-freezing in liquid nitrogen and stored at -80°C.

2.2 Electrophoretic Techniques

Gel electrophoresis is a technique widely used to separate biological macromolecules (basically proteins or nucleic acids) according to their length, conformation and charge. Using an electric field, molecules can be made to move through a gel. This electric field consists of a negatively charged cathode and a positively charged anode at each end of the gel, which drive the molecules through the gel according the their charge. The gel is placed in an electrophoresis buffer-filled chamber, which is connected to a power source. Samples being sorted are dispensed individually into wells in the gel. Applying the electric field, molecules move through the gel at different rates and then, they migrate different distances, which form distinct bands on the gel, one band per component.

The gel (matrix) is a polymer whose composition and porosity is chosen based on the specific weight and composition of the macromolecule to be analyzed. It is usually composed of different concentrations of acrylamide and a cross-linker or agarose, producing different sized mesh networks of polyacrylamide or agarose. Polyacrylamide gel matrix is formed through a free radical driven chemical reaction. On the other hand, agarose is composed of long unbranched chains of uncharged carbohydrate without cross-links, resulting in a gel with large pores allowing separation of superior macromolecules and macromolecular complexes.

2.2.1 SDS Polyacrylamide Gel Electrophoresis (SDS-PAGE)

Sodium dodecyl sulfate polyacrylamide gel electrophoresis (SDS-PAGE) is a method for separating molecules based on the difference of their molecular weight. The SDS-PAGE protocol followed in the present work is based on the discontinuous buffer system devised by Laemmli (Laemmli, 1970), which is the most popular electrophoresis system.

During sample preparation for SDS-PAGE, proteins are boiled in SDS-PAGE sample buffer containing 5% (v/v) of the reducing agent β-mercaptoethanol (Sigma-Aldrich)

and the detergent 2% (w/v) SDS (Sigma-Aldrich) (Table 2-3). This formulation simultaneously breaks disulfide bonds and disrupts the tertiary structure of proteins. SDS binds to linear proteins (polypeptide subunits) in a range of 1.4 g of SDS per g of polypeptide. SDS also coats the protein with a uniform negative charge, which masks the intrinsic charges on the R-groups of the amino acids. One of the most significant properties of this anionic detergent is that when it binds to polypeptides, all assume the same hydrodynamic shape, which means that their electrophoretic mobilities are nearly identical. Then, proteins separate by sieving on basis of size (molecular weight) through migrating towards the anode. The glycerol (Sigma-Aldrich) present in the sample buffer provides density for applying the sample on the gel, and bromophenol blue (Thermo Fisher Scientific) is used as a color marker to monitor the progression of the gel electrophoresis.

The gel is divided into two portions, a smaller upper "stacking" gel of lower percentage of acrylamide and pH 6.8, and a resolving gel with highest percentage of acrylamide, higher pH (8.8) with a different ionic content (Table 2-3). This allows the proteins in a loaded sample to be concentrated into one tight layer during the first few minutes of electrophoresis before entering the resolving portion of a gel.

Electrophoresis gels are formulated in buffers that enable electric field to flow through the matrix. The prepared solution is poured into the thin space (usually 0.75 mm or 1.5 mm) between two glass plates that form a "cassette". This process is referred to as "casting a gel". First, resolving portion is dispensed, then, prior to polymerization, a small layer of isopropanol is added on top of the gel to straighten the level of the gel. After the resolving gel is polymerized, isopropanol is removed and stacking gel solution is poured. Immediately after, a gel comb (a well-former template) is inserted. Once the gel polymerizes, the cassette is mounted (typically vertically) into the electrophoresis chamber so that the top and bottom edges are placed in contact with the running buffer, and the comb is removed.

The running buffer contains ions that conduct the current through the gel. SDS is also present in the gel and in the running buffer to make sure that once the proteins are

linearized and their charges are masked, they stay that way throughout the run. The compositions of the SDS-PAGE gel and buffers are listed in Table 2-3.

Table 2-3. SDS-PAGE gel and buffers composition.

SDS-PAGE GEL (10 cm × 15 cm × 1.5 mm thick)		
Reagent	Resolving (10 mL) (15% acrylamide, 0,4% bisacrylamide, 0.375 M Tris, 0.1% SDS)	Stacking (3 mL) (6% acrylamide, 0.16% bisacrylamide, 0.125 M Tris, 0.1% SDS)
30% acrylamide, 0.8% bisacrylamide	5 mL	0.6 mL
1.5 M Tris-HCl, pH 8.8	2.5 mL	-
10% SDS	100 µL	30 µL
0.5 M Tris-HCl, pH 6.8	-	0.75 µL
H_2O	2.3 mL	1.59 mL
TEMED [a]	4.5 µL	3 µL
10% APS [b]	75 µL	30 µL

SDS-PAGE RUNNING BUFFER		
Reagent	5× (1 L)	[1×]
Tris Base	30 g	0,01 M
Glycine	144 g	0,075 M
SDS	5 g	0,02 %

SDS-PAGE SAMPLE BUFFER		
Reagent	4× (10 mL)	[1×]
2 M Tris, pH 6.8	1.25 mL	62 mM
Glycerol	4 mL	10 %
SDS	0.8 g	2%
β-mercaptoethanol	2 mL	5 %
Bromophenol blue	Spatula tip	-

[a]N,N,N',N-Tetramethylethylenediamine (Sigma-Aldrich). [b]Ammonium persulfate (Bio-Rad).

SDS-PAGE gel preparation

Glass plates, combs, and spacers required were cleaned and dried. The gel cassette was assembled and the resolving gel was prepared following Table 2-3 and poured into the cassette. To avoid polymerization, TEMED was added when solution was well mixed. Immediately, a small layer of isopropanol was added to the top of the gel prior to polymerization. While the resolving gel was polymerizing, the preparation of the

stacking gel (Table 2-3) was started (TEMED was not added yet). Isopropanol layer was removed and the top layer of the gel was rinsed with ddH_2O and dried off as much of the water as possible by carefully using filter paper. TEMED was added to the stacking gel solution, mixed and quickly transferred the gel solution into the cassette until full, and then the appropriate comb was inserted.

Sample preparation

4x SDS-PAGE sample buffer was prepared following the Table 2-3. The required volume of 4x sample buffer (or 2x) was added to each protein sample and mixed. Samples were boiled for 3-6 min. Samples were spun and loaded onto the gel using a Hamilton. Syringe must be thoroughly rinsed with ddH_2O between applications to avoid cross contamination of different samples.

Protein samples (containing sample buffer) can be stored at -20°C and reboiled for 5 min when used the following time.

Electrophoresis

The gel cassette in the electrophoresis chamber containing 1× SDS-PAGE running buffer (Table 2-3) was placed on the bottom chamber. Air bubbles attached to the bottom ends of the glass plates were removed. The comb was removed carefully and the upper chamber was filled with running buffer until completely covering the wells. Protein samples were loaded in consecutive wells. The electrophoresis tank was connected to the power supply and the gel was run at constant voltage (100-130 V) for 45-60 min until the tracking dye (bromophenol blue) was about 1 cm from the bottom of the plates.

Protein detection with Coomassie® blue

To visualize the proteins sorted in the gel, they need to be stained. For that purpose, *Coomassie*® blue G-250 dye dissolved in isopropanol and acetic acid was used (see Table 2-4). This solution not only dyes but also fixes the proteins in the gel matrix.

After the electrophoresis is complete, the power supply was turned off and disconnected. The gel cassette was taken out from the chamber and the glass plates were removed carefully. The gel was placed in a container and enough staining solution was added to completely cover the gel. It was gently agitated during 60 min at room temperature on an orbital shaker.

Table 2-4. SDS-PAGE staining and unstaining solutions.

SDS-PAGE *COOMASSIE®* STAINING SOLUTION		
Reagent	Volume (2 L)	Concentration
Isopropanol	500 mL	25%
Acetic Acid	200 mL	10 %
Coomassie® Blue G-250 Dye	5 g	0.25 %

SDS-PAGE DESTAINING SOLUTION		
Reagent	Volume (2 L)	Concentration
Isopropanol	200 mL	10%
Acetic Acid	200 mL	10 %

After staining, a destaining step is needed to wash away excess unbound dye from the gel matrix background.

The gel was immersed into the destaining solution (Table 2-4) and left it shaking overnight. Next day, a clear gel with blue bands of protein was obtained. The gel can be then photographed and dried to maintain a permanent record.

Protein detection with silver staining

Alternatively, detection of proteins in gels has been performed using *SilverQuest™ Silver Staining Kit* (Invitrogen™) following the manufacturer's instructions. This is a rapid and easy method that allows detection of most proteins since it is 30-fold more sensitive than staining with *Coomassie® G-250* dye. The basis of the staining relies on the chemical reduction of silver ions (Ag^{+}) to metallic silver (Ag^{0}) on a protein band (Rabilloud et al., 1994).

For optimal results, it is recommended to use ultrapure water, to always use gloves to avoid fingerprint contamination and rinse them with deionized water previous to handling gels, to avoid applying pressure on gels, to use freshly made solutions and to use clean glass containers designated for silver staining purposes only.

2.2.2 Acetic Acid-Urea Polyacrylamide Gel Electrophoresis (AU-PAGE)

Panyim and Chalkley developed in 1969 a continuous acetic acid-urea polyacrylamide gel system that separates very similar basic proteins based on differences in size and effective charge (Panyim & Chalkley, 1969). The original method has been modified by replacing ammonium persulfate (APS) and tetramethylethylenediamine (TEMED) with thiourea and H_2O_2 (Hurley, 1977).

At the highly acidic pH of AU- PAGE system (around pH 3.5) and deprived of SDS detergent, the positively charged proteins of similar size are still subject to the sieving effect of the gel matrix, but their charges would vary according to their amino acid content. Subsequently, they can be also resolved from each other according to their charges, and not only by their size. The presence of urea, which is an efficient agent for breaking non-covalent protein interactions, improves the protein solubility and facilitates electrophoretic migration.

The compositions of the AU-PAGE gel and sample buffer are listed in Table 2-5. AU-PAGE running buffer is 5% acetic acid.

AU-PAGE gel casting and electrophoresis assembly are performed as already described in section 2.2.1 but gels are composed of only one phase (resolving gel) in this case. Gels are run under a constant current of 20 mA.

Table 2-5. AU-PAGE gel and sample buffer composition.

AU-PAGE GEL (10 cm × 15 cm × 1.5 mm thick)	
Reagent	Resolving (12 mL) (15% acrylamide, 0.1% bisacrylamida, 2.5 M Urea, 5.37% acetic acid)
30% acrylamide, 1% bisacrylamide	6 mL
20% acrylamide, 1% bisacrylamide	-
Acetic acid	1.5 mL
10 M Urea	3.32 mL
Thiourea	10.5 mg
H_2O_2	67.5 µL
H_20	Up to 12 mL

SDS-PAGE SAMPLE BUFFER		
Reagent	2x (10 mL)	[1×]
Urea	4.8 g	4 M
Acetic Acid	0.5 mL	2.5 %
β-mercaptoethanol	14 µL	10 mM
Methyl green	Spatula tip	-

Sample preparation

In some instances, in order to remove the high concentration of salt in the protein samples that could affect the resolution of the electrophoresis, the trichloroacetic acid (TCA)/acetone precipitation method was used. The samples were treated according to the protocol described next.

Trichloroacetic acid (TCA) was added to the samples up to a final concentration of 25%. Samples were placed on ice for 15 min and then centrifuged at 13,000 rpm for 5 min at 4°C (microfuge). The supernatant was carefully discarded and the sediment was washed with 1 mL of acetone and mixed (vortex). Samples were centrifuged at 13,000 rpm for 5 min at 4°C (microfuge), the supernatant was carefully discarded and samples were dried. Samples were resuspended in H_2O *milliQ®*. 2x AU-PAGE sample buffer (Table 2-5) was added to each protein sample and mixed. Each sample was loaded using a Hamilton syringe. Syringe must be thoroughly rinsed with ddH_2O between applications to avoid cross contamination of different samples.

Table 2-6. AU-PAGE staining and destaining solutions.

AU-PAGE *COOMASSIE*® STAINING SOLUTION		
Reagent	Volume (2 L)	Concentration
Methanol	1 L	50%
Acetic Acid	200 mL	10 %
Coomassie® Blue R-250 Dye	5 g	0.25 %

AU-PAGE DESTAINING SOLUTION		
Reagent	Volume (2 L)	Concentration
Methanol	1 L	50%
Acetic Acid	200 mL	10 %

Gel staining and destaining protocol is described in section 2.2.1.

2.2.3 Electrophoretic Mobility Shift Assay (EMSA)

The gel electrophoresis mobility shift assay (EMSA) is used to detect protein complexes with nucleic acids. The principle of EMSA is that DNA with a bound protein migrates through a polyacrylamide gel more slowly than the corresponding free unbound DNA.

This technique is simple to perform. Solutions of protein and nucleic acid are combined and incubated for a period of time. The resulting mixture is subjected to electrophoresis under native conditions through polyacrylamide gel. If the protein is capable of binding to a given DNA sequence, the complex is formed. The speed at which the molecules (and combinations thereof) move through the gel is determined by their size and charge. Consequently, after electrophoresis, DNA-protein complexes migrate less than the corresponding free nucleic acid.

Under appropriate conditions, EMSA can provide quantitative data for the determination of binding stoichiometries, affinities and kinetics. The complex stoichiometry varies according to the DNA sequence and the protein nature. Then, a range of DNA:protein ratios are tested in order to find conditions that best stabilize the DNA- protein complex. A negative control lane (DNA probe without protein

present), which is observed as a single band corresponding to the unbound DNA oligonucleotide, is also loaded in the gel.

Sample preparation

EMSA sample buffer does not include tracking dye to prevent any interference in the formation of complexes.

A set of samples containing different DNA-protein ratios were prepared and mixed softly in 0.3x TBE containing 3% glycerol. The mixtures were incubated at least 30 min at 4°C to allow the complex formation.

Table 2-7. EMSA Gel composition.

EMSA GEL (10 cm × 15 cm × 1.5 mm thick)	
Reagent	Resolving (12 mL) (8% acrylamide, 0.2% bisacrylamida)
30% acrylamide, 0.8% bisacrylamide	3.2 mL
5× TBE 54 g Tris Base, 27.5 boric acid, 20 mL 0.5 M EDTA, pH 8	0.8 mL
H_2O	7.83 mL
10 M Urea	3.32 mL
10% APS	60 µL
TEMED	12 µL

Electrophoresis

EMSA gel recipe is listed in Table 2-7. The electrophoresis assembly and gel casting are described in section 2.2.1. EMSA running buffer is 1× TBE pH 8 (see buffer composition in Appendix B).

EMSA gels are native gels (as opposed to SDS- and AU-PAGE); any factor that can disturb the integrity of labile DNA-protein complexes is not allowed. Thus, a prerunning step is needed to remove all traces of ammonium persulfate, to distribute/equilibrate any special stabilizing factors or ions from the running buffer, and to ensure a constant gel temperature. Also, as proteins and oligonucleotides are

temperature-sensitive, EMSA has to be performed at 4°C in a cold room and electrophoresis assembly is placed on ice.

The gel was pre-run at a constant voltage (75 V) for at least 60 min on ice in a cold room. After the prerunning step, samples were loaded gently and quickly using a Hamilton syringe and the voltage was re-applied. Electrophoresis was performed at 125 V constant voltage for 45-60 minutes, depending on the size of the DNA and complexes.

DNA detection

SYBR® Gold nucleic acid gel stain (Invitrogen™) is a sensitive fluorescent stain that allows the detection of DNA in electrophoretic gels using standard ultraviolet transilluminators. *SYBR® Gold* stain is not only less mutagenic than ethidium bromide (the DNA-intercalator compound commonly used to detect DNA), but also has a detection sensitivity comparable to that of ethidium bromide. Therefore, *SYBR® Gold nucleic acid gel stain* for DNA detection in EMSA gels was used.

Gel was immerse in a staining solution containing 50 mL 0.3x TBE containing 5 µL *SYBR® Gold*. The container was covered with aluminum foil or placed in the dark to protect the staining solution from light. Then, it was gently agitated for 20 min at room temperature on an orbital shaker. Stained gels were visualized and imaged in a UV transilluminator using a *Gel Doc XR System* (Bio-Rad).

2.2.4 Agarose Gel Electrophoresis

Agarose gel electrophoresis is the most effective electrophoresis method for separating DNA fragments of varying sizes (for visualization and/or purification). The matrix is comprised of agarose, one of the two main components of agar. Molecular sieving is determined by the size of pores generated by the bundles of agarose in the gel matrix, then the higher the concentration of agarose, the smaller the pore size.

Electrophoresis uses an electrical field to move the negatively charged DNA through an agarose gel matrix toward a positive electrode. Longer DNA fragments migrate through

the gel more slowly than shorter ones. An estimation of the DNA oligonucleotides lengths can be determined if a DNA ladder marker (a collection of DNA fragments of known lengths) is also loaded on the gel.

1% Agarose gel preparation

1g agarose was mixed with 100 mL 1× TAE (see buffer composition in Appendix B) in a microwavable flask and microwaved for 1-3 min until the agarose was completely dissolved. The solution was cooled down to about 50°C (e.g. until you can comfortably keep your hand on the flask) and 5 µL *SYBR™ Safe DNA Gel Stain* (Invitrogen™) were added for visualization of DNA (1 µL per 20 mL of buffer).

Both ends of the gel tray were sealed with tape and the dissolved agarose was poured slowly into a gel tray (cast) with the corresponding comb in place. Bubbles formation that will disrupt the gel should be avoided. When necessary, bubbles were pushed away from the gel with a pipette tip.

Electrophoresis

There are many types of electrophoresis units, but the horizontal electrophoresis unit is the most commonly used unit for separating DNA molecules on agarose gels. The horizontal electrophoresis apparatus is basically a rectangular-shaped box with electrodes at each end where the gel is completely submerged in buffer during electrophoresis.

Once the gel solidifies in the casting tray, the tape and comb were removed and the gel was placed in the electrophoresis chamber. Enough running buffer (1× TAE) was added to completely cover the gel. Samples were loaded in consecutive wells using a micropipete. The safety cover was attached, leads were connected to power source and the gel was run at constant voltage (90-100 V) for 45-60 min until the tracking dye is about 2-3 cm from the bottom of the plates.

2.2.5 DNA Supercoiling Assays

DNA topological changes such as bending, compaction and negative supercoiling can be induced by chromatin proteins and are related to crucial biological processes (Gilbert & Allan, 2014).

The supercoiling ability of the HMGA1a(Δ50-91) protein was evaluated by measuring the degree of circular DNA supercoiling, which indicates whether the DNA-bending activity of this protein is important enough to cause a topological stress.

First, the HMGA protein is incubated with previously relaxed circular DNA. Alterations in the DNA conformation due to the presence of the protein, may force a change in the DNA torsion or twisting, forming supercoils. Topoisomerase I is added, which dissipate the topological stress by unwinding the helix. Finally, the HMG protein is removed as well as the topoisomerase I, thus the twisting caused by the protein is removed but the changes caused by the topoisomerase remain. Thereby, DNA is rewound and there will be compensatory negative supercoils if the protein, in first instance, caused the topological change.

The resulting samples are analyzed by electrophoresis in an agarose to visualize the change in the degree of supercoiling of a circular DNA induced by the incubation of different concentrations of HMG protein (see Figure 2-4).

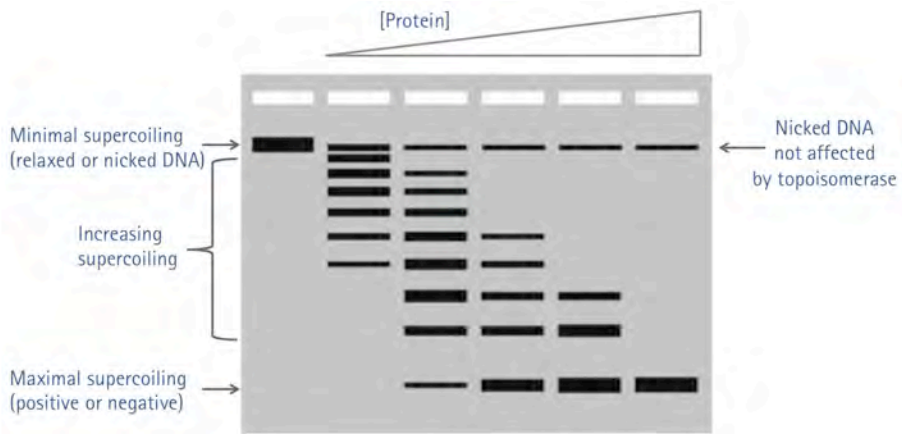

Figure 2-4. Scheme of a supercoiling assay.

Supercoiling Assay Protocol

The reaction buffer, water, supercoiled circular DNA (see Table 2-8) and 0.5 µL topoisomerase I were mixed and incubated 1 h at 37°C in a water bath in order to relax the plasmid. Once incubation was performed, the corresponding concentration of protein was added to each sample as well as 0.5 µL topoisomerase I. The mixture was incubated 1 h at 37°C in a water bath. 1 µL 10% SDS and 0.5 µL 10 mg/mL proteinase K were added to the sample. The mixture was incubated 30 min at 37°C in a water bath. 4.3 µL 6x TPE (see Appendix B) was added to the samples (4 µL to the SC control). The electrophoresis was performed in a 1% agarose gel using 1× TPE as running buffer for around 2 h at constant voltage of 90 V. DNA staining was carried out with 1× TPE containing *SYBR® Gold* (Invitrogen™) for 30 min with shaking. Then, the gel was visualized with a UV transilluminator and photographed.

Table 2-8. Reaction samples for a supercoiling assay.

DNA/Protein Ratio [M]	SC [a]	1:0	1:300	1:1000	1:3000
0.8 µg/µL DNA [µL]	3.75	3.75	3.75	3.75	3.75
50 µM protein [µL]	-	-	0.6	2	6
10x Reaction buffer [µL]	2	2	2	2	2
H_2O	14.25	13.25	12.65	11.25	7.25
Final Volume [µL]	20	19	19	19	19

Different 10x Reaction buffers were used containing 50 mM $MgCl_2$ and 350 mM Tris-HCl pH 7.5 varying the ionic strength with different concentrations of NaCl (0.8-1.9 M). [a] SC, a control sample of supercoiled circular DNA without adding topoisomerase I, SDS nor proteinase K.

2.3 *N*-phenylbenzamide Bis(2-aminoimidazoline) Derivatives

The antiparasitic minor groove binding drugs (MGBD) evaluated within this research work are a series of eleven diphenyl-based bis(2-aminoimidazolinium) compounds (Table 2-9): the lead compound FR60 (Ref 1), nine chloro, fluoro, and pyridinyl derivatives (Refs 2-10), and one CD27 *N*-hydroxy derivative called CDIV32 (Ref 11). The chemical structures of these dicationic compounds are listed in Table 2-9.

Table 2-9. Chemical structure of the bis(2-aminoimidazoline) compounds studied in this work.

REF	Compound	Structure	Salt	MW
1	FR60	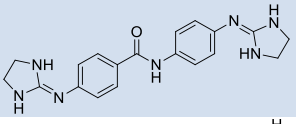	2 HCl	436.3
2	CRMV60	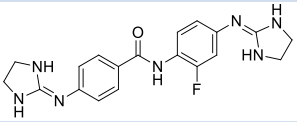	2 HCl	454.3
3	JNI33	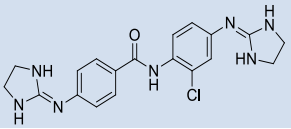	2 TFA	625.9
4	CRMV65	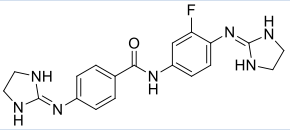	2 HCl	454.3
5	JNI18	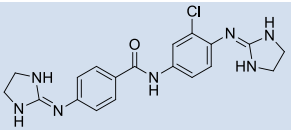	2 TFA	625.9
6	CRMV49	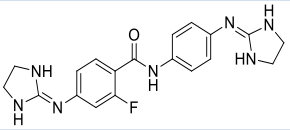	2 HCl	454.3
7	JNI17	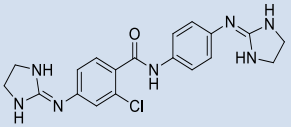	2 HCl	470.8
8	CRMV50	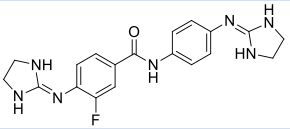	2 TFA	609.5
9	CRMV45	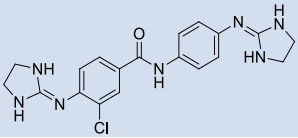	2 TFA	625.9
10	JNI32	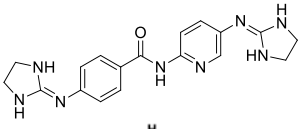	2 TFA	560.1
11	CDIV32	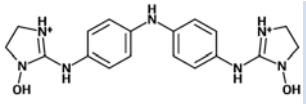	2 HCl	440.3

The compounds were prepared as dihydrochloride salts (2 HCl) or ditrifluoroacetates (2 TFA = CF_3CO_2H).

These promising antiprotozoal agents were synthetized by Dr. Dardonville's group at the Institute of Medicinal Chemistry, CSIC, Madrid. The synthesis of the lead FR60 (1) was performed following a procedure described previously in Rodríguez et al., 2008. The FR60 derivatives (compounds 2-10) were synthesized as described in Ríos Martínez et al., 2015b. Compound CDIV32 (11) was synthesized as described Nieto Garrido et al. 2011.

The samples are dissolved in dimethylsulfoxide (DMSO) (Sigma-Aldrich) by stirring vigorously with a vortex at atmospheric pressure and room temperature until completely homogeneous. 10 mM stock solutions in DMSO are stored at -20°C. Dilutions from the stock solution are performed by dilution with the corresponding buffer or media according to the experiment to be performed, to obtain a final amount of DMSO in the dissolved solution >5%.

2.4 DNA Oligonucleotides

Due to the high flexibility and polymorphism of AT-rich DNA, short oligonucleotides with maximum 23 bp were used (Table 2-10). Longer oligonucleotides induce disorder and complicate the aim of obtaining high quality ordered crystals. The length of the oligonucleotide, together with the sequence and oligonucleotide stacking interactions can influence periodicity and packing in the crystal by changing the length of the helical repeat unit. Due to this fact a considerable portion of structures in the PDB are decamers and dodecamers.

DNA samples for crystallography must comply high purity standards. Any impurity (as contaminant particles or degradation) could influence the crystallization process and disrupt the internal periodicity in the crystal. The oligonucleotides used for crystallographic essays must be in the range of 95 to 98% purity.

All the oligonucleotides used were synthesized at the Genomic Platform of the Pasteur Institute as the ammonium salt on an automatic synthesizer by the phosphoramidite method and purified by gel filtration and reverse-phase HPLC.

DNA powder samples were disolved in 25 mM sodium cacodylate pH 6.5, as it prevents the degradation of the sample due to its antimicrobial effect. Concentration of the oligonucleotide sample is verified by spectrophotometric quantification using the Lambert-Beer law (Equation 2-1).

$$A = \varepsilon C l$$

Equation 2-1. Lambert-Beer Law.

where A is absorbance at a given wavelength, C is the concentration in [M], l is the path length, which is usually 1 cm for typical cuvettes and ε is the extinction coefficient in [$cm^{-1}M^{-1}$] calculated based on the nearest-neighbor model (Cantor et al, 1970). In our case there are no contributions from DNA modifications and ε can be obtained with Equation 2-2. The data for ε are given at neutral pH, 25°C and 260 nm in Table 2-10.

$$\varepsilon_\lambda = 2\left(\sum_{1}^{n-1} \varepsilon_{dinucleotide@\lambda}\right) - \sum_{2}^{n-1} \varepsilon_{nucleotide@\lambda}$$

Equation 2-2. Extinction coefficient equation by Cantor et al. (1970).

Table 2-10. Extinction coefficient (ε) at 260 nm, neutral pH and 25°C.

DNA	ε [$L \cdot mmol^{-1}cm^{-1}$]	DNA	ε [$L \cdot mmol^{-1}cm^{-1}$]
pdA	15,4	dCpdG	9,0
pdC	7,4	dCpdT	7,6
pdG	11,5	dGpdA	12,6
pdT	8,7	dGpdC	8,8
dApdA	13,7	dGpdG	10,8
dApdC	10,6	dGpdT	10,0
dApdG	12,5	dTpdA	11,7
dApdT	11,4	dTpdC	8,1
dCpdA	10,6	dTpdG	9,5

Values from Cantor et al. (1970).

Absorbance is read in the range approximately of 210 nm to 310 nm in a spectrophotometer to verify maximum absorbance wavelength, which typically is

around 260 nm for DNA, corresponding to the aromatic rings of the nucleobases. This is used to calculate the concentration of the oligonucleotide, but can be also used to confirm the absence of other molecules and proteins as contaminant, which contribute with local maximums at different wavelengths.

For the UV-Vis spectrophotometry analysis a Carry 100 system from Agilent was used. The cuvette used for these measurements requires a relative large volume (0.5 mL), which is not typically available. Thus the original sample is diluted 1:1000 (in H_2O *milliQ®*) in order to make an easy measurement and calculate the concentration. The value obtained is then divided by two in order to obtain the double-stranded DNA concentration, which is the final concentration of the oligonucleotide used in the experiment calculations.

Table 2-11. Extinction coefficients (ε) and concentration and specifications of oligonucleotides used in this work.

DNA sequence	Length [bp]	ε [$L \cdot mmol^{-1} cm^{-1}$]	Vol [µL]	Conc [mM]	MW [$mol \cdot g^{-1}$]
1. CCAATAATCGCGATTATTGG	20	196.5	30	7.32	12232.2
2. ATTATTAATAAT	12	129.3	20	4.36	7285
3. AATATATATATT	12	131.3	10	3.38	7285
4. AAATATATTT	10	107.2	50	3.05	6050.2
5. CGAATTAATTCG	12	119.5	25	4.44	7289
6. ATTAATTAAT	10	107.2	50	5.28	6050.2
7. AATAAATTTATT	12	127.3	50	4.52	7285
8. ATATGCATAT	10	104.6	30	3.35	6052.2
9. ATATCGATAT	10	106.2	40	7.47	6052.2
10. AATAATCGCGATTATT	16	163.1	80	1.56	9758.6
11. AATTTAAATT	10	105.2	50	3.79	6050.2
12. ATTTATAAAT	10	107.2	10	5.61	6050.2
13. GGGAAATTTCCC	12	114.9	10	3.3	7290.8
14 AATAAATTTATTT	13	135.4	50	3.66	7902.4
15. AAATTT	6	63	40	2.6	3580.6
16. AATAATTATT	10	107.2	20	5.22	6050.2
17. CATATATATG	10	105.2	50	2.72	6050.2
18. AATTATAATT	10	107.2	40	5.03	6050.2
19. ATAATATTAT	10	109.2	40	2.515	6050.2

Oligonucleotide concentration is given in terms of DNA duplex.

The values of extinction coefficients and concentrations calculated for the oligonucleotides stocks prepared during this work are listed in Table 2-11.

2.5 Crystallization of Macromolecules

Crystallization of macromolecular complexes represents a crucial step for the analysis by X-ray crystallography, as it requires well-ordered single crystals of adequate size. Obtaining crystals does not necessarily imply that they are well ordered and have the appropriate atomic periodical arrangement for structure resolution by X-ray crystallography. This can result in poor diffraction patterns with low resolution. In particular, for AT-rich DNA, getting the right crystallization conditions to obtain diffraction-quality crystals is not an easy task.

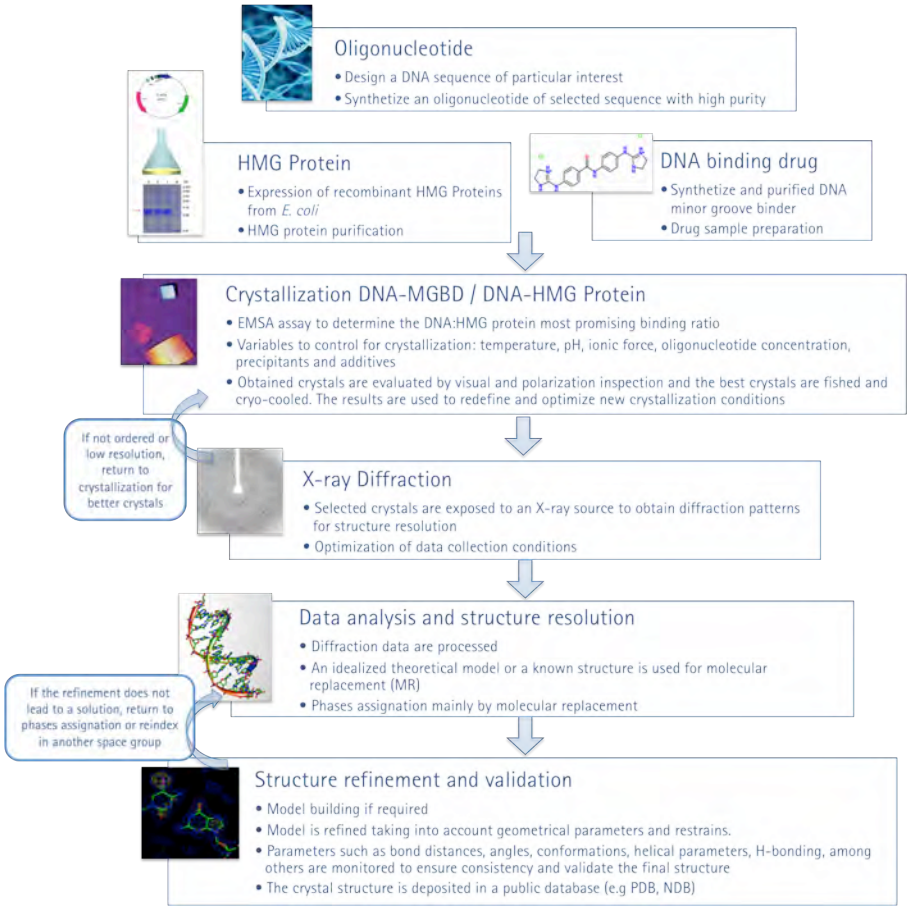

Figure 2-5. General scheme for DNA-ligand crystallization

The successful crystallization of macromolecules relies on several factors such as the physicochemical properties of the oligonucleotide, the purity of the samples, concentration, pH, temperature, ionic force, precipitants and additives, control of mass transfer (diffusion, convection) and pressure, and presence of electric and magnetic fields, among others.

The determination of the 3D structure by X-ray crystallography includes basically the following steps: (1) obtaining the target macromolecule (design and synthesis or expression, and purification), (2) search of initial crystallization conditions, (3) optimization of crystal quality, (4) diffraction data collection, (5) data analysis and processing, (6) structure determination, (7) refinement of the 3D model and (8) validation. Figure 2-5 represents a general scheme of the process for DNA-ligand crystallography.

2.5.1 Crystallization Fundaments and Parameters

The crystallization of macromolecules is a multi-parametric process involving three main steps:

1. *Nucleation*: the most difficult problem to address since it occurs when a specific number of macromolecules associate to form a critical mass that breaks the energetic barrier of a first-order phase transition and precipitates to the solid state as a nucleus. This step takes place when the solution is supersaturated, in a meta-equilibrium called labile zone to avoid amorphous precipitation (Figure 2-6).
2. *Crystal growth*: once a nucleus has formed, it serves as a scaffold center for incorporation of the macromolecules in a crystal network, usually from a monomeric state. This step takes place in a supersaturated state in meta-equilibrium, near the phase boundary called metastable zone (Figure 2-6). A solution reaches this state after nucleation, a consequence of the concentration decrease, as solute escapes to the solid state by forming

nucleus. The metastable phase favors diffusion conditions for ordered incorporation of molecules as layer addition over crystallographic faces.

3. *Halt in growth (or cessation of growth)*: after consumption of excess macromolecules during crystal growth, concentration decreases, reaching equilibrium when thermodynamic energetics are not enough for solute to pass to solid state, resulting in the stop of crystal growth.

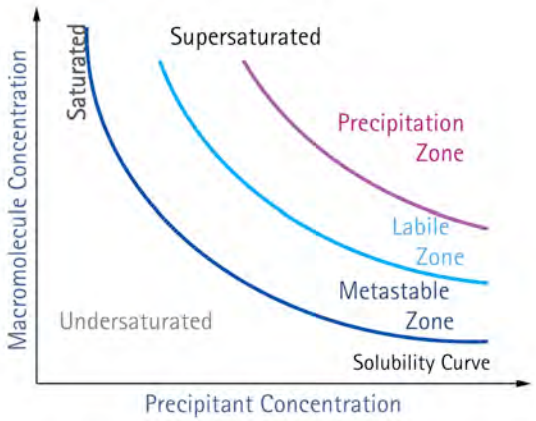

Figure 2-6. Schematic representation of a 2D phase diagram for the crystallization of macromolecules showing the compound solubility as function of precipitant. Labile and metastable zones, where nucleation and crystal growth respectively occur, are indicated.

The whole crystallization process can be suitably visualized in a two-dimensional phase diagram (Figure 2-6), representing the stable states as a function of two crystallization variables: macromolecule concentration and precipitant concentration. When the concentration of a protein solution is brought above its solubility limit, the solution becomes supersaturated. Depending on the level of supersaturation this zone of the diagram can be divided into three regions: very high supersaturation (precipitation), where molecules form amorphous aggregates; intermediate supersaturation (labile), where nucleation occur; and lower supersaturation (metastable), where only crystal growth is accomplished.

Supersaturation is the variable that drives the crystallization and determines their occurrence and extent as well as the kinetics that govern them. The best crystallization strategy is to induce nucleation at the lowest level of supersaturation, just within the

labile region. Regardless the variable condition manipulated to reach to this point, this should be done slowly in order to obtain well-ordered crystals. If this process takes the system excessively fast to supersaturation, protein aggregates having short-range order or disordered amorphous precipitate not suitable for X-ray diffraction may appear. On the other hand, if the system never reaches supersaturation, it will not crystallize.

The evolution of the three crystallization steps during the process usually generates diffusion from concentration gradients of precipitant, water and other components present in the crystallization solution. This process slowly brings the solution to the supersaturated state for nucleation, while crystal growth compensates for solute lost, extending the residence time in the metastable phase for better crystal growth. Changing the temperature, pressure or both can also change the thermodynamic state. The temperature control and variation is performed carefully according to the evolution of the crystallization process.

For the here presented work, the crystallization system is constantly modified as the process evolves by changing the concentrations in the equilibrium solution, in particular for the precipitant. The relationship between macromolecule solubility and precipitant concentration is a function of the type of precipitant, but usually, macromolecules solubility decreases proportionally as the precipitant concentration increases (Benvenuti & Mangani, 2007).

The crystallization of biomacromolecules is an exceptionally complex process. Some variables that influence crystallization of macromolecules are the concentration of components in the solution (e.g macromolecule concentrations and ratio, precipitants, additives), pH, temperature, ionic strength, pressure, electric fields, magnetic fields, properties that affect mass transfer (e.g. density, viscosity, volume, geometry, diffusion, convection), sample integrity and purity (i.e. heterogeneity of sequence and length, and presence of other molecules), contaminant, biochemical and biophysical properties of the macromolecule (eg. hydrophobicity, electrostatic interactions, conformational changes, flexibility, intermolecular interactions, ligands interaction). Additionally, there

are experimental contributions and external factors that perturb the system (e.g. vibrations) and influence crystallization. Therefore, this multi-variable process is largely empirical in nature, and demands patience, perseverance and intuition.

The large number of variables involved in crystallization makes this process particularly hard to control and specific for the crystallization of each macromolecule. Then, the number of possible screening conditions turns almost infinite when defining rationally the set of parameters to crystallize a given macromolecule. For this reason, commercial kits based on previous successful conditions described in literature have been developed. One of such kits is the Hampton Natrix HR2-116 (Scott et al., 1995), which can be used for the initial test. In any case, crystallization is commonly an iterative process where crystallization conditions are modified based on results of tested conditions.

The main parameters that are controlled during crystallization are:

- *Oligonucleotide concentration*; we have worked with oligonucleotide concentrations between 0.1 mM and 0.4 mM. A high concentration of oligonucleotide will reach supersaturation easily with little precipitant, whereas low oligonucleotide concentration will require more precipitant.
- *HMG protein concentration*; high protein concentration is normally used for crystallization in a range of 3 to 10 µg/µL. To carry it out samples were concentrated by ultrafiltration.
- *Sample purity and homogeneity*; very high macromolecule purity is required for crystallization. Impurities or heterogeneities can prevent crystallization or introduce irregularities limiting the quality of the obtained crystal. In the case of proteins, purity and homogeneity is determined by electrophoretic methods (see section 2.2). For DNA oligonucleotides, samples from the Pasteur Institute guarantee purity level of 98-99%. DNA stocks are conserved in sodium cacodylate to prevent bacteria or fungi contamination.
- *pH;* the role of pH in macromolecule crystallization is very important. A change of pH can modify solubility of the macromolecule, and more

dramatically when the pH is close to its pK_a. More importantly, pH affects the conformation and stability of the macromolecule, and plays a key role in the binding specificity, molecular hydration and in the interactions with small molecules and ions by modifying the intramolecular interactions in the crystal. Defining the right pH depends on which are the most beneficial configuration of conformation and intermolecular interactions for the crystallization of the desired complex, which vary from macromolecule to macromolecule. In particular for DNA, a starting point would be a range of pH from 6 to 7.5, which ensures base pairing, and has demonstrated good crystallographic results also for proteins.

- *Ionic strength*; the ionic concentration not only helps to stabilize the helical structure of DNA and the tertiary structure of proteins, but also stabilizes intermolecular interactions generated by packing in the crystal. Different ions have different affinities for specific groups of nucleobases and amino acid R-groups. Thus, defining the right ions for crystallization depends on the physicochemical properties of the oligonucleotide and/or protein, and the intermolecular and intramolecular interactions generated during crystallization, which are not easy to predict. Besides, the ionic strength modifies the solubility of the macromolecules.
- *Drugs*; DNA binding drugs are crystallized in complex with DNA in order to determine the specific interactions and structural features that confer a specific function. The presence of certain ligands can influence crystallization; they can stabilize specific configurations beneficial for the crystal packing, but can also prevent crystallization by the formation of unspecific interactions or steric hindrance. Drug samples must be perfectly dissolved and present high purity (see section 2.3).
- *Temperature*; it affects the solubility of the macromolecule, but more importantly, it also affects its stability and secondary structure. In the case of DNA, the temperature must be below the melting temperature to avoid denaturation. Some AT-rich oligonucleotides have melting temperatures around room temperature (25°C), so that it is convenient to use lower

temperatures for crystallization, usually between 4°C and 21°C when crystallizing DNA-drug complexes. For HGM proteins, we always work at low temperature (4°C) to ensure their stability.

- *Precipitants*; they change the solubility of the macromolecules to reach supersaturation and produce nuclei that later could grow as crystals. For DNA and protein crystallization, the most common precipitants are 2-methyl-2,4-pentanediol (MPD or Hexylene glycol) and polyethylene glycol (PEG), which work also as cryo-protectants. Additionally co-precipitants, such as isopropyl alcohol, can be used to force the system to reach supersaturation and later keep it in the metastable zone. Spermine is commonly used as a co-precipitant for DNA. It is a symmetric lineal polyamine that has its amino groups positively charged at pH 6-7.5 and contributes to neutralize the negative charges of the phosphate backbone and stabilize the helical structure.

During this research work, crystallization conditions were based on previous successful assays and are described next.

The droplets were prepared to a final volume of 3-5 µL. The pH screening values were 6.0, 6.5, 7.0, and 7.5, using buffers such as sodium cacodylate, potassium cacodylate, HEPES and Tris-HCl. For DNA-drug complexes, the typical starting point was pH 6.5 using sodium cacodylate above 25 mM.

The oligonucleotide is dissolved in the buffer containing determined ions needed for annealing process, ensuring correct base pairing and conformational homogeneity. The divalent ions used for crystallization were magnesium (Mg^{2+}), manganese (Mn^{2+}) and calcium (Ca^{2+}) and ammonium (NH_4^+). The anions used were chloride (Cl^{2-}) and acetate (CH_3-COO^-). Ion concentrations between 5 to 20 mM were used, since higher concentrations may lead to precipitation or denaturation.

Temperatures used for DNA-drug crystallization were: 4°C, 8°C, 11°C and 16°C. Temperature was modified depending on the first screening result, usually starting at 11°C. When droplets showed numerous crystalline nuclei, increasing the temperature

was beneficial to obtain fewer nuclei that lead to the growth of the adequate size crystals. Temperature changes were always made, in steps, transferring to the next lower temperature and left until equilibrium before transferring to the next temperature if required. DNA-protein crystallization was performed at 4°C.

Precipitants used were MPD and PEG 3350. A common practice is to set the initial precipitant concentration relatively low (typically at 20%) and wait until the system reaches equilibrium. Then, increments of 2 or 3% are performed until equilibrium is reached again, repeating this process until nucleation. When crystals are growing, precipitant concentration can be incremented in steps of 0.5-1% to promote crystal growth.

For crystallization of DNA, spermine as co-precipitant is occasionally added, in a molar ratio between 2:1 (DNA/spermine) to stabilize the helical structure while contributing to reach supersaturation. Other compounds used as co-precipitants are isopropyl alcohol in 3-10% concentration.

Commercial crystallization conditions were used mainly for the crystallization of the DNA-protein complex. The tested conditions were: Hampton Natrix HR2-116 (Scott et al., 1995): 7, 10, 15, 16, 22, 25, 31, 34, 42, 43, 46, and 48.

For the crystallization of the DNA-drug complex, the drug and the DNA were usually preincubated in buffer to promote interaction for 1-2 hours, while DNA-protein complex was preincubated from 1 hour to overnight periods.

In order to verify the DNA-protein complex formation, electrophoretic mobility shift assay (EMSA) was performed (see section 2.2.3), not only to detect the DNA-binding protein activity but also to evaluate the binding stoichiometries, which provide information of conditions that best stabilize the DNA-protein complex. For the crystallization of DNA-HMG protein complexes, DNA/Protein molar ratio of 1:1, 1:2, 1:3, 1:4 and rarely 1:8 were used.

2.5.2 Crystallization Method: Vapor Diffusion Technique

To obtain high quality single crystals is the basis of X-ray structure determination and also its limiting step. For this reason, multiple different macromolecular crystallization methods have been described, which use different approaches to control mass transfer and concentration of all components of the system to reach supersaturation for crystallization. The selection of the method employed depends on the particular requirements and the available amount of macromolecule(s) for each case. The most used macromolecular crystallization methods are vapor diffusion, microbatch, evaporation, microdialysis and free-interface diffusion. For the purpose of this research work, crystallization assays were performed using the technique of vapor diffusion, which is the most widely used method for macromolecular crystallization.

In this technique, a droplet of the solution of macromolecule, precipitants and additives in a non-supersaturated state is equilibrated by vapor diffusion against a reservoir with precipitant and additives at high concentration, the whole in a hermetic system. This process gradually changes concentration of all components, taking the system gently to a supersaturated state to obtain well-ordered crystals.

The two typical vapor diffusion set-ups are hanging-drop, where a droplet is placed on an inverted cover slip, and sitting-drop, where the droplet is placed on a pedestal (Figure 2-7). Modern crystallization robots use micro-fluidics technologies with the sitting-drop technique to generate large screens of crystallization conditions using low volume samples. Frequently, when favorable conditions are found with robots, they have to be replicated by hand in a larger volume to obtain suitable crystal for X-ray diffraction. Both set-ups, hanging-drop and sitting-drop, were performed in two different arrangements, either using a MRC Maxi 48-Well Crystallization Plate (Swissci) or individual capsules were used for crystallization of DNA-drug and DNA-protein, (Figure 2-7).

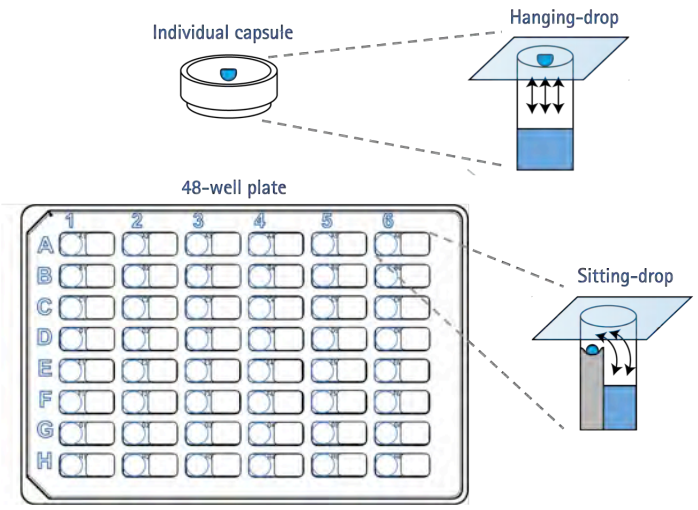

Figure 2-7. Schematic representation of the vapor diffusion crystallization set-ups used: hanging-drop and sitting-drop. This technique has two liquid phases: (1) the droplet, containing a crystallization solution with the macromolecule and (2) the reservoir, which contains the precipitant solution. A third gaseous phase is used to carry out vapor diffusion.

For the DNA-HMG protein complex study, screens of crystallization conditions were carried out using 48-well plates with 3 µL droplets, containing different defined concentrations of oligonucleotide and protein, buffer, ions, precipitant and other additives. The reservoir is filled with 200 µL of the precipitant solution at high concentration, and then a silylated coverslip is placed on top and sealed to promote vapor diffusion and reach the equilibrium that will drive the system to the supersaturated state required for crystallization. In this set-up, the conditions in the reservoir are not changed during the experiment.

Generally, DNA-protein and DNA-drug complexes crystallization studies were screened using individual capsules. This method has the advantage that parameters (such as temperature) can be modified individually for each condition. Another advantage of this set-up is that once the equilibrium is achieved, if the system has not reached supersaturation or produced crystals, the conditions in the reservoir can be changed to generate new equilibrium conditions. As evaporation affects directly the kinetics of supersaturation (Wilson et al., 1991), the idea of this process is the control of evaporation to slowly reach supersaturation in the labile zone, to produce only few

nuclei and extend the time in the metastable zone to promote crystal growth. Typically, a waiting time of 3 to 5 days prior to increasing the precipitant concentration was adopted. For MPD, it is normal to start at 20% precipitant and carefully increase concentration stepwise. In particular cases, once crystals appear, precipitant concentration can be increased to promote crystal growth.

The iterative process of obtaining diffraction-quality crystals can be divided into two main phases: coarse screening to identify initial crystallization conditions, followed by optimization of these conditions. There are several parameters and considerations to take into account during the optimization process of macromolecular crystallization.

During this work, the employed optimization strategies were grid screen and seeding technique. The first one was carried out starting on a positive condition in which obtained crystals were not presenting enough quality for X-ray diffraction. The screening is prepared using closely related experimental conditions to the ones performed before varying only two factors. If the results are negative, the procedure continues with a second choice of factors and so on until success is achieved. The other method employed includes two categories of the seeding technique: macroseeding and microseeding. Macroseeding consists in the transfer of one crystal (usually 5-10 µm in size) from a solution in which nucleation and initial growth have occurred to a less supersaturated solution to slowly continue the growth. In microseeding method, very small nuclei are transferred to solutions with metastable supersaturation.

2.5.3 Crystal Selection and Cryo-Crystallography

The crystals obtained are continuously evaluated and scored to monitor their evolution. The best crystals are selected initially based on a visual inspection that evaluates the size, the shape, and perceivable defects. A second inspection is carried out under polarized light to evaluate the birefringence of the crystal, which is an indicator of the internal order of the crystal. It can be used additionally to identify a twinned crystal (macle) by the presence of two polarizing domains.

Cryo-crystallography is a common and indispensable technique for macromolecular crystallography (Pflugrath, 2004) that is routinely used for single-crystal X-ray diffraction (section 2.6.3). It allows preserving the best crystals cryo-cooled at 100 K until diffraction to reduce radiation damage and disorder from thermal motion (Debye-Waller effect). Selected crystals are fished from the droplet using a cryo-loop that catches the crystal in a thin layer of liquid by surface tension (see Figure 2-8). A cryo-protectant, such as glycerol, MPD, ethylenglycol or PEG, may also be added by soaking the crystal in a solution that contains the cryo-protectant. During this research work, the crystallization conditions already contained either MPD or PEG, which work as cryo-protectants, and the crystals were directly transferred from the cryo-loop to a Dewar with liquid nitrogen for flash freezing immediately after fishing. Fished crystals are stored and transported at liquid nitrogen temperature until X-ray diffraction.

Figure 2-8. Diagram of a cryo-crystallography system (left) and a cryo-loop with a crystal mounted (right)

2.6 X-Ray Crystallography

The elucidation of the three-dimensional structure of biological macromolecules has contributed enormously to the current understanding of many basic mechanisms involved in life processes. X-ray diffraction from high quality crystals remains the most reliable approach to obtain accurate structural details at atomic resolution. It provides powerful insight into the molecular mechanisms in which macromolecules interact with each other to form complex supramolecular assemblies capable of performing specialized biological functions (Krauss et al, 2013). Moreover, knowledge of binding

sites at atomic detail allows a rational drug design, which is essential for searching of novel drugs. For this reason, X-ray crystallography has been the main technique used for DNA-ligand structure determination.

2.6.1 Crystalline Structure

X-ray diffraction by crystals is a reflection of the periodicity of crystal architecture. Crystals represent the most highly ordered state of matter, where molecules are organized in a three-dimensional network with a periodical motif based on a geometrical simple unit. The main elements that define this crystal network are the unit cell, the asymmetric unit and the space group.

The unit cell depicts the simplest portion of the crystalline structure that can be repeated by translation to reproduce the full crystal. In other words, it is defined as the smallest parallelepiped containing all the symmetry operations of the space group. It describes the distribution of atoms in the lattice from a simple motif and it comprises three vectors that are independent from the coordinate system. These vectors are described by six lattice parameters (Figure 2-9), the lengths of the cell or vectors modulus (a, b, c) and the angles between them (α, β, γ). Atomic positions are defined on this reference frame with the set of atomic position (x_i, y_i, z_i).

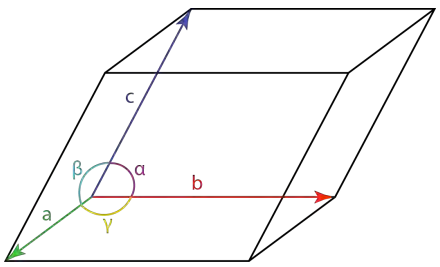

Figure 2-9. The unit cell is the simplest repeating unit in a crystal. It is determined by three vectors, which are described by six parameters: the lengths of the cell (a, b, c) and the angles between them (α, β, γ).

The minimum group of atoms that after applying a set of symmetry operations reproduce the content of the unit cell is called the asymmetric unit (Figure 2-10). The asymmetric unit does not necessarily correspond to one molecule in the crystal; it can be defined as fractions of the molecule or multiple molecules, including other atoms like ions and water. In spite of the fact that the asymmetric unit is a subset contained within the cell, this does not imply that the entirety of the asymmetric unit must lie within the boundaries of the unit cell. However, its distribution may be constrained by the Bravais lattice.

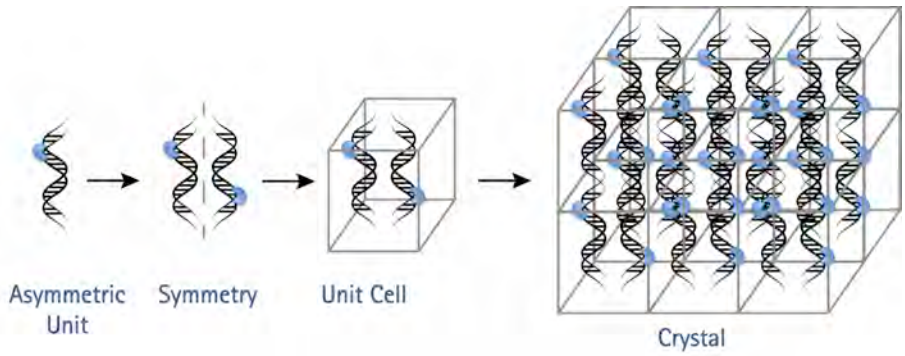

Figure 2-10. Schematic representation of the asymmetric unit as a group of atoms. After applying a set of symmetry operations the unit cell is obtained; when this cell is regularly repeated, the crystal is generated.

Bravais lattices, also referred to as space lattices, are a mathematical concept of an infinite distribution of discrete points with invariable structure under a certain group of translations. When the discrete lattice points correspond to atoms, molecules or ensembles of both, the Bravais lattice defines the crystalline arrangement. For a three dimensional space, there are seven crystalline systems with fourteen Bravais lattices (Table 2-12) geometrically defined by the parameters of the unit cell (a,b,c, α, β, γ). Distribution of the lattice points in the unit cell defines the lattice type as Primitive (P) with nodes in the corners; Body-Centered (I) with nodes in the corners and the cell center; Face-Centered (F) with nodes in the corners and the center of faces; Base-Centered (A, B, or C) with nodes in the corners and one in the center of the corresponding face; Rhombohedral (R) with nodes in the corners with $a = b = c$ and $\alpha = \beta = \gamma = 90°$.

Table 2-12. Bravais lattices.

Lattice System	Lattice Type	Distances	Axial Angles
Cubic	P, I, F	$a = b = c$	$\alpha = \beta = \gamma = 90°$
Tetragonal	P, I	$a = b \neq c$	$\alpha = \beta = \gamma = 90°$
Orthorhombic	P, I, F, C	$a \neq b \neq c$	$\alpha = \beta = \gamma = 90°$
Hexagonal	P	$a = b \neq c$	$\alpha = \beta = 90°, \gamma = 120°$
Rhombohedral	R or P	$a = b = c$	$\alpha = \beta = \gamma \neq 90°$
Monoclinic	P, C	$a \neq b \neq c$	$\alpha = \beta = 90°, \gamma \neq 90°$
Triclinic	P	$a \neq b \neq c$	$\alpha \neq \beta \neq \gamma \neq 90°$

Moreover, the symmetry operations (reflection, rotation, inversion and improper rotation) comprise 32 possible point groups or crystal classes. In addition to the point group, configuration of the atoms in space, which comprises additional symmetry operations (pure translation, screw axes and glide planes), originate 230 different space groups, from which only 65 are possible for chiral organic molecules.

Crystallographic vectors and planes in a Bravais lattice are described by the Miller index notation: h; k; l. The set (*hkl*) defines a point in reciprocal space; in real space they denote a plane that intercepts the three points *a/h, b/k, c/l*. Then, the Miller indices are proportional to the inverses of the intercepts of the plane with the unit cell. Any point in the reciprocal lattice can be expressed as a vector (q), which is the sum of integer multiples of the reciprocal axes (defined as *a*, b*, c**).

The Miller indices are very useful to work between the real and reciprocal space, and to identify the crystal planes that contribute to diffraction.

2.6.2 Fundamentals of X-Ray Crystallography

The purpose of macromolecular X-ray crystallography is to determine the three-dimensional structure of a macromolecule through the reconstruction of the electronic density of its atoms, which generate the diffraction pattern when the incident radiation interacts with the crystal. The electron density distribution of the macromolecular crystal is the Fourier transform of the waves diffracted by the crystal.

The Fourier transform can be expressed as a complex number with a magnitude and a phase. From the X-ray diffraction data, the information for the amplitude can be obtained because the intensity of reflections is proportional to the square of the structure factors amplitude.

For an ideal crystal, the Fourier transform has zero value except for the Bragg peaks, where the three dimensional vector corresponds to the nodes of the reciprocal lattice, known as Miller indices (hkl; described before). Therefore, the electronic density function can be expressed as the sum of structure factors amplitudes and phases as presented in Equation 2-3,

$$\rho(xyz) = \frac{1}{V}\sum_{\substack{hkl \\ -\infty}}^{+\infty} |F(hkl)| e^{-2\pi[hx+ky+lz-\phi(hkl)]}$$

Equation 2-3. Function defining the electron density in a point of the unit cell given by the coordinates (x, y, z).

where $\rho(xyz)$ represents the electronic density at a three dimensional vectorial position (x,y,z) in the crystal; $|F(hkl)|$ represents the resultant of the structure factors amplitudes of all atoms contained in the unit cell; h,k,l the Miller indices; and $\phi(hkl)$ the phases of the structure factors.

The diffraction data give all the information for the amplitude of the structure factors, but the information for the phases is still missing, lost during diffraction experiments. This is known in crystallography as "the phase problem". To complete this phase information, different mathematical methods have been developed, such as *Ab initio* phasing or direct methods (used for relatively small molecules) and anomalous X-ray scattering (Multi-wavelength Anomalous Diffraction (MAD) and Single-wavelength Anomalous Diffraction (SAD)), Multiple Isomorphous Replacement (MIR), and Molecular Replacement (MR), commonly used for macromolecules. The latter is used when structural information on the biological macromolecule under investigation is available.

2.6.2.1 Bragg's Law

The Bragg's Law (Bragg and Bragg, 1913) defines the condition for diffraction in terms of the scattering at a given wavelength.

When X-rays hit an atom, the electromagnetic wave interacts exciting the external electrons, which emit back the incident electromagnetic radiation in all directions with the same frequency. In practice, an elastic scattering process dominates the re-emitted radiation, but it can be slightly affected by various effects (Rayleigh scattering).

In a crystal, the molecules and their atoms are periodically distributed in the crystalline network. This can be conceptualized as a set of discrete scatterers distributed in parallel planes separated by a constant distance *d* (Figure 2-11). If the scattered radiation from different planes interferes constructively, it would produce a Bragg peak or X-ray diffraction. The Bragg condition establishes that an interference is constructive when the phase shift among the emitted radiation by different atoms is a multiple of 2π. This leads to Bragg's law, described in Equation 2-4:

$$2d \sin\theta = n\lambda$$

Equation 2-4. Bragg's Law.

where the path difference for two interfering waves is given by $2dsin\theta$, and the waves remain in phase only when this path difference produces a phase shift proportional to 2π; θ is the angle between the incident rays and the diffraction planes, 2θ is the scattering angle, n is an integer, λ is the wavelength of the x-ray radiation and d corresponds to the interplanar distance. Consequently, a diffraction pattern is produced by the cumulative effect of constructive and destructive interference from reflections in consecutive crystallographic planes.

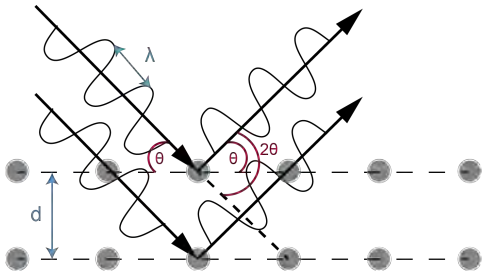

Figure 2-11. Bragg's law determines the angles for coherent scattering. Angle *2θ* is the scattering angle, *λ* is the wavelength and *d* is the interplanar distance. The lower beam travels an extra path *2dsinθ* for which constructive interference occurs if the path is a multiple of the wavelength (*nλ*)

Two common problems that enormously complicate the structure resolution are the presence of pseudo-translation and twinning. In particular, oligonucleotides with hexagonal packing have a high tendency to suffer pseudo symmetry and merohedral twinning (Abrescia & Subirana, 2002).

Pseudo-translation corresponds to two molecules or motifs with similar orientation that are related by non crystallographic symmetry (NCS). This can be usually identified in the Patterson map as an off origin peak with high intensity. The position of this peak can be used to identify its relative displacement and define the pseudo-translation vector to reproduce the molecule or motif from a known orientation.

In some cases, a special approach can be used to solve the structure by reindexing the data in a smaller cell (pseudo-cell) based on the translational vector. Here the density of the two related molecules is added and only one position needs to be identified. This position may give a clue of molecular packing, which later can be translated into the original cell. Some modern molecular replacement software like *Molrep* (Vagin & Teplyakov, 2010) and *Phaser* (McCoy et al., 2007) automatically detect any pseudo-translation peak and use it during MR.

Twinning, on the other hand, occurs when a multiple domain reorientation follows a transformation related to the crystal lattice but not of the symmetry of the point group (Koch, 2004).

The presence of twinning adds more symmetry to the crystal, which can lead to define the crystal in an apparent space group of higher symmetry than the real one. The twin lattice is formed by the overlap of lattices, which correspond to the different regions of the crystal. These regions are related by geometrical operations called twin operations, which include reflection that generates a twin plane, rotation that generates a twin axis and inversion that generates a twin center. The twin law is the set of twin operations used to map two regions of a twin.

Polarized light can be used to detect twinned crystals, which never reach, complete extinction by rotation (crystallization setup can interfere with this detection). In addition, a visual inspection is useful for the identification of potential twinned crystals that share a common growth center. Nevertheless, most of the twinned crystals are not detected until analysis of the diffraction data. Programs such as SFCHECK (Vaguine et al., 1999), Scala-Pointless (Evans, 2006) and Xtriange (Zwart et al., 2005) use these methods to detect twinning. Molecular replacement can be affected by the presence of twinning that adds noise to the rotation and translation. For the refinement of the model, programs such as *SHELX* (Herbst-Irmer and Sheldrick, 1998), *REFMAC5* (Murshudov et al., 2011) and *phenix.refine* (Afonine et al., 2005) already include procedures for twinning treatment.

2.6.2.2 Ewald Sphere

A crystal can be defined as a lattice of nodes (reflections) of equal symmetry. The requirement for constructive interference in a diffraction experiment means that in momentum (or reciprocal space) the values of momentum transfer where constructive interference occurs also form a lattice (the reciprocal lattice). The Ewald's sphere is a geometrical construction in that reciprocal space (Figure 2-12) that allow to determine which planes of the crystalline network will result in a diffracted signal for an incident radiation at a given wavelength λ.

For an incident wave vector S_i, if considering no energy is gained or lost in the diffraction (elastic process), the diffracted wave vector S_o has the same length as S_i.

The scattering vector ΔS is defined as $\Delta S = S_o - S_i$, a condition satisfied for diffraction when reciprocal lattice nodes lie on the sphere of radius 1/λ. This sphere is called the Ewald's sphere.

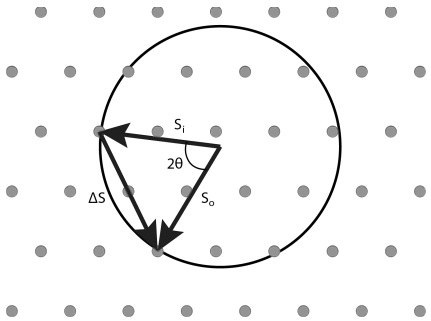

Figure 2-12. Ewald's Sphere of radius 1/λ. In reciprocal space, the lattice nodes that lie on the sphere satisfy that the diffraction vector ΔS is the difference between the incident wave vector S_i and the diffracted vector S_o. This establishes the relationship between the wavelength of the incident radiation (wave vector) with the reciprocal lattice of the crystal and the diffraction angle 2θ

The reciprocal lattice nodes are the values of momentum transfer where the Bragg diffraction condition is satisfied (see section 2.6.2.1). For diffraction to occur, the scattering vector must be equal to a reciprocal lattice vector.

2.6.3 Single-Crystal X-Ray Diffraction

For single-crystal X-ray diffraction, a beam of X-rays is focused on a single-crystal of the macromolecule to produce a diffraction pattern. There are various diffraction methods to obtain a diffraction pattern such as the Laue method, the Weisenberg method, the precession method and the oscillation method. The latter is the method employed during this work.

The oscillation method is the most widely used, especially for macromolecules. In this method, a single wavelength is used and the crystal is rotated an angle (ϕ) that defines multiple regions of reciprocal space that intersect the Ewald's sphere to produce diffraction. Modern detector efficiency allows operating with small angles (ϕ) for each frame to collect the diffraction from the large unit cells of macromolecules.

For this work, the angle of rotation (ϕ) and resolution ($2sin\theta_{max}/\lambda$) or detector distance are defined after performing a preliminary diffraction test. For crystals with low resolution and few diffractions spots, the angle ϕ is between 8 and 12°. For high resolution cases ϕ is between 0.5 and 1°. When the orientation of the crystal is not optimal (e.g. the axial helical axis is perpendicular to the X-rays during all the collection), the angle (ϕ) can be modified to reorient the crystal.

When a monochromatic X-ray beam is passed through a single crystal, the radiation interacts with the electrons in the atoms, resulting in scattering of the radiation to produce a unique image pattern. Multiple images are recorded with an area X-ray detector as the crystal is rotated in the X-ray beam. The diffraction patterns obtained have a symmetry center described by the Friedel's law. Friedel's pairs have the same amplitude due to the symmetry of the Fourier transform (Equation 2-5), where a complex number and its conjugate correspond to the same real part.

$$|F(hkl)|^2 = |F(\bar{h}\bar{k}\bar{l})|^2$$

Equation 2-5. Friedel's Law.

From this, collecting an angle of 180° will provide the complete data for 360°. Furthermore, the symmetry of the space group may reduce the angle of collection required for a complete dataset.

X-rays can be produced by conventional generators, synchrotrons and by plasma sources. Conventional X-ray sources are sealed anode or rotating anode, which are commonly used in home source equipment.

A synchrotron radiation source is a very intense, tunable source of radiation that generates a bright X-ray beam from the velocity change of electrons accelerated nearly to the speed of light in an electron storage ring.

The single-crystal X-ray diffraction studies were performed using synchrotron radiation (ESFR - BM16 and ALBA - Xaloc bl13). Relevant specifications of these synchrotron lines can be found in Appendix C.

In a synchrotron, the X-ray beam passes through a monochromator to filter all non-desired wavelengths. Then, mirrors redirect and concentrate the beam in a focusing step and finally the beam passes through a collimator. All these processes aim to obtain a narrow coherent X-ray beam that can be focused in the single-crystal to generate the best diffraction patterns with high resolution and less possible noise.

The diffracted light is collected using electronic detectors such as point detectors or area detectors. Area detector was used for this work, which has the advantage of recording simultaneously multiple diffraction spots, which are essential for macromolecular crystallography.

The crystal is mounted in a goniometer using a cryo-loop, which should remain all the time under a stream of liquid nitrogen (at 100 K) to preserve the crystal and to reduce radiation damage.

The parameters controlled during X-ray diffraction are:

- The wavelength and size of the beam
- The centering of the crystal within the X-ray beam on rotation
- The angle of rotation defines the number of diffraction spots per frame. If the direct cell is big, then a small angle should be used to avoid spots overlapping (usually between 0.5 and 1°)
- The collection angle, which is usually 180°. For more redundancy, 360° can be used
- The exposition time, which should be used the longest exposition before saturating the detector. The time varies considerably with crystal size
- The distance to the detector, which defines the maximum resolution for the collected diffractions (small distances for high resolution and large distances for low resolution)

The recorded set of two-dimensional diffraction patterns corresponding to a different crystal orientation are collected during single crystal X-ray diffraction and taken to the next step of the process: data diffraction analysis.

2.7 Structure Determination

The steps of the structure resolution process are: the determination of the unit cell parameters and the space group, assignation of the Miller indices to all diffractions in each frame, integration of diffractions, merge of diffractions and scaling of intensities, conversion of intensities to amplitudes, initial phase assignation, model building, model refinement and finally validation. To perform all these steps, computer packages that include specific software to perform each task are available. A comprehensive list of software for crystallography can be found in www.iucr.org/resources/other-directories/software. The software's packages employed in this work are *CCP4* (Winn et al., 2011) and *Phenix* (Adams et al., 2010).

2.7.1 Data Processing

Once X-ray diffraction has been performed on the selected crystals and the data has been collected, a mathematical analysis has to be done with the diffraction patterns.

The main purpose of analysis and interpretation of diffraction data is to solve the density function $\rho(xyz)$ in order to solve the structure of the macromolecule(s) studied. The dimensions of the unit cell, the space group symmetry and the amplitude term $|F(hkl)|$ for all diffraction directions are information that can be extracted from the diffraction patterns. The phase $\phi(hkl)$ of the diffractions cannot be directly determined.

Data analysis is done in two stages: (1) data reduction, which involves indexing, parameter refinement and integration; and (2) merge and scaling.

Data processing begins with "indexing" the reflections, i.e. to identify the dimensions of the unit cell and which image peak corresponds to which position in reciprocal space. To perform indexing and integration the programs *iMOSFLM* (Battye et al., 2011) and *XDS* (Kabsch, 2010) were used.

Each diffraction pattern corresponds to a segment of the reciprocal space and each spot corresponds to a different type of variation in the electron density. Then, it is

necessary to define which variation corresponds to which spot. When indexing, a reconstruction of peaks in the reciprocal space allows estimating the crystal lattice, dimensions of the unit cell (a, b, c, α, β, γ) and the orientation of the crystal from a subset of the data collection. The parameters obtained are refined together with the rotation matrix, center of the beam, masked regions (e.g. beam stop, ice rings), mosaicity (i.e. spread of crystal plane orientations), beam divergence, y-scale, twist, tilt and distance to detector. With the optimized parameters the diffraction spots are integrated, summarized as full or partial reflections and stored in a single file containing the unit cell dimensions, space group and for each reflection the Miller indices, position, intensity and its associated error.

To verify the space group, the integrated reflections must follow the diffraction conditions of the selected space group, for which the program *Pointless* (Evans, 2006) was used. This software confirms conditions for the Laue group, point group and space group systematically, giving a probability for all possible space groups, with the additional possibility to reindex the dataset in a new best space group.

To converge multiple observations of reflections and produce a file that contains averaged (equivalent) intensities for each reflection, the data obtained is then merged and scaled into a set of unique reflections with the proper intensity value. The programs used in this part of the process are *Scala* or *Aimless* (Evans, 2006).

An indicator used to assess the quality of the dataset is R_{merge} defined by Equation 2-6:

$$R_{merge} = \frac{\sum_{hkl} \sum_j |I_{hkj,j} - < I_{hkl} > |}{\sum_{hkl} \sum_j I_{hkj,j}}$$

Equation 2-6. R_{merge} equation.

However, due to its dependence on redundancy, R_{merge} may be substituted for an alternative improved version independent of redundancy parameter: R_{meas} (Equation 2-7).

$$R_{meas} = \frac{\sum_{hkl} \sqrt{\frac{n}{n-1}} \sum_{j=1}^{n} |I_{hkj,j} - < I_{hkl} > |}{\sum_{hkl} \sum_{j} I_{hkj,j}}$$

Equation 2-7. R_{meas} equation.

Common criteria for resolution cut-off are the average ratio of signal to noise the highest resolution shell $<I> / \sigma (<I>) \approx 2$, completeness in all shells > 90% and R_{merge} < 0.25 in the highest resolution shell. However, recent approaches recommend to not to cut resolution, but use all available data and only define the effective resolution (Evans & Murshudov, 2013; Diederichs & Karplus, 2013).

Finally, using the program *TRUNCATE* (French and Wilson, 1978) from the *CCP4* package (Winn et al., 2011) intensities are converted to amplitudes and placed on an approximate absolute scale using a scale factor obtained from a Wilson plot, as presented in Equation 2-8.

$$I_{hkj} = K \cdot A \cdot L \cdot p \, ||F(hkl)|^2$$

Equation 2-8. Relation between the structure factors and the intensity.

where K is a scale factor ($K = C^{-½}$); A the absorption factor; L the Lorentz factor; and p is the polarization factor.

2.7.2 Phasing: Molecular Replacement Method

To address the phase problem in the case of macromolecular structure determination, initial phase estimates can be obtained with different methods: multiple isomorphous replacement (MIR), anomalous X-ray scattering (MAD or SAD phasing) and molecular replacement (MR).

The MIR method is based on the Patterson method (Patterson, 1934). It uses the presence of heavy atoms in the crystal by soaking or co-crystallization. These atoms should not interfere with crystallization or change unit cell dimensions, as the crystal should be isomorphic with the native form. The heavy atoms act as large scatters that

can be identified with the Patterson function. The difference in the scattering amplitudes from the heavy and the native structures are used to calculate initial phases.

Anomalous X-ray scattering (MAD or SAD phasing) is based also on the changes in the intensity produced by the introduction of heavy atoms, but in this case using radiation at different energies (i.e. different wavelengths). When the frequency of the X-ray radiation is close to the natural vibration frequency of the electrons in a given atom, the atom behaves as an anomalous scatterer and the atomic scattering factor is modified. By analyzing the differences between diffraction data, it is possible to calculate initial phases.

By taking advantage of the homology between macromolecules, the MR method was used in this research work. This technique uses a related known structure as a search model to find the orientation and position of the molecules within the unit cell. The initial phases are assigned using the phases from the replaced homologous structure.

For proteins, sequence identity with more than 40% is used to select possible candidate models for MR. For DNA, it is more common to use an ideal model of the double helix with information inferred from the diffraction data, such as the rise, rotation and possible packing. The molecular symmetry of the double helix structure and the similarity between base pairs containing different nucleobases makes it difficult to rely only on the sequence, and even more if MR is done with a truncated resolution.

When the MR is performed, the unknown molecule orientation is obtained first with the rotation function, and then, a translation defined by the interatomic cross vectors between molecules is applied to place the molecule in the right position within the unit cell. The main purpose of the MR method is to find these two operators: the rotation and the translation functions.

The programs used for MR are *Molrep* (Vagin and Teplyakov, 2010) and *Phaser* (McCoy et al., 2007). Each program has its own correlation factor to identify solutions, but

Phaser uses a different approach by computing the likelihood of the solution. These programs also provide the *R* and the *C* parameters, which provide the suitability of positioning solutions regarding the data, as shown in Equation 2-9 and Equation 2-10.

$$R = \frac{\sum_{hkl} \left| |F_{hkl}^{obs}| - k\,|F_{hkl}^{calc}| \right|}{\sum_{hkl} |F_{hkl}^{obs}|}$$

Equation 2-9. *R* parameter calculation.

$$C = \frac{\sum_{hkl} \left[\left| |F_{hkl}^{obs}|^2 - \overline{|F_{hkl}^{obs}|^2} \right| \cdot \left| |F_{hkl}^{calc}|^2 - \overline{|F_{hkl}^{calc}|^2} \right| \right]}{\left[\sum_{hkl} \left| |F_{hkl}^{obs}|^2 - \overline{|F_{hkl}^{obs}|^2} \right| \cdot \sum_{hkl} \left| |F_{hkl}^{calc}|^2 - \overline{|F_{hkl}^{calc}|^2} \right| \right]^{1/2}}$$

Equation 2-10. *C* parameter calculation.

where F^{obs} and F^{calc} are the observed and calculated structure factor amplitudes; *R* is the reliability index or *R* factor, which represents the error between the model and diffraction data; and *C* is the correlation coefficient between the adequacy of the model and the observed data.

Besides, for MR of oligonucleotides, not only an existing known structure can be used, but it is also common to generate a theoretical structure with programs like *Turbo-Frodo* (Roussel et al., 1998) or *3DNA* (Lu & Olson, 2003). The particular anisotropy of nucleic acids, together with the typical crystal arrangement of pseudo-continuous helices and the similarity between base pairs, may turn the process of MR especially difficult.

For MR of DNA-protein complexes, a strategy that has previously shown its relevance within the hosting research group was used: perform the MR first with a B-DNA model theoretically generated, and once this molecule is positioned, the MR of an existing known structure can be used to find the protein.

In general, if the model replaced is similar, model building can be performed using the program *Coot* (Emsley et al., 2010) to fix the model. Computer software like *Pymol* (Schrödinger, LLC, 2015) and *CCP4mg* from the *CCP4* package (McNicholas et al. 2011)

are molecular visualization programs used to view and manipulate the molecular model obtained.

2.7.3 Structure Refinement

The aim of structure refinement is to maximize the consistency between the electronic density (X-ray diffraction data) and the atomic model. Several specialized optimization methods have been developed to refine macromolecules, such as the least squares method, conjugate gradient minimization, maximum-likelihood refinement and dynamics-based simulated annealing.

The program used for structure refinement is *REFMAC5* (Murshudov et al., 2011), which uses maximum-likelihood restrained refinement. The target function (Equation 2-11) for optimization *(f_{total})* is defined using Bayesian methods (Equation 2-12), in terms of a prior knowledge that depends on the geometry of the model *(f_{geom})* and a likelihood function *(f_{xray})* that define the link between the model parameters and the experimental data. The idea that unifies these two parameter realms is a common means for assessing the correctness of the model.

$$f_{total} = f_{geom} + w\, f_{xray}$$

Equation 2-11. Maximum-likelihood restrained refinement function.

$$P_{model;obs} = \frac{P_{model} + P_{obs;model}}{P_{obs}}$$

Equation 2-12. Bayesian function.

Geometrical parameters include chemical information of the molecule and its residues, internal consistency and structural knowledge such as known interatomic distances and secondary structure. The restrains commonly used for refinement include bond distances, bond angles, torsion angles, chiral centres, planar groups, van der Waals repulsions, van der Waals interactions, torsion, H-bond, chain bond B values, long-range B values and NCS. The latter is very useful if the model is close to correct. NCS restrains are useful when molecules in the asymmetric unit have highly similar

conformation, but are not related by the crystal symmetry. An alternative to secondary-structure restraints are the Ramachandran restraints, performed in *phenix.refine* to restrain the protein backbone, two different target functions are implemented based on the (ϕ, Ψ) distributions.

If necessary, *REFMAC5* can perform twin refinement. Rigid body refinement is usually done during MR, but it can also be used for further optimization of the orientation and the position of the macromolecule in the cell. TLS refinement is used for modeling anisotropic displacements, a set of rigid body domains are defined in the molecule and its rigid-body motion is described by translation (T), libration (L) and screw (S) tensors. TLS should not be used until the latest stages of refinement, since in early stages it could induce bias and set the system in a local minimum. Real space refinement is performed using the program *Coot* (Emsley et al., 2010), where residues can be optimized or refined to follow an electron density map or difference map.

The correlation between the X-ray data and the model quality equation (Equation 2-9) is measured, among other factors, by the improvement of two refinement statistics: R_{work} and R_{free}. R_{free}, is used to assess possible overmodeling (overfitting) of the data. It is calculated according to the Equation 2-9, but on a subset of data that usually corresponds to 5% of the total diffractions. This set of diffractions is not used for refinement. R_{work} uses the set of refined diffractions.

During each cycle of refinement the *R-factors* are reduced and atom positions (x,y,z), phases $\phi(hkl)$ and B factors are optimized. Optimum values of R depend on the resolution, but usually should be below 0.30, and the difference between R_{work} and R_{free} should not exceed 0.05. B-factor should be on the order of 100 Å^2 for resolutions around 3 Å and 40 Å^2 for resolutions around 2 Å. If after extensive refinement R_{work} and R_{free} cannot reach that value, potential reasons could be errors in MR, wrong space group, twinning or pseudo-translation.

2.7.4 Structure Validation

The final step in macromolecular structure resolution is the validation. In other words, it is the process of evaluating reliability for the three-dimensional atomic model.

To validate the structure is to locate incongruities, such as bond lengths, bond angles, dihedral angles, chirality, planarity, short atom contacts, electron density correlation, B-factors, and conformations.

Common programs used for this purpose are SFCHECK (Vaguine et al., 1999) and MolProbity (Chen et al., 2010). Using the graphical viewer *Coot* (Emsley et al., 2010) is possible to assess and fix geometry parameters, real space correlation, conformations (i.e. Ramachandran plot) and other parameters. The program 3DNA (Lu and Olson, 2008) is used additionally for oligonucleotides, to analyze and validate base pairing, sugar puckering, type of DNA, bending, local base pair parameters, local base pair helical parameters and local base pair step parameters; all described in Figure 1-4. In this thesis, the atomic model figures were prepared either with *Pymol* (Schrödinger, LLC, 2015), *Coot* (Emsley et al., 2010) or *CCP4mg* (McNicholas et al. 2011).

Once the molecular structure is analyzed and validated, the final model is deposited in a crystallographic database providing the atomic coordinates, the related experimental data and the structure resolution details. The most popular database for macromolecules is the Protein Data Bank (PDB). Once the PDB validation is complete, an identification code of the macromolecule or complex is assigned and the atomic coordinates of this new structure become freely accessible to the scientific community.

2.8 SPR-Biosensor Assays

Surface plasmon resonance (SPR) binding analysis methodology is an optical technique used for detecting molecular interactions. It allows the real-time detection and monitoring of biomolecular binding events of two different molecules in which one is mobile and one is fixed on a thin film.

Biacore® technology have been employed in this work to perform the SPR binding analysis. *Biacore®* is a widely used technique due to its high sensitivity, great precision, fast assay development and because of the wide range of interactions that this system supports for analysis. This technology provides high-quality qualitative and quantitative data in a range of fields such as immunogenicity studies, vaccine development, biological research, biotherapeutics and small-molecule drug discovery and development.

In our case, SPR binding analysis is performed to aid in understanding the molecular interaction between the bis(2-aminoimidazoline) compounds or HMG proteins with AT-rich oligonucleotides, and to analyze and compare the selectivity, affinity and kinetics of these DNA-binding molecules.

SPR is a phenomenon that occurs in thin conducting films at an interface between media of different refractive index. In the case of this work, the media are the glass of the sensor chip and the sample solution, and the conducting film is a thin layer of gold on the sensor chip surface. In an SPR experiment, the ligand (interacting molecule) is bound to the biosensor surface while the analyte is delivered to the surface in a continuous flow through a microfluidic system (Figure 2-13). When polarized light is applied to the surface of the sensor chip and is reflected, the intensity of the reflected light is reduced at a certain incident angle, the SPR angle. The interacting molecules at the surface of the sensor chip increase the refractive index, which alters the SPR angle (see Figure 2-13). The detector reveals position changes of the intensity dips in the wedge of the reflected light corresponding to the SPR angle. Consequently, the binding of biomolecules to the sensor surface will cause a shift in the SPR angle, which is directly proportional to the increased mass. The response (signals) generated is measured in resonance units (RU).

All SPR experiments were performed at the Institute of Medicinal Chemistry, CSIC, Madrid, using a *Biacore® X-100* apparatus (Biacore GE). The sensor chip employed was *Sensor Chip SA* from *Biacore®* due to its suitability to work with nucleic acid ligands. *Sensor Chip SA* consists in a dextran matrix to which streptavidin has been covalently

attached. Streptavidin is a protein with a high affinity for biotin. Therefore, the surface of the chip is able to capture biotinylated ligands (Figure 2-15). This binding is equivalent in stability to covalent immobilization of the ligand.

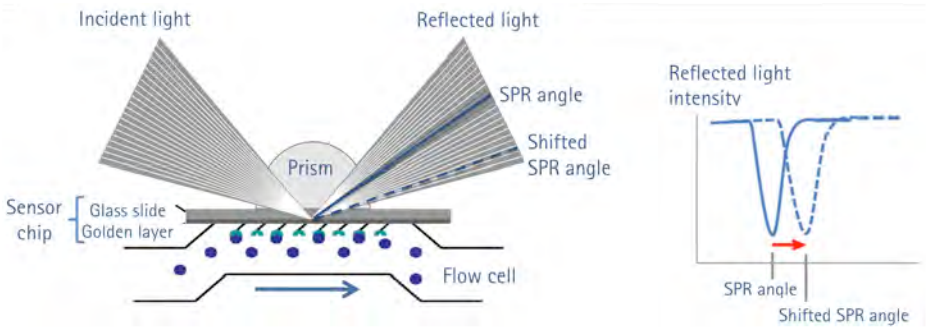

Figure 2-13. The principle of surface plasmon resonance (SPR).

The duplex immobilization can be formed through hybridization of an unlabeled DNA strand that is complementary to a biotin labeled previously immobilized strand. However, it is possible that some of the non-immobilized complementary strands may be lost through dissociation. For that reason, DNA hairpins have been employed, where the two single-strands of the duplex are connected through a loop of nucleotides (see Figure 2-14).

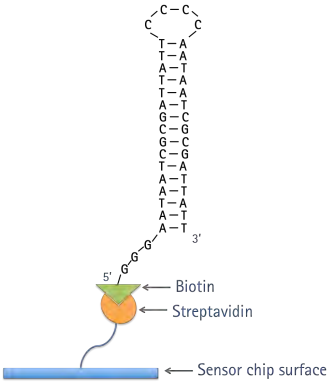

Figure 2-14. Scheme of a streptavidin-biotin immobilization of a DNA hairpin used during SPR experiments.

Once the ligand is immobilized, a set of solutions containing different concentrations of analyte are injected one by one over the sensor surface using the automated sample

handling facilities of the *Biacore® X-100*. At the end of each injection, sample is replaced by a flow of running buffer and bound analyte is dissociated from the surface in a process called regeneration. The aim of regeneration step is to remove all non-covalently bound molecules from the surface without affecting the activity of the ligand. The three process steps (surface preparation, analysis and regeneration) are monitored in a sensorgram (Figure 2-15), which records changes in terms of molecular concentration at the sensor surface with time. Binding is monitored in real time as the sample passes over the surface.

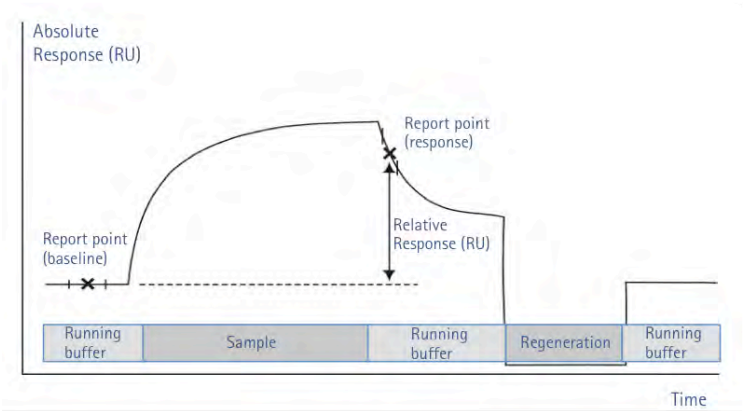

Figure 2-15. Schematic illustration of a SPR sensorgram. The bars below the sensorgram curve indicate the solutions that pass over the sensor surface.

In addition to binding assays, competitive experiments were performed using SPR technique. For this purpose, the set of analyte solutions used was composed of a fix concentration of an HMG protein and increasing concentrations of the diamidine compound. The goal was to detect the destabilization and disruption of the complex DNA-HMG by the dicationic compound.

The 5'-biotin labeled DNA hairpins studied by SPR were purchased from Sigma-Aldrich with reverse-phase HPLC purification. The DNA hairpin sequences are included in Table 2-13.

The oligonucleotides were dissolved in 150 mM NaCl, 10 mM HEPES pH 7.4. The DNA hairpins were immobilized on the *Sensor Chip SA* by injection of a 25 nM hairpin DNA

solution with a flow rate of 1 µL/min until 400 RU were reached. Flow cell 1 was used as reference while flow cell 2 was immobilized with the hairpins in different chips.

Table 2-13. DNA hairpin sequences studied by SPR.

Short name	Sequence
[AATAAT_ATTATT]	5'-biotin-GGGAATAATCGCGATTATTCCCCAATAATCGCGATTATT-3'
[AATT]	5'-biotin-CGAATTCGTCTCCGAATTCG-3'
[(AT)$_7$]	5'-biotin-CATATATATCCCCATATATATG-3'
[(CG)$_7$]	5'-biotin-CGCGCGCGTTTTCGCGCGCG-3'

The latter sequence was selected as a control.

SPR binding and competitive experiments were performed at 25°C. Running buffer used (designated as *HEPES 1*) contained 10 mM HEPES, 3 mM EDTA, 200 mM NaCl, and surfactant P-20 at 0.05% (v/v) pH 7.4. Proteins and diamidines compounds samples were also diluted in *HEPES 1* buffer.

Direct binding of the HMGA1a[Δ50-91] and HMGB1 Box AB proteins was measured by injection of increasing the protein concentration over the immobilized DNA surfaces at a flow rate of 50 µL/min for a period of 60 s followed by a dissociation period of 120 s. Regeneration of the surface was made with 200 mM NaCl/10 mM NaOH using a flow rate of 10 µL/min during 30 s. The binding affinity was determined by fitting the results to a two-site binding model according to the Equation 2-13:

$$r = \frac{K_1 C_f + 2K_1 K_2 C_f^2}{1 + K_1 C_f + K_1 K_2 C_f^2}$$

Equation 2-13. Two-site binding model.

where r is the moles of bound compound per mole of DNA hairpin duplex, C_f is the free concentration at the equilibrium, and K_1 and K_2 the microscopic binding constants.

Direct binding analysis of the bis(2-aminoimidazolinium) compounds was measured by injection of increasing drug concentrations over the immobilized DNA surfaces at a flow rate of 18 µL/min for a period of 300 s followed by a dissociation period of 300 s. Regeneration of the surface was made with 200 mM NaCl/10 mM NaOH using a flow

rate of 10 µL/min during 60 s. The binding affinity was determined by fitting the results to a two-site binding model according to the Equation 2-13.

The competition experiments were prepared with samples containing a fixed concentration of HMGA1a and HMGB1 proteins (2 µM) and a series of concentrations of the bis(2-aminoimidazolinium) compounds ranging from 0.05 to 200 µM (for HMGA1a) or 400 µM (for HMGB1) in *HEPES 1* buffer. The samples were injected to the immobilized DNA surfaces at a flow rate of 50 µL/min for a period of 60 s followed by a dissociation period of 150 s. The regeneration conditions were similar to the binding experiments described above. The binding responses (RU) at steady state were averaged and normalized by setting the RU with the proteins HMGA1a and HMGB1 alone as 100% binding to DNA and the RU with saturation by the inhibitor as 0%. IC_{50} values were determined by fitting the inhibition data with a model according to a competition system with 1:1 binding stoichiometry for HMGA1a and HMGB1 and two-site binding for competitor (Equation 2-14)

$$\%\ \text{proteins binding to DNA} = 100 \Big/ \left[\frac{1 + C(1 + K_{c2}C)}{IC_{50}(1 + K_{c2}IC_{50})}\right]$$

Equation 2-14. Two-site binding for competitor.

where K_{c2} is a macroscopic binding constant for inhibitor binding to DNA, IC_{50} is the concentration of the inhibitor that causes 50% inhibition of HMGA1a and HMGB1 binding to DNA, and C is the concentration of inhibitor (Miao et al., 2008).

2.9 Effect of Bisimidazolinium Diphenyl Compounds on *Trypanosoma brucei*

The antitrypanosomal activity and mechanism of action of the bis(2-aminoimidazolinium) compounds listed in Table 2-9 were evaluated *in vitro* against the parasite *Tryanosoma brucei* during two 4-month research stays with Dr. Harry de Koning at the Institute of Infection, Immunity & Inflammation, University of Glasgow, United Kingdom.

2.9.1 Strains and Cultures

Three parasite cultures of *Trypanosoma brucei brucei* bloodstream forms (BF) were analyzed: (1) the strain Lister 427/MiTat1.2 (wild-type, Tb427WT); (2) TbAT1-B48, which is derived from the Tb427WT strain by the deletion of both alleles coding for the TbAT1/P2 transporter (this s427-WT derivative strain is also called TbAT1-KO) (Matovu et al., 2003) and also by selection through exposure to increasing concentrations of pentamidine until the cells also lost the high-affinity to pentamidine transporter, HAPT1 (Bridges et al., 2007), leading to high resistance to diminazene, pentamidine and melaminophenyl arsenicals; and (3) ISMR1, which is a clonal, Tb427WT-derived dyskinetoplastid cell line, adapted to *in vitro* growth in 1 µM of isometamidium (ISM) by stepwise increases in the medium concentration of the drug (Eze et al., 2016).

All *T. b. brucei* strains were cultured under standard conditions (37°C under a humidified 5% CO_2 atmosphere) in HMI-9 medium (Gibco) (Hirumi & Hirumi, 1989) supplemented with 2 mM β-mercaptoethanol (Sigma-Aldrich) and 10% fetal bovine serum (FBS; Gibco) at pH 7.4 (see Appendix B). Passage was done three times per week in vented flasks.

Additionally, three *Trypanosoma congolense* BF cell lines were studied in this project. The wild type strain IL300 and two diminazene-resistant cell lines (growing at a concentration of 800 nM of diminazine) called 6C3 and 4C2. *T. congolense* strains were cultured in TcBSF-3 medium (see Appendix B) in log-phase culture at 34°C, 5% CO_2 by changing the medium every 3 days.

All medium was sterilized inside a flow cabinet by filtration through 0,22 µm Millipore Express PLUS membranes (PES) filters.

2.9.2 Drug Sensitivity Assays

2.9.2.1 Alamar Blue Assay in BF T. brucei

Fifty percent effective concentrations (EC_{50}) were determined using the fluorescence viability indicator dye Alamar Blue (resazurin sodium salt, Sigma-Aldrich) as described (Gould et al., 2008), with small modifications. Resazurin is metabolized by live cells to resorufin and the fluorescent signal generated is thus proportionate to the number of live cells (Gould et al., 2008) (Figure 2-16).

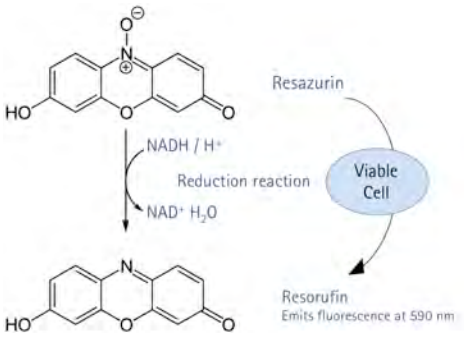

Figure 2-16. Conversion of resazurin to resorufin by viable cells results in a fluorescent product. The fluorescence produced is proportional to the number of viable cells.

Drug stock solutions (see section 2.2.5) were diluted to 400 µM with HMI-9 medium with 10% FBS. 200 µL of these test compound dilutions were added to the first well of rows A, C, E and G of a white-bottomed 96-well microplate (Greiner - Bio-One) (Figure 2-17). A volume of 100 µL of HMI-9 medium with 10% FBS was loaded into all remaining wells. Up to four drugs could be tested in one plate. Doubling dilutions of test compounds were prepared, leaving the last well drug-free as a control, before the addition of an equal volume of cell suspension to each well, to get a final cell density of 1×10^4 cells/mL. The plates were incubated at 37°C/5% CO_2 for 72 h after which 20 µL of resazurin solution (125 µg/mL in phosphate-buffered saline, pH 7.4) were added followed by another incubation for 24 h.

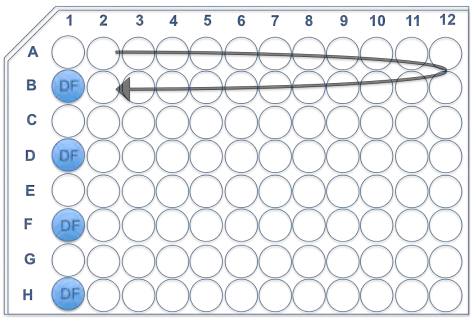

Figure 2-17. 96-well microplate diagram. Arrow explains the way the drugs are doubly diluted down two rows across the plate. DF; drug free, negative control.

Pentamidine and isometamidium were used as positive controls throughout the study.

Viable cells reduce the dark blue dye to a pink colour. The change in fluorescence was determined using a *FLUOstar Optima* plate reader (BMG Labtech), at excitation and emission wavelengths of 530 and 590 nm, respectively. Data were analyzed and plotted to a sigmoid curve with variable slope using *Prism 5.0* (GraphPad). Each experiment was performed at least on three independent occasions.

2.9.2.2 *Alamar Blue Assay in BS* T. congolense

Alamar blue end point assays were also used to estimate the drug sensitivity in *Trypanosoma congolense* cell lines as described in the previous section. Stock solutions of drugs were diluted to 200 µM with TcBSF-3 medium. Cell density was adjusted to reach a final density of 2.5×10^5 cells/mL. Diminazene was used as positive control throughout this study. The plates were incubated at 34 °C + 5% CO_2 for 48 h after which 20 µL of sterile resazurin solution (125 µg/mL in phosphate-buffered saline, pH 7.4) was added to every well, followed by a further incubation of 24 h in the same conditions. Each experiment was performed at least on three independent occasions.

2.9.3 Drug Sensitivity Assay using Cell Count

The effects of the bis(2-aminoimidazolinium) compounds on growth of BF *Trypanosoma brucei brucei* strain Lister 427 were investigated by incubating cultures

under standard conditions (HMI-9/10% FBS; 37°C, 5% CO_2) in the presence or absence of 0.5, 1, 2.5 and 5 times their EC_{50} values for up to 48 h. Cells were seeded at a density of 2×10^4 cells/mL using a haemocytometer. Cells were counted in triplicate at the following times (h) after initiation of the experiment: 0, 4, 8, 24, 36 and 48.

2.9.4 Assessment of Cell Cycle Progression in *T. brucei*

2.9.4.1 Fluorescence Microscopy

Nuclei and kinetoplasts were visualized by using the fluorescent dye 4',6-diamidino-2-phenylindole (DAPI) on BF trypanosomes after fixation. 50 µL of cells at 2×10^6 cells/mL were spread onto a glass microscope slide, left to dry in a fume hood and fixed in 4% paraformaldehyde in fresh PBS for 10 min at room temperature. The slides were washed with 1× PBS. The PBS was gently removed by inclining the slide on a soft tissue and a drop of *Vectashield® mounting medium with DAPI* (Vector Laboratories) was placed on the slide before covering with a cover slip. The slide was then viewed under UV light on a *Zeiss Axioskop 2* fluorescent microscope (Carl Zeiss Microscopy). 500 cells were recorded for each sample, and scored for DNA configuration following these groups: 1N1K, 1N2K, 2N2K(Early) and 2N2K(Late) (N, nucleus; K, kinetoplast; Early, early stage of division; Late, late stage of division;) (see Figure 1-22). The effect of test compounds on DNA configuration was determined at 0, 8 and 24 h. Untreated cultures served as control.

2.9.4.2 Flow Cytometry

DNA content of BF trypanosomes was measured by flow cytometry using the fluorescent dye propidium iodide (PI), as described (Ibrahim et al., 2011; Hammarton et al., 2003) with minor modifications. Cell density was adjusted to 2×10^6 cells/mL. Five milliliters of sample were transferred at each time point into microfuge tubes and centrifuged at 1620 g for 10 min at 4 °C, washed once in 1× PBS with 5 mM of EDTA and re-suspended and fixed in 1 mL of 70% methanol and 30% PBS with 5 mM EDTA (first re-suspend in 300 µL of PBS with 5mM EDTA and then add, drop-wise while

vortexing gently, the 700 µL of methanol). The tube containing the cells was covered in foil paper and leave at 4 °C overnight. After storage, the samples were washed once with 1 mL of 1× PBS with 5 mM EDTA and subsequently re-suspended in 1 mL 1× PBS with 5 mM EDTA containing 10 µg/mL RNase A and 10 µg/mL propidium iodide and incubated at 37 °C for 45 min while protected from light.

Samples were analyzed using a *BD FACSCalibur™ system* (BD Biosciences). Data were acquired from the FSC, SSC, FL2- W and FL2-A detectors using *BD CellQuest™* software (BD Biosciences), and further analyzed and graphically represented using the *©FlowJo® 10.2* software.

2.9.5 Mitochondrial Membrane Potential Assay

The mitochondrial membrane potential of treated and untreated cells was assessed by using tetramethylrhodamine ethyl ester (TMRE) following a protocol previously described (Ibrahim et al., 2011). TMRE is a cell permeant, positively-charged, red-orange dye that accumulates in active mitochondria due to their relative negative charge. Depolarized or inactive mitochondria have decreased membrane potential and fail to sequester TMRE.

Cell density was adjusted to 2 × 10^6 cells/mL and the drugs were added to make a concentration corresponding to their EC_{50} and 5 times their EC_{50} values; a negative control (drug free sample) was also prepared. One milliliter of sample was transferred at each time point into a microfuge tube and centrifuged at 1,500 g for 10 min at 4°C. The pellet was washed once with 1× PBS and re-suspended in 1 mL PBS containing 25 nM of TMRE. Then, cells were incubated at 37°C for 30 min and subsequently placed on ice for at least 30 min.

Samples were analyzed using a BD *FACSCalibur™ system* (BD Biosciences). Data were acquired from the FL2-height detector using *BD CellQuest™* software (BD Biosciences), and further analyzed and graphically represented using the *©FlowJo software*, version 10.2. Valinomycin (100 nM) and troglitazone (10 µM) were employed as depolarization and hyperpolarization controls, respectively (Denninger et al., 2007). Mitochondrial

membrane potential was determined at 0, 3, 6 and 12 h. The detector was calibrated so that the peak of control cells (Tb427WT not exposed to any test compound) was set at 100 arbitrary units, i.e. with 50% of cells at >100 A.U. and 50% at <100 A.U. The data are presented as percent of the cell population with a fluorescence >100 A.U.

2.9.6 Cellular Localization of Compounds in BF *T. brucei*

The localization and distribution of the fluorescent compounds in the BF trypanosomes was studied by fluorescence microscopy. After measuring the fluorescence of all the compounds studied in this project, only the compound JNI18 was found fluorescent in DMSO. The fluorescence emission spectral peak of JNI18 in solution was determined in the region of 450 nm (Table 2-14), which is exactly the emission wavelength of DAPI.

Table 2-14. Fluorescence parameters of the compound JNI18 in DMSO.

Emission (nm)	450
Molar extinction coefficient	23708
Quantum yield	0.42
Fluorescence intensity	9957

Parameters obtained at the Instituto de Química Médica IMQ-CSIC, in Madrid.

Therefore, in order to visualize both nuclei and kinetoplast DNA of the parasites, instead of DAPI, the green-fluorescent counterstain *SYTOX® Green nuclei acid stain* was used, which emits fluorescence at 523 nm. Thus, the fluorescence due to our compound JNI18 and to the stained DNA can be differentiated. The red-fluorescent (λ_{em}= 599 nm) dye *MitoTracker® Red CMXRos*, which stains mitochondria in live cells, was also used.

Trypanosome cultures were grown in HMI-9/FCS media, cell density was adjusted to 2 × 10^6 cells/mL and the compound JNI18 was added to make a concentration of 5 µM; a negative control (drug free sample) was also prepared. 1 mL of sample was taken every time point and transferred into an empty tube, and 1 µL of 100 µM solution of *MitoTracker® Red CMXRos* (Thermo Fisher Scientific) in DMSO was added to make a

final concentration of 100 nM. Samples were incubated at 37°C and 5% CO_2 for 5 min. Subsequently, samples were washed with filter-sterilized 1× PBS and spun at 1,500 × g. Pellets were re-suspended in 50 µL of PBS and spread into a glass microscope slide. The cells were dried in a fume hood and fixed in 4% formaldehyde/PBS fresh for 10 min at room temperature. Cells were permeabilized with cooled methanol for 5 to 10 min at -20°C, washed once or twice with 1× PBS and then washed twice with Hanks' Balanced Salt Solution (HBSS) (see Appendix B). Enough solution 1:30,000 (167 nM) of green-fluorescent counterstain *SYTOX® Green nuclei acid stain* (Thermo Fisher Scientific) in HBSS to cover all the cells was added to the slides and incubated for 15 to 30 min protected from light.

Finally, cells were washed twice with HBSS and the slides were covered with a cover slip. The location of the test compound was determined at 0, 3, 6 and 24 h. The slide was then viewed under *DeltaVision Core* microscope (Image Solutions - Applied Precision, United Kingdom) under several fluorochromes (blue for JNI18, green for the *SYTOX®* and red for the *Mitotracker®*), as well as under UV light. Image acquisition was controlled using *Zen* software (Zeiss) and *SoftWorx* was used for further image processing.

2.9.7 Transmission Electron Microscopy Analysis

Transmission electron microscopy was used to assess the action of the compounds on *T. brucei* ultrastructure. Cells were harvested and the density was adjusted to 2 × 10^6 cells/mL. The samples incubated 3 and 24 h with 5 µM of the compound, as well as untreated cells for control were centrifuged at 610 × g for 10 min at room temperature and the pellet was washed once with 1× PBS and re-suspended in 1 mL of the fixative solution containing 2.5% of glutaraldehyde and 4% paraformaldehyde in 0.1 M phosphate buffer (pH 7.4) and left at 4°C overnight. Then, samples were centrifuged at 4,000 rpm for 8 min and pellet was washed three times with 0.1 M phosphate buffer (pH 7.4). Cells were post-fixed in a solution of 1% osmium tetroxide for one hour on ice, and washed with the phosphate buffer to remove excess of osmium tetroxide. Then, cells were kept in the 0.5% uranyl acetate solution for 30 min,

washed three times with distilled water and dehydrated by using a series of increasing concentrations of acetone (30, 50, 70, 90 and 100%). Next, cell infiltration was performed using an epoxy resin. Thin sections (50-60 nm) were observed in a Tecnai T20 (FEI) at 200 kV.

2.9.8 PCR Amplification of Kinetoplast DNA Markers

Polymerase chain reaction (PCR) of kinetoplastid and nuclear markers was used to verify the presence of kinetoplast in Tb427WT treated 0, 3, 6, 9, 12, 24 and 32 h with the bisimidazolinium diphenyl compounds.

Trypanosome cultures were grown under standard conditions (HMI-9/10% FBS; 37°C, 5% CO_2), cell density was adjusted to 2×10^6 cells/mL and the compound JNI18 was added to make a concentration of 5 µM; 1 mL of cells were transferred into a tube and processed each time point. Full genomic DNA (nuclear and kinetoplast) from *T. b. brucei* was obtained using the *NucleoSpin® tissue kit* (Machery-Nagel, Düren, Germany) according to the manufacturer's instructions, quantified using a NanoDrop ND1000 spectrophotometer, and stored at -20 °C. PCR master mix 1× in a total volume of 19 µL (11.8 µL nuclease free water, 4 µL Green GoTaq reaction buffer, 1 µL of 10 mM dNTPs, 1 µL forward primer and 1 µL reverse primer along with 0.2 µL GoTaq DNA polymerase) was prepared for each primer pair and DNA sample. One milliliter of extracted DNA was added in the relevant tubes. Primer sequences specific for maxicircle and minicircle kinetoplast (kDNA) are listed in Table 2-15.

Cycle conditions for maxicircle sequences were 95 °C for 5 min and 30 cycles of 95 °C for 1 min, 54 °C for 1 min, and 72 °C for 30 s followed by a final elongation step at 72 °C for 8 min. On the other hand, cycle conditions for minicircle sequences were 94 °C for 5 min and 35 cycles of 94 °C for 40 s, 59.4 °C for 1 min, and 72 °C for 90 s followed by a final elongation step at 72 °C for 10 min. All samples were run on 1% (w/v) agarose gels and visualized using *SYBR™ Safe DNA Gel Stain* (Invitrogen™) as described in section 2.2.4.

Table 2-15. Oligonucleotide primer sequences used in this study.

Primer for gene	Nucleotide sequence	Product size
A6	Fwd: 5'-AAAAATAAGTATTTTGATATTATTAAAG-3' Rev: 5'-TATTATTAACTTATTTGATC-3'	381 bp
ND4	Fwd: 5'-TGTGTGACTACCAGAGAT-3' Rev: 5'-ATCCTATACCCGTGTGTA-3'	256 bp
ND5	Fwd: 5'-TGGGTTTATATCAGGTTCATTTATG-3' Rev: 5'-CCCTAATAATCTCATCCGCAGTACG-3'	395 bp
ND7	Fwd: 5'-ATGACTACATGATAAGTA-3' Rev: 5'-CGGAAGACATTGTTCTACAC-3'	161 bp
Actin	Fwd: 5'-CCGAGTCACACAACGT-3' Rev: 5'-CCACCTGCATAACATTG-3'	456 bp
Minicircle Type A	Fwd: 5'-GGGTTTTTTAGGTCCGAG-3' Rev: 5'-CCGAAAATAGCACGTG-3'	1001 bp
Minicircle Type A-like	Fwd: 5'-GGGTTTTTAGGTCCGAG-3' Rev: 5'-CCGAAAATAGCACGTG-3'	1000 bp
TbAT-1	Fwd: 5'-CGTCACATCTTTCTTCTCG-3' Rev: 5'-CTTGGGAAGCCCCTCATTGACAGCC-3'	889 bp

A6, ND4, ND5, ND7: fragments of 4 genes known to be encoded only by the kinetoplast maxicircles from Tb427WT. Actin: Tb427WT nuclearly encoded gene. Minicircles Type A, Type A-like: representative minicircle genes. TbAT-1: Tb427WT nuclearly encoded single copy gene.

RESULTS AND DISCUSSION

CHAPTER 3

HMG PROTEINS

3.1 Obtaining HMG proteins

The proteins of interest were expressed in *E. coli* and purified following the protocol described in section 2.1.

3.1.1 Expression and Purification of HMGA1a(Δ50-91)

HMGA1a(Δ50-91) protein was expressed several times to obtain enough amount to perform crystallographic and binding assays. Each expression batch was obtained from 1 L of starting culture as described section 2.1.1.

The recombinant pET-3a plasmid containing the human HMGA1a(Δ50-91) gene (Figure 2-2) was transformed into *E. coli* Rosetta (DE3) pLysS strain. A transformed colony was used to obtain a saturated liquid culture from which 1 L of culture was inoculated into LB medium containing ampicillin at 37°C. Protein expression was induced when the culture featured an OD_{600} of about 0.6-0.7 by adding 1 mM IPTG (see 2.1.1). The culture was incubated for 3 h to allow the bacteria to synthesize the recombinant protein and then the cells were recovered by centrifugation. The bacterial pellet was processed using 5% $HClO_4$/0.5% Triton X-100 as described section 2.1.1. The recombinant protein was extracted and precipitated from the supernatant using 25% TCA to obtain a pellet enriched in HMGA1a(Δ50-91). Figure 3-1 shows the AU-PAGE gel of the induction process (0 h, 1.5 h and 3 h) and the enriched extract after the pellet preparation.

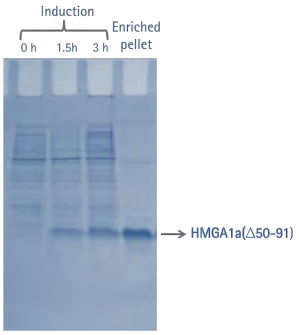

Figure 3-1. AU-PAGE showing induction of the HMGA1a(Δ50-91) protein expression.

The pellet enriched in HMGA1a(Δ50-91) was admitted to a multi-stage purification process described in section 2.1.2.

The purification process started with a cation-exchange chromatography based on the conditions described by Reeves & Nissen (1999) with small modifications. A carboxymethyl cellulose (CM52, Whatman) column of 20 cm in length, 1.5 cm internal diameter and 25 mL column volume was used. Equilibration buffer was 50 mM NaCl, 25 mM Tris-HCl, pH 7 and protein elution was achieved by increasing the concentrations of NaCl from 50 mM (buffer A) to 600 mM (buffer B). Flow rate was 1 mL/min and 4 mL samples were collected.

Figure 3-2a shows a chromatogram obtained from the cation-exchange chromatography. Peaks of absorbance at 220 nm were collected and analyzed by AU-PAGE (Figure 3-2b). As expected, HMGA1a(Δ50-91) protein was identified in the fractions forming the major peak of the chromatogram. Secondary peaks, from which samples 5 and 57 were analyzed, were not containing our target protein.

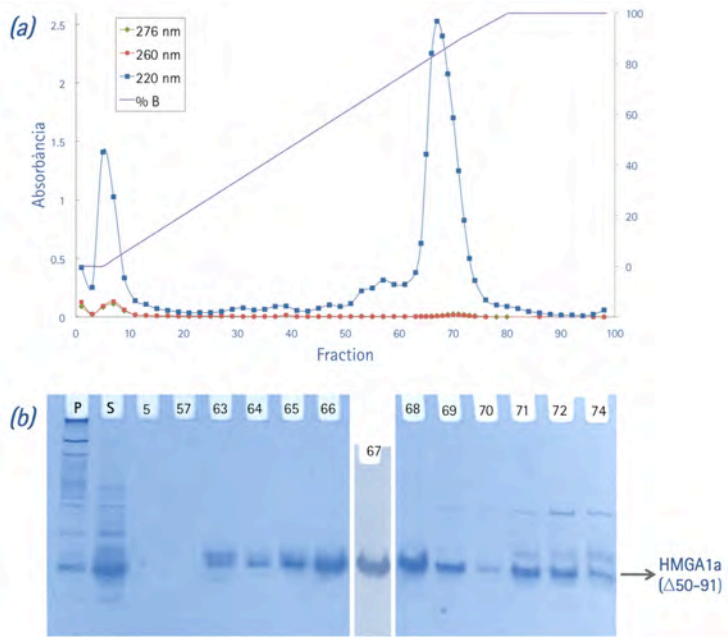

Figure 3-2. ***(a)*** **Cation-exchange chromatogram and** ***(b)*** **AU-PAGE analysis of HMGA1a(Δ50-91) protein. Sample P corresponds to the pellet obtained in a previous-to-load centrifugation of S, which is the protein sample loaded into the column. B, buffer containing 600 mM NaCl, 25 mM Tris-HCl, ph7.**

Fractions 65 to 70, which corresponded to the most pure samples, were concentrated to proceed with the second purification step. Sample concentration was carried out using the ultra-concentration device *Vivaspin® 20 mL MWCO 3000* following the manufacturer's instructions until the sample volume was around 1 mL.

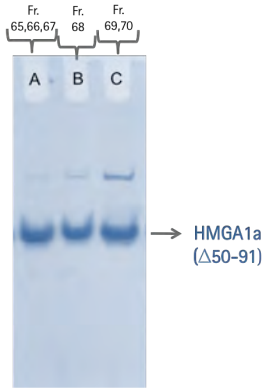

Figure 3-3. AU-PAGE of HMGA1a(Δ50-91) concentrated samples after cation-exchange chromatography.

The electrophoretic analysis of the concentrated samples of HMGA1a(Δ50-91) protein (Figure 3-3) shows that most of the unwanted proteins were eliminated during the cation-exchange chromatography. Nevertheless, it also confirmed the necessity to continue with the purification of HMGA1a(Δ50-91) since it contained (in different proportion) a few impurities (Figure 3-3).

For that purpose, the HMGA1a(Δ50-91) samples were submitted to a last "polishing" purification step by size-exclusion chromatography following the protocol described in section 2.1.2. An *ÄKTA Purifier 10 system* (GE Healthcare) and a 24 mL column volume *Superdex™ Peptide 10/300 GL* (GE Healthcare) with Mr 100 - 7,000 were used.

Samples A, B and C (see Figure 3-3) were loaded to the column in two/three independent injections per sample. The equilibration and elution buffer used was 100 mM NaCl, 25 mM Tris-HCl, pH 7.5, flow rate was 0.5 mL/min and elution was achieved with 1.5 column volumes. As an example, Figure 3-4 shows the chromatogram of the size-exclusion column for one run of sample A. Peaks of absorbance at 220 nm were collected and analyzed by AU-PAGE (Figure 3-2).

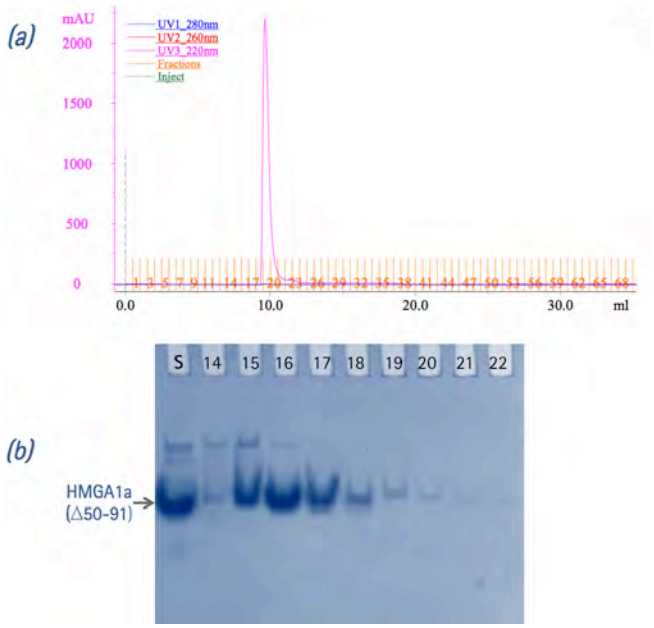

Figure 3-4. *(a)* Size-exclusion chromatogram and *(b)* AU-PAGE analysis of the fractions from the main peak. S corresponds to the HMGA1a(Δ50-91) protein sample loaded into the column.

The electrophoretic gel displayed in Figure 3-4 shows how the band above the HMGA1a(Δ50-91) protein band (corresponding to a higher molecular weight protein) elute first.

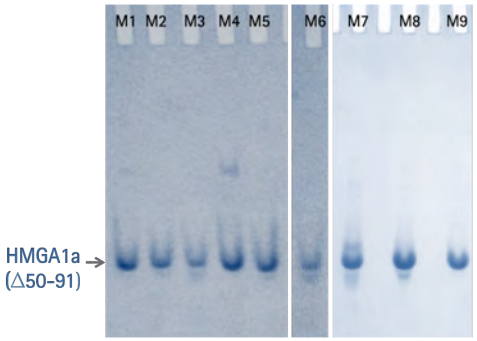

Figure 3-5. AU-PAGE of HMGA1a(Δ50-91) final samples.

Fractions containing the target protein from all the size-exclusion column runs were pooled according to their degree of purity, dialyzed and concentrated using the ultra-concentration device *Vivaspin® 6 mL MWCO 3000*. Dialysis was carried out washing the sample twice with 6 mL final buffer (80 mM NaCl, 25 mM Tris-HCl, pH 7.5).

Samples were concentrated until the volume was around 100 µL. Final sample absorbance was measured and the concentration was calculated using Equation 2-1. Finally, samples were analyzed by AU-PAGE gel (Figure 3-5).

The concentration and volume of HMGA1a(Δ50-91) protein samples obtained are listed in Table 3-1.

Table 3-1. Final HMGA1a(Δ50-91) protein samples obtained during this work.

Sample	Volume [µL]	Concentration	
		[µg/µL]	[mM]
M1	75	8,7602	1,8321
M2	108	19,9704	4,1765
M3	100	1,6023	0,3351
M4	80	4,8149	1,0070
M5	102	7,1325	1,4917
M6	113	0,3863	0,0808
M7	100	28.5391	5.9685
M8	100	23.1827	4.8483
M9	50	8.1957	1.7140

All samples were in 80 mM NaCl, 25 mM Tris-HCl, pH 7.5 buffer and stored at -20°C.

Due to the high purity and suitable concentration of samples M2 and M8, they were used for crystallization assays. For SPR assays sample M5 was used.

3.1.2 Expression and Purification of HMGB1 Proteins

HMGB1 Box B(Δ93-165) and Box AB(Δ8-165) proteins were expressed following the same methodology. Each protein expression batch was obtained from 1 L of starting culture as described section 2.1.3.

The recombinant pGEX-2T plasmid containing GST-tagged rat HMGB1 proteins Box AB and Box B (Figure 2-3) was transformed into *E. coli* Rosetta (DE3) pLysS strain. A transformed colony was used to obtain a saturated liquid culture which was diluted in 1 L LB medium containing ampicillin and chloramphenicol at 37°C. Protein expression was induced when the culture featured an OD_{600} of about 0.8 by adding 0.5 mM IPTG and incubated for 3 h.

Figure 3-6 displays the SDS-PAGE gel of samples collected during induction of GST-HMGB1 Box B and GST-HMGB1 Box AB fusion proteins expression. An increase in the amount of the corresponding GST-HMGB1 fusion protein can be observed as the induction progressed.

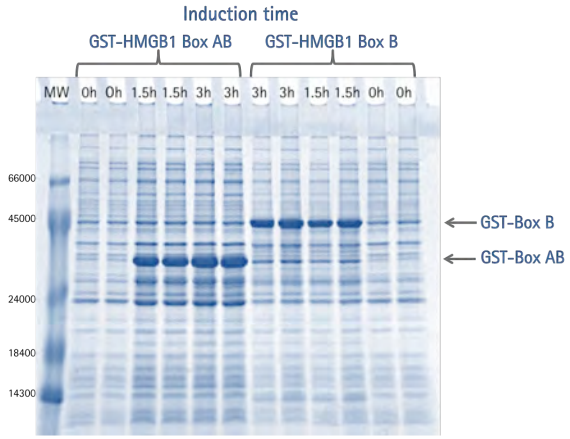

Figure 3-6. SDS-PAGE of the induction of GST-fusion HMGB1 proteins expression. MW, molecular weight marker *MW-SDS-6 Dalton Mark™ VI* (Sigma).

Cell disruption was performed as described in section 2.1.3, by sonication on a *Bandelin SONOPULS Ultrasonic Homogenizer HD 2200*. The clarified lysate (supernatant from sonication) was purified by a multi-stage purification process described in section 2.1.4. First, the sample was loaded and incubated for at least 2 h with gentle rotation in a column packed with 6.5 mL *Glutathione Sepharose™ 4B* matrix (GE Healthcare), where the GST moiety bound to the glutathione coupled to the Sepharose beads. After incubation, the flow through (FT) was collected and the column was rinsed with wash buffer (W). Thrombin buffer was added to the column and eluted (ThW), followed by incubation with 200 U thrombin diluted in 1 mL thrombin buffer at 4°C overnight. Here, the GST tag was removed from the fusion protein. Next, thrombin was inactivated with EDTA and eluted (FTc) and finally the HMGB1 protein fragments were eluted with elution buffer and collected as E1, E2 and E3. Figure 3-7 shows all the fractions collected during the affinity chromatography as well as a small sample of resin (beads) that was used as control.

Bacterial proteins were discarded in the first fractions washed from the glutathione Sepharose column (FT, W) as shown in Figure 3-7. The fractions FTc E1, E2 and E3, eluted after the GST tag removal, contained the target protein (Figure 3-7). Those fractions were pooled together into a single sample and loaded into a cation-exchange column.

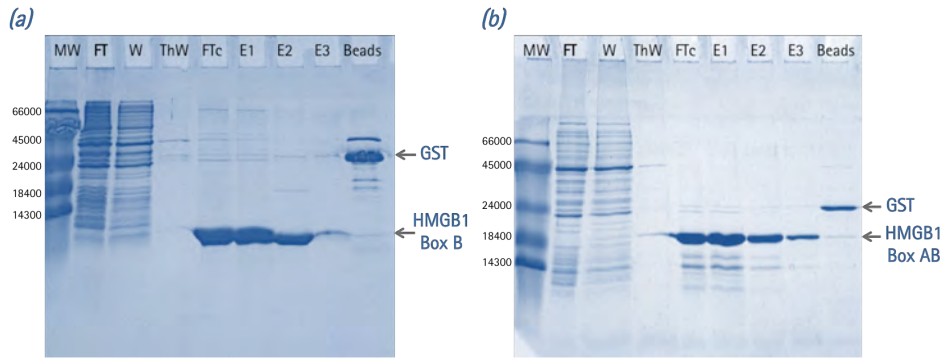

Figure 3-7. SDS-PAGE gels of the fractions eluted from the affinity column corresponding to *(a)* the GST-HMGB1 Box B fusion protein and *(b)* the GST-HMGB1 Box AB fusion protein. MW, molecular weight marker; FT, flow through; W, column wash; THW, thrombin buffer wash; FTc, flow through after tag cleavage; El, E2 and E3, eluted fractions; Beads, sample from microparticles of the column matrix taken at the end of the elution as a control.

As described in section 2.1.4, the *ÄKTA Purifier 10 system* and a 5 mL *HiTrap SP FF* column were used. The sample of about 24 mL was filtered through a 0.22 µm filter membrane and loaded into the column in three consecutive injections with a 10 mL loop. The chromatography was performed with a constant flow of 2 mL/min at 4°C and 5 mL fractions were collected.

The column was equilibrated with 10 bed volumes buffer A (100 mM NaCl, 1 mM EDTA, 1 mM DTT, 10 mM Tris-HCl, pH 7.9) and a 45 min gradient (18 bed volumes) from buffer A to buffer B (1 M NaCl, 1 mM EDTA, 1 mM DTT, 10 mM Tris-HCl, pH 7 9) was applied.

Figure 3-8 shows the *HiTrap SP FF* column chromatograms corresponding to the purification of the protein HMGB1 Box B and Box AB, and the SDS-PAGE gels for the fractions conforming the main absorption peak at 280 nm. For the HMGB1 Box B protein, the fractions 2, 3, 5, 6, 9 and 10 corresponding to the three-sample injection,

were also analyzed. HMGB1 Box B fractions 22 to 27 and HMGB1 Box AB protein fractions 28 to 34, containing the target protein were pooled and concentrated to proceed with the last purification step: size-exclusion chromatography.

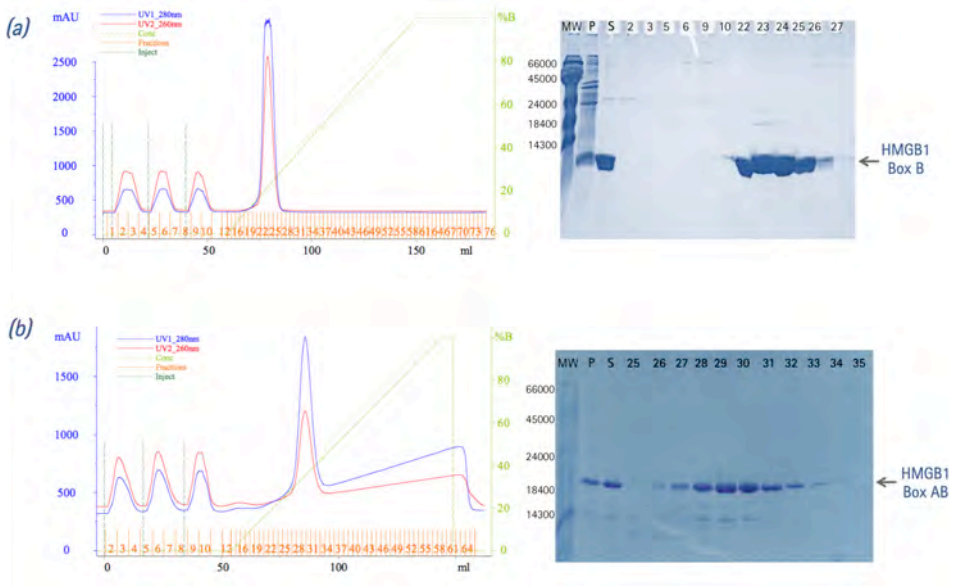

Figure 3-8. Cation-exchange chromatogram (left) and SDS-PAGE analysis of the fractions from the main peak (right). MW, molecular weight marker; S, HMGB1 protein sample loaded into the column.

The concentration of protein sample was carried out using the ultra-concentration device *Vivaspin® 20 mL MWCO 3,000* (for the HMGB1 Box B) and *MWCO 5,000* (for the HMGB1 Box AB) following the manufacturer's instructions until the sample volume was around 0.5 mL.

Size-exclusion chromatography was performed as described section 2.1.4 using a *HiLoad Superdex™ 75* (GE Healthcare) column, Mr 3,000 - 70,000 Da. The samples were filtered through a 0.22 µm filter membrane and loaded into the column in two independent injections with a 500 µL loop. The equilibration and elution were performed with 150 mM NaCl, 1 mM DTT, 50 mM HEPES, pH 7.4 with a constant flow of 0.5 mL/min at 4°C and 0.5 mL fractions were collected.

Figure 3-9 shows the chromatograms obtained during the polishing step of the HMGB1 proteins.

Pure fractions were pooled together according to their degree of purity and concentrated/dialyzed in buffer containing in 50 mM NaCl, 1 mM DTT in 25 mM HEPES, pH 7.4 to a final volume of 100 µL using a *Vivaspin® 6 mL MWCO 3,000* (for the HMGB1 Box B) and *4 mL MWCO 5,000* (for the HMGB1 Box AB). Final samples were analyzed by SDS-PAGE gel (Figure 3-10).

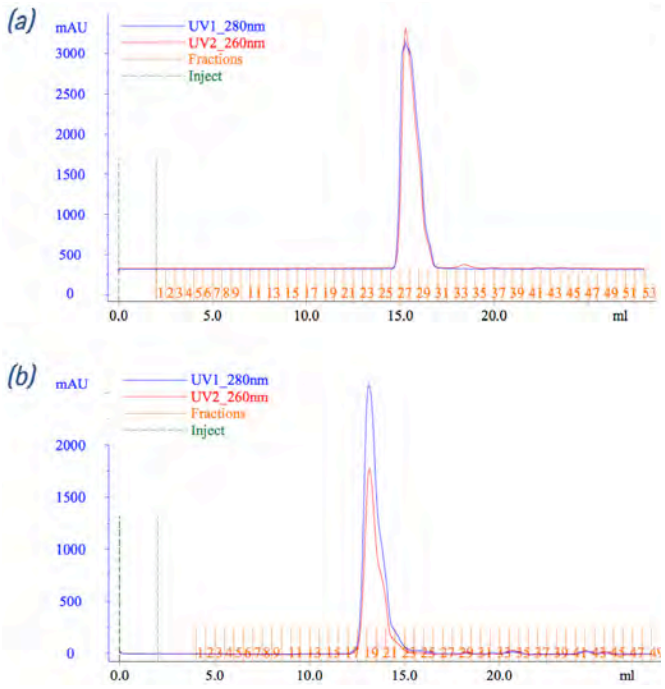

Figure 3-9. Size-exclusion chromatogram of *(a)* HMGB1 Box B protein sample and *(b)* HMGB1 Box AB protein sample.

Finally, samples were flash-frozen in liquid nitrogen and stored at -80ºC. The concentration and volume of HMGB1 protein samples prepared during this research work are listed in Table 3-2.

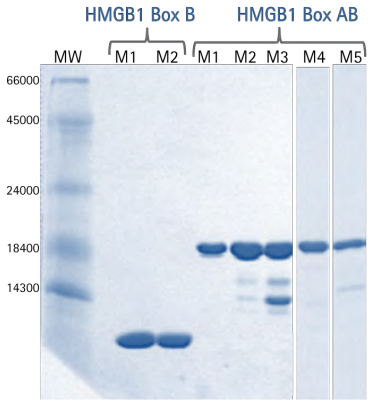

Figure 3-10. SDS-PAGE of HMGB1 protein (Box B and Box AB) concentrated samples after size-exclusion chromatography. MW, molecular weight marker *MW-SDS-6 Dalton Mark™ VI* (Sigma).

Table 3-2. Final HMGB1 protein samples obtained during this work.

Sample Name	HMGB1 Protein	Volume [µL]	Concentration	
			[µg/µL]	[mM]
M1	B	400	33.9528	4.02
M2	B	1,700	1.23	0.1467
M1	AB	300	48.5259	2.6253
M2	AB	300	15.1387	0.8190
M3	AB	200	6.7985	0.3678
M4	AB	200	16.9630	0.9177
M5	**AB**	275	9.1438	0.4947

All samples were in 50 mM NaCl, 1 mM DTT, 25 mM HEPES, pH 7.4 buffer and stored at -20°C.

Due to the high purity and suitable concentration, samples HMGB1 box B M1 and box AB M1 were used them for crystallization assays. For SPR assays, HMGB1 box AB sample M1 was used.

3.2 Interaction of HMGA1a(Δ50-91) Protein with AT-rich DNA

In order to evaluate its activity, the most pure samples of HMGA1a(Δ50-91) protein obtained (M2, M5 and M8; see Figure 3-5 and Table 3-1) were used for supercoiling assays, crystallography assays and SPR experiments.

3.2.1 Supercoiling Induced by HMGA1a Proteins

Supercoiling is a non-covalent and elusive topological modification modulated by DNA- and chromatin-binding proteins (Gilbert & Allan, 2014). The functionality of the HMGA1a(Δ50-91) protein was verified as regarding to its ability to induce supercoiling by measuring the degree of circular DNA supercoiling in presence of topoisomerase I. The protocol performed in this assay is described in section 2.2.5.

The plasmid used during these experiments has been constructed by Dr. Joaquim Roca from the Molecular Biology Institute of Barcelona (IBMB), CSIC, Barcelona. This 4.6 kb pSTAT-CEN2-S2 plasmid contains two inserts $[AT]_{11}$ in opposing sites.

The induction of supercoiling in the circular plasmid by HMGA1a(Δ50-91) has been measured using three different salt concentrations in the reaction buffer: 50 mM NaCl (low ionic strength), 100 mM (medium ionic strength) and 150 mM (high ionic strength) (Figure 3-11). Opposite to previous published studies with other HMG proteins (Štros et al., 1994; Teo et al., 1995), the most favorable ionic strength for the HMGA1a supercoiling assays proved to be at very high salt concentration (150 mM NaCl; (1) in Figure 3-11).

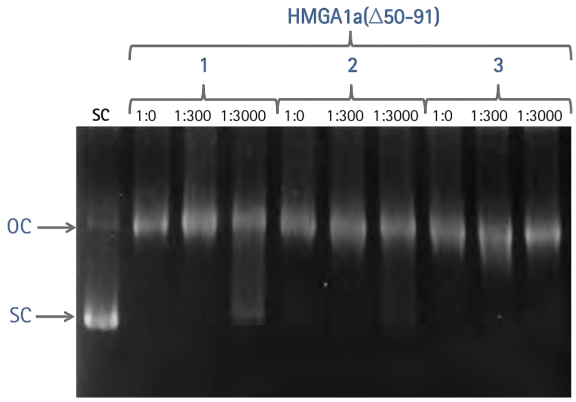

Figure 3-11. Supercoiling activity of the HMGA1a(Δ50-91) in the presence of different salt concentrations: (1) 150 mM NaCl (high ionic strength), (2) 100 mM NaCl (medium ionic strength) and (3) 50 mM NaCl (low ionic strength). DNA/protein molar ratio is specified for each sample. SC, supercoiled DNA; OC, nicked form (open circular DNA).

In addition, the supercoiling effect of the HMGA1a protein from amino acid 1 to 90, i.e. the fraction containing the three AT-hook domains, was analyzed in order to compare it with that caused by the (Δ50-91) fraction (see Figure 2-1). The pure HMGA1a(Δ1-90) sample tested in this experiment was provided by a member of MACROM research group.

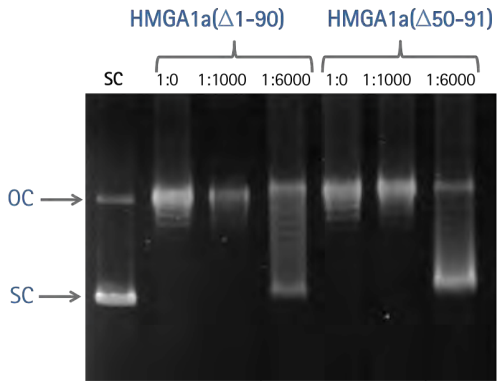

Figure 3-12. Supercoiling activities at high ionic strength of two fragments of the HMGA1a(Δ50-91) and the complete protein lacking the acidic tail HMGA1a(Δ1-90). DNA/protein molar ratio is specified for each sample. SC, supercoiled DNA; OC, nicked form (open circular DNA).

At high ionic strength, a clear supercoiling effect is seen for both protein fragments HMGA1a(Δ50-91) and HMGA1a(Δ1-90) as shown in Figure 3-12. The degree of unwinding observed on nicked circular DNA depends on the DNA/protein molar ratio, but is very similar for both proteins. Therefore, the truncated HMGA1a protein (Δ50-91) containing only two AT-hook domains seems to be as functional and active as the HMGA1a(Δ1-90), which contains the three AT-hook motifs.

The untwist provoked by the protein in the circular DNA previously relaxed is compensated with a positive supercoiling at other region of the plasmid. This positive supercoiling is dissipated by the topoisomerase I. But when both, the protein and the topoisomerase are excluded, topoisomeres are obtained with negative supercoiling. Then, the negative supercoiling introduced by two fractions of HMGA1a protein is correlated with its unwinding activity.

3.2.2 HMGA1a(Δ50-91) Crystallography Assays

The crystallography assays of the HMGA1a-DNA complexes were evaluated with a set of AT-rich oligonucleotides by the vapor diffusion crystallization technique using the two typical set-ups: hanging-drop and sitting-drop. The oligonucleotides used are shown in Table 3-3.

Table 3-3.Oligonucleotide sequences used for crystallographic assays with HMGA1a(Δ50-91)

DNA sequence	Length [bp]	MW [mol·g^{-1}]
1. CCAATAATCGCGATTATTGG	20	12232.2
2. ATTATTAATAAT	12	7285
3. AATATATATATT	12	7285
4. AAATATATTT	10	6050.2
5. CGAATTAATTCG	12	7289
6. ATTAATTAAT	10	6050.2

Molecular weight is given in terms of DNA duplex.

The complexes formation was evaluated first by EMSA electrophoresis in order to determine the ability of the protein to form complexes with DNA following the protocol described in section 2.2.3. DNA-protein samples containing 3% glycerol in 0.3x TBE were incubated for 1 h at 4°C to allow the complex formation. The EMSA gel was run around for 1 h after a 30 min pre-run, and stained with *SYBR® Gold* (Invitrogen™) for 20 min. Figure 3-13 shows the EMSA gels performed with HMGA1a(Δ50-91) protein. For these assays, 1 µM oligonucleotide was incubated with increasing concentrations of protein (from 0.25 to 7 µM). Although a different amount of protein may be needed in each case, the formation of complex with all the tested oligonucleotides was confirmed.

Crystallography assays were performed varying a series of parameters as DNA/protein ratio, buffer, salt, pH and MPD concentration. Hampton Natrix HR2-116 (Scott et al., 1995) 7, 15, 16, 25, 31, 42, 43, 46 and 48 (see Appendix D).

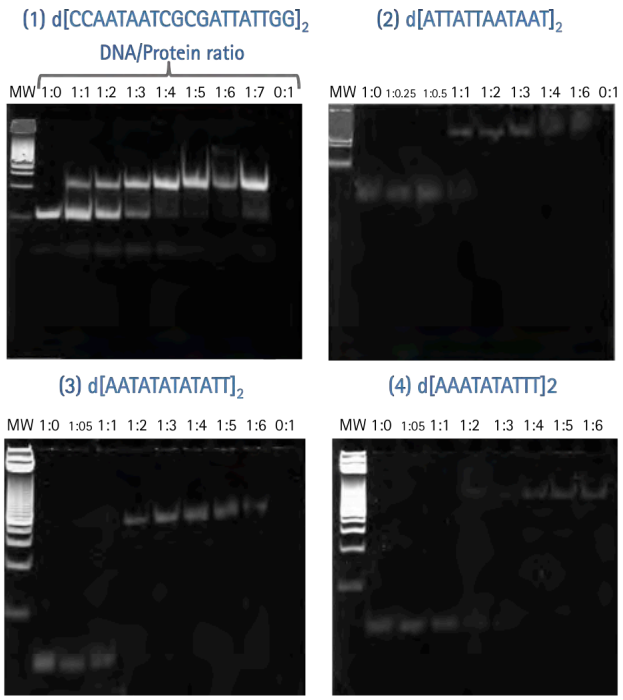

Figure 3-13. EMSA assays of HMGA1a(Δ50-91) in complex with AT-rich oligonucleotides: (1) $d[CCAATAATCGCGATTATTGG]_2$, (2) $d[ATTATTAATAAT]_2$, (3) $d[AATATATATATT]_2$ and (4) $d[AAATATATTT]_2$.

3.2.3 DNA-HMGA1a(Δ50-91) Protein Binding Analysis by SPR

AT-rich sites of DNA are typically recognized by the HMGA proteins through their AT-hook binding domains. EMSA assays were a useful procedure for analyzing the binding of the protein HMGA1a(Δ50-91) with DNA. However, in order to investigate quantitatively the affinity of this protein with AT-rich DNA, measurements of SPR using *Biacore®* technology were performed. Therefore, HMGA1a(Δ50-91) protein binding affinity and kinetics were analyzed following the protocol described in section 2.8. The DNA hairpin 5'-biotin-GGGAATAATCGCGATTATTCCCCAATAATCGCGATTATT-3' [AATAAT_ATTATT] (see Table 2-13 and Figure 2-14) was immobilized in the *SA* sensor chip. Multiple sensorgrams for direct protein binding were collected, keeping the hairpin concentration constant at ~400 RU and varying the HMGA1a(Δ50-91) protein concentration from 10 nM to 10 μM. The best sensorgrams were obtained in HEPES,

instead of MES or Phosphate buffer. Figure 3-14a shows the SPR sensorgrams of the HMGA1a(Δ50-91) binding to DNA hairpin [AATAAT_ATTATT], obtained with running buffer *HEPES 1* containing 10 mM HEPES, 3 mM EDTA, 200 mM NaCl, and surfactant P-20 at 0.05% (v/v) pH 7.4) at a flow rate of 50 µL/min for a period of 60 s followed by a dissociation period of 120 s. Results were fitted to a two-site binding model according to the Equation 2-13 in order to determine the binding affinity (Figure 3-14b).

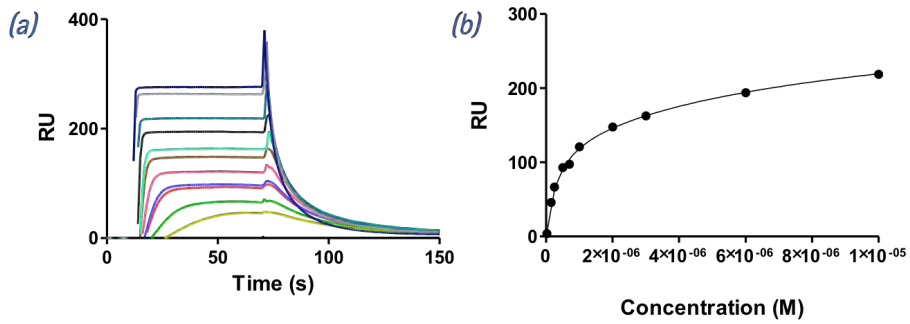

Figure 3-14. ***(a)*** **SPR sensorgrams of HMGA1a (10 nM to 10 µM) binding to dsDNA biotin-GGGAATAATCGCGATTATTCCCCAATAATCGCGATTATT in** ***HEPES 1*** **at 25°C.** ***(b)*** **Binding curve for interaction of HMGA1a(Δ50-91) with target DNA and fitting curve for a two-site affinity model. Graphs were created with** ***Prism 5.0*** **(*GraphPad* Software).**

During the experiments, HMGA1a(Δ50-91) protein showed a high affinity binding site to the AT sequences of the [AATAAT_ATTATT] oligonucleotide and a weaker secondary binding site that most likely accounts for nonspecific binding to the hairpin loop (K_2/K_1 = 32). The K_D values are K_1= 0.35 × 10^{-6} M and K_2= 11.3 × 10^{-6} M.

3.3 Interaction of HMGB1 Protein with AT-rich DNA

The analysis of the interactions of HMGB1 box B and box AB proteins with a series of AT-rich DNA sequences was studied by X-ray crystallography assisted with EMSA assays, and by SPR experiments. For this purpose, the most pure samples of the HMGB1 proteins (see section 3.1.2) were used, which were sample M1 of HMGB1a Box B and sample M1 HMGB1 box AB (see Figure 3-10 and Table 3-2).

3.3.1 DNA-HMGB1 Crystallography Assays

The main goal during this phase was to obtain high quality ordered crystals of DNA-HMGB1 protein complexes for structure resolution by X-ray crystallography. For this, multiple crystallization conditions were screened (see Appendix E). The oligonucleotides used with HMGB1 box B and HMGB1 box AB proteins are listed in Table 3-4. See Table 2-11 for more details.

Table 3-4. Oligonucleotide sequences used for crystallographic assays with HMGB1 proteins.

DNA sequence	Length [bp]	MW [mol·g^{-1}]	HMGB1 Box B	HMGB1 Box AB
1. CCAATAATCGCGATTATTGG	20	12232.2	✓	✓
6. ATTAATTAAT	10	6050.2	✓	
7. AATAAATTTATT	12	7285	✓	
8. ATATGCATAT	10	6052.2	✓	
9. ATATCGATAT	10	6052.2	✓	✓
10. AATAATCGCGATTATT	16	9758.6	✓	✓
11. AATTTAAATT	10	6050.2		✓
12. ATTTATAAAT	10	6050.2	✓	
13. GGGAAATTTCCC	12	7290.8		✓
14. AATAAATTTATTT	13	7902.4		✓

Molecular weight is given in terms of DNA duplex. ✓ Oligonucleotide studied with the HMGB1 fragment indicated.

The formation of complexes with different oligonucleotide sequence was first evaluated by EMSA electrophoresis (see section 2.2.3). For these assays, a set of samples containing increasing concentrations of protein from 1 to 6 µM were incubated for 1 h at 4°C with 1 µM oligonucleotide (Figure 3-15).

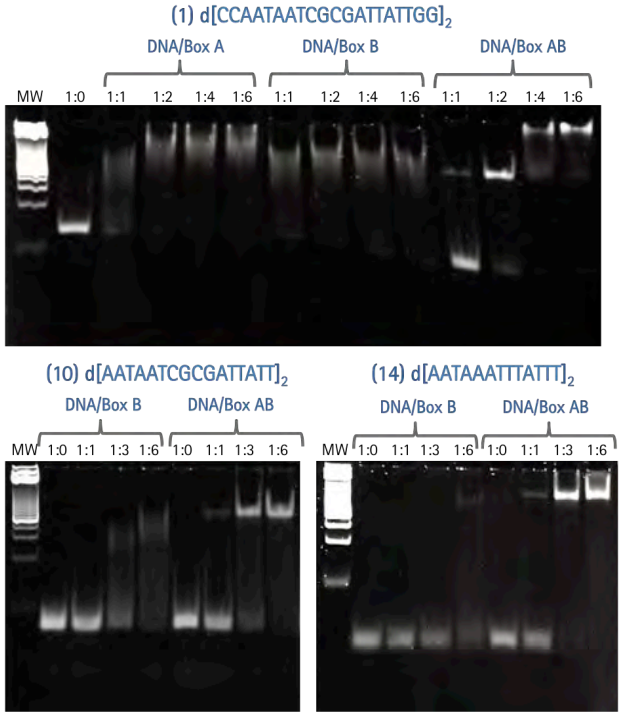

Figure 3-15. EMSA assays of a HMGB1 protein fragments in complex with AT-rich oligonucleotides: (1) d[CCAATAATCGCGATTATTGG]$_2$, (10) d[AATAATCGCGATTATT]$_2$ and (14) d[AATAAATTTATTT]$_2$. HMGB1 box A, residues 7-80; box B, residues 93-165; and box AB residues 1-165 of HMGB1 protein. HMGB1a box A sample was provided by a member of MACROM research group.

From the EMSA assays, the formation of complex was confirmed in each case. HMGB1 box AB was able to start complex formation since 1:1 molar ratios, whereas HMGB1 box B (and box A) complexes were not as stable as with the HMGB1 box AB, leading to association/dissociation of the complex, which resulted in fuzzy extended bands (see Figure 3-15).

Initial crystallography assays were performed using Hampton Natrix HR2-116 numbers 15 and 43, both of them containing $MgCl_2$ (see Appendix D). Due to the lack of success, new crystallization conditions were tested by changing the composition of the salts and precipitant. Thus, $CaCl_2$, NH_4 acetate and Mg acetate, and PEG 3350 as precipitant were also tested. Detailed information of crystallization conditions used for DNA-HMGB1 protein complexes is found in Appendix E.

3.3.1.1 HMGB1 Box B – d[AATAAATTTATT]$_2$

Crystallization assays with oligonucleotide (7) d[AATAAATTTATT]$_2$ in complex with HMGB1 box B were performed by the vapor diffusion technique using the sitting-drop set-up into 48-well crystallization plates. Crystals appeared after a few days in wells containing buffer T6 (10 mM $MgCl_2$, 1 mM DTT, 5% MPD, 25 mM Tris-HCl, pH 7.5) and C6 (10 mM $MgCl_2$, 1 mM DTT, 5% MPD, 25 mM sodium cacodylate buffer pH 6). Therefore, it was decided that a new screening has to be done varying the $MgCl_2$ concentration. Crystals were obtained in droplets containing buffers C9 (12.5 mM $MgCl_2$, 1 mM DTT, 5% MPD, 25 mM sodium cacodylate buffer pH 6), T9 (12.5 mM $MgCl_2$, 1 mM DTT, 5% MPD, 25 mM Tris-HCl, pH 7.5) and C10 (7.5 mM $MgCl_2$, 1 mM DTT, 5% MPD, 25 mM sodium cacodylate buffer pH 6).

Using those buffers, crystallization assays were performed into individual capsules as an attempt to obtain better-sized crystals in a 4 µL droplet equilibrated against 800 µL reservoir containing initially 30% MPD. Precipitant concentration was gradually increased until 45% MPD. Eleven crystals were fished from droplets containing buffers T6 and T9 and diffracted as described in section 2.6.3. Figure 3-16 and Figure 3-17 show the images and diffraction patterns of the best crystallization conditions found in droplets 4C4 and IG5, respectively.

The diffraction patterns of crystal 4C4-2 (Figure 3-16) indicate a very large and complex unit cell, as shown by the rows of closely spaced spots. It is expected an arrangement of the oligonucleotides in two directions due to the cross lines formed in the patterns. Unfortunately the spots are diffused and the patterns could not be properly indexed.

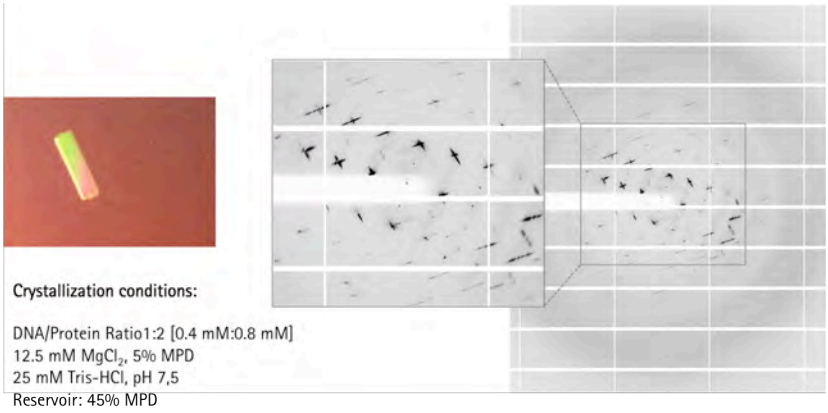

Figure 3-16. Crystal 4C4-2 image and diffraction pattern of oligonucleotide (7) d[AATAAATTTATT]$_2$ with HMGB1 box B. Crystallization conditions are detailed below the image.

The diffraction patterns of the crystal IG5-6 (Figure 3-17) show fiber-like diffraction mixed with define spots at low resolution. In this case, the duplexes show a parallel orientation, as demonstrated by the parallel layer-line streaks (perpendicular to the duplexes axis). The low resolution indicates that the parallel duplexes are randomly displaced in the vertical direction.

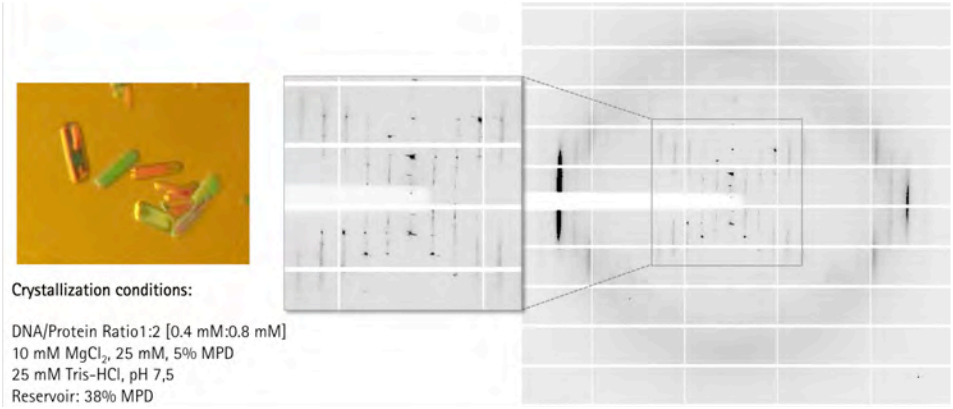

Figure 3-17. Image of the crystal IG5-6 of oligonucleotide (7) d[AATAAATTTATT]$_2$ with HMGB1 box B (left). Its diffraction pattern corresponds to a mixture of fiber-like diffraction and defined spots at low resolution. Crystallization conditions are detailed below the image.

3.3.1.2 HMGB1 Box B – d[CCAATAATCGCGATTATTGG]$_2$

The oligonucleotide (1) d[CCAATAATCGCGATTATTGG]$_2$ was widely studied during this work. Different crystallization conditions were tested for oligonucleotide 1-HMGB1 box B (see Appendix E). Crystallization screening was performed in individual capsules using magnesium as divalent ion and MPD as precipitant.

The best crystallization conditions found were 0.4 mM DNA duplex, 0.8 mM HMGB1 box B, buffer C9 (25 mM sodium cacodylate buffer pH 6, 25 mM $MgCl_2$ and 5% MPD), and equilibrated against a 43% MPD reservoir. Figure 3-18 shows an image of the crystal NC5-1 and its diffraction patterns.

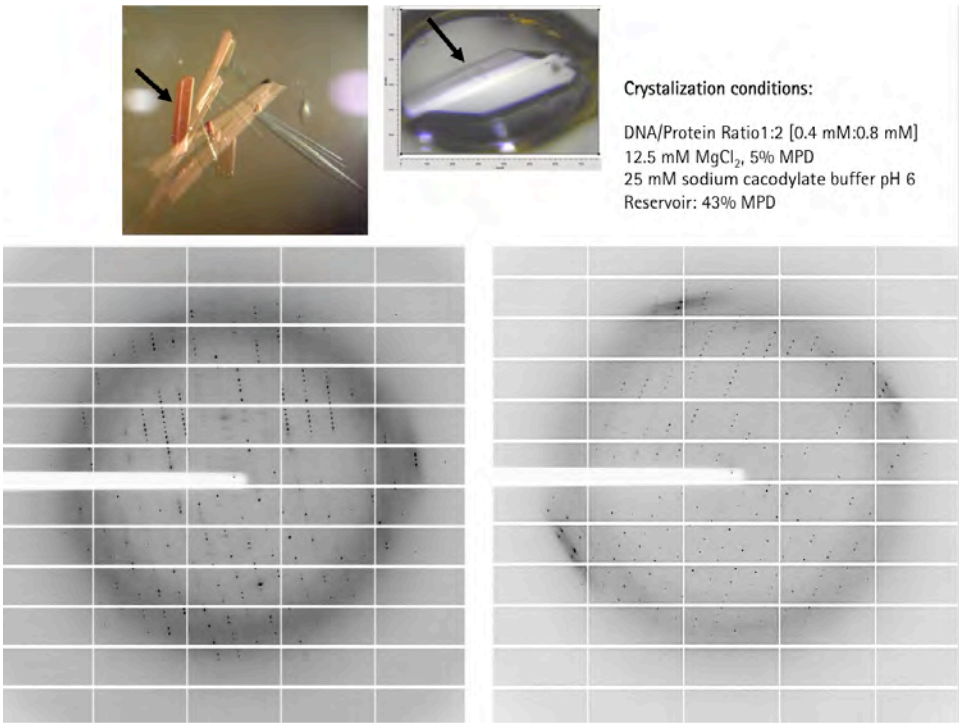

Figure 3-18. Image of crystal NC5-1 and diffraction pattern of oligonucleotide (1) d[CCAATAATCGCGATTATTGG]$_2$ with HMGB1 box B. Crystallization conditions and an image of the crystal in the loop taken at the moment of the diffraction are also shown. Arrows indicate the crystal diffracted. The patterns on the left show two orientations of diffraction that are at ~90° to each other.

The diffraction patterns of the crystal NC5-1 show well-defined spots of two orientations of stacked columns of DNA helices that are at ~90° to each other (see Figure 3-18 right panel).

The diffraction patterns of the crystal NC5-1 was indexed using the program *iMOSFLM* (Battye et al., 2011) as orthorhombic with cell parameters a = 29.94 Å, b = 89.65 Å, c = 109.1 Å, $\alpha = \beta = \gamma = 90°$ in space group $P22_12_1$. The cutoff resolution limit was set to 2.68 Å. The data were scaled using the program *Scala* (Evans, 2006). R_{merge} and R_{meas} values were 0.049 and 0.054. The search DNA model for molecular replacement (MR) was constructed using the program *Turbo-Frodo* (Roussel et al., 1998), taking the full length of the oligonucleotide on a first attempt. Due to the difficulties that finding the 20 bp oligonucleotide presented, fragments of 6 and 10 bp, as DNA models, were created. Despite all the DNA models used for MR, it was not possible to find the molecule. Therefore, MR with numerous PDB structures was used to find the HMGB1 box B protein including HMGD protein (PDB ID: 3NM9), TFAM protein (PDB ID: 4NNU and PDB ID: 3TQ6), transcription factor SOX-9 (PDB ID: 4EUW), among others.

MR in this crystal structure faced a particular difficulty. When DNA models were replaced, they adopted an L-shape similar to the HMGB1 box B structure and the electron density map partially followed those replacements. Nevertheless, a good correlation within the electron density map and the oligonucleotide could not be obtained. On the other hand, the MR with HMG protein structure models positioned the HMG-box in the same place where the oligonucleotide was set when DNA models were used for MR. This probably happened due to the oligonucleotide configuration in the crystal. The HMGB1 box B protein, by its ability to recognize the DNA minor groove and provoke a dramatic distortion on it, may have bent 90° the linear DNA oligonucleotides. That whould explain the two orientations of diffraction obtained in this crystal.

3.3.1.3 Electrophoretic Verification of the Presence of HMGB Protein in the Diffracted Crystals

In order to test the protein content in the obtained crystals, they were analyzed by SDS-PAGE once X-ray diffraction had been performed (see section 2.2.1).

After diffraction, crystals were re-stored in liquid nitrogen to avoid degradation until their analysis by electrophoresis. Once the SDS-PAGE was ready to be performed, each crystal was dissolved in 4.5 µL H_2O *milliQ®* (cold). 1.5 µL of 4x SDS sample buffer was added to the sample. Samples were boiled for 6 min and loaded into the SDS gel. Gel was run for 1 h at constant voltage of 100 V and stained with *SilverQuest™ Silver Staining Kit* (Invitrogen™) for 20 min. Figure 3-19 show the SDS-PAGE of crystals NC5-1, 4C4-1, 4C4-2, 1G5-6 and 1G5-17.

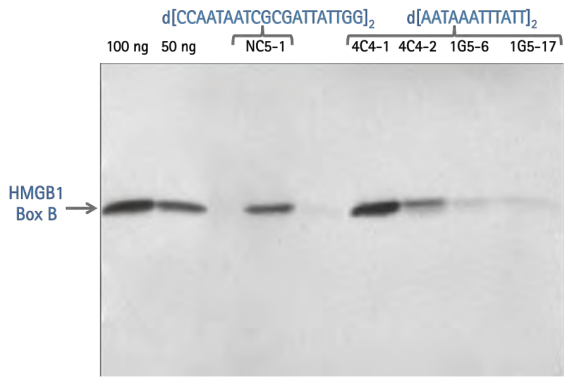

Figure 3-19. SDS-PAGE of crystals of HMGB1 box B with DNA. Sample of HMGB1 box B were used as control (50 and 100 ng).

Intense bands corresponding to the crystals NC5-1, 4C4-1 and 4C4-2 clearly show the presence of the HMGB1 box B. On the other hand, crystals 1G5-6 and -17 show also the presence of the HMGB1 box B but with a poorer protein content.

3.3.2 DNA-HMGB1 Protein Binding Analysis

In contrast to the HMGA proteins, HMGB1 binds more non-specifically to DNA. Measurements of SPR using a *Biacore® X-100* apparatus were also performed for the

protein HMGB box AB to analyze the protein binding affinity and kinetics to an AT-rich DNA following the protocol described in section 2.8.

To study the binding interactions between HMGB1 and the DNA hairpin [AATAAT_ATTATT] (see Table 2-13), a dilution series of HMGB1 box AB samples was prepared (from 10 nM to 10 µM) by dilution into *HEPES 1* buffer. Multiple sensorgrams were collected, keeping the DNA concentration constant at ~400 RU, and injecting the series of protein samples over the immobilized DNA at a flow rate of 50 µL/min for a period of 60 s followed by a dissociation period of 120 s (Figure 3-20a). *HEPES 1* was used as the running buffer. A solution containing 200 mM NaCl/10 mM NaOH was used to regenerate the free DNA surface after each injection using a flow rate of 10 µL/min during 30 s. The binding affinity was determined by fitting the results to a two-site binding model according to Equation 2-13 (Figure 3-20b).

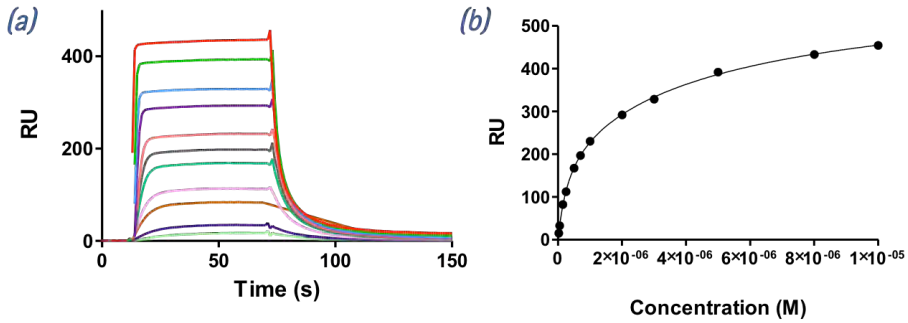

Figure 3-20. ***(a)*** **SPR sensorgrams of HMGB1 box AB (10 nM to 10 µM) binding to dsDNA biotin-GGGAATAATCGCGATTATTCCCCAATAATCGCGATTATT hairpin in** ***HEPES 1*** **at 25°C and** ***(b)*** **Binding curve for interaction of HMGB1 box AB with target DNA and fitting curve for a two-site affinity model. Graphs were created with** ***Prism 5.0*** **(*GraphPad* Software).**

Similar to HMGA1a(Δ50-91), HMGB1 box AB protein showed two K_D values: a high affinity binding site to the AT sequences of the [AATAAT_ATTATT] oligonucleotide (K_1= 0.33 × 10^{-6} M), and a weaker secondary binding site (K_2= 5.91 × 10^{-6} M; K_2/K_1 = 18) that most likely accounts for nonspecific binding to the hairpin loop. The higher affinity of HMGB1, compared to the HMGA1a(Δ50-91) (K_2= 11.3 × 10^{-6} M), to this nonspecific secondary binding site is compatible with HMGB proteins binding more

non-specifically to DNA compared to the higher preference of HMGA proteins to bind AT-rich DNA.

3.4 GENERAL DISCUSSION

Several goals were achieved in this chapter regarding the obtainment of the HMG proteins of interest and their characterization and analysis.

First, the human HMGA1a(Δ50-91) protein containing two AT-hook DNA binding domains has been expressed with the recombinant DNA technology in the bacterium *E. coli* (Rosetta (DE3) pLysS strain) using a pET vector. Pure protein samples were obtained by cation-exchange chromatograpy followed by size-exclusion chromatography. On the other hand, two fractions of the HMGB1 protein [the box B, HMGB1(Δ93-165) and the two tandem boxes AB, HMGB1(Δ1-165)] were also successfully expressed as GST-fusion proteins in the same *E. coli* strain transformed with a plasmid pGEX-2T. HMGB1 proteins were purified by a multi-stage purification strategy, which involved affinity chromatography, cation-exchange chromatography and size-exclusion chromatography.

Using the high-purity samples, an analysis of DNA supercoiling induced by the HMGA1a(Δ50-91) protein was performed. The verification of the functionality of the recombinant protein was achieved by demonstrating the capacity of this HMGA1a fragment to induce supercoiling in a DNA plasmid containing two alternating AT inserts. In addition, the activity of the protein was compared with a fragment containing the three AT-hook domains, HMGA1a(Δ1-90), finding a similar behavior for both proteins. Then, it can be assumed that two-AT-hook DNA motifs could act comparably to the three-AT-hook fragment in terms of inducing changes in the DNA configuration.

HMGA1a(Δ50-91) and HMGB1 box AB showed high affinity binding to the AT region of the 39 bases (GGGAATAATCGCGATTATTCCCCAATAATCGCGATTATT) hairpin used for the SPR assays. They also presented a weaker secondary binding site due to nonspecific binding to the hairpin loop, weaker for the HMGA1a than for the HMGB1. This could

be probably due to the HMGA higher specificity for AT sites compared to the HMGB proteins.

In the DNA-protein interaction analysis by EMSA, HMGA1a(Δ50-91) showed good binding at 1:1 and 1:2 DNA/protein ratios with the oligonucleotides $d[AAATATATTT]_2$, $d[CCAATAATCGCGATTATTGG]_2$, $d[ATTATTAATAAT]_2$ and $d[AATATATATATT]_2$. On the other hand, DNA-HMGB1 box AB complex formation was achieved with $d[CCAATAATCGCGATTATTGG]_2$, $d[AATAATCGCGATTATT]_2$ and $d[AATAAATTTATTT]_2$. DNA complexes with HMGB1 box B displayed fuzzy extended bands due probably to the formation of an instable complex. A similar behavior has been described for the HMGB1 box A (Sánchez-Giraldo et al., 2015). Nevertheless, DNA-HMGB1 box AB complexes were observed as a neat band at 1:1 molar ratios.

Although the structure of a single AT-hook in complex with DNA has been previously solved for the first time in our reaserch group, all the attempts to crystalize the two-AT-hook domains protein HMGA1a(Δ50-91) have not succeed. HMGA1a is an intrinsically disordered protein and even though the crystallographic assays were performed in complex with DNA, no crystals with any of the oligonucleotides analyzed were obtained. However, the crystallization of the HMGB1 with several DNA sequences has been achieved.

Crystals of macromolecular complexes containing HMGB1 box B-$d[AATAAATTTATT]_2$ and HMGB1 box B-$d[CCAATAATCGCGATTATTGG]_2$ were diffracted at ALBA Syncrothron. Crystals containing the oligonucleotide $d[AATAAATTTATT]_2$ showed fiber-like diffraction patterns at low resolution. On the other hand, a complex with the HMGB1 box B and $d[CCAATAATCGCGATTATTGG]_2$ presented a well-ordered diffraction pattern at 2.68 Å resolution. Data collection were indexed in orthorhombic $P22_12_1$ space group with cell parameters a = 29.94 Å, b = 89.65 Å, c = 109.1 Å, $\alpha = \beta = \gamma = 90°$. Well-defined spots of two orientations of diffraction ~90° to each other were shown in the diffraction patterns. Consequently, it is expected that the oligonucleotides have packed in a crossed column configuration, or, that DNA interaction with HMGB1 box B protein had

provoked a ~90° kink on the DNA, as previously reported (Ngo et al., 2014; Ngo et al., 2011; Rubio-Cosials et al., 2011; Sánchez-Giraldo et al., 2015).

CHAPTER 4

BIS(2-AMINOIMIDAZOLINE) COMPOUNDS

4.1 Interaction of Minor Groove Binding Drugs with AT-Rich DNA

The high affinity and selectively recognition of the HMG proteins to AT-rich binding sites offers an excellent opportunity for rational design of AT minor grove binding drugs (MGBD) to contest important human diseases. For that reason, in this work the binding and interactions of eleven bis(2-aminoimidazoline) compounds (listed in Table 2-9) with AT-rich DNA have been analyzed.

4.2 DNA-MGBD Binding Analysis by SPR

Surface Plasmon Resonance (SPR) experiments were carried out to study the direct binding affinity of the bis(2-aminoimidazoline) compounds to dsDNA hairpins containing GGAATAATCGCGATTATTCC [AATAAT_ATTATT], CGAATTCG [AATT], CATATATAT [$(AT)_4$], and CGCGCGCG [$(CG)_4$] sequences (Table 2-13).

As an initial analysis, a binding screening of the eleven compounds to the DNA hairpin [AATAAT_ATTATT] (see Table 2-13) were evaluated. The compound CD27 (Figure 1-18) was also added in this assay. Samples with a fix concentration of 24 µM of each compound in *HEPES 1* were prepared and injected over the immobilized DNA surfaces (~400 RU) followed by running buffer injection, which was also *HEPES 1*. The flow rate used for these experiments was 18 µL/min for an association period of 300 s followed by a dissociation period of 300 s. Subsequently, a solution containing 200 mM NaCl/10 mM NaOH was used to regenerate the free DNA surface after each injection using a flow rate of 10 µL/min during 60 s.

Figure 4-1 shows that the FR60 and derivatives (Ref 1-10 in Table 2-9) as well as the drug CD27 exhibited, in general, an affinity for the DNA hairpin [AATAAT_ATTATT] similar to that showed by the lead drug FR60. The compound JNI18 was the FR60 derivative that showed the higher affinity for the DNA hairpin, presenting a slightly better affinity than FR60. On the other hand, compound CRMV49 was not able to bind

to the DNA, probably because of the fluorine atom position, which permits the formation of an H-bond with the central [–NH] group of the drug and thus the DNA-drug binding could be obstructed. Interestingly, a unique pattern of interaction was observed between DNA-CDIV32. Compound CDIV32 (see Table 2-9) presented higher affinity compared to the rest of compounds, and a particularly slow rate of dissociation.

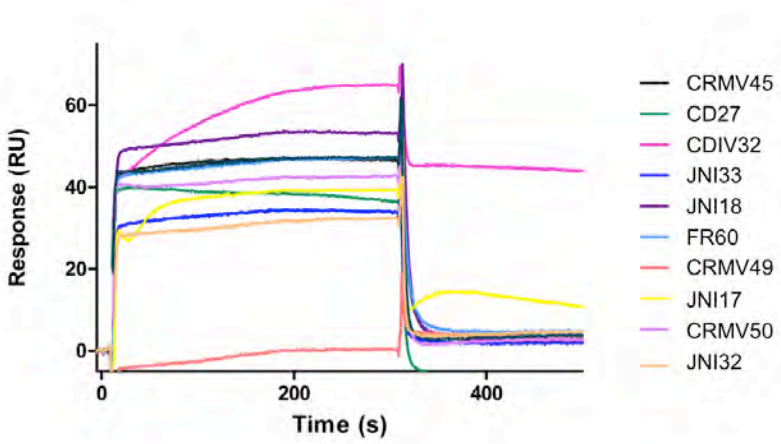

Figure 4-1. Binding screening by SPR of bis(2-aminoimidazoline) compounds to biotin-GGGAATAATCGCGATTATTCCCCAATAATCGCGATTATT hairpin in *HEPES 1* at 25°C.

Based on those results, next experiments were performed with the there compounds that showed the most interesting binding features: FR60, JNI18 and CDIV32.

Direct binding affinity assays of the compounds FR60, JNI18 and CDIV32 were performed as described section 2.8. Drug samples were prepared at a series of concentrations (from 0.25 nM to 57.6 µM) by dilution into *HEPES 1* buffer. These experiments were performed using the same conditions as in the previous binding screening. Figure 4-2 shows the sensorgrams for FR60 binding to hairpin [AATAAT_ATTATT] and the binding curve adjusted to a two-site binding model.

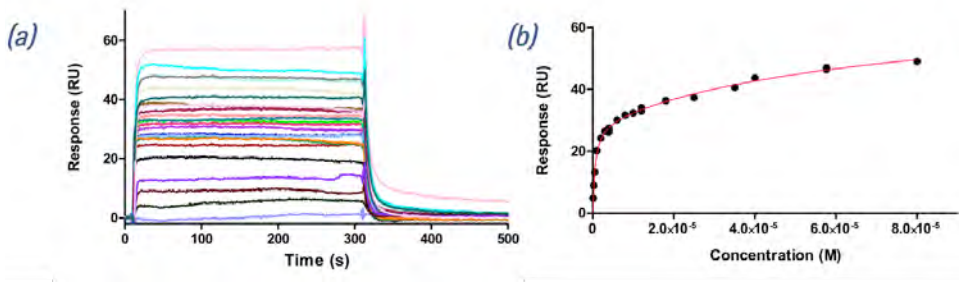

Figure 4-2. ***(a)*** **SPR sensorgrams for binding of drug FR60 to dsDNA biotin-GGGAATAATCGCGATTATTCCCCAATAATCGCGATTATT in** ***HEPES 1*** **at 25°C, using increasing concentrations of the ligand in the range of 0.25-57.6 µM.** ***(b)*** **Binding curve for interaction of FR60 with target DNA and fitting curve for a two-site affinity model.**

SPR binding affinity for the drugs FR60 and CDIV32 binding to the DNA hairpin [AATT], $[(AT)_4]$ and $[(CG)_4]$ are given by Ríos Martínez et al. (2015a). Figure 4-3 and Figure 4-4 show the binding affinity of drug CDIV32 to DNA hairpin [AATAAT_ATTATT] and drug JNI18 to the four DNA hairpin sequences studied, respectively. Binding curves for interactions of the drugs with DNA $[(CG)_4]$ were adjusted to one-site binding (K_2 = 0). The summary of the binding constants of all compounds is listed in Table 4-1.

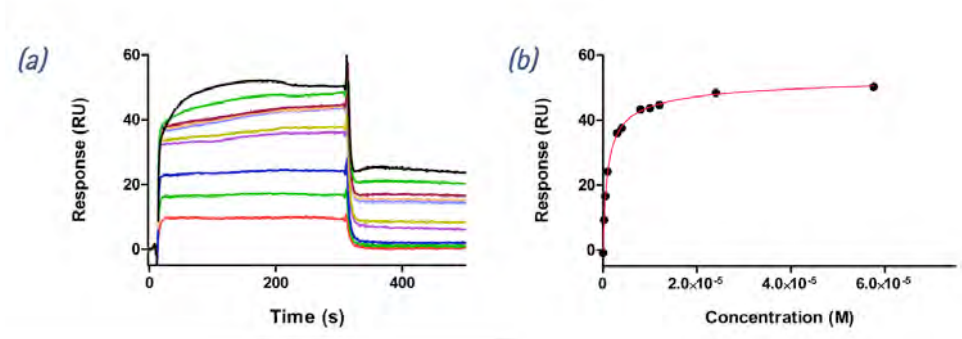

Figure 4-3. ***(a)*** **SPR sensorgrams for binding of drug CDIV32 to dsDNA biotin-GGGAATAATCGCGATTATTCCCCAATAATCGCGATTATT in** ***HEPES 1*** **at 25°C, using increasing concentrations of the ligand in the range of 0.25-57.6 µM.** ***(b)*** **Binding curve for interaction of CDIV32 with target DNA and fitting curve for a two-site affinity model.**

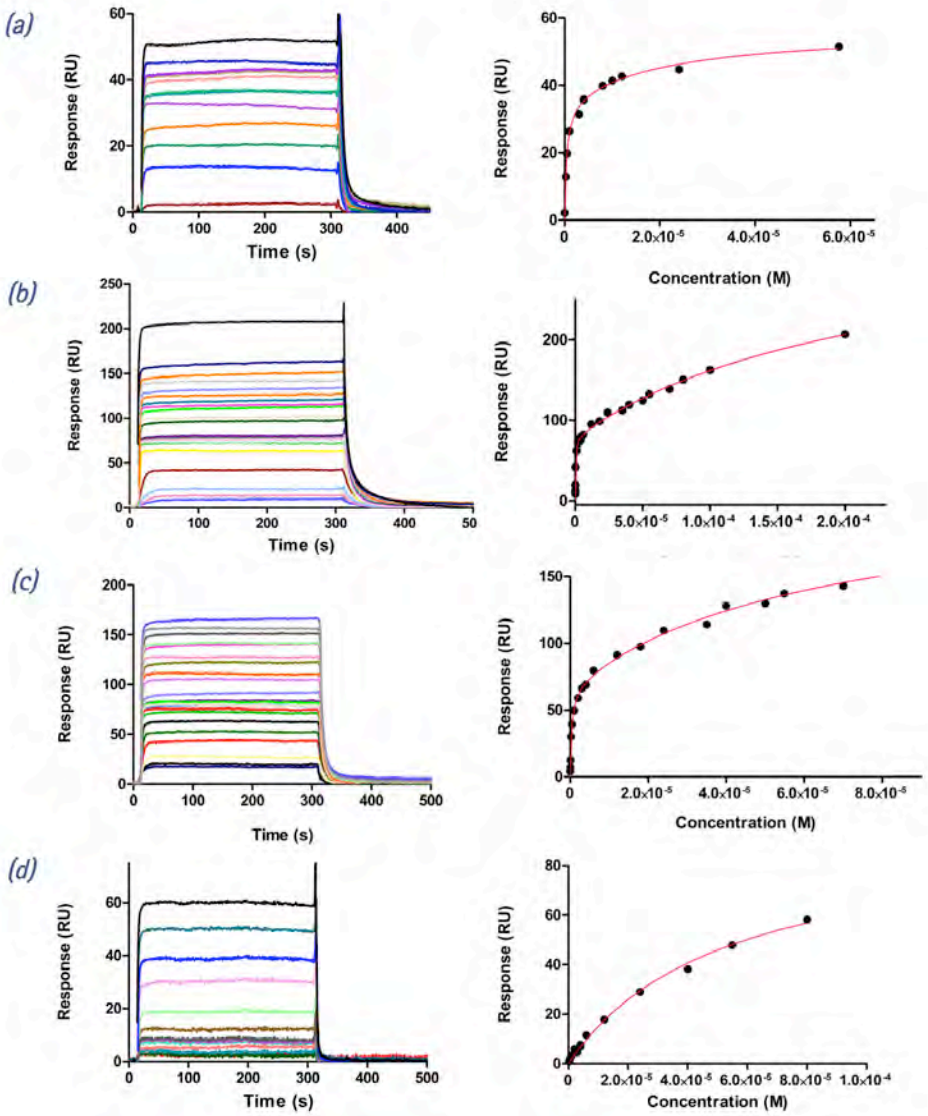

Figure 4-4. SPR sensorgrams and binding curves for interaction of drug JNI18 with hairpins *(a)* biotin-GGGAATAATCGCGATTATTCCCCAATAATCGCGATTATT; *(b)* biotin-CGAATTCGTCTCCGAATTCG; *(c)* biotin-CATATATATCCCCATATATATG; and *(d)* biotin-CGCGCGCGTTTTCGCGCGCG in *HEPES 1* at 25°C, using increasing concentrations of the ligand in the range of 0.25-57.6 µM. For the AT-rich sequences, the curve was adjusted to a two-site affinity model and for the CG-rich sequence to a one-site binding model.

Compounds FR60 and JNI18 bound selectively to AT-containing DNA versus CG-containing DNA (from >10-fold to >60-fold). Binding curves of both compounds were

adjusted to a two-sites affinity model where primary binding constants were in the submicromolar range with slight selectivity toward [AATT] versus [$(AT)_4$] (1.8- to 2.5-fold) or [AATAAT_ATTATT] oligonucleotides (1.6- to 3-fold). With the DNA hairpin [AATAAT_ATTATT], compounds FR60 and JNI18 displayed submicromolar primary binding constants (high affinity binding site) and a 133- and 48-times weaker secondary binding constant, respectively.

Moreover, compound CDIV32 bound more selectively to AT-containing DNA versus CG-containing DNA than the other two compounds (~120-fold). Primary binding constants were in the submicromolar range and for [$(AT)_4$] in the micromolar range. CDIV32 showed slight selectivity toward [AATT] versus [$(AT)_4$] or [AATAAT_ATTATT] similar to the compounds FR60 and JNI18 (3.1-fold and 1.6-fold, repectively). Compound CDIV32 displayed a high affinity binding site to the AT sequences and 22-, 185 and -46 times weaker secondary binding with [AATAAT_ATTATT], [AATT] and [$(AT)_4$], respectively.

In these experiments, secondary binding generally accounts for non-specific binding interaction with the DNA hairpin loop as previously reported (Ríos Martínez et al., 2015c).

Table 4-1. DNA binding constants determined by SPR for dsDNA containing AATAAT_ATTATT, AATT, $(AT)_4$, and $(CG)_4$ sequences.

Compound	K_D ($\times 10^{-6}$ M) [a]			
	dsDNA GGAATAATCGCGATTATTCC	dsDNA CGAATTCG	dsDNA CATATATAT	dsDNA CGCGCGCG
FR60	K_1 = 0.56 K_2 = 74.7	K_1 = 0.166 [b] K_2 = 207	K_1 = 0.307 [b] K_2 = 20.91	> 10 [b]
JNI18	K_1 = 0.43 K_2 = 20.8	K_1 = 0.262 K_2 = 230	K_1 = 0.65 K_2 = 39	K = 6.85 [c]
CDIV32	K_1 = 0.92 K_2 = 20.2	K_1 = 0.568 [b] K_2 = 105	K_1 = 1.79 [b] K_2 = 83.4	K = 66.7 [b,c]

[†]dsDNA hairpins used in the study: 5'-biotin-GGGAATAATCGCGATTATTCCCCAATAATCGCGATTATT [AATAAT_ATTATT], 5'-biotin-CGAATTCGTCTCCGAATTCG-3' [AATT], 5'-biotin-CATATATATCCCCATATATATG-3' [$(AT)_4$], and 5'-biotin-CGCGCGCGTTTTCGCGCGCG-3' [$(CG)_4$]. [a]Binding constants for fitting to a two-site binding model. K_1 corresponds to the primary binding constant for fitting to a two-site binding model. The secondary binding constant (K_2) corresponds to nonspecific binding to the hairpin loop (Nguyen & Wilson, 2009). [b]Reference (Ríos Martínez et al., 2015a). [c]Binding constant for fitting to a one-site binding model.

4.3 DNA Binding Competition Assay: HMG Proteins vs Bis(2-aminoimidazoline) Derivatives

Competition assays were performed to test the capacity of compound JNI18 to inhibit the formation of HMGA1a–DNA and HMGB1–DNA complexes (Figure 4-5). Solutions of fixed concentration of HMGA1a(Δ50–91) or HMGB1 box AB proteins (2 μM) in the presence of increasing concentrations of drug JNI18 were injected over the DNA immobilized surface. The sensorgrams showed a clear decrease in RU signal when increasing the concentration of JNI18 indicating a dose-dependent inhibition of HMGA1a and HMGB1 binding to DNA (Figure 4-5).

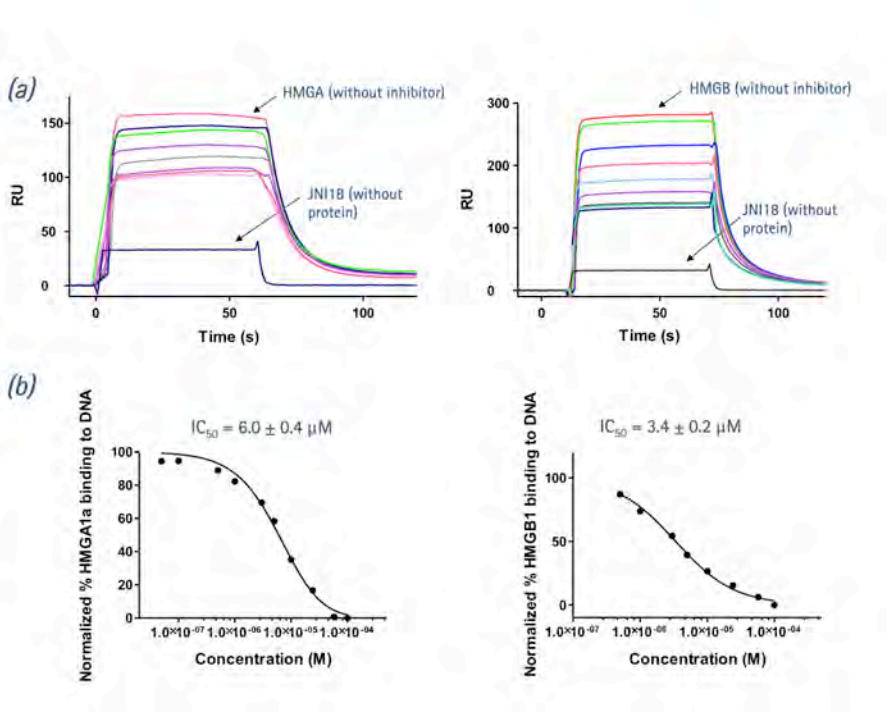

Figure 4-5. *(a)* SPR competition sensorgrams showing the inhibition of a fixed concentration (2 μM) of HMGA1a1a(Δ50-91) (Top left panel) and HMGB1 box AB (top right panel) binding to dsDNA containing [AATAAT_ATTATT] oligonucleotide in the presence of increasing concentration of JNI18. Drug concentration range from 0.05 to 200 μM (for HMGA1a[Δ50-91]) and 0.05 to 400 μM (for HMGB1). *(b)* Inhibition curves and IC_{50} values for inhibition of binding of HMGA1a(Δ50-91) (lower left panel) and HMGB1 box AB (lower right panel) to dsDNA by compound JNI18.

IC_{50} values, determined by fitting the inhibition data with a model according to a competition system with 1:1 binding stoichiometry for HMGA1a(Δ50-91) and HMGB1 box AB and two-site binding for competitor (Miao et al., 2008) were in the low micromolar range (6.0 and 3.4 μM for HMGA1a and HMGB1, respectively). Thus, it can be concluded that drug JNI18 competes with HMGA1a and HMGB1 binding to DNA and it is able to displace the proteins from its binding sites.

4.4 DNA-Bis(2-aminoimidazoline) Crystallography Assays

Crystallography assays were performed with AT-rich DNA and the bis(2-aminoimidazoline) compounds studied following the protocol described in section 2.5 in order to obtain X-ray quality crystals and solve the 3D structure of the complex. For this purpose, multiple crystallization conditions were screened.

For the crystallization of drugs FR60, JNI18 and CDIV32, 6-12 base pair all-AT or AT-rich oligonucleotides used are listed in Table 4-2.

Table 4-2. Oligonucleotide sequences used for crystallographic assays with bis(2-aminoimidazoline) compounds.

DNA sequence	Length [bp]	MW [mol·g^{-1}]
2. ATTATTAATAAT	12	7285
4. AAATATATTT	10	6050.2
6. ATTAATTAAT	10	6050.2
11. AATTTAAATT	10	6050.2
12. ATTTATAAAT	10	6050.2
15. AAATTT	6	3580.6
16. AATAATTATT	10	6050.2
17. CATATATATG	10	6050.2
18. AATTATAATT	10	6050.2
19. ATAATATTAT	10	6050.2

Molecular weight is given in terms of DNA duplex.

DNA-drug crystallography assays were performed in individual capsules by vapor diffusion hanging-drop technique. A set of crystallization buffers were prepared using

the salts $MgCl_2$, $Mg(CH_3COO)_2$, $MnCl_2$ and NH_4CH_3COO in sodium cacodylate pH 6 adding spermine to get a final concentration 2:1 DNA/spermine molar ratio. In all cases, MPD was used as precipitant (18-20% MPD initial concentration). Droplets of 3 to 4 µL size were set up. The Hampton Natrix HR2-116 number 7 and 42 were also employed, both of them containing $MgCl_2$ (see Appendix D). Detailed information on the crystallization conditions used for DNA-drugs complexes is found in Appendix E.

4.4.1 Structure of CDIV32 – $d[AAATTT]_2$

Extensive crystallization assays were performed with complexes of DNA-CDIV32, using several oligonucleotide sequences. However, special attention was given to the 6 bp DNA (15) $d[AAATTT]_2$ during this research work due to its capacity to form crystals with the compounds studied. Crystallization screening was performed in individual capsules using different crystallization conditions as described in Appendix E. Several crystals appeared after 16 weeks in different droplets containing 1:2 and 1:4 DNA/drug molar ratios using the buffers D1 and D3 (see Appendix D) (Figure 4-6).

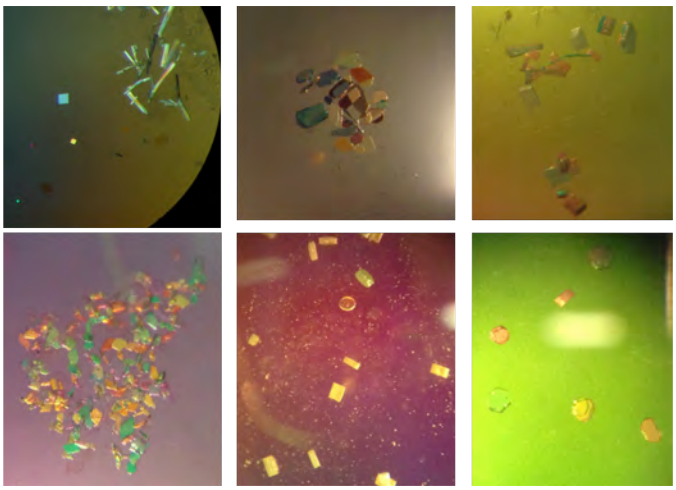

Figure 4-6. Crystals of $d[AAATTT]_2$ with drug CDIV32 with different morphologies.

Numerous crystals were fished and diffracted. The best crystallization condition was obtained in the presence of Mn^{2+} (25 mM sodium cacodylate buffer pH 6, 0.2 mM

oligonucleotide, 0.8 mM drug CDIV32, 0.1 mM spermine) (buffer D1, Appendix D) against 55% MPD reservoir (Figure 4-7).

Diffraction of the best crystal (DB.5-4-1) (see Figure 4-7) was indexed and integrated using the program *iMOSFLM* as orthorhombic crystalline system with a space group $C222_1$. The parameters of the unit cell are a = 62.79, b = 451.08 and c = 80.93; $\alpha = \beta = \gamma = 90°$. The resolution range was 69.27-3.10 Å.

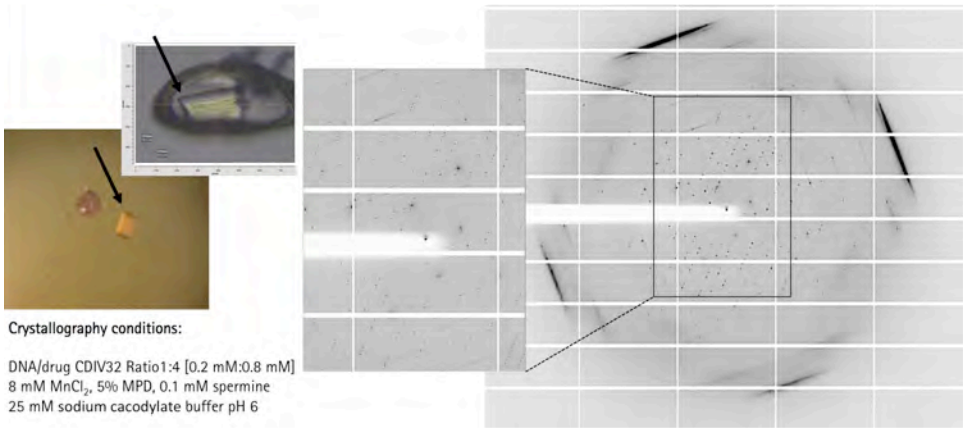

Figure 4-7. Image of crystal DB.5-4-1 and diffraction pattern of oligonucleotide (15) d[AAATTT]$_2$ with drug CDIV32. Crystallization conditions and an image of the crystal in the loop taken at the moment of the diffraction are also shown. Arrows indicate the crystal diffracted.

The diffraction patterns of this crystal show well-defined spots of two orientations of diffraction that are at ~90° to each other. The best approximation of a solution was obtained by the construction of a theoretical straight column with 16 oligonucleotides; the model of B-form AAATTT dsDNA was generated with *Turbo-Frodo* (Roussel et al., 1998) with base-pair staking of 3.25 Å, a uniform twist of 36° and Watson–Crick base-pair pairing. The column of the stacked oligonucleotides forming a pseudo-continuous helix was created with *Pymol* (Schrödinger, LLC, 2015), considering that the virtual step T-A, in the end-to-end interaction of stacked oligonucleotides, had a negative rotational setting angle ω_T (i.e. helical twist) of about -25° for WC conformation. The distance between oligonucleotides was adjusted to 3.446 Å by measuring the total distance between symmetric columns. The program *Molrep* (Vagin and Teplyakov, 2010)

was used for molecular replacement of the partial solution. The refinement of this partial solution (3.10 Å, R_{work}/R_{free} 0.3817/0.4584, using *REFMAC5* (Murshudov et al., 2011) shows the DNA molecules are organized in a crossed column configuration of sixteen stacked oligonucleotides at about 90° (Figure 4-8).

The presence of the CDIV32 drug has modulated this structure of oligonucleotides. In spite of the low resolution, solving this structure could be of interest to determine if the drug may act as a cross-linking agent, forming links between neighbour DNA columns and consequently, causing the crossed column organization found, as reported for alternative DNA-drug complexes (Moreno et al., 2010; Acosta-Reyes et al., 2014).

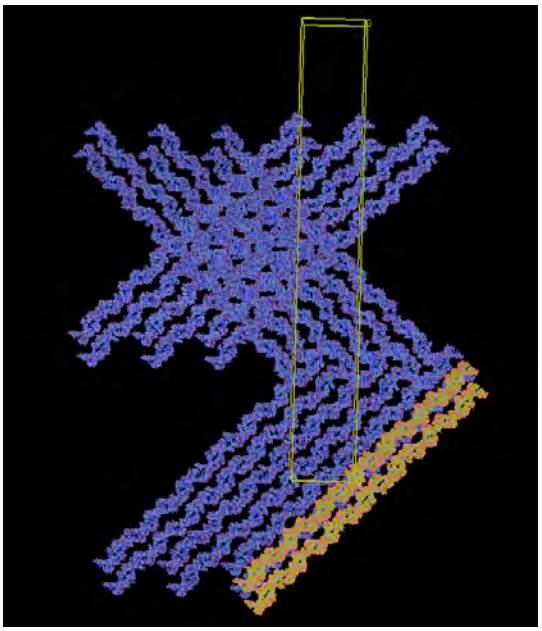

Figure 4-8. View of the packing of the model, where the crossed columns organization and the asymmetric unit are visible.

The analysis of the Patterson function by *Phenix.Xtriange* (Zwart et al., 2005) reveals a significant off-origin peak (0.5, 0.217, 0) corresponding to 40.46% of the origin peak, indicating pseudo translational symmetry. This detectable translational NCS hinders the full resolution of the structure.

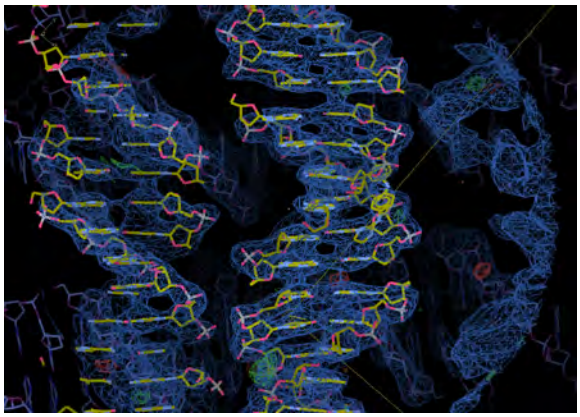

Figure 4-9. View of the electron density map at 1σ and difference map at 3σ of the stacked oligonucleotides d[AAATTT]$_2$ in crossed columns at 3.10 Å resolution. The virtual step A-T between oligonucleotides has an helical twist of about -25°.

4.4.2 Structure of FR60 – d[AAATTT]$_2$

The lead compound FR60 was widely studied by crystallography assays with (15) d[AAATTT]$_2$ oligonucleotide. The crystallization of this oligonucleotide was tested in the presence of various divalent ions (Appendix E). The best crystallization conditions were obtained with the divalent ion Mg^{2+} (D2 buffer: 25 mM sodium cacodylate buffer pH 6, 0.2 mM oligonucleotide, 0.4 mM drug CDIV32, 0.1 mM spermine) (see Appendix D) against gradually increased concentration of MPD up to 50% in the reservoir. A single perfectly defined crystal (F6-1, see Figure 4-10 left panel) in a droplet with those conditions appeared after 14 months.

Crystallography conditions:

DNA/drug FR60 Ratio 1:2 [0.2 mM:0.4 mM]
8 mM $Mg(CH_3COO)_2$, 5% MPD, 0.1 mM spermine
25 mM sodium cacodylate buffer pH 6

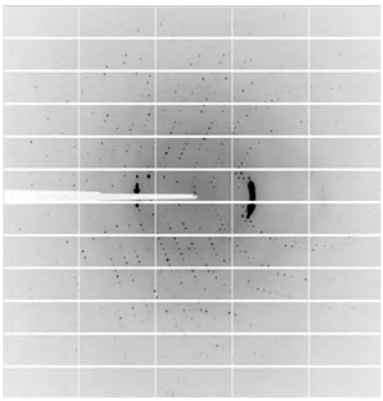

Figure 4-10. Image of crystal F6-1 and diffraction pattern of oligonucleotide (15) d[AAATTT]$_2$ with drug FR60. Crystallization conditions are also shown.

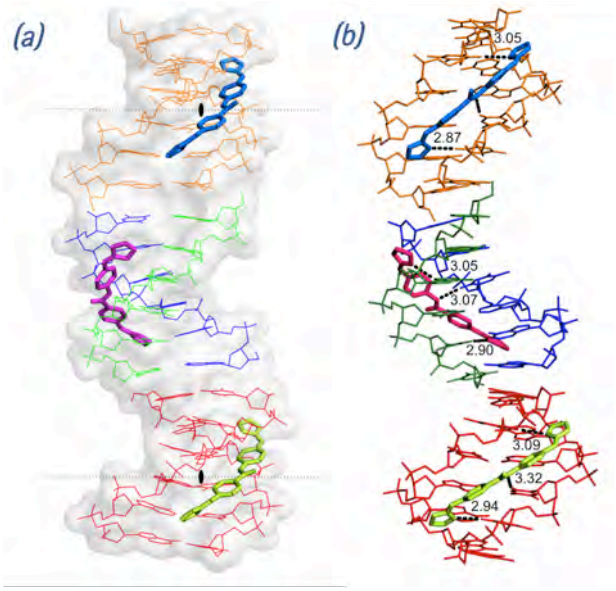

Figure 4-11. View of the different crystallographic units of the complex. The black lozenge indicates the dyad axes. Four independent single oligonucleotides chains are shown; two of them (blue-green) form the central duplex and the other two single strands (orange and red) form two different DNA duplexes with their symmetrical chain. Three crystallographically independent drug molecules are indicated in different colours. Drug F (pink), Drugs E (green) and G (blue). (b) Hydrogen bonds formed by the drugs with the minor-groove atoms of the DNA duplexes show similar interactions. The orientation of the aromatic rings in the central drug (F, pink) differs from to the other two drugs. Drug E and G have two possible inverted positions in the groove; for clarity only one of them is shown. Image prepared with *PyMOL* (http://www.pymol.org).

The single-crystal was diffracted and data was collected with a maximum resolution of 1.2 Å. Diffraction data were integrated using *iMOSFLM* (Battye et al., 2011) and scaled with *Aimless Pointless* (Evans, 2006) from the *CCP4* suite (Winn et al., 2011). The space group turned out to be the monoclinic space group I121 with unit cell parameters (a, b, c, α, β, γ) 22.33 40.25 72.42 90.0 93.67 90.0. A theoretical B-DNA model was constructed using Turbo-Frodo (Roussel et al., 1998), with a base-pair stacking of 3.286 Å, a uniform twist of 36° and Watson–Crick base-pair pairing. This was a starting search model for molecular replacement with *MOLREP* (Vagin & Teplyakov, 2010). Due to the lack of success after an extensive search in different monoclinic space groups, another theoretical model was generated, formed by half of the oligonucleotide and placed it in the correct position by molecular replacement using *Phaser* (McCoy et al., 2007). The missing base pairs of the oligonucleotide were added

with *Coot* (Emsley et al., 2010) following the well-defined electron density map. The replacement was next refined with *REFMAC5* (Murshudov et al., 2011) and real-space refinement was performed with *Coot*.

One duplex and two single strands of DNA in the asymmetric unit were placed. The coordinates and stereochemical restraint dictionary of the drug FR60 molecule were generated with *Phenix* (Adams et al., 2010), and one drug per duplex was placed in the minor groove of the DNA structure using *Coot* following the well-defined electron density map.

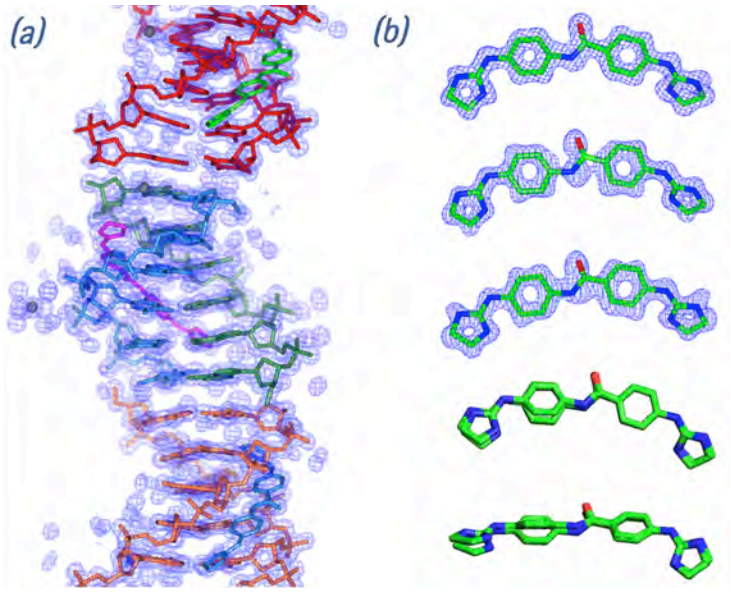

Figure 4-12. ***(a)*** **View of the electron density map at 1σ of the stacked oligonucleotides d[AAATTT]$_2$ at 1,25 Å resolution.** ***(b)*** **OMIT $2F_o$–F_c electron-density map (1 σ level) of the three drugs in the complex. Drug F is at the top, followed by E and G below. The bottom two frames show a superposition of the three drugs in two perpendicular views. Image prepared with the program *CCP4mg* (McNicholas et al. 2011).**

The asymmetric unit in the final model contained three FR60 molecules (two of them show half-occupancy), plus one DNA duplex and two DNA single strands. Three complete duplexes and three drug molecules are shown in Figure 4-11 (electronic map is displayed in Figure 4-12a). Several cycles of maximum-likelihood isotropic restrained refinement were performed with *REFMAC5* to 1.247 Å resolution. Finally, a last round of refinement with anisotropic restrictions was completed to obtain the final values of

R_{work}/R_{free} 0.1205/0.1668 in a resolution range of 36.137-1.247 Å, with a completeness of 92.54%. Four magnesium ions were detected. A summary of crystal data and refinement statistics is given in Table 4-3.

Table 4-3. Data collection and refinement statistics of the crystal F6-1.

Data collection	
Beamline	BL13-XALOC, ALBA
Wavelength	0.998
Resolution range (Å)	36.14 - 1.25 (1.279 - 1.247)
Space group	I 1 2 1
Unit cell parameters (Å, °)	a =22.33, b = 40.25, c =72.42, α= 90.00 β = 93.67 γ = 90.00
Total reflections	245821 (22828)
Unique reflections	16801 (1594)
Multiplicity	14.7 (14.2)
Completeness (%)	92.54 (90.67)
Mean I/sigma(I)	14.1 (5.5)
Wilson B-factor	9.90
R-merge †	0.069 (0.227)
Refinement statistics	
Reflections used in refinement	15741 (1122)
Reflections used for R-free	850 (89)
R-work ‡	0.1205 (0.141)
R-free §	0.1668 (0.200)
Number of non-hydrogen atoms	730
DNA	480
FR60 (PDB name: 6XV)	81
Water	165
Mg^{2+}	4
RMS(bonds)	0.022
RMS(angles)	2.52
Average B-factor, all atoms (Å^2)	13.0
DNA	10.43
FR60 (PDB name: 6XV)	10.33
Water	22.38
PDB-ID	5LIT

Statistics for the highest-resolution shell are shown in parentheses. † R_{merge} was calculated with **Equation 2-6**. ‡ R_{work} and R_{free} were calculated as R following the **Equation 2-9**. § R_{free} is the R factor evaluated for the reflections (5%) used for cross-validation during refinement.

Solution coordinates have been deposited in the Protein Data Bank as PDB ID: **5LIT** (drug FR60 corresponds to 6XV in PDB). The DNA structural parameters were calculated using the *3DNA* software (Lu & Olson, 2003).

The asymmetric unit contains one molecule of drug F, one half-occupancy drug E and one half-occupancy drug G. All of them interact in the middle of the DNA duplex, the central AATT sequence, as found in several other cases (Sheng et al., 2013). The 1σ $2F_o$-F_c omit map of each drugs (F, E and G from top to bottom) are shown in Figure 4-12b, as well as two perpendicular superposition views of the three drugs.

Drug E and G are practically identical (r.m.s. differences of 0.172 Å). Both drugs form three hydrogen bonds with two consecutive thymines from one DNA strand (T4 and T5) and another thymine (T5) from its symmetric strand, as shown in Figure 4-13. Values are given in Table 4-4. The nitrogen atoms that are not hydrogen bonded to oligonucleotides are associated with water molecules, as shown in Figure 4-13.

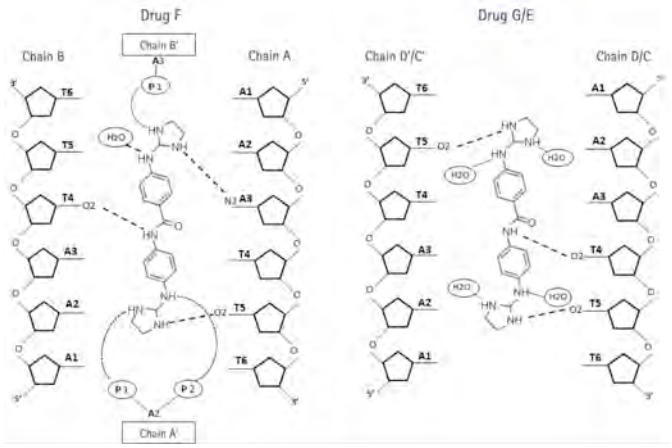

Figure 4-13. Schematic representation of interactions between F and G or E drugs and d[AAATTT]$_2$. In the crystal, drugs G and E may be found in two alternative positions, up and down, which are structurally identical. Symmetric chains are indicated with apostrophe.

The central drug molecule F has maximum r.m.s. differences of 1.250 and 1.269 Å with drug E and G, respectively. Drug F forms also three hydrogen bonds with DNA (adenine 3 (A3) and thymine 5 (T5), both from chain A, and thymine 4 (T4) from chain B).

Table 4-4. Hydrogen bonds formed by drug FR60 in the minor groove of d[AAATTT]$_2$ and interactions with neighbouring phosphates.

Atoms involved	Drug E	Drug F	Drug G
O2(T4)-N3(FR60)	3.32	3.07	3.30
O2(T5)-N22(FR60)	--	2.9	--
N3(A3)-N13(FR60)	--	3.05	--
O2(T5)-N25(FR60)	2.94	--	2.87
O2(T5')-N13(FR60)	3.09	--	3.05
N10(FR60)-OP1(A3 oligo B')	--	2.82	--
N20(FR60)-OP2(A2 oligo A')	--	2.79	--
N25(FR60)-OP1(A2 oligo A')	--	2.79	--

Values are given in Å.

Moreover, the drug F molecules are well positioned and centered in their corresponding duplex, allowing that its central nitrogen atom (N3) interacts with the oxygen from thymine 4 [O2(T4)] either in the 3'-5' direction (drug F with chain B) or in the 5'-3' direction (drugs G and E) (Figure 4-13). A remarkable feature of this drug is its interactions with two phosphates from neighboring DNA molecules, as shown in Figure 4-14 and Table 4-4.

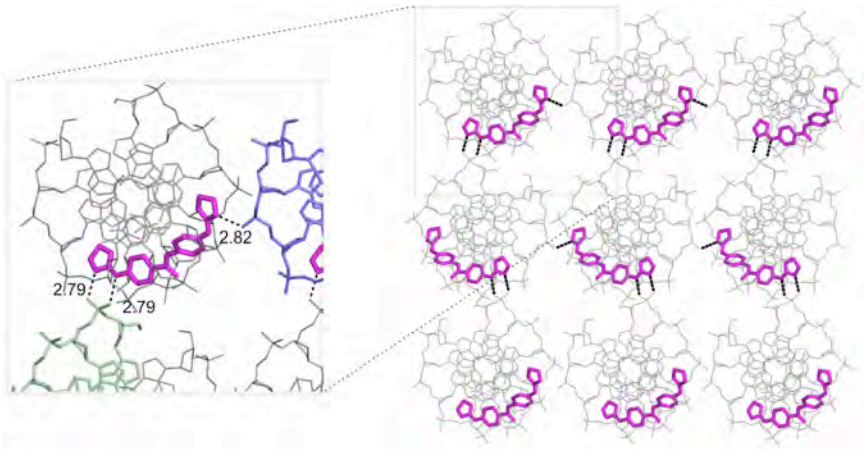

Figure 4-14. Packing of a layer of A-B duplexes. An enlarged view of the interactions of drug F with the neighbouring phosphates of symmetrical DNA chains is shown at the left. Images prepared with the program *CCP4mg* (McNicholas et al. 2011).

The duplexes are stacked and organized as infinite continuous parallel columns, which are packed in a pseudo-tetragonal way (Figure 4-15) and stabilized in part by the interaction of the central molecule, drug F (pink) with the DNA phosphates of neighbouring molecules (Figure 4-14). Drug G (blue) and E (green) do not participate in the interactions with neighbour DNA duplexes.

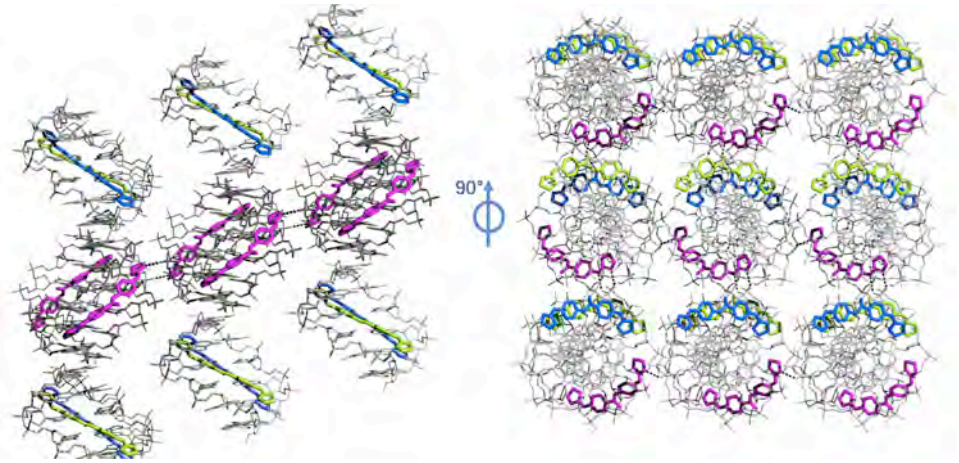

Figure 4-15. Views of the pseudo-tetragonal crystal packing of d[AAATTT]$_2$ and the drug FR60. Image prepared with *PyMOL* (http://www.pymol.org).

The three different DNA duplexes in the structure have similar and standard conformational parameters. The main difference is found in the twist angles in the pseudo base step T-A between the ends of neighbor duplexes in oligonucleotide columns, see Figure 4-16. As found in previous studies (Campos et al., 2006), the helical twist angle had a negative value (-21°) in the end-to-end interaction of stacked oligonucleotides at the virtual step T-A between oligos A-B and D-D'. Nevertheless, a peculiar feature of the present structure is the positive twist angle (29°) between oligos A-B and C-C', allowing these two oligonucleotides form a pseudo-continuous B-DNA helix Figure 4-16. These differences are probably due to packing constraints induced by interactions between neighboring duplexes (Figure 4-14).

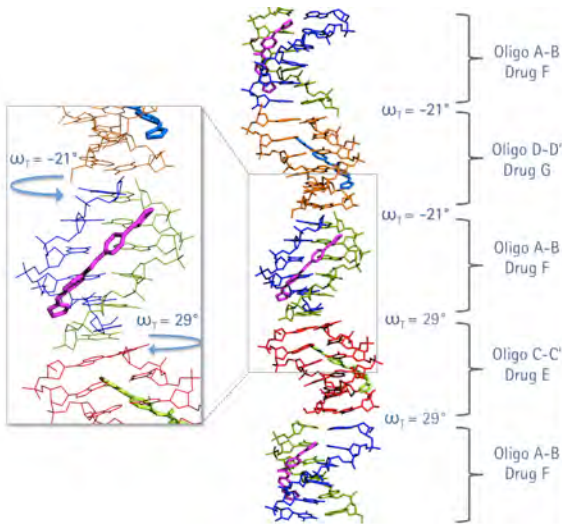

Figure 4-16. End-to-end interaction helical twist (ω_T) angles of a single stacked oligonucleotide column. The virtual step T-A between oligos A-B and D-D' form a ω_T of -21°, while between oligos A-B and C-C' ω_T. value is 29°. Image prepared with *PyMOL* (http://www.pymol.org).

4.5 GENERAL DISCUSSION

The binding analysis and structural studies of the interaction of the bis(2-aminoimidazoline) compounds to AT-rich DNA were examined in this chapter.

Direct DNA binding of all compounds to a 39 bases AT-rich DNA hairpin was confirmed by SPR. The bis(2-aminoimidazoline) derivatives CDIV32, JNI18 and FR60 were the strongest DNA binders. However, different binding behaviors and affinities were observed. Compound CDIV32 showed a distinctive association and dissociation patterns.

The interaction of FR60, JNI18 and CDIV32 directly with four DNA hairpin sequences was measured by SPR. Strong affinity was found for the three AT-rich hairpin duplexes containing: [AATAAT_ATTATT], [AATT] and [$(AT)_4$]. In contrast, none of the compounds bind significantly to the dsDNA containing [$(CG)_4$] sequences as expected for this class of minor groove binders. This confirmed that FR60, JNI18 and CDIV32 are strong DNA minor groove binders and specifically target AT- over GC-rich sequences.

In addition, SPR experiments were performed in order to investigate whether the bis(2-aminoimidazolinium) compounds could potentially compete with HMG-box proteins for binding to DNA. It was found that compound JNI18 was able to displace HMGB1 box AB and the HMGA1a(Δ50-91) proteins from their DNA binding sites.

By X-ray crystallography, structural analyses of the DNA-drug complex at the molecular level were accomplished. The best crystals were found with the all-AT oligonucleotide $d[AAATTT]_2$. A crystal containing this DNA sequence with the drug CDIV32 was studied thoroughly. The partial structure solution of the drug CDIV32 with $d[AAATTT]_2$ at 3.10 Å resolution indicated that DNA columns were constituted by sixteen stacked oligonucleotides forming a pseudo-continuous helix with average helical twist of the T-A virtual step between stacked oligonucleotides (ω_T) of about -25°. The DNA molecules were conserved a related organization of crossed column. The drug CDIV32 could have coordinated this structure of oligonucleotides by the formation of cross-links between crossed columns. However, the analysis of the Patterson function revealed pseudo translational symmetry, which complicated the resolution of the structure.

On the other hand, the crystal structure of drug FR60 in complex with the DNA $d[AAATTT]_2$ at atomic resolution of 1.25 Å was solved (PDB: **5LIT**; FR60 PDB name: 6XV). The space group turned out to be the monoclinic I121. The asymmetric unit was containing three FR60 drugs, one per DNA duplex, interacting with DNA in several alternative positions (molecule F, G and E). The drugs were covered the minor groove of the DNA duplexes, filling the central part of the minor groove [AATT]. More remarkable, the drug was forming cross-link with neighboring DNA molecules stacked as infinite parallel columns in pseudo-tetragonal organization. Cross-linking interactions contribute to stabilize the crystal lattice. End to end oligonucleotides stacking were found forming a combination of negative helical twist (-21°) and WC configuration (positive ω_T of about 29).

It has been confirmed through genomic analysis that the number of occurances of the motif [AATT] in a kinetoplast minicircle of *T. brucei* Tb427WT is 14 times (Appendix G).

CHAPTER 5

EFFECT OF THE BIS(2-AMINOIMIDAZOLINES) ON *TRYPANOSOMA BRUCEI*

5.1 *In vitro* Activity of Bis(2-aminoimidazoline) Compounds Against *Trypanosomes*

Alamar blue assays were carried out according to the protocol described in section 2.9.2, to obtain the half maximal effective concentration (EC_{50}) values for the drugs FR60, JNI18 and CDIV32 against *T. brucei* Tb427WT, pentamidine-resistant strain TbAT1-B48 and isometamidium-resistant strain ISMR1. Compounds activity against *T. congolense* wild type IL3000 and diminazine-resistant cell lines 4C2 and 6C3 were also evaluated.

5.1.1 Drug sensitivity in *Trypanosoma brucei*

As the starting hypothesis was that kDNA might be a target for the bis(2-aminoimidazoline) compounds, they were tested in parallel against the standard *T. brucei* wild type strain Tb427WT and against ISMR1 cell line (Table 5-1). ISMR1 is an isometamidium-adapted strain (Eze et al., 2016), which is dyskinetoplastic, meaning that the cell line has adapted to the loss of its kinetoplast. The compound CDIV32 was also tested against the pentamidine-resistant cell line TbAT1-B48 (Table 5-2).

Table 5-1. Activity of bis(2-aminoimidazoline) compounds against *T. brucei* 427WT and the isometamidium-resistant strain ISMR1.

Compound	EC_{50} [µM] ± SEM		Resistance Factor ISMR1 vs. Tb247WT
	427WT [a]	ISMR1 [b]	
FR60	0.83 ± 0.08 [c]	105.26 ± 3.22	127 ***
JNI18	0.220 ± 0.06 [c]	28.97 ± 0.75	132 ***
CDIV32	29.98 ± 2.17	118.87 ± 4.22	4 ***
Compound	**EC_{50} [nM] ± SEM**		**Resistance Factor ISMR1 vs. Tb247WT**
Isometamidium	0.015 ± 0.0007	1464 ± 94.56	92522 ***

EC_{50} values are given as mean of at least 3 independent determinations and SEM. The resistance factor (RF) is the ratio of the EC_{50} values of the adapted strain and the wild-type control. Statistical significance was determined using a two-tailed unpaired t-test. [a] Bloodstream form (BF) trypomastigotes of *T. b. brucei* Tb427WT. [b] BF trypomastigotes of *T. b. brucei* ISMR1. [c] Reference (Eze et al., 2016). Asterisks represent P-values for statistically significant resistance, as calculated using a two-tailed unpaired Student's t-test: ***, P-value <0.0001.

In vitro drug sensitivity assay established that ISMR1 was highly resistant to isometamidium (ISM) when the EC_{50} values of the resistant clone were compared to those of the parent Tb427WT strain (Table 5-1**).** Significant cross-resistance was displayed by ISMR1 to the compounds FR60 and JNI18, with 127- and 132-fold increases in EC_{50} values, respectively, indicating that the independence from kDNA had made the cells resistant to the test compounds.

Table 5-2. Activity of drug CDIV23 against *T. brucei* TbAT1-B48.

Compound	EC_{50} (µM) [a] ± SEM
CDIV32	20.82 ± 2.25
Pentamidine	0.35 ± 0.003

EC_{50} values are given as mean of at least 3 independent determinations and SEM. [a] TbAT1-B48, *T. b. brucei* strain that is resistant to diminazene, pentamidine, and melaminophenyl arsenicals.

Minor loss of sensitivity was shown for the compound CDIV32 for ISMR1 (4-fold), which also presented less activity than drugs FR60 and JNI18 (36 and 136 times) to the *T. brucei* 427WT. No significant cross-resistance with FR60, JNI18 nor CDIV32 was observed to TbAT1-B48 cell line (see Table 1-5 and Table 5-2), presenting resistance factors (AT1-B48 vs 427WT) of 1.05, 1.6 and 0.7, respectively.

5.1.2 Drug sensitivity in *Trypanosoma congolense*

The bis(2-aminoimidazoline) compounds FR60, JNI18 and CDIV32 were tested against three strains of *Trypanosoma congolense* (Table 5-3).

Table 5-3. Activity of bis(2-aminoimidazoline) compounds against *T. congolense.*

Compound	EC_{50} (µM) ± SEM		
	IL3000 [a]	*4C2* [b]	6C3 [c]
FR60	3.95 ± 0.59	2.72 ± 0.01	3.73 ± 0.53
JNI18	7.37 ± 1.37	7.27 ± 0.25	5.94 ± 0.17
CDIV32	2.07 ± 0.26	1.94 ± 0.04	2.16 ± 0.49
Compound	EC_{50} (nM) ± SEM		
Diminazine	258.5 ± 15.8	2473 ± 150	2609 ± 120

EC_{50} values are given as mean of at least 3 independent determinations and SEM. [a] Trypomastigotes of *T. congolense* wild type IL3000 and, [b] 4C2 and [c] 6C3 diminazine-resistant cell lines.

Compounds FR60 and JNI18 presented better activity against *T. brucei* 427WT than against *T. congolense* IL3000WT (4.75 and 33.5 times, respectively). However, drug CDIV32 displayed around 14 times better activity against *T. congolense* IL3000. No cross-resistance was observed by the diminazine-resistant cell lines to any of the compounds.

Next experiments were performed by testing the compounds only in *Trypanosoma brucei* Tb427WT.

5.2 *In vitro* Efficacy and Effect of Bis(2-aminoimidazoline) Compounds on Trypanosome Growth

In order to determinate how fast these compounds act on cell proliferation and cell survival, *T. b. brucei* s427WT was exposed to each compound at four different concentrations according to their EC_{50}: 0.5×, 1×, 2.5× and 5× EC_{50} values (see Table 5-1).

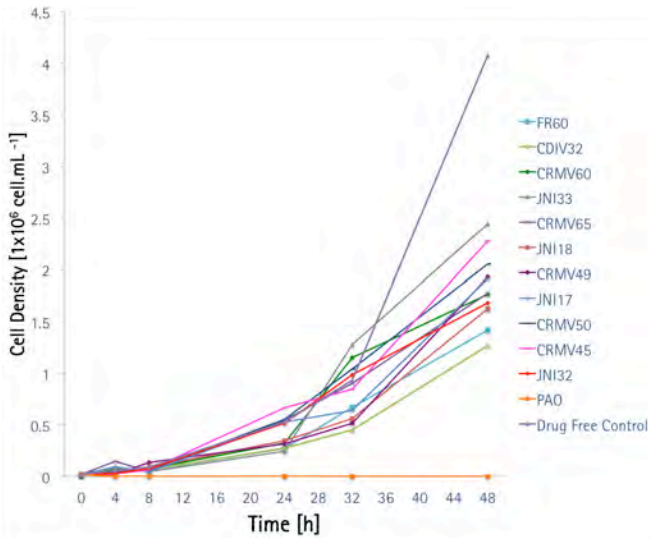

Figure 5-1. Effect of the bis(2-aminoimidazoline) compounds on the growth curve of bloodstream form *T. brucei* 427WT. Microscopic cell counts were performed in duplicate using a haemocytometer. The results shown are the average of the duplicate determinations. Phenylarsine oxide (PAO) 1 µM and untreated cells (Drug Free Control) are taken as controls.

Figure 5-1 shows the growth curve for all the compounds at each EC_{50} concentration. Analyzing the effect of the compounds on the growth and survival of the trypanosomes it can be implied that this set of diamidine-like derivatives tested are, in general, effective in reducing the normal growth rate of the parasite. At concentrations equal to the EC_{50} value, CDIV32, FR60, JNI18, CRMV49 and JNI17 inhibit the growth by more than 50% compared to the untreated cells after 24 h of incubation with the compounds.

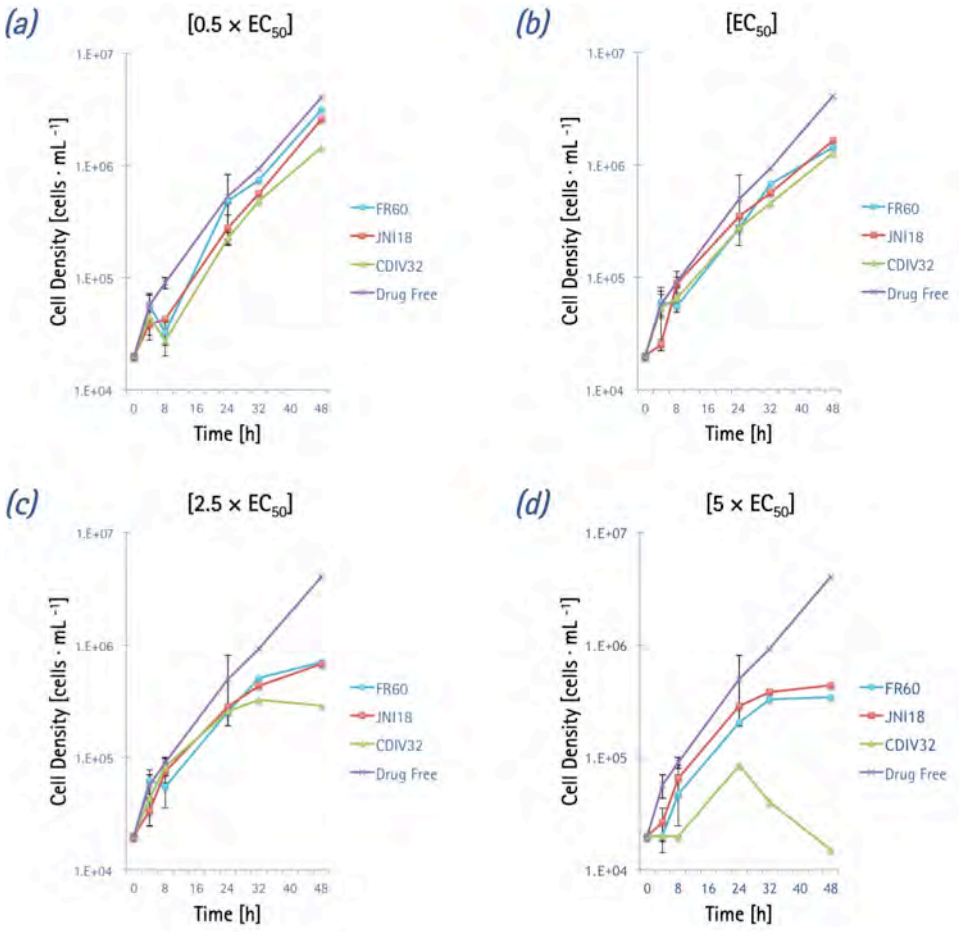

Figure 5-2. Growth curves of untreated control (Drug Free) *T. brucei* 427WT and of parallel cultures treated with compounds FR60, JNI18 and CDIV32 at 0.5, 1, 2.5 and 5× their EC_{50} values. Microscopic cell counts were performed in triplicate, using a haemocytometer. Error bars show the standard error of the mean for three independent determinations.

Figure 5-2 depicts the growth curve for the four concentrations tested of the three compounds (FR60, JNI18 and CDIV32). The initial cell concentration was 2×10^4 cell/mL as described in section 2.9.3, and growth curves were produced by assessing trypanosome counts at 4, 8, 24, 36 and 48 h after incubation with appropriate concentrations of drugs.

Treated with 2.5 times the EC_{50} values, the growth rate was decreased for cells treated with every compound compared to the control. Nevertheless, cells are still increasing the population after the 48 h of incubation. Therefore, the compounds are affecting the growth rate of the trypanosomes but not killing them even at those concentrations.

Drug concentrations of 0.5× and 1× EC_{50} (Figure 5-2a & b) do not appear to have a significant effect on the growth curve of *T. b. brucei* 427WT after 24 h of incubation. However, cell population was reduced to half when parasites are incubated with 0.5× and 1× EC_{50} for 32 h. After 48 h incubated with 0.5× CDIV32 EC_{50}, and 1× EC_{50} concentrations of FR60 and JNI18, two-thirds of the population of parasites was decreased. Moreover, for concentrations above EC_{50} (2.5× & 5×), FR60 and JNI18 blocked almost completely the cell proliferation after the first 24 h of incubation, and allowed only a gradual, slow increase in the cell population at 32 and 48 h of incubation, while the compound CDIV32 blocked completely the cell proliferation after 24 h. The observations show that the compounds have a growth-limiting, trypanostatic effect rather than an immediate trypanocidal effect.

5.3 Cell Cycle Analysis of Bis(2-aminoimidazoline)-Exposed *Trypanosoma brucei*

In the *T. brucei* cell cycle, replication and division of kDNA necessarily precedes nuclear division (Gluenz et al., 2011), and bis(2-aminoimidazoline) compounds that directly impact on kDNA are thus expected to interfere with cell division. Indeed, compounds FR60, JNI18 and CDIV32 dose-dependently reduced *T. brucei* growth rates and, at concentrations above EC_{50}, appeared to induce growth arrest after 24 h (Figure 5-2).

To analyze whether compounds have an effect on the cell cycle, the DNA content was measured by flow cytometry, with emphasis on the ratio between cells with G1 phase of cell cycle and those cells synthesizing DNA (S phase of cell cycle), as well as on the appearance of cells in G2 phase. Moreover, in order to observe cell cycle progression in detail, i.e. to visualise DNA configuration from nuclei and kinetoplast, fluorescence microscopy was carried out.

Trypanosomes were exposed to the compounds during 24 h and flow cytometry assay was performed as described in section 2.9.4.2. Cell density was adjusted to 2×10^6 cells/mL, exposed with 1× and 5× EC_{50} concentrations of each compound and incubated for the duration of the experiment. Samples were taken at 0, 12 and 24 hour and a *Becton Dickinson FACSCalibur* was used to analyze them. Table 5-4 shows the histograms of treated and untreated cells for 0, 12 and 24 h of one of three independent assays performed. *CellQuest™* and *©FlowJo* software have been used to analyze the flow cytometry data by modelling the histogram peaks and defining the percentages of the population at each cell cycle phase. Thus, G1 is the non-dividing stage of the cell, i.e. cells that have one kinetoplast and one nucleus; S phase is where DNA replication occurs; and in G2 cells have two kinetoplasts and two nuclei.

Table 5-4. Histograms of flow cytometric analysis of propidium iodide fluorescence associated with Tb427WT trypanosomes treated with the bis(2-aminoimidazoline) compounds.

Compound	0 h	12 h	24 h
Untreated (Control)	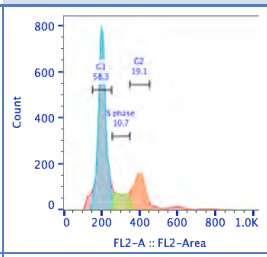	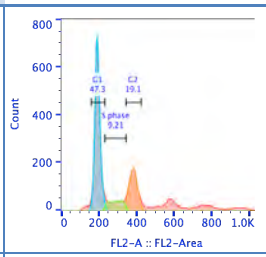	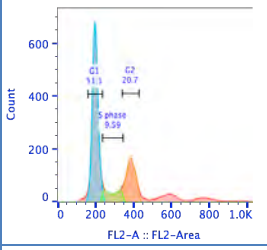
FR60 (EC_{50})	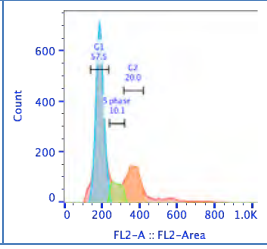	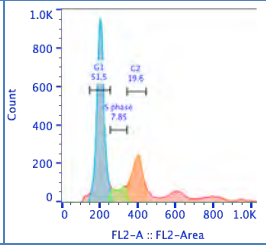	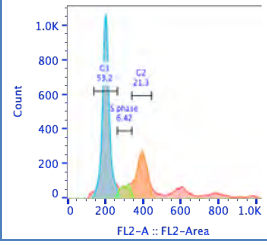

Compound	0 h	12 h	24 h
FR60 ($5 \times EC_{50}$)	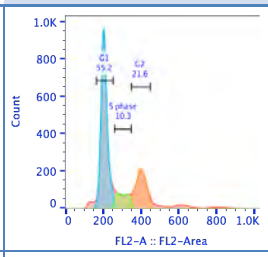	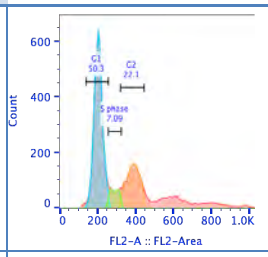	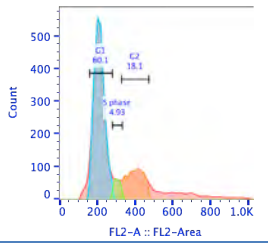
JNI18 (EC_{50})	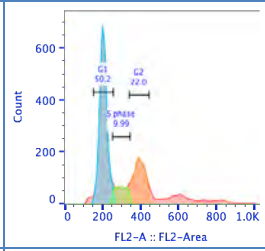	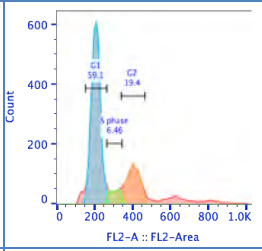	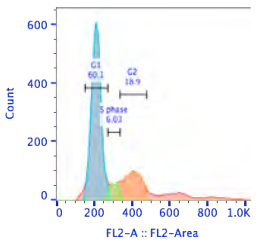
JNI18 ($5 \times EC_{50}$)	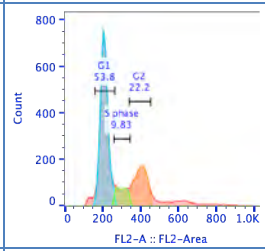	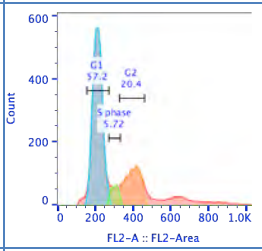	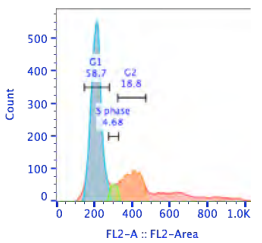
CDIV32 (EC_{50})	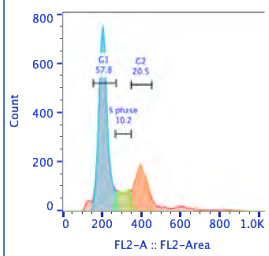	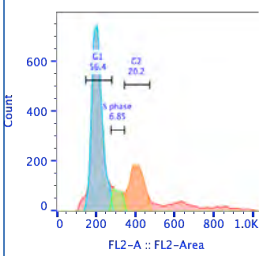	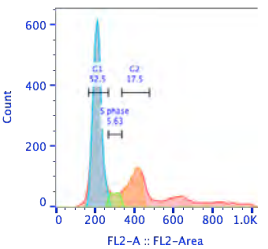
CDIV32 ($5 \times EC_{50}$)	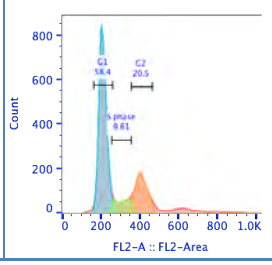	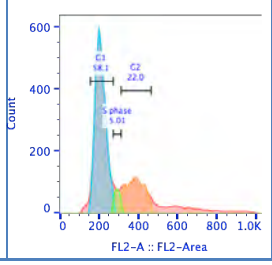	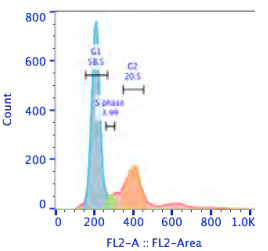

Cells in G1 phase (blue peak) contain a single set of chromosomes; S-phase (green), DNA synthesis and G2 phase (orange), cells with 2 sets of chromosomes. Results from one of three independent experiments that produced similar results are shown. Percentage of the population at each cell cycle phase is shown above its histogram peak. Untreated cells were included in each assay as control.

The results show a clear effect of the tested compounds on the S phase of the cell cycle after 12 h and even more remarkable alteration after 24 h of incubation (Table

5-4 and Figure 5-3). The proportion of cells in G2 phases initially showed a slight increase (at 12 h of treatment), and a small reduction later (after 24 h), while an increase of cells in G1 phase was observed. The percentage of treated cells in S phase decreased dose-dependently throughout the experiment, whereas there was no significant change in the S phase for the control which maintained a normal growth rate (Table 5-4).

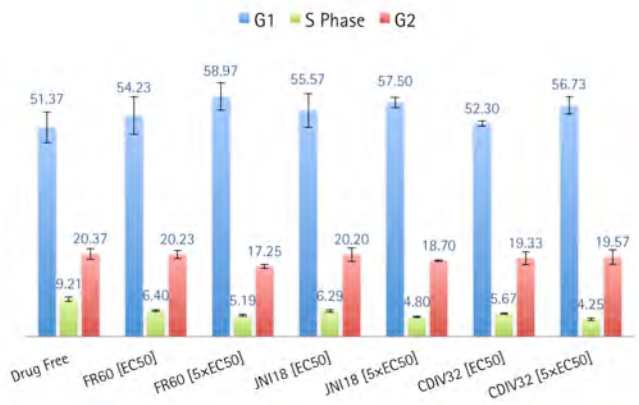

Figure 5-3. Percentage of *T. brucei* 427WT in each stage of the cell cycle after 24 h incubated with the compounds FR60, JNI18 and CDIV32. Parasites were treated with 1× and 5×EC_{50} values of each compound. Error bars show the standard error of the mean for three independent determinations. G1: all cells have one kinetoplast and one nucleus; G2: all cells have two kinetoplast and two nucleus; S phase: DNA synthesis. Untreated cells (Drug Free) as control was included in each assay.

The most outstanding result to emerge from the data is the strong relationship between the S phase and the growth curve (see Figure 5-2). A significant S phase reduction coincides with an inhibition of the growth after 24 h treatment with the drugs. Apparently, the observed decrease of DNA synthesis led to a reduction of growth and finally to a complete arrest of cell proliferation.

To evaluate whether nuclear and/or kinetoplast division was affected and to observe cell cycle progression in detail, the cellular DNA configuration was assessed by fluorescence microscopy using the dye DAPI for compound FR60 and CDIV32 and *SYTOX® Green nuclei acid stain* for compound JNI18 (as this compound fluoresces at a similar wavelength as DAPI). Following the protocol described in section 2.9.4.2, cells exposed to the compounds for 8 h and 24 h were scored into the following standard

groups (Figure 5-4): 1N1K (one nucleus and one kinetoplast), 1N2K (one nucleus and two kinetoplasts), 2N2K-E (two nuclei and two kinetoplasts, but no clear furrow towards cell division), 2N2K-L (two nuclei and two kinetoplasts when cells were almost completely divided into two daughter cells. Another group was added to the classification: 1N/2N (1 or 2 nuclei and no kinetoplast) due to the high incidence of cells with such a DNA configuration after 8h (Figure 5-5a) or 24 h of treatment (Figure 5-5b).

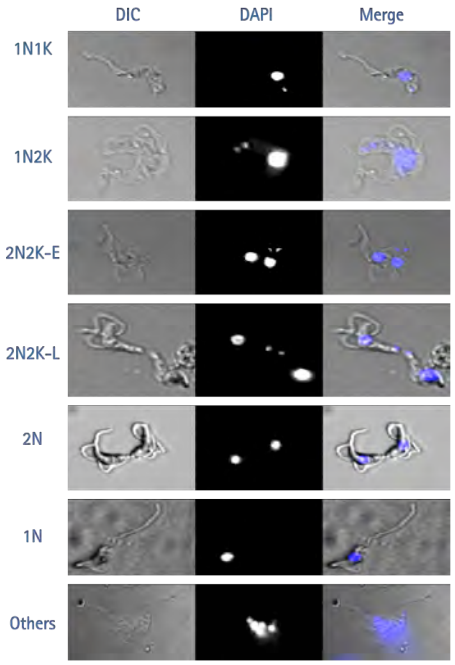

Figure 5-4. Classification of the DNA content analysis. Images taken by the *Zeiss Axioskop 2* fluorescent microscope of Tb427WT cells stained with DAPI. The outline of all cells is shown by DIC imaging. Images were processed using the program *Fiji* (ImageJ). N, nucleus; K, kinetoplast; E, early stage of division; L, late stage of division.

In cells treated with either compound there was a dose-dependent reduction in cells with 1 nucleus and 2 kinetoplasts, indicative of a failure to initiate a new cell division cycle. Similarly, the number of cells in the early stages of cell division, with 2 kinetoplasts and nuclei, was approximately halved after 24 h of exposure to the compounds. At the same time, cells without any kinetoplast (1N/2N) started to appear in the treated populations (about 10% of cells after 24 h of exposure), having

apparently concluded mitosis despite the non-division of the kinetoplasts. In addition, completely aberrant cells ('others') also appeared in the treated cultures, which typically contained DNA fragmentation, multiple nuclei and/or kinetoplasts, or none at all. The combined evidence shows that the three compounds tested affect the normal progression of the *T. brucei* cell cycle, most likely by preventing kinetoplast division.

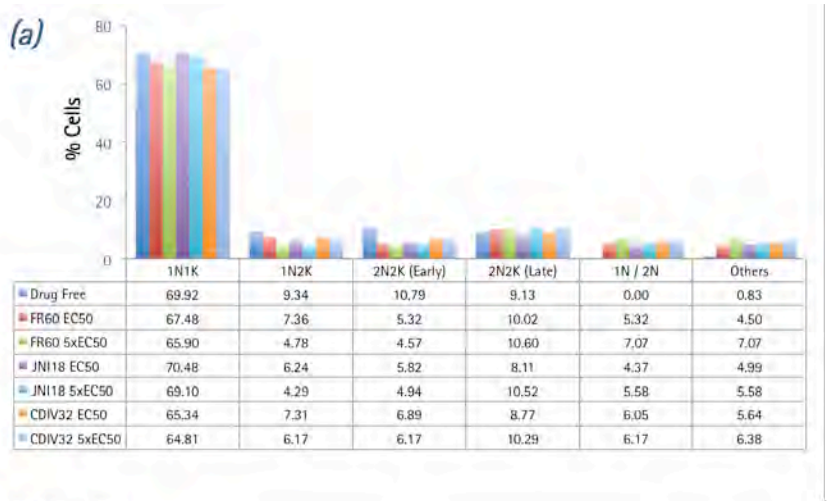

	1N1K	1N2K	2N2K (Early)	2N2K (Late)	1N / 2N	Others
Drug Free	69.92	9.34	10.79	9.13	0.00	0.83
FR60 EC50	67.48	7.36	5.32	10.02	5.32	4.50
FR60 5xEC50	65.90	4.78	4.57	10.60	7.07	7.07
JNI18 EC50	70.48	6.24	5.82	8.11	4.37	4.99
JNI18 5xEC50	69.10	4.29	4.94	10.52	5.58	5.58
CDIV32 EC50	65.34	7.31	6.89	8.77	6.05	5.64
CDIV32 5xEC50	64.81	6.17	6.17	10.29	6.17	6.38

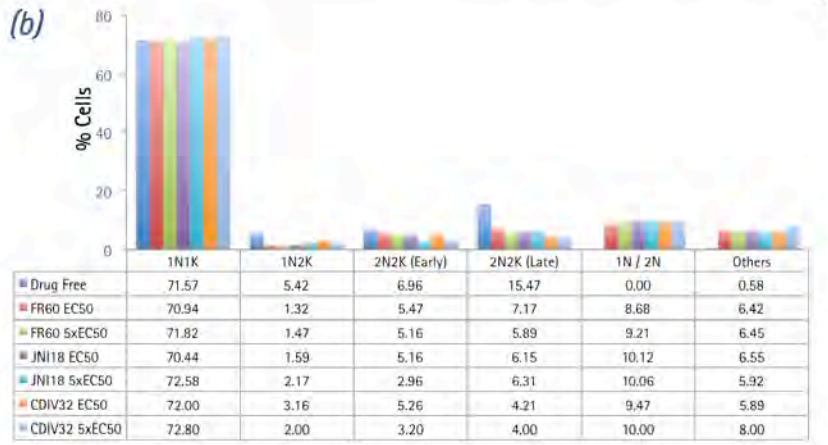

	1N1K	1N2K	2N2K (Early)	2N2K (Late)	1N / 2N	Others
Drug Free	71.57	5.42	6.96	15.47	0.00	0.58
FR60 EC50	70.94	1.32	5.47	7.17	8.68	6.42
FR60 5xEC50	71.82	1.47	5.16	5.89	9.21	6.45
JNI18 EC50	70.44	1.59	5.16	6.15	10.12	6.55
JNI18 5xEC50	72.58	2.17	2.96	6.31	10.06	5.92
CDIV32 EC50	72.00	3.16	5.26	4.21	9.47	5.89
CDIV32 5xEC50	72.80	2.00	3.20	4.00	10.00	8.00

Figure 5-5. DNA content of cells treated *(a)* 8 and *(b)* 24 h with compounds FR60, JNI18 and CDIV32 at 1× and 5× EC_{50} as determined by fluorescence microscopy. For each sample, about 500 cells were counted and scored in terms of nuclei and kinetoplasts. N, nucleus; K, kinetoplast; 1N/2N, cells with one or two nuclei but no observable kinetoplastid. E, early stage of division; L, late stage of division.

5.4 Cellular Localization of the Compound JNI18

To study the cellular distribution of the bis(2-aminoimidazolinium) compounds, cells were incubated with the fluorescent compound JNI18 (emission: 450 nm), using the green-fluorescent *SYTOX® Green nucleic acid stain* (excitation/emission: 504/523 nm) to visualize the nuclei and kinetoplasts. The *T. brucei* mitochondrion was further visualized with the red-fluorescent dye *MitoTracker Red CMXRos* (excitation/emission: 579/599 nm), which produces a highly specific stain of *T. brucei* mitochondria (Vassella et al., 1997; Huang et al., 2013).

After 3 h of exposure, compound JNI18 can just be detected inside of the cell but no particular distribution is discernible (Figure 5-6). After 6 h, compound JNI18 shows a homogeneous distribution throughout the cytoplasm, and is becoming concentrated in the mitochondria. At that moment, the kinetoplast is no longer visible in many of the cells, although the *SYTOX® Green* still strongly highlights the nuclei. After 24 h of treatment, drug JNI18 seems to be even more concentrated in the mitochondrion with intense spots of the fluorescence coinciding with the most intense *MitoTracker* staining; kinetoplast staining with *SYTOX® Green* was absent from almost all cells.

In untreated cells grown in parallel, no changes in fluorescence were observed at the blue wavelength that visualized JNI18, and normal kinetoplast staining with *SYTOX® Green* was visualized (see Appendix F).

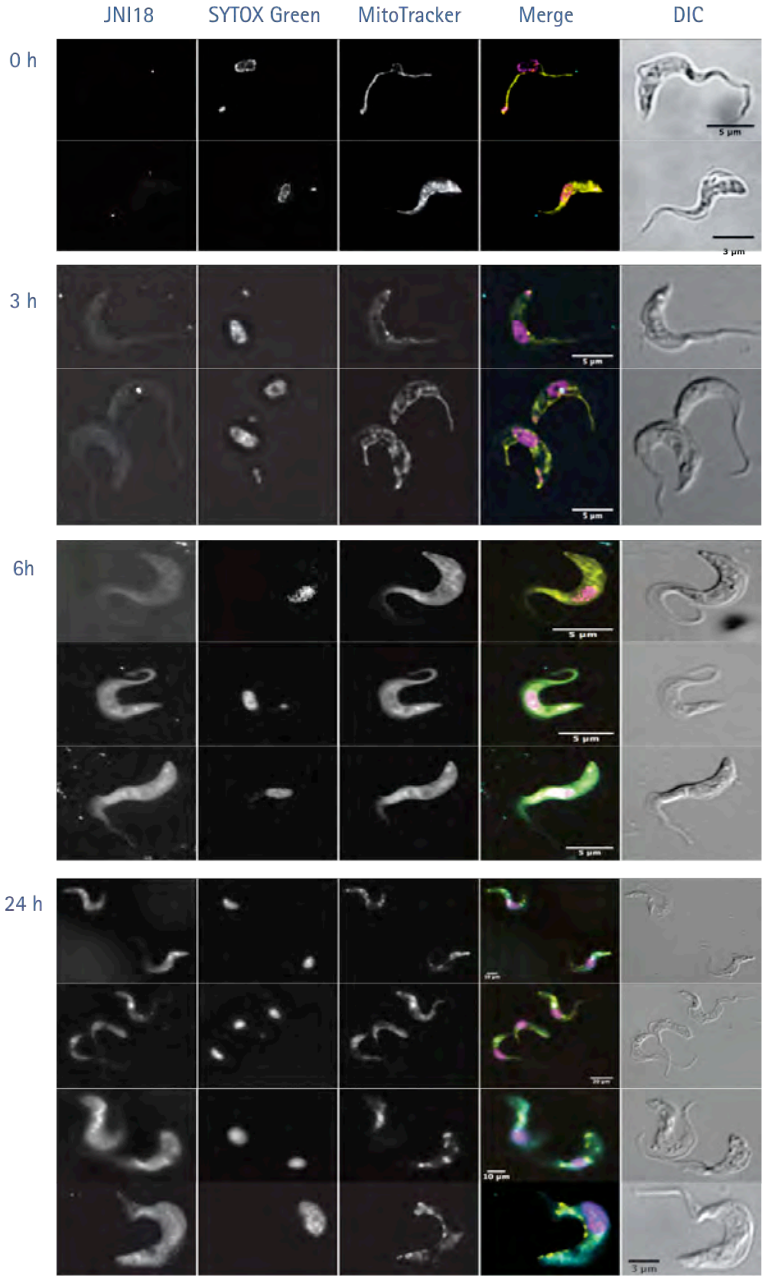

Figure 5-6. Fluorescence localization of the JNI18 in *Trypanosoma brucei* 427WT cells. Images were taken at 0, 3, 6 and 24 h of incubation with 5 µM compound JNI18. All fluorescent images are shown with compound 2 (λ=450, blue channel), *SYTOX Green* (λ=523, green channel), *MitoTracker* (λ=599, red channel), and merge, where arbitrary colours were used to visualise the various dyes: blue for JNI18, purple for *SYTOX*, yellow for *Mitotracker*. The outline of all cells is shown by differential interference contrast (DIC) imaging. Images were acquired using a *DeltaVision* imaging system and deconvolved using the ratio conservative method, on *SoftWoRx* software.

5.5 Effect of the Bis(2-aminoimidazoline) Derivatives on the Mitochondrial Membrane Potential of *T. brucei*

In order to investigate whether the compounds affect the mitochondrial function of the *Trypanosome brucei*, flow cytometry was carried out. Bloodstream forms of *T. brucei* were cultured for up to 12 h in the presence and absence of compounds FR60, JNI18 and CDIV32. Samples were taken at 0, 3, 6 and 12 h of incubation. The quantitative changes in the mitochondrial membrane potential were measured by using tetramethylrhodamine ethyl ester (TMRE) following the protocol described in section 2.9.5. A shift to higher fluorescence indicates an increase of Ψm (hyperpolarisation), whereas a shift to lower fluorescence indicates a decrease of Ψm (depolarization) (Denninger et al., 2007). Valinomycin was used as control for depolarization and troglitazone as control for hyperpolarization. Samples were analyzed via flow cytometry by using a FL2-height detector and data were processed with CellQuest and FlowJo software.

The summary of the results of three independent determinations of TMRE fluorescence of treated and untreated cells with FR60, JNI18 and CDIV32 for 3, 6 and 12 h is shown as a line graph in Figure 5-7. Histograms from the three determinations performed are shown Appendix F. Values are given as the percentage of cells with fluorescence above 100 arbitrary units (AU), which was set to approximately 50% for the controls. A shift to higher fluorescence signifies increased Ψ_m; lower fluorescence signifies depolarization of the mitochondrial membrane; for the untreated cell culture, Ψ_m remained stable for the duration of the experiment, at approximately 50%.

As expected, Ψm for untreated cells was remained unaffected throughout the 12 h experiment. In contrast, valinomycin rapidly induced a deep depolarization of the mitochondrial membrane while troglitazone induced a clear hyperpolarisation.

Compounds FR60 and JNI18 acted in a dose dependent form, progressively reducing Ψ_m, with only minor effects at 3 h but significantly progressing by 6 h, and a clear,

dose-dependent depolarization of the Ψ_m evident at 12 h (Figure 5-7). Slightly more significant Ψ_m depolarization was caused by the compound CDIV32 at 3 h, and more significant by 6 h as compared to the other two compounds, causing a depolarization of about 30% an 60% when parasites are treated with 1× and 5× EC_{50} concentrations, respectively. At 12 h, CDIV32 induced a deep Ψ_m depolarization of *T. brucei* (Figure 5-8).

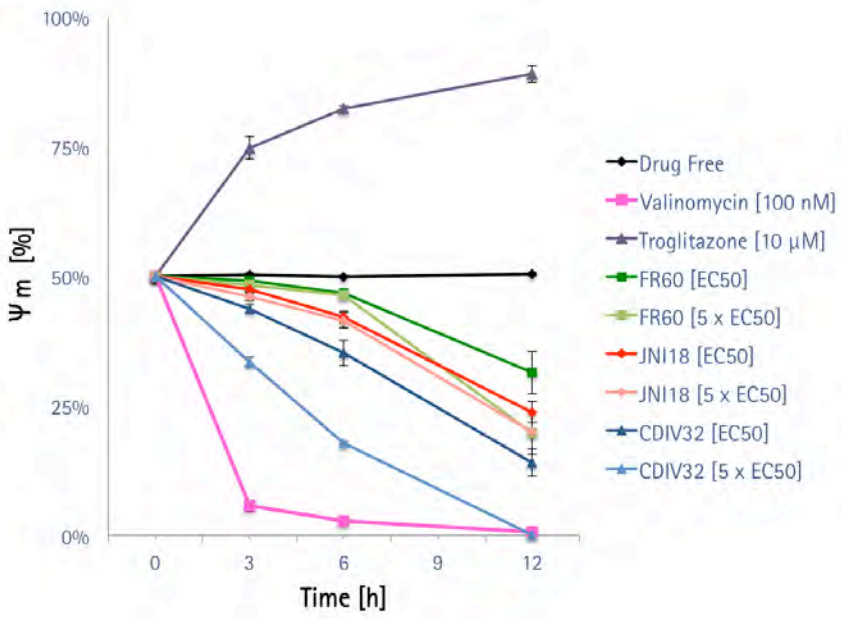

Figure 5-7. Effect of compounds FR60, JNI18 and CDIV32 on mitochondrial membrane potential (Ψ_m) of *T. b. brucei* 427WT. The results shown are the mean of three independent determinations; error bars depict standard errors. Untreated cells (drug free), valinomycin (depolarization) and troglitazone (hyperpolarization) are employed as controls.

The data are consistent with mitochondrial targeting of the compounds as cations, but their effect on the membrane potential is slower than has been reported for some other compounds such as bisphosphonium salts, which appeared to impact directly on the F_oF_1-ATPase (Alkhaldi et al., 2016).

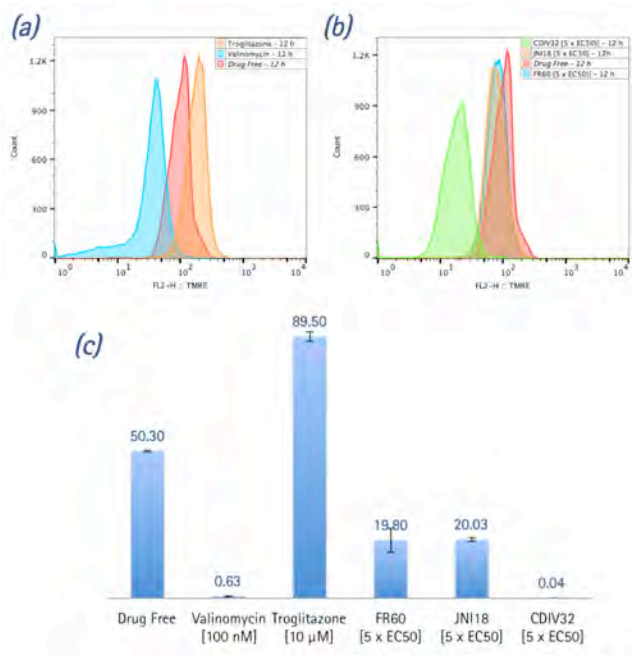

Figure 5-8. Superposed histograms of *T. b. brucei* 427WT mitochondrial membrane potential (Ψm) assay after 12 h incubation for *(a)* the controls: drug free, valinomycin and troglitazone and *(b)* with the compounds FR60, JNI18 and CDIV32 at 5×EC_{50} concentrations. *(c)* Graph bar with Ψm percentage of cells treated 12 h with the compounds with fluorescence above the 100 AU (50% of untreated cells). The results shown are the mean of three independent determinations; error bars depict standard errors.

5.6 PCR Amplification of Kinetoplast DNA Markers

In order to determine whether the mitochondrial genome of *T. brucei* had been completely eliminated when parasites were treated with the compound JNI18, rendering it undetectable by DAPI staining, DNA was extracted and subjected to PCR analysis. Fragments of 4 genes known to be encoded only by the kinetoplast maxicircles, two representative minicircles genes and two nuclearly-encoded genes were specifically amplified from parental Tb427WT DNA and PCR detected in treated tripanosomes.

Entire genome from trypanosomes exposed with 5 µM JNI18 for 0, 3, 6, 9, 12, 24 and 32 h were purified and forward and reverse PCR primers described in Table 2-15 were used following the protocol described in section 2.9.8. PCR products were run on 1% agarose gel to observe the PCR products (Figure 5-9).

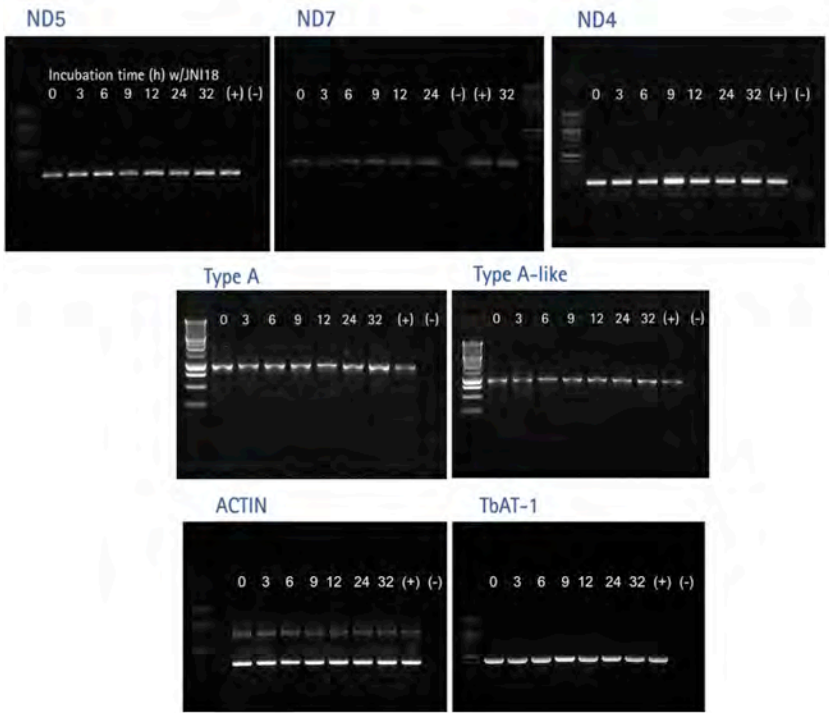

Figure 5-9. PCR amplification of the maxicircles genes ND5, ND7 and ND4; minicircles genes Type A and Type A –like; nuclearly encoded actin & TbAT-1 gene as a positive control for a nuclearly-encoded single copy gene from *Trypanosoma brucei* 427WT. Time of exposure with the compound JNI18 is indicated above of each band. (-) Negative control (no DNA in the PCR sample). (+) Positive control of Tb427-WT DNA.

Figure 5-9 shows that both kinetoplast and nuclear DNA standard markers were amplified by PCR even after 32 h exposure with compound JNI18. Nevertheless, no information was provided about the abundance or organisation of these genes in the cell, which was therefore further investigated using Transmission Electron Microscopy (TEM).

5.7 Effect of Compounds FR60 and JNI18 on the Kinetoplast Network

Transmission Electron Microscopy (TEM) was used to study the trypanosomes' ultrastructure after exposure to 5 µM compounds FR60 and JNI18, in order to analyze the effects of these compounds on the cellular structure of the parasite. Based on the information obtained with the cellular localization of the compounds in the cell by fluorescence microscopy (see section 5.4), TEM samples were taken after 3 h and 24 h incubation, as 'early' and 'late' time points to determine the structural effects of the compounds.

Figure 5-10 shows the TEM images for untreated cells (drug free control) after 3 and 24 h of experiment. Kinetoplast appears normal in all the cases.

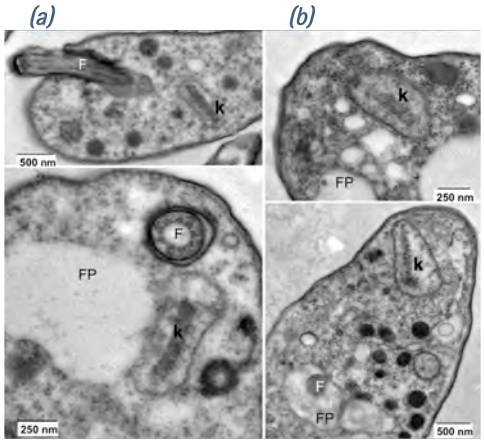

Figure 5-10. TEM images showing normal ultrastructure of untreated cells of Tb427WT after *(a)* 3 h of experiment and *(b)* 24 h. F, flagellum, FP, flagellum pocket, k, kinetoplast. Images were observed in a Tecnai T20 (FEI) at 200 kV.

Analyzing the images obtained with TEM of cells treated 3 h (Figure 5-11) and 24 h (Figure 5-12), it can be confirmed that compounds FR60 and JNI18 have the same mechanism of action in the cell. Both compounds cause ultrastructural abnormalities in the kinetoplast, which were clearly far more severe at 24 h than at 3 h of incubation, when many cells appeared still undamaged, i.e., the drug has not yet impacted on the kinetoplast (top row images, Figure 5-11). However, different cells in the same

population show dark dots or empty space inside the kinetoplast (bottom row; arrows indicate the abnormalities), which confirm an initial level of damage in the kDNA of some cells during the first 3 h exposure with the compounds.

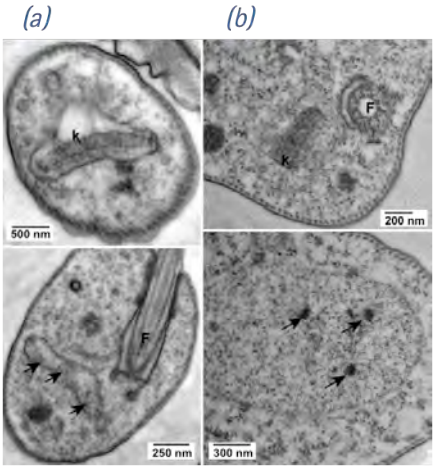

Figure 5-11. TEM images showing cells of Tb427WT treated with *(a)* FR60 and *(b)* JNI18 for 3 h. F, flagellum, k, kinetoplast. Images were observed in a Tecnai T20 (FEI) at 200 kV. Irregular structures in the kinetoplast are shown with arrows and arrowheads, indicating kDNA damage.

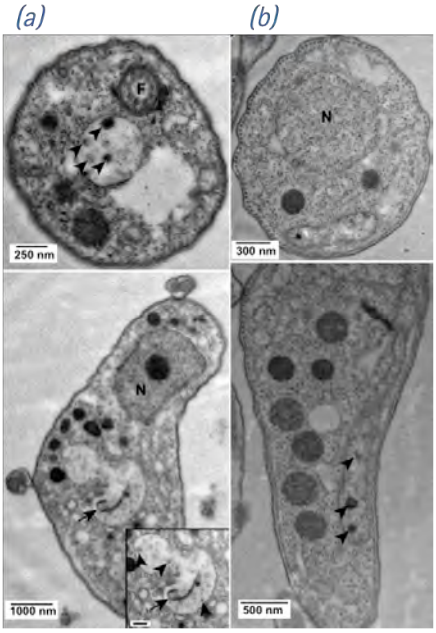

Figure 5-12. TEM images showing cells of Tb427WT treated with *(a)* FR60 and *(b)* JNI18 for 24 h. F, flagellum, k, kinetoplast. Images were observed in a Tecnai T20 (FEI) at 200 kV. Irregular structures in the kinetoplast are shown with arrows and arrowheads, indicating kDNA severe damage.

After 24 h of treatment with compounds FR60 and JNI18, all cells displayed clear damage to kinetoplasts, which has completely lost the characteristic disk-like structure of uniform electron-density, a structure of intercalating minicircles and maxicircles that is essential for both the functioning and replication of the kinetoplast (Povelones, 2014). This is completely consistent with the lack of kDNA staining observed with SYTOX Green (see Figure 5-6). Since no other structures were found to be affected at 24 h but only the mitochondrial DNA is largely absent and completely disorganised, it can be concluded that they directly affect the kinetoplast.

5.8 *In vivo* Activity in a Mouse Model of First Stage HAT

In vivo efficacy studies were conducted at the Swiss Tropical and Public Health Institute (Basel) according to the rules and regulations for the protection of animal rights of the Swiss 'Bundesant für Veterinärwesen'. They were approved by the veterinary office of Canton Basel-stadt, Switzerland.

The *in vivo* activity of FR60, assessed before this research work, showed that this compound is 100% curative in the STIB900 mouse model of acute *T. b. rhodesiense* infection by intraperitoneal (4×5 mg/kg/day) and oral (4×50 mg/kg/day) dosage (Ríos Martínez el at., 2015c; Rodríguez et al., 2008).

During this work, the *in vivo* activity of JNI18 against *T. b. rhodesiense* was assessed in the same mouse model. For that reason, JNI18 was administered to a group of four female NMRI mice by intraperitoneal route using a 4-day treatment regimen of 20 mg/kg/day using a previously reported protocol described in Ríos Martínez et al., 2014. Parasitemia was monitored over a 60-day observation period. Mice were considered cured when no relapse was detected in the tail blood over the observation period.

The intraperitoneal administration of JNI18 at 4×4 mg/kg/day increased the mean day of relapse of parasitemia (17.5 days) in mice although no cures were obtained. However, a 5-fold higher dosage (4×20 mg/kg/day i.p.) provided a 100% cure rate in this mouse model of stage 1 HAT.

5.9 GENERAL DISCUSSION

Trypanocidal dications such as diamidines and bisimidazolinium compounds have long been speculated to act on mitochondrial targets (Lanteri et al., 2008; Roy Chowdhury et al., 2010) and some clearly bind to DNA (see section 1.6.1.1). However, although their abilities to act as minor groove binding drugs (MGBD) are well established, it is much less clear whether this is necessarily the principal trypanocidal mode of action, and whether binding to kDNA and/or nuclear DNA contributes most to cell death. In this chapter is presented the most comprehensive analysis to date that one class of aromatic dications, the bis(2-aminoimidazolines), directly act on the kinetoplast.

Significant resistance (>100-fold) by the dyskinetoplastic cell line ISMR1, relative to the wild type cell line, indicated the kinetoplast as a probable target of compounds FR60 and JNI18. Moreover, a study of the *T. brucei* cell cycle by flow cytometry showed that incubation with the FR60, JNI18 and CDIV32 compounds caused a progressive cell cycle arrest in G1 phase, reflected in the major decrease in S-phase cells after 24 h. The failure to initiate DNA synthesis was almost certainly the result of damage to the kinetoplast, as kDNA division necessarily precedes nuclear division (McKean, 2003), and both fluorescence microscopy and TEM showed major damage to the kinetoplast but not to the nucleus. Starting at just 8 h, as fluorescent compound JNI18 had accumulated in the mitochondrion, significant numbers of cells were found without an observable kinetoplast or with one kinetoplast and two, or even three nuclei, which clearly evidence a defect in kinetoplast replication. By 24 hours this was leading to the gross destruction and/or disorganisation of the kinetoplast as observed by TEM and concomitant growth arrest. Importantly, the electron microscopy did not reveal any damage to the nuclei or other cellular structures.

Despite the absence of ultrastructural damage to the mitochondrion, Ψ_m began to decrease from 6 h of incubation. In bloodstream trypanosomes, which lack the common oxidative phosphorylation complexes, Ψ_m is generated by the F_oF_1 ATPase pumping protons from the mitochondrial matrix, using ATP (Dean, et al., 2013; Schnaufer et al., 2005; Bhat et al., 1990) clearly this process would progressively be

impeded as the lack of functional kDNA precludes the production of the A6 subunit of F_o, leading to the slow membrane depolarization observed. Accumulation of cationic compounds in the mitochondria, driven by the negative electrostatic potential (negative inside), is a well-described phenomenon for cationic and dicationic compounds (Ibrahim et al., 2011; Alkhaldi et al., 2016; Fueyo Gonzalez et al., 2017) but the relatively slow effect of compounds FR60 and JNI18 on the Ψ_m compared with CDIV32, and with that of compounds that act directly on the F_1F_0-ATPase complex (Alkhaldi et al., 2016) is consistent with the hypothesis that the antiparasitic effect derives from preventing the accurate replication of kDNA and consequently the assembly of F_0.

Altogether, these results show that the *N*-phenylbenzamide bis(2-aminoimidazolinium) compounds FR60 and JNI18 act specifically on the kinetoplast DNA of the *T. brucei* by altering its structure and replication.

Finally, the *in vivo* screening for trypanocidal activity against *Trypanosoma brucei rhodesiense* of compounds FR60 and JNI18 showed, for both compounds, 100% curative action in a mouse model of first stage Human African Trypanosomiasis (HAT).

CONCLUSIONS

CONCLUSIONS

Part I. DNA–ligand interactions

1. HMGA1a (Δ50-91) as well as HMGB1 box B and HMGB1 box AB fragments were expressed in *E. coli* strain Rosetta (DE3) pLysS and purified.

2. A clear supercoiling effect on circular DNA was induced by HMGA1a (Δ50-91), demonstrating its functionality and unwinding activity.

3. Surface plasmon resonance (SPR) successfully demonstrated a strong binding affinity of the HMGA1a and HMGB proteins towards an immobilized AT-rich DNA oligonucleotide containing [AATAAT_ATTATT]. The K_D was found similar and in the low micromolar range for both proteins (K_D =0.35 × 10^{-6} M and K_D =0.33 × 10^{-6} M, respectively).

4. After more than 100 crystallization assays with 6 different AT-rich oligonucleotides and the protein HMGA1a (Δ50-91), the appropriate crystallization condition was not found.

5. Numerous crystallization trials with the HMGB box B and 10 different AT-rich oligonucleotides were performed, from which 20 crystals suitable for X-ray crystallography were diffracted.

6. A crystal of HMGB1 box B in complex with the 20 bp oligonucleotide d[CCAATAATCGCGATTATTGG]$_2$ diffracted to 2.68 Å resolution, presented well-defined spots revealing two diffraction orientations. The space group was $P22_12_1$ with a = 29.94 Å, b = 89.65 Å, c = 109.1 Å, α = β = γ = 90°.

7. The capacity of bis(2-aminoimidazoline) compounds to selectively bind AT-rich sequences over CG-containing DNA was confirmed by SPR. All K_D were found in the submicromolar range.

8. Compound JNI18 was able to displace the HMG proteins from their DNA binding sites, showing IC_{50} values for inhibition of binding of 6.0 µM and 3.4 µM for HMGA1a and HMGB1, respectively.

9. Several crystallization trials with the bis(2-aminoimidazolines) FR60, JNI18 and CDIV32 and 10 different AT-rich oligonucleotides permitted the diffraction of about 50 crystals suitable for X-ray crystallography.

10. The compound CDIV32 in complex with the all-AT oligonucleotide $d[AAATTT]_2$ was crystallized in a pseudo-continuous helix, packed in a crossed column configuration. Sixteen stacked oligonucleotides with average helical twist of about -25° conformed the asymmetrical unit. The cell parameters were a = 62.79 Å, b = 451.08 Å and c = 80.93 Å; $\alpha = \beta = \gamma = 90°$ in $C222_1$ space group. The drug modulates the crossed helical arrangement. Pseudo translational symmetry detected in the crystal impeded complete resolution of the structure.

11. Crystal structure of the FR60-$d[AAATTT]_2$ complex at atomic resolution of 1.25 Å revealed important features: FR60 interacts in the middle of the DNA duplex, the central [AATT] sequence; it fills the minor groove of the all-AT oligonucleotide and displaces water from the hydration spine. The drug also protrudes from DNA, forming hydrogen bond interactions with phosphates from neighboring DNA molecules acting as a cross-linking agent. This originates the packing in a pseudo-tetragonal configuration.

Part II. Functional analysis of the effect of bis(2-aminoimidazoline) compounds on *Trypanosoma brucei*

1. *In vitro* drug sensitivity assays established that *T. brucei* isometamidium-adapted dyskinetoplastic cell line ISMRI was highly resistant to compounds FR60 and JNI18 when EC_{50} values were compared to those of the *Trypanosoma brucei* Tb427 wild type strain, pointing to kDNA as a target for these compounds.

2. A series of FR60 derivatives and CDIV32 dose-dependently reduced the *T. brucei* growth rates and, at concentrations above EC_{50} appeared to induce growth arrest after 24 h.

3. Bis(2-aminoimidazolines) FR60, JNI18 and CDIV32 caused a progressive cell cycle arrest in G1 phase, as reflected by a major decrease in S-phase cells after 24 h.

4. Failure to initiate a new cell division cycle in treated *T. brucei* was confirmed by the reduction of cell population replicating the kinetoplast (kDNA).

5. FR60 and JNI18 drugs caused a slow decline in mitochondrial membrane potential (Ψ_m) of *T. brucei*, showing its partial depolarization after a 12 h exposure. Compound CDIV32 reduced the Ψ_m more strongly at 6 h exposure, and completely after 12 h of treatment.

6. Fluorescent compound JNI18 (a chloro derivative of the lead FR60) tended to accumulate in the mitochondrion of *T. brucei*. Cells showed a homogeneous distribution throughout the cytoplasm after 6 h of treatment with the drug, but a visible accumulation in the mitochondrion after 24 h exposure.

7. TEM images of trypanosomes treated with FR60 and JNI18 showed dark dots or empty space inside the kinetoplast, confirming initial kDNA damage. After 24 h, kinetoplast was largely absent and completely disorganized. No damage to the nuclei or other cellular structures was displayed.

8. Compounds JNI18 and FR60 share the same mechanism of action and cellular target against *Trypanosoma brucei*, acting specifically on the integrity of the kinetoplast by altering the structure and replication of kDNA. Direct effect on kinetoplast DNA causing the destruction of the network was confirmed.

9. As both compounds showed 100% curative activity in a mouse model of *T. brucei rhodesiense* infection, they have a potential as effective chemotherapeutic agents for the treatment of sleeping sickness.

PUBLICATION RELATED TO THIS THESIS

Millan, C. R., Acosta-Reyes, F. J., Lagartera, L., Ebiloma, G. U., Lemgruber, L., Nué Martínez, J. J., Saperas, N., Dardonville, C., de Koning, H. P., & Campos, J. L. (2017). Functional and structural analysis of AT-specific minor groove binders that disrupt DNA–protein interactions and cause disintegration of the *Trypanosoma brucei* kinetoplast. *Nucleic Acids Research*. https://doi.org/10.1093/nar/gkx521

ABSTRACT

Trypanosoma brucei, the causative agent of sleeping sickness (Human African Trypanosomiasis, HAT), contains a kinetoplast with the mitochondrial DNA (kDNA), comprising of >70% AT base pairs. This has prompted studies of drugs interacting with AT-rich DNA, such as the N-phenylbenzamide bis(2-aminoimidazoline) derivatives 1 [4-((4,5-dihydro-1Himidazol-2-yl)amino)-N-(4-((4,5-dihydro-1H-imidazol-2-yl)amino) phenyl)benzamide dihydrochloride] and 2 [N-(3-chloro-4-((4,5-dihydro-1H-imidazol-2-yl)amino)phenyl)-4-((4,5-dihydro-1H-imidazol-2-yl)amino)benzamide] as potential drugs for HAT. Both compounds show *in vitro* effects against *T. brucei* and *in vivo* curative activity in a mouse model of HAT. The main objective was to identify their cellular target inside the parasite. We were able to demonstrate that the compounds have a clear effect on the S-phase of *T. brucei* cell cycle by inflicting specific damage on the kinetoplast. Surface plasmon resonance (SPR)–biosensor experiments show that the drug can displace HMG box-containing proteins essential for kDNA function from their kDNA binding sites. The crystal structure of the complex of the oligonucleotide d[AAATTT]2 with compound 1 solved at 1.25 °A (PDB-ID: 5LIT) shows that the drug covers the minor groove of DNA, displaces bound water and interacts with neighbouring DNA molecules as a cross-linking agent. We conclude that 1 and 2 are powerful trypanocides that act directly on the kinetoplast, a structure unique to the order Kinetoplastida.

APPENDIXES

APPENDIXES

Appendix A

IPTG INDUCTION OF PROTEIN EXPRESSION

Isopropyl β-D-1-thiogalactopyranoside (IPTG) is a molecular mimic of allolactose, a lactose metabolite that triggers transcription of the lac operon, and it is therefore used to induce recombinant protein expression where the gene is under the control of the lac operator.

Usually, the gene of interest is inserted into a commercial vector pET that contains: (1) a gene coding for antibiotic resistance (e.g. amp^R); (2) the lacI gene (lac I^q) from the lac operon that codes for the lac repressor (LacI); and (3) the gene of interest inserted just after the T7 promoter DNA sequence, the lac operator DNA sequence, and the ribosome binding site (at the start of the future mRNA transcript).

The lac repressor protein (LacI) evolved to sense the presence of lactose. In the absence of lactose, the lac repressor binds to the operator sequence on DNA and bends the DNA by 40° (as seen in the crystal structure PDB ID: 1EFA). This blocks access of T7 RNA polymerase to the promoter site and thus prevents leaky transcription of the gene before induction.

When lactose binds to LacI it induces a conformational change in the protein structure that renders it incapable of binding to the operator DNA sequence. IPTG, like allolactose, also binds to the lac repressor and induces a similar conformational change (PDB ID: 2P9H) that greatly reduces its affinity for DNA. Unlike lactose, IPTG is not part of any metabolic pathways and so will not be broken down or used by the cell. This ensures that the concentration of IPTG added remains constant, making it a more useful inducer of the lac operon than lactose itself.

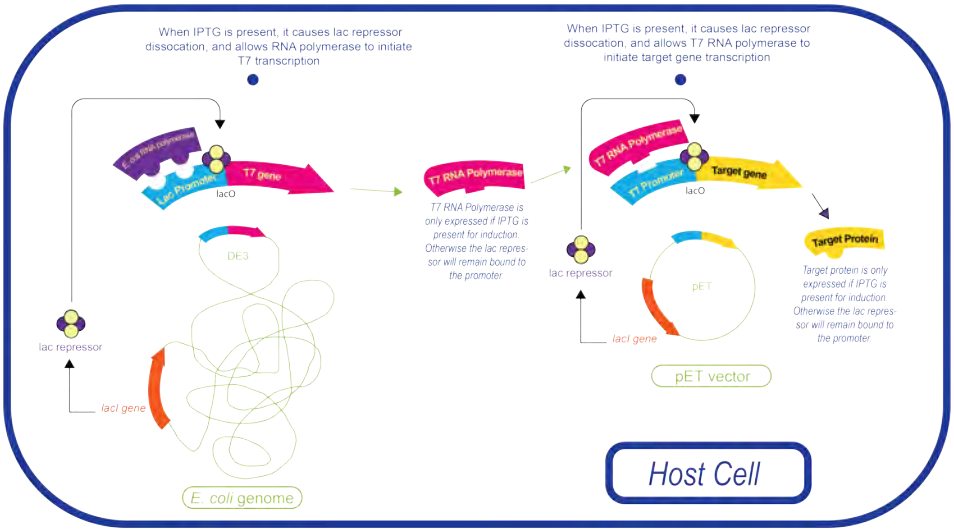

Figure A1. Mechanism of action of the IPTG induction. Image taken from https://www.goldbio.com/blog/493/a-deep-dive-into-iptg-induction.

Appendix B

CULTURE MEDIA

- HMI-9 medium (10% FCS)

A pack of HMI-9 powder (Gibco®) was emptied into a 5-litre capacity beaker, followed by 4.5 L of ddH_2O and 15 g of $NaHCO_3$. After stirring on a magnetic stirrer for about 1 h at room temperature, 500 mL of FBS (Fetal Bovine Serum; Gibco®) and 71.5 µl of β-mercaptoethanol were added. The solution was left stirring overnight at 4°C. The pH was adjusted to 7.4 the next day. Finally, the media was filtered into 10 sterile 500 ml reagent bottles and stored at 4°C.

- TcBCF-3 medium

Table B-1. *Trypanosoma congolense* culture media TcBCF-3 composition.

Basal medium (mM)									Supplements (mM)		Serum (% v/v)	
Base powder	Hep	Gluc	Pyr	Ade	Hypo	Thy	Bac	Gln	2 Me	RBC	FGS	SP
MEM	25	5.5	1	0.04	0.1	0.02	0.02	2	0.2	0.5	20	5

MEM, Eagle's Minimum Essential Medium powder medium (M0643, Sigma-Aldrich), supplemented with 2.2 g of sodium bicarbonate (Sigma-Aldrich). Basal medium components were resuspended in 1 L Versol water (Revol, Villeurbanne) and after adjustment of the pH to 7.3 with 5 N NaOH, the medium was filter sterilized (Millipore 0.22 um), stored at 4°C and used within 10 days. Before use, basal medium was supplemented with the components listed (Sigma-Aldrich) and serum. Hep, HEPES Acid; Gluc, D-Glucose; Pyr, Sodium Pyruvate; Ade, Adenosine; Hypo, Hypoxanthine; Thy, Thymidine; Bac, Bathocuproin; Gln, Glutamine; 2 Me, 2-mercaptoethanol. RBC, Red Blood Cell lysate was obtained after centrifugation (1 min 2000 rpm) of 100 µl of mouse blood, and resuspending of the pellet in 50 µl sterile distilled water. FGS, Fresh Goat Serum; SP, Serum Plus (SAFC Biosciences, United Kingdom).

BUFFER SOLUTIONS

Table B-2. Hanks' Balanced Salt Solution (HBSS) formulation.

Components	Molecular Weight	Concentration	
		[mg/L]	[mM]
Inorganic Salts			
Calcium Chloride ($CaCl_2$) (anhyd.)	111.0	140.0	1.2612612
Magnesium Chloride ($MgCl_2$-$6H_2O$)	203.0	100.0	0.49261084
Magnesium Sulfate ($MgSO_4$-$7H_2O$)	246.0	100.0	0.40650406
Potassium Chloride (KCl)	75.0	400.0	5.3333335
Potassium Phosphate monobasic (KH_2PO_4)	136.0	60.0	0.44117647
Sodium Bicarbonate ($NaHCO_3$)	84.0	350.0	4.1666665
Sodium Chloride (NaCl)	58.0	8000.0	137.93103
Sodium Phosphate dibasic (Na_2HPO_4) anhydrous	142.0	48.0	0.33802816
Other Components			
D-Glucose (Dextrose)	180.0	1000.0	5.5555553

HBSS, calcium, magnesium, no phenol red. Hanks & Wallace, 1949.

Table B-3. Electrophoresis buffers.

Buffer	Working Solution	Stock Solution [per 1 L]
TAE	**1×** 40 mM Tris-acetate 1 mM EDTA	**50x** 242 g Tris base 57.1 mL of glacial acetic acid 100 mL of 0.5 M EDTA (pH 8.0)
TPE	**1×** 90 mM Tris-phosphate 2 mM EDTA	**10x** 108 g Tris base 15.5 mL of phosphoric acid (85%, 1.679 g/mL) 40 mL of 0.5 M EDTA (pH 8.0)
TBE	**1×** 90 mM Tris-phosphate 2 mM EDTA	**5×** 54 g Tris base 27.5 g of boric acid 20 mL of 0.5 M EDTA (pH 8.0)

Passing the concentrated buffer stocks through a 0.45-µm filter can prevent or delay formation of precipitates.

Appendix C

RELEVANT SPECIFICATIONS OF THE USED SYNCHROTRON LINE

Beamline Xaloc bl13

- Source type bending magnet
- Energy Range: 5-22 keV
- Wavelength Range: 2.4-0.58 Å
- 12-foil attenuators ESRF type
- Fast shutter: FPS400 CEDRAT
- Slits: JJ-Xray ESRF type
- Automatic Sample Changer: CATS - IRELEC
- Detector: PILATUS 6M - Dectris
- Cryostream: 700 series - Oxford Cryosystems
- Monochromator: Si(111) channel-cut, cryocooled
- KB Mirrors, Elliptically bent mirror (Si, Rh, Ir) (2)

Appendix D

CRYSTALLIZATION CONDITIONS

Table D-1. Crystallization Kit Natrix HR2-116 Hampton.

No.	Composition
1	0.01 M Mg Chloride, 0.05 M MES pH 5.6, 2.0 M Lithium Sulfate
2	0.01 M Mg Acetate, 0.05 M MES pH 5.6, 2.5 M Ammonium Sulfate
3	0.1 M Mg Acetate, 0.05 M MES pH 5.6, 20% MPD
4	0.2 M K Chloride, 0.01 M Mg Sulfate, 0.05 M MES pH 5.6, 10% PEG 400
5	0.2 M K Chloride, 0.01 M Mg Chloride, 0.05 M MES pH 5.6, 5% PEG 8000
6	0.1 M Ammonium Sulfate, 0.01 M Mg Chloride, 0.05 M MES pH 5.6, 20% PEG 8000
7	0.02 M Mg Chloride, 0.05 M MES pH 6.0, 15% iso-Propanol
8	0.005 M Mg Sulfate, 0.1 M Ammonium Acetate, 0.05 M MES pH 6.0, 0.6 M NaCl
9	0.1 M K Chloride, 0.01 M Mg Chloride, 0.05 M MES pH 6.0, 10% PEG 400
10	0.005 M Mg Sulfate, 0.05 M MES pH 6.0, 5% PEG 4000
11	0.01 M Mg Chloride, 0.05 M Na Cacodylate pH 6.0, 1.0 M Lithium Sulfate
12	0.01 M Mg Sulfate, 0.05 M Na Cacodylate pH 6.0, 1.8 M Lithium Sulfate
13	0.015 M Mg Acetate, 0.05 M Na Cacodylate pH 6.0, 1.7 M Ammonium Sulfate
14	0.1 M K Chloride, 0.025 M Mg Chloride, 0.05 M Na Cacodylate pH 6.0, 15% iso-Propanol
15	0.04 M Mg Chloride, 0.05 M Na Cacodylate pH 6.0, 5% MPD
16	0.04 M Mg Acetate, 0.05 M Na Cacodylate pH 6.0, 30% MPD
17	0.2 M K Chloride, 0.01 M Ca Chloride, 0.05 M Na Cacodylate pH 6.0, 10% PEG 4000
18	0.01 M Mg Acetate, 0.05 M Na Cacodylate pH 6.5, 1.3 M Lithium Sulfate
19	0.01 M Mg Sulfate, 0.05 M Na Cacodylate pH 6.5, 2.0 M Ammonium Sulfate
20	0.1 M Ammonium Acetate, 0.015 M Mg Acetate, 0.05 M Na Cacodylate pH 6.5, 10% iso-Propanol
21	0.2 M K Chloride, 0.005 M Mg Chloride, 0.05 M Na Cacodylate pH 6.5, 10% 1,6 Hexanediol
22	0.08 M Mg Acetate, 0.05 M Na Cacodylate pH 6.5, 15% PEG 400
23	0.2 M K Chloride, 0.01 M Mg Chloride, 0.05 M Na Cacodylate pH 6.5, 10% PEG 4000
24	0.2 M Ammonium Acetate, 0.01 M Ca Chloride, 0.05 M Na Cacodylate pH 6.5, 10% PEG 4000
25	0.08 M Mg Acetate, 0.05 M Na Cacodylate pH 6.5, 30% PEG 4000
26	0.2 M K Chloride, 0.1 M Mg Acetate, 0.05 M Na Cacodylate pH 6.5, 10% PEG 8000
27	0.2 M Ammonium Acetate, 0.01 M Mg Acetate, 0.05 M Na Cacodylate pH 6.5, 30% PEG 8000
28	0.05 M Mg Sulfate, 0.05 M HEPES - Na pH 7.0, 1.6 M Lithium Sulfate
29	0.01 M Mg Chloride, 0.05 M HEPES - Na pH 7.0, 4.0 M Lithium Chloride
30	0.01 M Mg Chloride, 0.05 M HEPES - Na pH 7.0, 1.6 M Ammonium Sulfate
31	0.005 M Mg Chloride, 0.05 M HEPES - Na pH 7.0, 25% PEG Monomethyl Ether 550

32	0.2 M KCl, 0.01 M Mg Chloride, 0.05 M HEPES - Na pH 7.0, 20% 1,6 Hexanediol
33	0.2 M Ammonium Chloride, 0.01 M Mg Chloride, 0.05 M HEPES - Na pH 7.0, 30% 1,6 Hexanediol
34	0.1 M K Chloride, 0.005 M Mg Sulfate, 0.05 M HEPES - Na pH 7.0, 15% MPD
35	0.1 M K Chloride, 0.01 M Mg Chloride, 0.05 M HEPES - Na pH 7.0, 5% PEG 400
36	0.1 M K Chloride, 0.01 M Ca Chloride, 0.05 M HEPES - Na pH 7.0, 10% PEG 400
37	0.2 M K Chloride, 0.025 M Mg Sulfate, 0.05 M HEPES - Na pH 7.0, 20% PEG 200
38	0.2 M Ammonium Acetate, 0.15 M Mg Acetate, 0.05 M HEPES - Na pH 7.0, 5% PEG 4000
39	0.1 M Ammonium Acetate, 0.02 M Mg Chloride, 0.05 M HEPES - Na pH 7.0, 5% PEG 8000
40	0.01 M Mg Chloride, 0.05 M Tris HCl pH 7.5, 1.6 M Ammonium Sulfate
41	0.1 M KCl, 0.015 M Mg Chloride, 0.05 M Tris HCl pH 7.5, 10% PEG Monomethyl Ether 550
42	0.01 M Mg Chloride, 0.05 M Tris HCl pH 7.5, 5% iso-Propanol
43	0.01 M Mg Chloride, 0.05 M Ammonium Acetate, 0.05 M Tris HCl pH 7.5, 10% MPD
44	0.2 M K Chloride, 0.05 M Mg Chloride, 0.05 M Tris HCl pH 7.5, 10% PEG 4000
45	0.025 M Mg Sulfate, 0.05 M Tris HCl pH 8.5, 1.8 M Ammonium Sulfate
46	0.005 M Mg Sulfate, 0.05 M Tris HCl pH 8.5, 35% 1,6 Hexanediol
47	0.1 M K Chloride, 0.01 M Mg Chloride, 0.05 M Tris HCl pH 8.5, 30% PEG 400
48	0.01 M Ca Chloride, 0.2 M Ammonium Chloride, 0.05 M Tris HCl pH 8.5, 30% PEG 4000

Table D-2. Crystallization conditions for DNA-HMG protein complex.

Name	Ion	Buffer	pH	Precipitants	Additive
C1	10 mM $NH_4(OAc)$	25 mM NaCac	6	3% PEG 3350	1 mM DTT
C2	10 mM $NH_4(OAc)$	25 mM NaCac	6	5% MPD	1 mM DTT
C3	10 mM $Mg(OAc)_2$	25 mM NaCac	6	3% PEG 3350	1 mM DTT
C4	10 mM $Mg(OAc)_2$	25 mM NaCac	6	5% MPD	1 mM DTT
C5	10 mM $MgCl_2$	25 mM NaCac	6	3% PEG 3350	1 mM DTT
C6	10 mM $MgCl_2$	25 mM NaCac	6	5% MPD	1 mM DTT
C7	10 mM $CaCl_2$	25 mM NaCac	6	3% PEG 3350	1 mM DTT
C8	10 mM $CaCl_2$	25 mM NaCac	6	5% MPD	1 mM DTT
C9	12.5 mM $MgCl_2$	25 mM NaCac	6	5% MPD	1 mM DTT
C10	7.5 mM $MgCl_2$	25 mM NaCac	6	5% MPD	1 mM DTT
T1	10 mM $NH_4(OAc)$	25 mM Tris-HCl	7.5	3% PEG 3350	1 mM DTT
T2	10 mM $NH_4(OAc)$	25 mM Tris-HCl	7.5	5% MPD	1 mM DTT
T3	10 mM $Mg(OAc)_2$	25 mM Tris-HCl	7.5	3% PEG 3350	1 mM DTT
T4	10 mM $Mg(OAc)_2$	25 mM Tris-HCl	7.5	5% MPD	1 mM DTT
T5	10 mM $MgCl_2$	25 mM Tris-HCl	7.5	3% PEG 3350	1 mM DTT
T6	10 mM $MgCl_2$	25 mM Tris-HCl	7.5	5% MPD	1 mM DTT
T7	10 mM $CaCl_2$	25 mM Tris-HCl	7.5	3% PEG 3350	1 mM DTT
T8	10 mM $CaCl_2$	25 mM Tris-HCl	7.5	5% MPD	1 mM DTT
T9	12.5 mM $MgCl_2$	25 mM Tris-HCl	7.5	5% MPD	1 mM DTT
T10	7.5 mM $MgCl_2$	25 mM Tris-HCl	7.5	5% MPD	1 mM DTT
T11	7 mM $MgCl_2$	25 mM Tris-HCl	7.5	5% MPD	1 mM DTT 40 mM NaCl
T12	7 mM $MgCl_2$	25 mM Tris-HCl	7.5	5% MPD	1 mM DTT 40 mM NaCl
CA1	10 mM $Mg(OAc)_2$	25 mM NaCac	6	-	-
CA2	10 mM $MgCl_2$	25 mM NaCac	6	-	-
CA3	25 mM $Mg(OAc)_2$	25 mM NaCac	6	-	-
CA4	25 mM $MgCl_2$	25 mM NaCac	6	-	-
TA1	10 mM $Mg(OAc)_2$	25 mM Tris-HCl	7.5	-	-
TA2	10 mM $MgCl_2$	25 mM Tris-HCl	7.5	-	-
TA3	25 mM $Mg(OAc)_2$	25 mM Tris-HCl	7.5	-	-
TA4	25 mM $MgCl_2$	25 mM Tris-HCl	7.5	-	-

OAc; acetate.

Table D-3. Crystallization conditions for the DNA and *N*-phenylbenzamide bis(2-aminoimidazolinium) compounds complexes.

Name	Ion	Buffer	pH	Precipitants	Additives
D1	8 mM $MnCl_2$	25 mM NaCac	6	5% MPD	0.1 mM Spermine
D2	10 mM $Mg(OAc)_2$	25 mM NaCac	6	5% MPD	0.1 mM Spermine
D3	8 mM $MgCl_2$	25 mM NaCac	6	5% MPD	0.1 mM Spermine
D4	10 mM $NH_4(OAc)$	25 mM NaCac	6	5% MPD	0.1 mM Spermine
D2.2	8 mM $Mg(OAc)_2$	25 mM NaCac	6	5% MPD	0.1 mM Spermine
D4.2	8 mM $NH_4(OAc)$	25 mM NaCac	6	5% MPD	0.1 mM Spermine

OAc; acetate.

Appendix E

CRYSTALLIZATION CONDITIONS

Table E-1. Crystallization assays with DNA-HMGA1a protein complexes.

Complex with HMGA1a(Δ50-91)					
DNA Sequence	DNA [mM]	Ratio [DNA/Prot]	Buffer	Reservoir final concentration [% MPD]	Observations
CCAATAATCGCGATTATTGG	0.1 0.1 0.2 0.25	1:2 1:4 1:6 1:8	Natrix HR2-116: 7, 15, 16, 25, 31, 42, 43, 46. T6, T9, T11, T12 CA1, CA2, CA3, CA4, TA1, TA2, TA3, TA4. 0.25 mM $NiCl_2$	Up to 69%	-Phase separation -Liquid crystals -Amorphous precipitate -Crystalline points
ATTATTAATAAT	0.1 0.2 0.3	1:2 1:4 1:8	Natrix HR2-116: 15, 16, 25, 43, 48.	Up to 70%	Phase separation Liquid crystals
AATATATATATT	**0.3** **0.2**	1:3 1:6 1:9	Natrix HR2-116: 7, 15, 16, 43.	Up to 55%	-Phase separation -Amorphous precipitate
AAATATATTT	**0.3** **0.2** **0.15**	1:4 1:6 1:8	Natrix HR2-116: 7, 15, 16, 43.	Up to 55%	-Phase separation -Crystalline precipitate
CGAATTAATTCG	**0.2**	1:4	Natrix HR2-116: 43 T6, T9, T11, T12 CA1, CA2, CA3, CA4, TA1, TA2, TA3, TA4. 0.25 mM $NiCl_2$	Up to 50%	-Amorphous precipitate -Crystalline points
ATTAATTAAT	**0.2**	1:4	T6, T9, T11, T12	Up to 50%	-Amorphous precipitate

Table E-2. Crystallization assays with DNA-HMGB1 proteins complexes.

Complex with HMGB1 box B and box AB					
DNA Sequence	DNA [mM]	Ratio [DNA/Prot]	Buffer	Reservoir final conc. [%]	Observations
CCAATAATCGCGATTATTGG	0.2 0.4	1:2 1:4	Natrix HR2-116: 15, 43. T1-T10 (T6, T9) C1-C10 (C9)	MPD: Up to 69% PEG 3350: 20%, 30%, 40%	-Rectangular crystals -Amorphous crystals -Crystalline sheets
ATTAATTAAT	0.25 0.4	1:2	Natrix HR2-116: 15, 43. T6, T9, T10 C6, C9, C10	Up to 70%	-Phase separation -Liquid crystals -Small rods and needles
AATAAATTTATT	**0.2** **0.4**	1:2	C1-C8 T1-T10 (T6, T9, T10)	MPD: 30%, 40%, 50%. PEG 3350: 20%, 30%, 40%	-Precipitate -Small needles - Amorphous crystals - Small rectangular crystals -Crystals with different morphologies
ATATGCATAT	**0.2** **0.4**	1:2	C1-C8 T1-T8	MPD: 30%, 40%, 50%. PEG 3350: 20%, 30%, 40%	-Phase separation -Liquid crystals -Amorphous precipitate
ATATCGATAT	**0.2** **0.4** **0.6**	1:2	C1-C8 T1-T8	MPD: 30%, 40%, 50%. PEG 3350: 20%, 30%, 40%	-Phase separation -Amorphous precipitate
AATAATCGCGATTATT	**0.2** **0.25**	1:3 1:4	Natrix HR2-116: 15, 43. C1-C8 T1-T10	MPD: Up to 70%	-Phase separation -Liquid crystals
AATTTAAATT	**0.2**	1:2 1:4	Natrix HR2-116: 15. T6, T9, T10 C6, C9, C10	MPD: Up to 50%	-Phase separation -Crystalline points -Small rectangular crystals
ATTTATAAAT	**0.2**	1:2	Natrix HR2-116: 15. T6, T9 C6, C9	MPD: Up to 50%	-Phase separation -Crystalline points

DNA Sequence	DNA [mM]	Ratio [DNA/Prot]	Buffer	Reservoir final conc. [%]	Observations
GGGAAATTTCCC	**0.2**	1:2	Natrix HR2-116: 15. T6, T9 C6, C9	MPD: Up to 50%	-Phase separation
AATAAATTTATTT	**0.2**	1:2 1:4	T6, T9, T10 C6, C9, C10	MPD: Up to 40%	-Phase separation -Amorphous precipitate

Best crystallization conditions found are underlined.

Table E-3. Crystallization assays with DNA-bis(2-aminoimidazolines) complexes.

Complex with FR60, JNI18 and CDIV32 compounds					
DNA Sequence	DNA [mM]	Ratio [DNA/Drug]	Buffer	Reservoir final concentration [% MPD]	Observations
ATTATTAATAAT	0.2	1:2 1:4	Natrix HR2-116: 7, 42. D1, D2, D3, D4, D2.2, D4.2. C2, C4, C6	Up to 60%	-Phase separation -Small needles -Crystalline precipitate -Small crystals -Amorphous precipitate
AAATATATTT	**0.2**	1:2	D1, D2, D3, D4	Up to 40%	-Amorphous precipitate -Crystalline precipitate -Small rectangular crystals - Amorphous crystals
ATTAATTAAT	**0.2**	1:2	D1, D2, D3, D4	Up to 50%	-Amorphous precipitate -Crystalline precipitate
AATTTAAATT	**0.2**	1:2 1:4	D1, D2, D3, D4	Up to 30%	-Small rectangular and amorphous crystals -Small needles -Crystalline precipitate
ATTTATAAAT	**0.2**	1:2 1:4	D1, D2, D3, D4	Up to 30%	-Amorphous crystals -Small needles
AAATTT	**0.2**	1:2 1:4	D1, D2, D3, D4	Up to 60%	-Rectangular, trapezoidal and hexagonal crystals -Small rhombic crystals -One single crystal
AATAATTATT	**0.2**	1:2 1:4	D1, D2, D3, D4	Up to 30%	-Small needles -Crystalline precipitate -Crystalline points
CATATATATG	**0.2**	1:2	D1, D2, D3, D4	Up to 53%	-Amorphous precipitate -Rectangular crystals
AATTATAATT	**0.2**	1:2	D1, D2, D3, D4	Up to 50%	-Amorphous precipitate -Crystalline precipitate
ATAATATTAT	**0.2**	1:2	D1, D2, D3, D4	Up to 30%	-Small needles -Liquid crystals -Crystalline precipitate

Best crystallization conditions found are underlined.

Appendix F

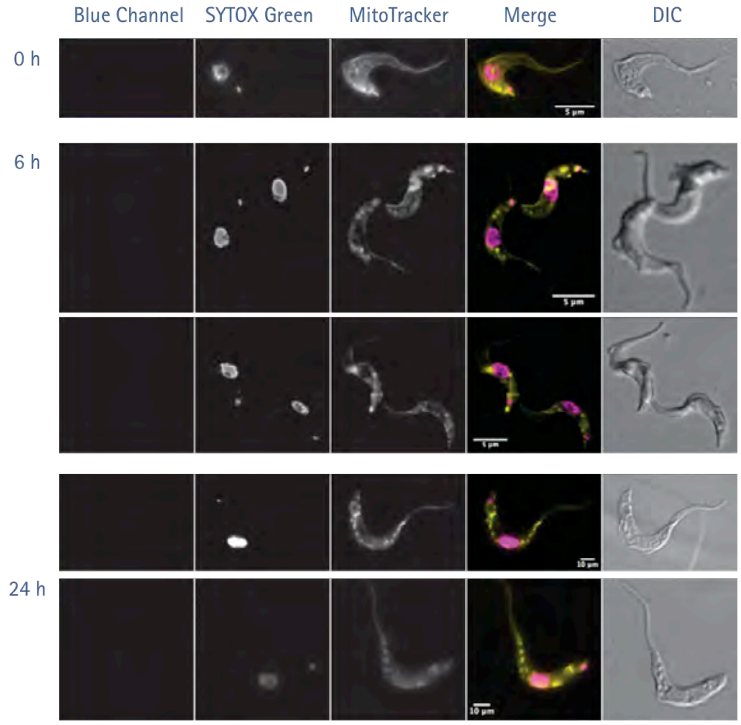

Figure F1. Fluorescence images of untreated cell samples of *Trypanosoma brucei* 427WT cells taken at 0, 3, 6 and 24 h of experiment. All fluorescent images are shown with Blue channel (λ=450), *SYTOX Green* (λ=523, green channel), *MitoTracker* (λ=599, red channel), and merge, where arbitrary colours were used to visualise the various dyes: blue for Blue channel, purple for *SYTOX*, yellow for *Mitotracker*. No changes in fluorescence were observed at blue wavelength as untreated cells (no fluorescent compound JNI18 added) were visualized. Normal cells were observed containing 1N1K (one nuclei and one kinetoplast). The outline of all cells was shown by differential interference contrast (DIC) imaging. Images were acquired using a *DeltaVision* imaging system and deconvolved using the ratio conservative method, on *SoftWoRx* software.

Table F 1. Mitochondrial membrane potential assay.

Untreated cells (drug free)

Time	Repeat 1	Repeat 2	Repeat 3
0 h	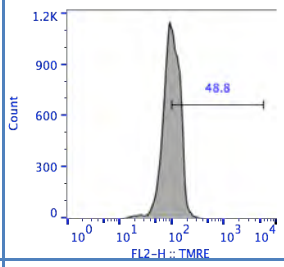	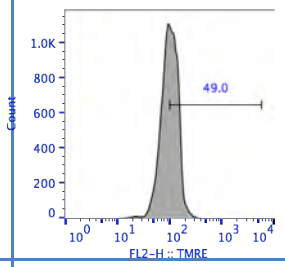	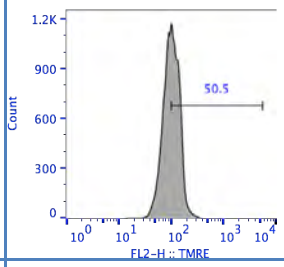
3 h	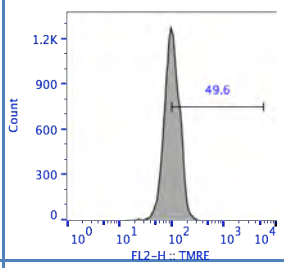	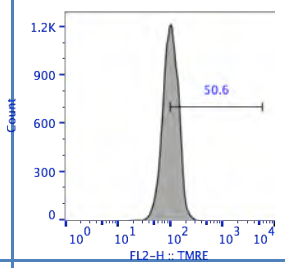	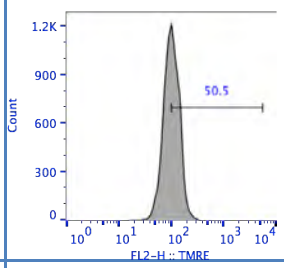
6 h	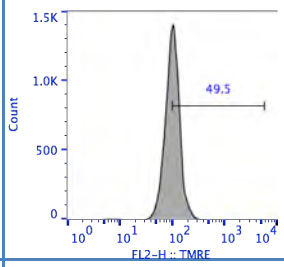	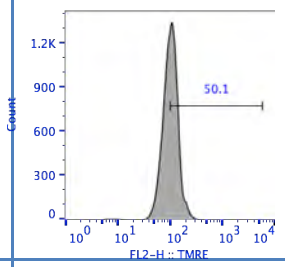	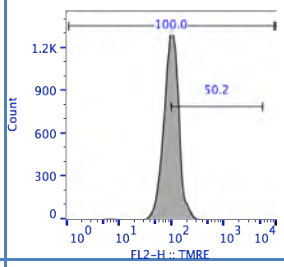
12 h	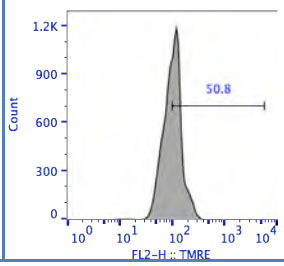	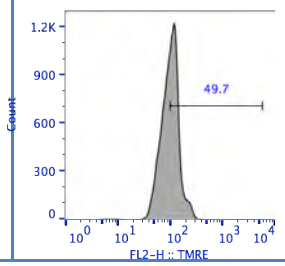	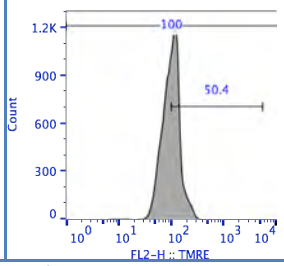

Values are given as the percentage of cells with fluorescence above 1×10^2 arbitrary units (AU), equivalent to approximately 50% for the untreated cells. Samples are taken at 0, 3, 6 and 12 h by a BD FACSCalibur™ using a FL2-height detector. Data were processed with CellQuest™ and ©FlowJo software.

Treated cells with 1× EC_{50} FR60 (0.83 µM)

Time	Repeat 1	Repeat 2	Repeat 3
3 h	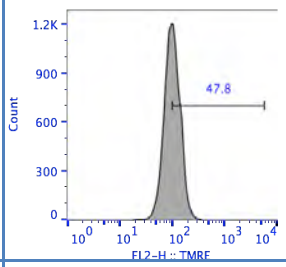	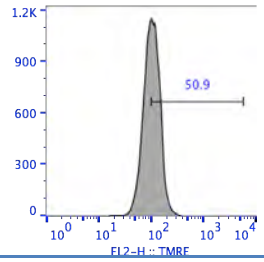	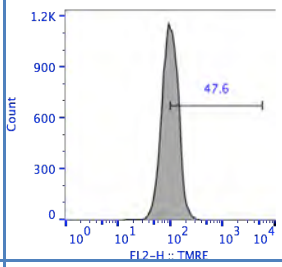
6 h	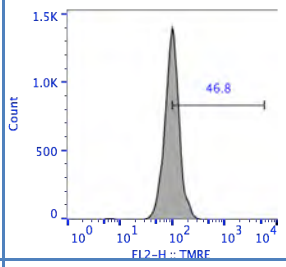	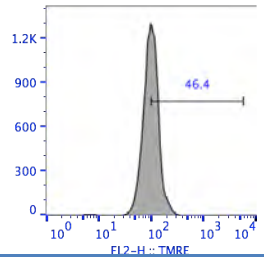	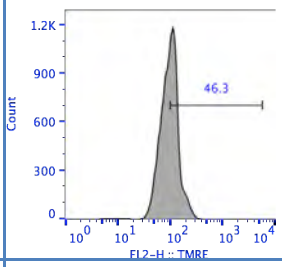
12 h	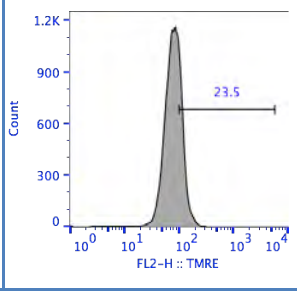	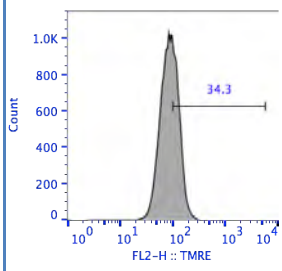	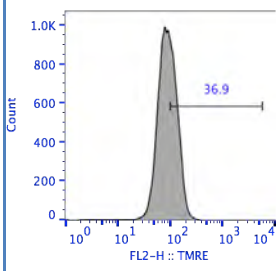

Values are given as the percentage of cells with fluorescence above 1 × 10^2 arbitrary units (AU), equivalent to approximately 50% for the untreated cells. Samples are taken at 3, 6 and 12 h by a BD FACSCalibur™ using a FL2-height detector. Data were processed with CellQuest™ and ©FlowJo software.

Treated cells with 5× EC_{50} FR60 (4.15 µM)

Time	Repeat 1	Repeat 2	Repeat 3
3 h	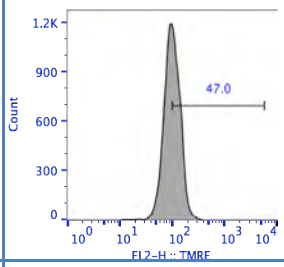	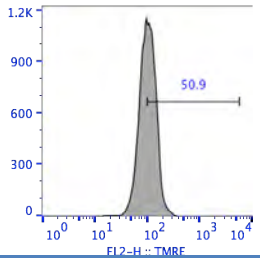	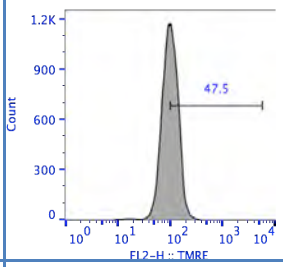
6 h	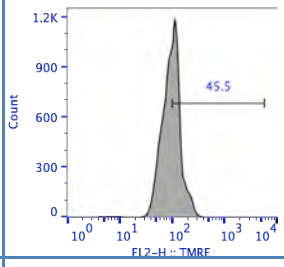	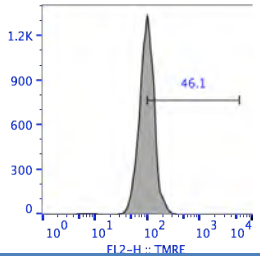	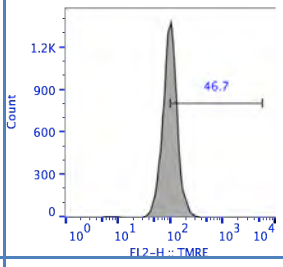
12 h	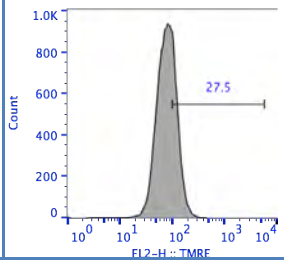	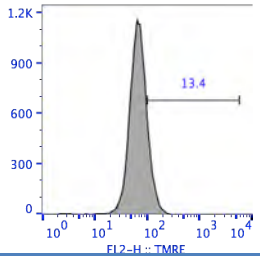	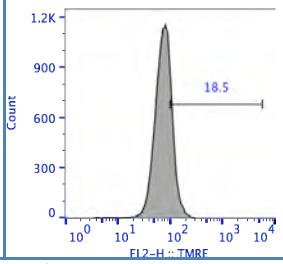

Values are given as the percentage of cells with fluorescence above 1 × 10^2 arbitrary units (AU), equivalent to approximately 50% for the untreated cells. Samples are taken at 3, 6 and 12 h by a BD FACSCalibur™ using a FL2-height detector. Data were processed with CellQuest™ and ©FlowJo software.

Treated cells with 1× EC_{50} JNI18 (0.22 µM)

Time	Repeat 1	Repeat 2	Repeat 3
3 h	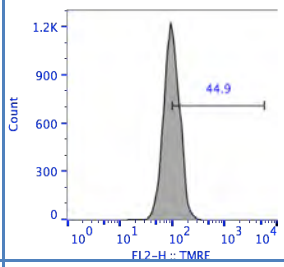	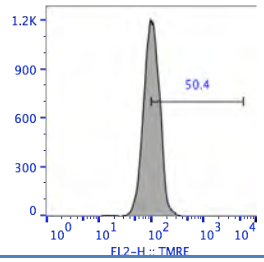	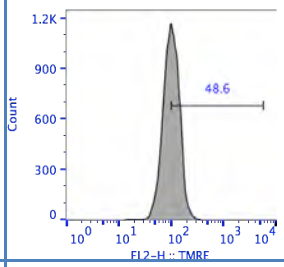
6 h	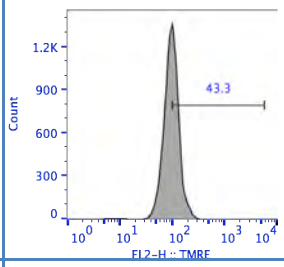	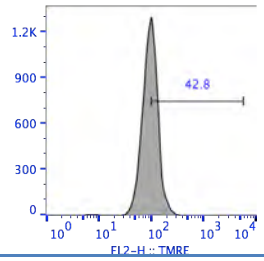	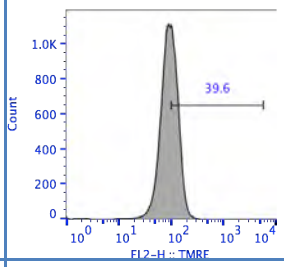
12 h	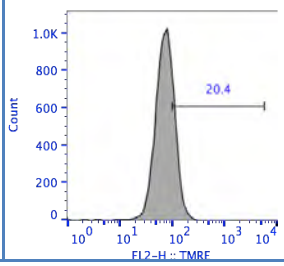	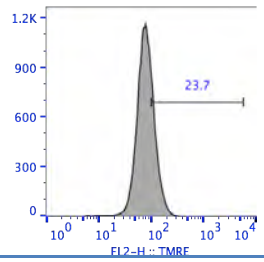	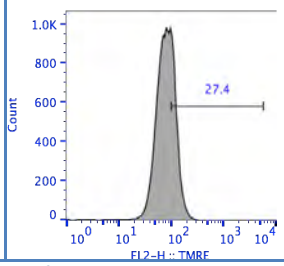

Values are given as the percentage of cells with fluorescence above 1 × 10^2 arbitrary units (AU), equivalent to approximately 50% for the untreated cells. Samples are taken at 3, 6 and 12 h by a BD FACSCalibur™ using a FL2-height detector. Data were processed with CellQuest™ and ©FlowJo software.

Treated cells with 5× EC_{50} JNI18 (1.1 µM)

Time	Repeat 1	Repeat 2	Repeat 3
3 h	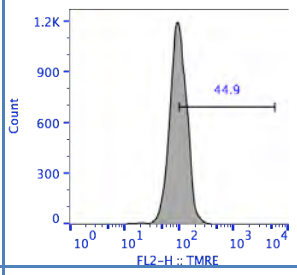	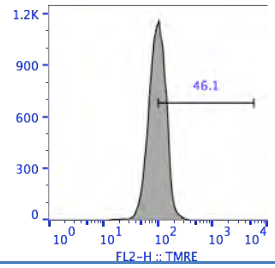	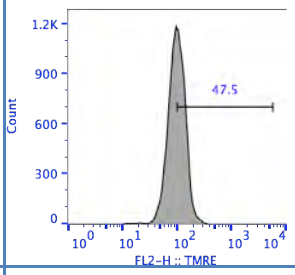
6 h	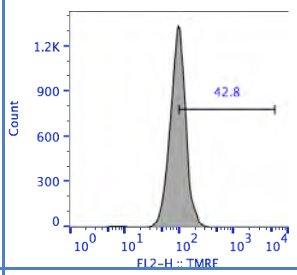	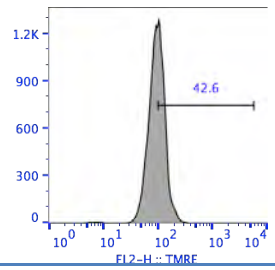	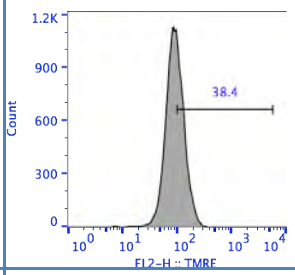
12 h	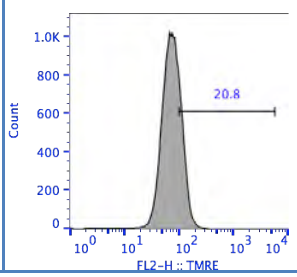	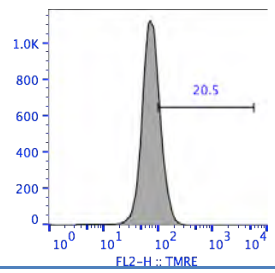	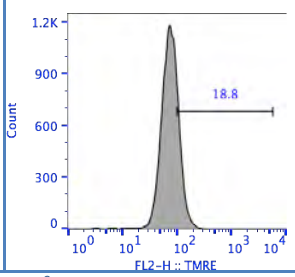

Values are given as the percentage of cells with fluorescence above 1 × 10^2 arbitrary units (AU), equivalent to approximately 50% for the untreated cells. Samples are taken at 3, 6 and 12 h by a BD FACSCalibur™ using a FL2-height detector. Data were processed with CellQuest™ and ©FlowJo software.

Treated cells with 1× EC_{50} CDIV32 (29.98 µM)

Time	Repeat 1	Repeat 2	Repeat 3
3 h	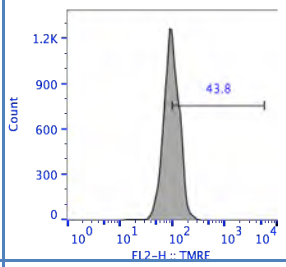	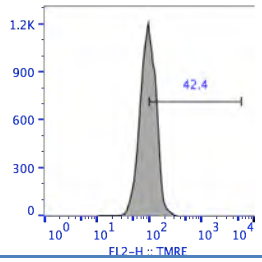	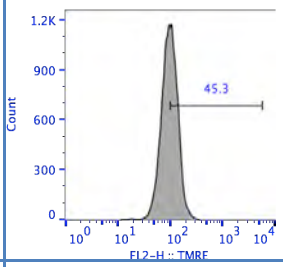
6 h	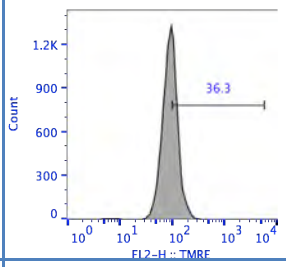	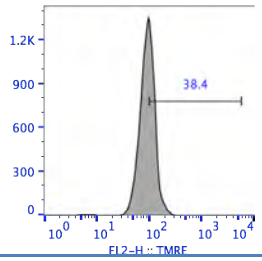	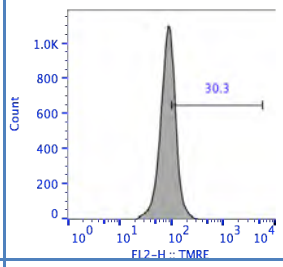
12 h	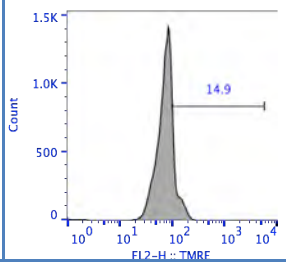	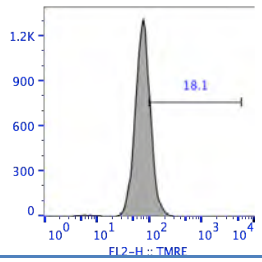	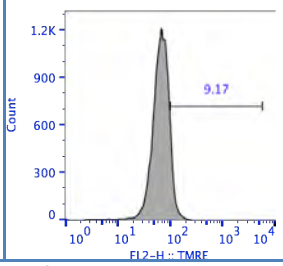

Values are given as the percentage of cells with fluorescence above 1 × 10^2 arbitrary units (AU), equivalent to approximately 50% for the untreated cells. Samples are taken at 3, 6 and 12 h by a BD FACSCalibur™ using a FL2-height detector. Data were processed with CellQuest™ and ©FlowJo software.

Treated cells with 5× EC_{50} CDIV32 (149.9 µM)

Time	Repeat 1	Repeat 2	Repeat 3
3 h	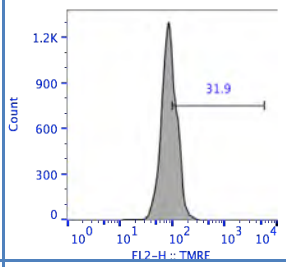	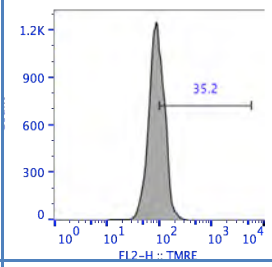	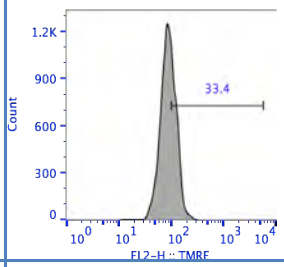
6 h	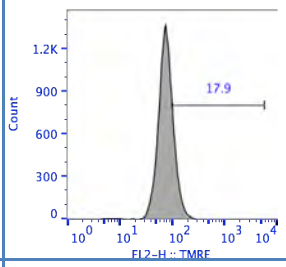	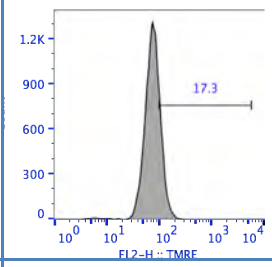	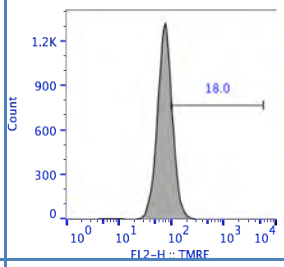
12 h	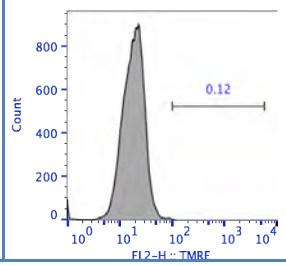	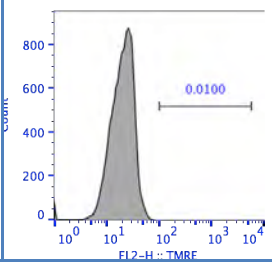	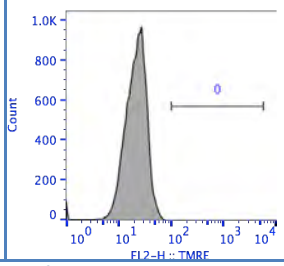

Values are given as the percentage of cells with fluorescence above 1 × 10^2 arbitrary units (AU), equivalent to approximately 50% for the untreated cells. Samples are taken at 3, 6 and 12 h by a BD FACSCalibur™ using a FL2-height detector. Data were processed with CellQuest™ and ©FlowJo software.

Valinomycin (100 nM)			
Time	Repeat 1	Repeat 2	Repeat 3
3 h	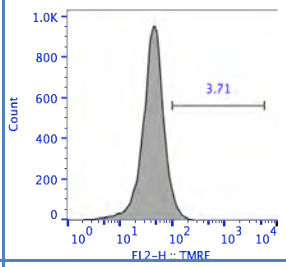	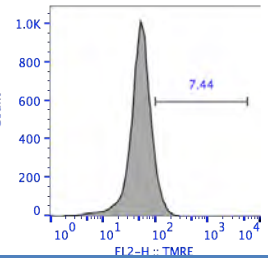	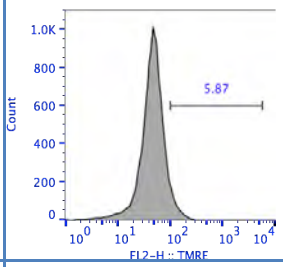
6 h	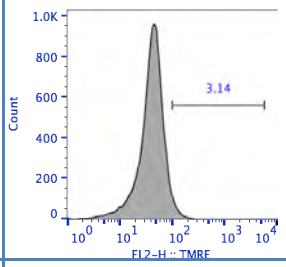	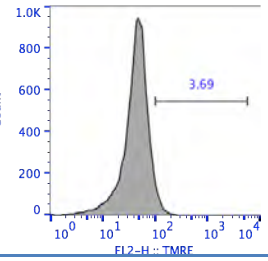	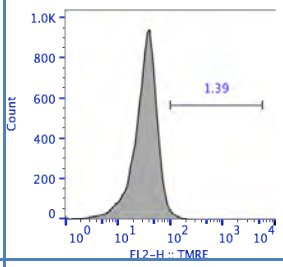
12 h	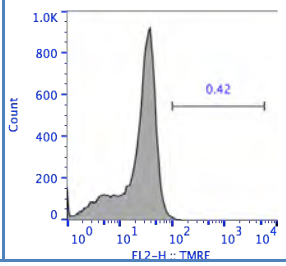	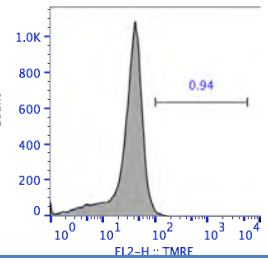	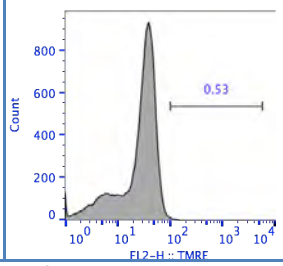

Values are given as the percentage of cells with fluorescence above 1×10^2 arbitrary units (AU), equivalent to approximately 50% for the untreated cells. Samples are taken at 3, 6 and 12 h by a BD FACSCalibur™ using a FL2-height detector. Data were processed with CellQuest™ and ©FlowJo software.

Troglitazone (10 µM)			
Time	**Repeat 1**	**Repeat 2**	**Repeat 3**
3 h	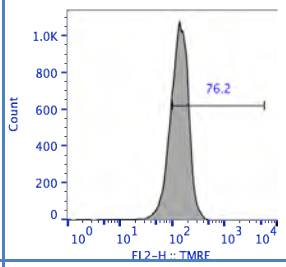	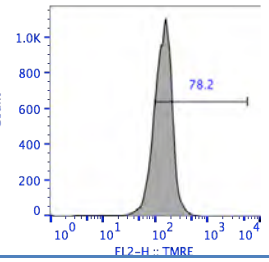	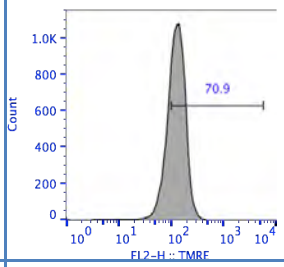
6 h	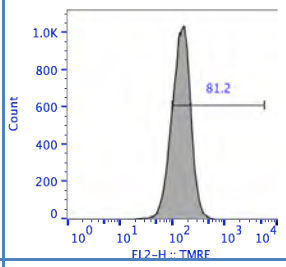	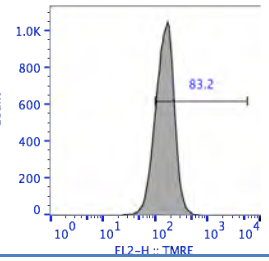	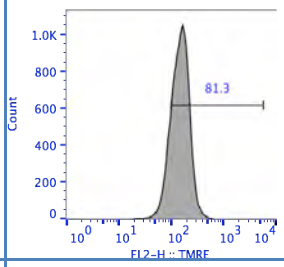
12 h	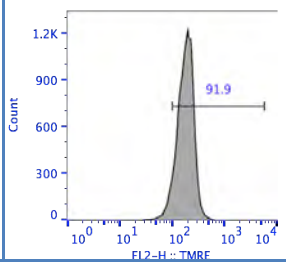	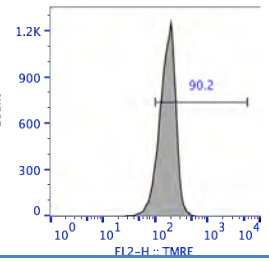	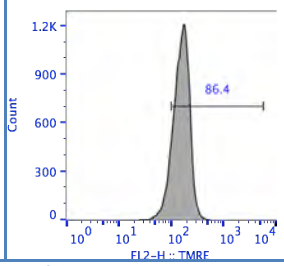

Values are given as the percentage of cells with fluorescence above 1×10^2 arbitrary units (AU), equivalent to approximately 50% for the untreated cells. Samples are taken at 3, 6 and 12 h by a BD FACSCalibur™ using a FL2-height detector. Data were processed with CellQuest™ and ©FlowJo software.

Appendix G

Trypanosoma brucei brucei strain Lister 427 (Tb427WT) minicircle, complete sequence; kinetoplast (Dean, et al., 2013)

LOCUS: KF293288 1001 bp DNA circular

GGGGTTGGTGTAATACACACAGGGTTTTCCCGTAGAAATTATATTAATTTGGATCATTTGGTGTTTTC
TATTGATAAAAGAATAAGATAATAGATAGATTAATTGATATTATATAGATATTATATATAAGACGCATAT
AAGTGAGTCTATATACAGATAATGATGATAATTTATATATATGTTAACTTTAATATTTATTTATTATTTTC
TTTTCTATATTAGGAGAAATGTGATAATAGATAAGTAATGAGAGTAATTTAGATATTTAATTGTATATA
ATTACACACACAGATACGTGATATATAGAGTGTTAAGATAATATGATGTATATATATGTAAATTAAAAAA
CTATTTATTATTTTATGTTAAGTAGATGGAGAAATAATAGTTAAATAAGAGGTAGTACTTTGAGGAGG
TATAAGGTAATATTAACATTGAGAATCTTAGATAACTGATAAAATACTGTTATTTCTGCATCTAAAAGA
GGGTTTTAAGCTGTCTAAAAGGGTAAAATGAGGTAATAGATAAGGTATAGATAATATAATATTTAAT
ATAATATATATAATAACAATAGCAGGTAAAGGTAAGAAAGTGAAGATATCATATAAGATTGTATATTT
AATGTTAAACTATATTTATTATTTTATTTATAATTAGTAGATAAGATTAGTAGAAGTGAAGTAGTAATTG
TAAAACTGATAGTAAGATGGGAATAAGGTGTGAGATATAAATAGAAAGGTTAAGTTAATTGTAGTTA
TAATTGGAAGTGCAGAAAGTGTTGTAGATGGAGTATTAGGTTGATTAGAGAGAGAGTAGTATAAAGT
GTAAAAAGTTTGTGTTGGATGGTAGAGATAGAAGGGAGAAGTTAGAAATTCAGAGAAAATTGGGG
AAAAATCAGGGAAAATCGGGCTGAAAAACCGAAAATCTTATGGGCGTGCAGATTTCACCATACAC
AAATCACGTGCTATTTTCGGGGGGTTTTAGGTCCGAGGTACTTCGAAA.

The **AT content** represents the **73.6%** of the minicircle genome of Tb427WT (**A = 394** and **T = 342**); and **CG-content** the **26.5%** (**G = 206** and **C = 59**). The sequence **AAA** appears **28** times and the sequence **TTT 26** times; both are shown in red, bold font. The sequence **AATT** exists **14** times and is highlighted in yellow. Tracts with more than 10 **A/T** are found 15 times (red and underlined).

REFERENCES

REFERENCES

Abrescia, N. G. A. & Subirana, J. A. (2002). When pseudosymmetry and merohedral twinning come across: the case of the d(ApTpApTpApT) oligonucleotide in a hexagonal lattice. *Acta crystallographica. Section D, Biological crystallography*, *58*(Pt 12), 2205-2208.

Abrescia, N. G. A., Gonzalez, C., Gouyette, C., & Subirana, J. A. (2004). X-ray and NMR studies of the DNA oligomer d(ATATAT): Hoogsteen base pairing in duplex DNA. Biochemistry, 43(14), 4092–4100. https://doi.org/10.1021/bi0355140

Abrescia, N. G. A., Thompson, A., Huynh-Dinh, T., & Subirana, J. A. (2002). Crystal structure of an antiparallel DNA fragment with Hoogsteen base pairing. Proceedings of the National Academy of Sciences of the United States of America, 99(5), 2806–2811. http://doi.org/10.1073/pnas.052675499

Acosta-Reyes, F. J., Alechaga, E., Subirana, J. A., & Campos, J. L. (2015). Structure of the DNA duplex d(ATTAAT)2 with Hoogsteen hydrogen bonds. PloS One, 10(3), e0120241. https://doi.org/10.1371/journal.pone.0120241

Acosta-Reyes, F. J., Dardonville, C., de Koning, H. P., Natto, M., Subirana, J. A., & Campos, J. L. (2014). In and out of the minor groove: interaction of an AT-rich DNA with the drug CD27. *Acta Crystallographica Section D Biological Crystallography*, 70(6), 1614–1621. https://doi.org/10.1107/S139900471400697X

Adams, P. D., Afonine, P. V., Bunkóczi, G., Chen, V. B., Davis, I. W., Echols, N., … Zwart, P. H. (2010). *PHENIX* : a comprehensive Python-based system for macromolecular structure solution. *Acta Crystallographica Section D Biological Crystallography*, *66*(2), 213–221. https://doi.org/10.1107/S0907444909052925

Afonine, P., Grosse-Kunstleve, R. & Adams, P. (2005). The Phenix refinement framework. *CCP4 newsletter*, *42*(8), 1-7.

Akiyoshi, B., & Gull, K. (2013). Evolutionary cell biology of chromosome segregation: insights from trypanosomes. *Open Biology*, 3(5), 130023. http://doi.org/10.1098/rsob.130023

Alkhaldi, A. A. M., Martinek, J., Panicucci, B., Dardonville, C., Zíková, A., & de Koning, H. P. (2016). Trypanocidal action of bisphosphonium salts through a mitochondrial target in bloodstream form *Trypanosoma brucei*. *International Journal for Parasitology: Drugs and Drug Resistance*, *6*(1), 23–34. https://doi.org/10.1016/j.ijpddr.2015.12.002

Almaqwashi, A. A., Paramanathan, T., Rouzina, I., & Williams, M. C. (2016). Mechanisms of small molecule–DNA interactions probed by single-molecule force spectroscopy. Nucleic Acids Research, 44(9), 3971–3988. http://doi.org/10.1093/nar/gkw237

Anand, A., & Chada, K. (2000). *In vivo* modulation of Hmgic reduces obesity. *Nature Genetics*, 24(4), 377–380. https://doi.org/10.1038/74207

Andrews, K. T., Fisher, G., & Skinner-Adams, T. S. (2014). Drug repurposing and human parasitic protozoan diseases. *International Journal for Parasitology: Drugs and Drug Resistance*, 4(2), 95–111. https://doi.org/10.1016/j.ijpddr.2014.02.002

Aravind, L., & Landsman, D. (1998). AT-hook motifs identified in a wide variety of DNA-binding proteins. *Nucleic Acids Research*, 26(19), 4413–4421.

Aravind, L., Iyer, L. M., Wellems, T. E., & Miller, L. H. (2003). Plasmodium biology: genomic gleanings. *Cell*, 115(7), 771–785.

Aulner, N., Monod, C., Mandicourt, G., Jullien, D., Cuvier, O., Sall, A., Janssen, S., Laemmli, U.K., & Kas, E. (2002). The AT-Hook Protein D1 Is Essential for Drosophila melanogaster Development and Is Implicated in Position-Effect Variegation. *Molecular and Cellular Biology*, 22(4), 1218–1232. https://doi.org/10.1128/MCB.22.4.1218-1232.2002

Avliyakulov, N. K., Lukeš, J., & Ray, D. S. (2004). Mitochondrial Histone-Like DNA-Binding Proteins Are Essential for Normal Cell Growth and Mitochondrial Function in Crithidia fasciculata. *Eukaryotic Cell*, *3*(2), 518–526. https://doi.org/10.1128/EC.3.2.518-526.2004

Babine, R. E., & Bender, S. L. (1997). Molecular Recognition of Protein−Ligand Complexes: Applications to Drug Design. *Chemical Reviews*, 97 (5), 1359-1472. https://doi.org/10.1021/cr960370z

Babokhov, P., Sanyaolu, A. O., Oyibo, W. A., Fagbenro-Beyioku, A. F., & Iriemenam, N. C. (2013). A current analysis of chemotherapy strategies for the treatment of human African trypanosomiasis. *Pathogens and Global Health*, *107*(5), 242–252. http://doi.org/10.1179/2047773213Y.0000000105

Bachvarov, D & Moss, T. (1991). The RNA polymerase I transcription factor xUBF contains 5 tandemly repeated HMG homology boxes. *Nucleic Acids Research*l, 19 (9), 2331-2335. https://doi.org/10.1093/nar/19.9.2331

Bailly, C. (2003). Sequence-specific minor groove binding by bis-benzimidazoles: water molecules in ligand recognition. *Nucleic Acids Research*, 31(5), 1514–1524. https://doi.org/10.1093/nar/gkg237

Baldassarre, G., Belletti, B., Battista, S., Nicoloso, M.S., Pentimalli, F., Fedele, M., Croce, C.M., & Fusco, A. (2005). HMGA1 protein expression sensitizes cells to cisplatin-induced cell death. *Oncogene*, 24(45), 6809–6819. https://doi.org/10.1038/sj.onc.1208831

Banerjee, S., de Freitas, A., Friggeri, A., Zmijewski, J. W., Liu, G., & Abraham, E. (2011). Intracellular HMGB1 negatively regulates efferocytosis. *Journal of Immunology* (Baltimore, Md. : 1950), 187(9), 4686–4694. http://doi.org/10.4049/jimmunol.1101500

Baron, R., Setny, P., & Andrew McCammon, J. (2010). Water in Cavity−Ligand Recognition. *Journal of the American Chemical Society*, 132(34), 12091–12097. https://doi.org/10.1021/ja1050082

Barrett, M. P., Burchmore, R. J. S., Stich, A., Lazzari, J. O., Frasch, A. C., Cazzulo, J. J., & Krishna, S. (2003). The trypanosomiases. *Lancet (London, England)*, 362(9394), 1469–1480. https://doi.org/10.1016/S0140-6736(03)14694-6

Barrett, M. P., Gemmell, C. G., & Suckling, C. J. (2013). Minor groove binders as anti-infective agents. *Pharmacology & Therapeutics*, 139(1), 12–23. https://doi.org/10.1016/j.pharmthera.2013.03.002

Battye, T. G. G., Kontogiannis, L., Johnson, O., Powell, H. R., & Leslie, A. G. W. (2011). *iMOSFLM* : a new graphical interface for diffraction-image processing with *MOSFLM*. *Acta Crystallographica Section D Biological Crystallography*, *67*(4), 271–281. https://doi.org/10.1107/S0907444910048675

Baxevanis, A. D., & Landsman, D. (1995). The HMG-1 box protein family: classification and functional relationships. *Nucleic Acids Research*, 23(9), 1604–1613.

Beck, K., Acestor, N., Schulfer, A., Anupama, A., Carnes, J., Panigrahi, A. K., & Stuart, K. (2013). *Trypanosoma brucei* Tb927.2.6100 Is an Essential Protein Associated with Kinetoplast DNA. *Eukaryotic Cell*, *12*(7), 970–978. http://doi.org/10.1128/EC.00352-12

Behe, M., & Felsenfeld, G. (1981). Effects of methylation on a synthetic polynucleotide: the B–Z transition in poly (dG-m5dC). poly (dG-m5dC). *Proceedings of the National Academy of Sciences*, 78(3), 1619–1623.

Benini, F., Onorati, M., Altamura, S., Manfioletti, G., & Vignali, R. (2006). Identification and developmental expression of Xenopus hmga2beta. *Biochemical and Biophysical Research Communications*, 351(2), 392–397. https://doi.org/10.1016/j.bbrc.2006.10.074

Benvenuti, M., & Mangani, S. (2007). Crystallization of soluble proteins in vapor diffusion for x-ray crystallography. *Nature Protocols*, *2*(7), 1633–1651. https://doi.org/10.1038/nprot.2007.198

Berman, H. M. & Young, P. R. (1981). The interaction of intercalation drugs with nucleic acids. *Cancer*, 10(60):87-114.

Bhat, G. J., Koslowsky, D. J., Feagin, J. E., Smiley, B. L., & Stuart, K. (1990). An extensively edited mitochondrial transcript in kinetoplastids encodes a protein homologous to

ATPase subunit 6. *Cell*, *61*(5), 885-894. https://doi.org/10.1016/0092-8674(90)90199-O

Bianchi, M. E., & Agresti, A. (2005). HMG proteins: dynamic players in gene regulation and differentiation. *Current Opinion in Genetics & Development*, 15(5), 496–506. https://doi.org/10.1016/j.gde.2005.08.007

Bragg, W. H . & Bragg, W. L. (1913). The Reflexion of X-rays by Crystals . *Proceedings of the Royal Society A: Mathematical, Physical and Engineering Sciences*, *88*(605), 428–438. http://doi:10.1098/rspa.1913.0040

Bridges, D. J., Gould, M. K., Nerima, B., Maser, P., Burchmore, R. J. S., & de Koning, H. P. (2007). Loss of the high-affinity pentamidine transporter is responsible for high levels of cross-resistance between arsenical and diamidine drugs in African trypanosomes. *Molecular Pharmacology*, *71*(4), 1098–1108. https://doi.org/10.1124/mol.106.031351

Bruhn, D. F., Sammartino, M. P., & Klingbeil, M. M. (2011). Three Mitochondrial DNA Polymerases Are Essential for Kinetoplast DNA Replication and Survival of Bloodstream Form *Trypanosoma brucei*. *Eukaryotic Cell*, *10*(6), 734–743. http://doi.org/10.1128/EC.05008-11

Bustin, M. (1999). Regulation of DNA-dependent activities by the functional motifs of the high-mobility-group chromosomal proteins. *Molecular and Cellular Biology*, 19(8), 5237–5246.

Cai, X., Gray Jr., P. J., & Von Hoff, D. D. (2009). DNA minor groove binders: Back in the groove. *Cancer Treatment Reviews*, 35(5), 437–450. https://doi.org/10.1016/j.ctrv.2009.02.004

Campos, L., Valls, N., Urpí, L., Gouyette, C., Sanmartín, T., Richter, M., Alechaga, E., Santaolalla, A., Baldini, R., Creixell, M., Ciurans, R., Skokan, P., Pous, J., & Subirana, J. A. (2006). Overview of the Structure of All-AT Oligonucleotides: Organization in Helices

and Packing Interactions. *Biophysical Journal*, 91(3), 892–903. https://doi.org/10.1529/biophysj.106.084210

Canals, A., Arribas-Bosacoma, R., Albericio, F., Álvarez, M., Aymamí, J., & Coll, M. (2017). Intercalative DNA binding of the marine anticancer drug variolin B. *Scientific Reports*, *7*, 39680. http://doi.org/10.1038/srep39680

Cantor, C. R., Warshaw, M. M., & Shapiro, H. (1970). Oligonucleotide interactions. III. Circular dichroism studies of the conformation of deoxyoligonucleotides. *Biopolymers*, *9*(9), 1059–1077. https://doi.org/10.1002/bip.1970.360090909

Carlton, J. M., Angiuoli, S. V., Suh, B. B., Kooij, T. W., Pertea, M., Silva, J. C., Ermolaeva, M.D., Allen, J.E., Selengut, J.D., Koo, H.L., et al. (2002). Genome sequence and comparative analysis of the model rodent malaria parasite Plasmodium yoelii yoelii. *Nature*, *419*(6906), 512–519. https://doi.org/10.1038/nature01099

Carr, K.M., & Kaguni, J.M. (2001). Stoichiometry of DnaA and DnaB protein in initiation at the Escherichia coli chromosomal origin. *The Journal of Biological Chemistry*, 276(48), 44919-25. https://doi.org/10.1074/jbc.M107463200

Cavalcanti, D. P., Shimada, M. K., Probst, C. M., Souto-Padrón, T. C. B. S., de Souza, W., Goldenberg, S., … Motta, M. C. M. (2009). Expression and subcellular localization of kinetoplast-associated proteins in the different developmental stages of *Trypanosoma cruzi*. *BMC Microbiology*, *9*, 120. http://doi.org/10.1186/1471-2180-9-120

Chappuis, F., Loutan, L., Simarro, P., Lejon, V., & Büscher, P. (2005). Options for Field Diagnosis of Human African Trypanosomiasis. Clinical Microbiology Reviews, 18(1), 133–146. http://doi.org/10.1128/CMR.18.1.133-146.2005

Chen, K. K., & Donelson, J. E. (1980). Sequences of two kinetoplast DNA minicircles of Tryptanosoma brucei. *Proceedings of the National Academy of Sciences of the United States of America*, 77(5), 2445–2449.

Chen, V. B., Arendall, W. B. 3rd, Headd, J. J., Keedy, D. A., Immormino, R. M., Kapral, G. J., Murray, L. W., Richardson, J. S., Richardson, D. C. (2010). MolProbity: all-atom structure

validation for macromolecular crystallography. *Acta Crystallographica. Section D, Biological Crystallography*, *66*(Pt 1), 12–21. https://doi.org/10.1107/S0907444909042073

Chiefari, E., Tanyolac, S., Paonessa, F., Pullinger, C. R., Capula, C., Iiritano, S., … Brunetti, A. (2011). Functional variants of the HMGA1 gene and type 2 diabetes mellitus. *JAMA*, 305(9), 903–912. https://doi.org/10.1001/jama.2011.207

Cleynen, I., & van de Ven, W. J. M. (2008). The HMGA proteins: A myriad of functions (Review). *International Journal of Oncology*, *32*, 289-305.

Coll, M., Aymami, J., van der Marel, G. A., van Boom, J. H., Rich, A., & Wang, A. H. (1989). Molecular structure of the netropsin-d(CGCGATATCGCG) complex: DNA conformation in an alternating AT segment. *Biochemistry*, 28(1), 310–320.

Crick, F. H. C. (1966). Codon–anticodon pairing: The wobble hypothesis. *Journal of Molecular Biology*, *19*, 548–555.

Crick, F. H., Barnett, L., Brenner, S., & Watts-Tobin, R. J. (1961). General nature of the genetic code for proteins. *Nature*, 192 (4809): 1227–32. Bibcode:1961Natur.192.1227C. doi:10.1038/1921227a0. PMID 13882203.

Dardonville, C., & Brun, R. (2004). Bisguanidine, bis(2-aminoimidazoline), and polyamine derivatives as potent and selective chemotherapeutic agents against *Trypanosoma brucei rhodesiense*. Synthesis and *in vitro* evaluation. *Journal of Medicinal Chemistry*, *47*(9), 2296–2307. https://doi.org/10.1021/jm031024u

Dardonville, C., & Nué Martínez, J. J. (2017). Bis(2-aminoimidazolines) and Bisguanidines: Synthetic Approaches, Antiparasitic Activity and DNA Binding Properties. *Current Medicinal Chemistry*, *24*. https://doi.org/10.2174/0929867324666170623091522

Dardonville, C., Barrett, M. P., Brun, R., Kaiser, M., Tanious, F., & Wilson, W. D. (2006). DNA Binding Affinity of Bisguanidine and Bis(2-aminoimidazoline) Derivatives with *in Vivo* Antitrypanosomal Activity. *Journal of Medicinal Chemistry*, *49*(12), 3748–3752. https://doi.org/10.1021/jm060295c

Dasari, S., & Tchounwou, P. B. (2014). Cisplatin in cancer therapy: molecular mechanisms of action. *European Journal of Pharmacology*, 0, 364–378. http://doi.org/10.1016/j.ejphar.2014.07.025

De Belle, I., Cai, S., & Kohwi-Shigematsu, T. (1998). The Genomic Sequences Bound to Special AT-rich Sequence-binding Protein 1 (SATB1) *In Vivo* in Jurkat T Cells Are Tightly Associated with the Nuclear Matrix at the Bases of the Chromatin Loops . *The Journal of Cell Biology*, 141(2), 335–348.

De Rosa, M., de Sanctis, D., Rosario, A. L., Archer, M., Rich, A., Athanasiadis, A., & Carrondo, M. A. (2010). Crystal structure of a junction between two Z-DNA helices. *Proceedings of the National Academy of Sciences*, 107(20), 9088–9092.

Dean, S., Gould, M. K., Dewar, C. E., & Schnaufer, A. C. (2013). Single point mutations in ATP synthase compensate for mitochondrial genome loss in trypanosomes. *Proceedings of the National Academy of Sciences of the United States of America*, *110*(36), 14741–14746. https://doi.org/10.1073/pnas.1305404110

Denninger, V., Figarella, K., Schönfeld, C., Brems, S., Busold, C., Lang, F., … Duszenko, M. (2007). Troglitazone induces differentiation in *Trypanosoma brucei*. *Experimental Cell Research*, *313*(9), 1805–1819. https://doi.org/10.1016/j.yexcr.2007.03.003

Dickerson R. E. (1989): Definitions and nomenclature of nucleic acid structure parameters. *Journal of Biomolecular Structure and Dynamics*, 6, 627—634.

Diederichs, K., & Karplus, P. A. (2013). Better models by discarding data? *Acta Crystallographica Section D: Biological Crystallography*, *69*(Pt 7), 1215–1222. http://doi.org/10.1107/S0907444913001121

Driessen, R. P. C., Sitters, G., Laurens, N., Moolenaar, G. F., Wuite, G. J. L., Goosen, N., & Dame, R. T. (2014). Effect of Temperature on the Intrinsic Flexibility of DNA and Its Interaction with Architectural Proteins. *Biochemistry*, 53(41), 6430–6438. https://doi.org/10.1021/bi500344j

Du, W., & Maniatis, T. (1994). The high mobility group protein HMG I(Y) can stimulate or inhibit DNA binding of distinct transcription factor ATF-2 isoforms. *Proceedings of the National Academy of Sciences of the United States of America*, 91(24), 11318–11322.

Dunker, A. K., Oldfield, C. J., Meng, J., Romero, P., Yang, J. Y., Chen, J. W., Vacic, V., Obradovic, Z., & Uversky, V. N. (2008). The unfoldomics decade: an update on intrinsically disordered proteins. *BMC Genomics*, 9(Suppl 2), S1. http://doi.org/10.1186/1471-2164-9-S2-S1

Emsley, P., Lohkamp, B., Scott, W. G., & Cowtan, K. (2010). Features and development of Coot. *Acta Crystallographica. Section D, Biological Crystallography*, *66*(Pt 4), 486–501. https://doi.org/10.1107/S0907444910007493

Englund, P. T., Agbo, E. E. C., Lindsay, M. E., Liu, B., Liu, Y., Motyka, S. A., … Zhao, Z. (2005). RNAi libraries and kinetoplast DNA. *Biochemical Society Transactions*, *33*(6), 1409. https://doi.org/10.1042/BST0331409

Erlandsson Harris, H., & Andersson, U. (2004). Mini-review: the nuclear protein HMGB1 as a proinflammatory mediator. *European Journal of Immunology*, 34(6), 1503–1512.

Evans, P. (2006). Scaling and assessment of data quality. *Acta Crystallographica Section D Biological Crystallography*, *62*(1), 72–82. https://doi.org/10.1107/S0907444905036693

Evans, P. R., & Murshudov, G. N. (2013). How good are my data and what is the resolution? *Acta Crystallographica Section D: Biological Crystallography*, *69*(Pt 7), 1204–1214. http://doi.org/10.1107/S0907444913000061

Eze, A. A., Gould, M. K., Munday, J. C., Tagoe, D. N. A., Stelmanis, V., Schnaufer, A., & De Koning, H. P. (2016). Reduced Mitochondrial Membrane Potential Is a Late Adaptation of *Trypanosoma brucei brucei* to Isometamidium Preceded by Mutations in the γ Subunit of the F1Fo-ATPase. *PLOS Neglected Tropical Diseases*, *10*(8), e0004791. https://doi.org/10.1371/journal.pntd.0004791

Fairlamb, A. H. (2003). Chemotherapy of human African trypanosomiasis: current and future prospects. *Trends in Parasitology*, *19*(11), 488–494.

Feagin, J. E. (2000). Mitochondrial genome diversity in parasites. *International Journal for Parasitology*, *30*(4), 371–390.

Feig, M., & Pettitt, B. M. (1998), A molecular simulation picture of DNA hydration around A- and B-DNA. *Biopolymers*, 48: 199–209. https://doi.org/10.1002/(SICI)1097-0282(1998)48:4<199::AID-BIP2>3.0.CO;2-5

Feig, M., & Pettitt, B.M. (1998). A molecular simulation picture of DNA hydration around A- and B-DNA. *Biopolymers*, 48, 199–209. https://doi.org/10.1002/sici1097-0282

Fèvre, E. M., Picozzi, K., Jannin, J., Welburn, S. C., & Maudlin, I. (2006). Human African Trypanosomiasis: Epidemiology and Control. In David H. Molyneux (Ed.), *Advances in Parasitology* (Vol. Volume 61, pp. 167–221). Academic Press. https://doi.org/10.1016/S0065-308X(05)61005-6

Field, M. C., & Carrington, M. (2009). The trypanosome flagellar pocket. *Nature Reviews Microbiology*, 7(11), 775–786. https://doi.org/10.1038/nrmicro2221

Fitzgerald, D. J., & Anderson, J. N. (1999). Selective Nucleosome Disruption by Drugs That Bind in the Minor Groove of DNA. *Journal of Biological Chemistry*, 274(38), 27128–27138. https://doi.org/10.1074/jbc.274.38.27128

Flickinger, R. (2015). AT-rich repetitive DNA sequences, transcription frequency and germ layer determination. *Mechanisms of Development*, 138, Part 3, 227–232. https://doi.org/10.1016/j.mod.2015.10.004

Fonfría-Subirós, E., Acosta-Reyes, F., Saperas, N., Pous, J., Subirana, J. A., & Campos, J. L. (2012). Crystal Structure of a Complex of DNA with One AT-Hook of HMGA1. *PLoS ONE*, 7(5), e37120. https://doi.org/10.1371/journal.pone.0037120

Franco, J. R., Simarro, P. P., Diarra, A., & Jannin, J. G. (2014). Epidemiology of human African trypanosomiasis. *Clinical Epidemiology*, 6, 257–275. http://doi.org/10.2147/CLEP.S39728

Franklin, R. E., & Gosling, R. G. (1953). Molecular configuration in sodium thymonucleate. *Nature*, 171(4356), 740-1.

French, S. & Wilson, K. (1978). On the treatment of negative intensity observations. *Acta Crystallographica Section A: Crystal Physics, Diffraction, Theoretical and General Crystallography*, *34*(4), 517-525. https://doi.org/10.1107/S0567739478001114

Fujikane, R., Komori, K., Sekiguchi, M., & Hidaka, M. (2016). Function of high-mobility group A proteins in the DNA damage signaling for the induction of apoptosis. *Scientific Reports*, 6, 31714. http://doi.org/10.1038/srep31714

Fusco, A., & Fedele, M. (2007). Roles of HMGA proteins in cancer. *Nature Reviews Cancer*, 7(12), 899–910. https://doi.org/10.1038/nrc2271

Gangelhoff, T. A., Mungalachetty, P. S., Nix, J. C., & Churchill, M. E. A. (2009). Structural analysis and DNA binding of the HMG domains of the human mitochondrial transcription factor A. *Nucleic Acids Research*, 37(10), 3153–3164. http://doi.org/10.1093/nar/gkp157

Gao, N., Jiang, W., Gao, H., Cheng, Z., Qian, H., Si, S., & Xie, Y. (2013). Structural basis of human transcription factor Sry-related box 17 binding to DNA. *Protein and Peptide Letters*, 20(4), 481–488.

Garcia, H. G., Grayson, P., Han, L., Inamdar, M., Kondev, J., Nelson, P. C., … Wiggins, P. A. (2007). Biological consequences of tightly bent DNA: The other life of a macromolecular celebrity. *Biopolymers*, 85(2), 115–130. https://doi.org/10.1002/bip.20627

Gardner, M. J., Hall, N., Fung, E., White, O., Berriman, M., Hyman, R. W., … Barrell, B. (2002). Genome sequence of the human malaria parasite Plasmodium falciparum. *Nature*, 419(6906), 498–511. https://doi.org/10.1038/nature01097

Geggier, S., & Vologodskii, A. (2010). Sequence dependence of DNA bending rigidity. *Proceedings of the National Academy of Sciences*, 107(35), 15421–15426.

Geierstanger, B. H., Volkman, B. F., Kremer, W., & Wemmer, D. E. (1994). Short peptide fragments derived from HMG-I/Y proteins bind specifically to the minor groove of DNA. *Biochemistry*, 33(17), 5347–5355.

Gilbert, N., & Allan, J. (2014). Supercoiling in DNA and chromatin. *Current Opinion in Genetics & Development*, *25*(100), 15–21. http://doi.org/10.1016/j.gde.2013.10.013

Glass, L. S., Nguyen, B., Goodwin, K. D., Dardonville, C., Wilson, W. D., Long, E. C., & Georgiadis, M. M. (2009). Crystal Structure of a Trypanocidal 4,4′-Bis(imidazolinylamino)diphenylamine Bound to DNA ·. *Biochemistry*, *48*(25), 5943–5952. https://doi.org/10.1021/bi900204w

Gluenz, E., Povelones, M. L., Englund, P. T., & Gull, K. (2011). The Kinetoplast Duplication Cycle in *Trypanosoma brucei* Is Orchestrated by Cytoskeleton-Mediated Cell Morphogenesis. *Molecular and Cellular Biology*, 31(5), 1012–1021. https://doi.org/10.1128/MCB.01176-10

Goodwin, G.H., Sanders, C. & Johns, E.W. (1973). A new group of chromatin-associated proteins with a high content of acidic and basic amino acids. *European Journal of Biochemistry*, 38, 14-19.

Gurova, K. (2009). New hopes from old drugs: revisiting DNA-binding small molecules as anticancer agents. *Future Oncology (London, England)*, 5(10), 1685. http://doi.org/10.2217/fon.09.127

Halford, S. E., & Marko, J. F. (2004). How do site-specific DNA-binding proteins find their targets? *Nucleic Acids Research*, 32(10), 3040–3052. http://doi.org/10.1093/nar/gkh624

Hamilton, P. L., & Arya, D. P. (2012). Natural product DNA major groove binders. *Natural Product Reports*, 29(2), 134–143. https://doi.org/10.1039/c1np00054c

Hammarton, T. C. (2007). Cell cycle regulation in *Trypanosoma brucei*. *Molecular and Biochemical Parasitology*, 153(1-4), 1–8. http://doi.org/10.1016/j.molbiopara.2007.01.017

Hammarton, T. C., Clark, J., Douglas, F., Boshart, M., & Mottram, J. C. (2003). Stage-specific Differences in Cell Cycle Control in *Trypanosoma brucei* Revealed by RNA Interference of a Mitotic Cyclin. *Journal of Biological Chemistry*, 278(25), 22877–22886. https://doi.org/10.1074/jbc.M300813200

Hanks, J. H. & Wallace, R. E. (1949). Relation of Oxygen and Temperature in the Preservation of Tissues by Refrigeration. *Proceedings of the Society for Experimental Biology and Medicine*, *71*,196.

Hardman, C. H., Broadhurst, R. W., Raine, A. R., Grasser, K. D., Thomas, J. O. & Laue, E. D. (1995). *Biochemistry*, 34, 16596–16607.

Hart, C. M., & Laemmli, U. K. (1998). Facilitation of chromatin dynamics by SARs. *Current Opinion in Genetics & Development*, 8(5), 519–525. https://doi.org/10.1016/S0959-437X(98)80005-1

Herbst-Irmer, R. & Sheldrick, G. M. (1998). Refinement of twinned structures with SHELXL97. *Acta Crystallographica Section B: Structural Science*, *54*(4), 443-449. https://doi.org/10.1107/S0108768197018454

Hill, K. L. (2003). Biology and Mechanism of Trypanosome Cell Motility. *Eukaryotic Cell*, 2(2), 200–208. http://doi.org/10.1128/EC.2.2.200-208.2003

Hirumi, H. & Hirumi, K. (1989). Continuous cultivation of *Trypanosoma brucei* blood stream forms in a medium containing a low concentration of serum protein without feeder cell layers. *The Journal of Parasitology*, *75*(6), 985-989.

Hizver, J., Rozenberg, H., Frolow, F., Rabinovich, D., & Shakked, Z. (2001). DNA bending by an adenine–thymine tract and its role in gene regulation. *Proceedings of the National Academy of Sciences*, 98(15), 8490–8495.

Hock, R., Furusawa, T., Ueda, T., & Bustin, M. (2007). HMG chromosomal proteins in development and disease. *Trends in Cell Biology*, 17(2), 72–79. https://doi.org/10.1016/j.tcb.2006.12.001

Hofr, C., Farrell, N., & Brabec, V. (2001). Thermodynamic properties of duplex DNA containing a site-specific d(GpG) intrastrand crosslink formed by an antitumor dinuclear platinum complex. *Nucleic Acids Research*, 29(10), 2034–2040.

Hol, W. G. J. (2015). Three-dimensional structures in the design of therapeutics targeting parasitic protozoa: reflections on the past, present and future. Acta Crystallographica. *Section F, Structural Biology Communications*, 71(Pt 5), 485–499. https://doi.org/10.1107/S2053230X15004987

Hoogsteen, K. (1963). The crystal and molecular structure of a hydrogen-bonded complex between 1-methylthymine and 9-methyladenine. *Acta Crystallographica*, 16, 907-916. https://doi.org/10.1107/S0365110X63002437

Huang, G., Vercesi, A. E., & Docampo, R. (2013). Essential regulation of cell bioenergetics in *Trypanosoma brucei* by the mitochondrial calcium uniporter. *Nature Communications*, *4*, 2865. http://doi.org/10.1038/ncomms3865

Hud, N. V. and Plavec, J. (2003), A unified model for the origin of DNA sequence-directed curvature. *Biopolymers*, 69: 144–158. https://doi.org/10.1002/bip.10364

Hurley, C.K. (1977). Electrophoresis of histones: A modified Panyim and Chalkley system for slab gels. *Analytical Biochemistry, 80*, 624-626.

Huth, J. R., Bewley, C. A., Nissen, M. S., Evans, J. N. S., Reeves, R., Gronenborn, A. M., & Clore, G. M. (1997). The solution structure of an HMG-I(Y)-DNA complex defines a new architectural minor groove binding motif. *Nature Structural & Molecular Biology*, 4(8), 657–665. https://doi.org/10.1038/nsb0897-657

Ibrahim, H. M. S., Al-Salabi, M. I., El Sabbagh, N., Quashie, N. B., Alkhaldi, A. A. M., Escale, R., Smith, T. K., Vial, H. J., de Koning, H. P. (2011). Symmetrical choline-derived dications display strong anti-kinetoplastid activity. *Journal of Antimicrobial Chemotherapy*, *66*(1), 111–125. https://doi.org/10.1093/jac/dkq401

Javaherian, K., Liu, J.F. & Wang, J.C. (1978). Nonhistone proteins HMG1 and HMG2 change the DNA helical structure. *Science*. *199*, 1345-1346.

Jensen, R. E., Simpson, L., & Englund, P. T. (2008). What happens when *Trypanosoma brucei* leaves Africa. *Trends in Parasitology*, *24*(10), 428–431. https://doi.org/10.1016/j.pt.2008.06.007

Kabsch, W. (2010). *XDS. Acta Crystallographica Section D: Biological Crystallography*, *66*(Pt 2), 125–132. http://doi.org/10.1107/S0907444909047337

Kang, R., Zhang, Q., Zeh, H. J. 3rd, Lotze, M. T., & Tang, D. (2013). HMGB1 in cancer: good, bad, or both? *Clinical Cancer Research : An Official Journal of the American Association for Cancer Research*, 19(15), 4046–4057. https://doi.org/10.1158/1078-0432.CCR-13-0495

Kelly, B. L., Singh, G., & Aiyar, A. (2011). Molecular and cellular characterization of an AT-hook protein from Leishmania. *PloS One*, 6(6), e21412.

Kennedy, P. G. E. (2004). Human African trypanosomiasis of the CNS: current issues and challenges. Journal of Clinical Investigation, 113(4), 496–504. http://doi.org/10.1172/JCI200421052

Klingbeil, M. M., & Englund, P. T. (2004). Closing the gaps in kinetoplast DNA network replication. *Proceedings of the National Academy of Sciences of the United States of America*, *101*(13), 4333–4334. https://doi.org/10.1073/pnas.0401400101

Koch, E. Twinning. *In International Tables for Crystallography Volume C: Mathematical, physical and chemical tables*, pages 10-14. Springer, 2004.

Kowalski, D., & Eddy, M. J. (1989). The DNA unwinding element: a novel, cis-acting component that facilitates opening of the Escherichia coli replication origin. *The EMBO Journal*, 8(13), 4335-4344.

Krauss, I. R., Merlino, A., Vergara, A., & Sica, F. (2013). An Overview of Biological Macromolecule Crystallization. *International Journal of Molecular Sciences*, *14*(6), 11643–11691. http://doi.org/10.3390/ijms140611643

Laemmli, U. K. (1970). Cleavage of structural proteins during the assembly of the head of bacteriophage T4. *Nature*, *227*(5259), 680–685.

Lai, D.-H., Hashimi, H., Lun, Z.-R., Ayala, F. J., & Lukes, J. (2008). Adaptations of *Trypanosoma brucei* to gradual loss of kinetoplast DNA: *Trypanosoma equiperdum* and *Trypanosoma evansi* are petite mutants of *T. brucei*. *Proceedings of the National Academy of Sciences of the United States of America*, *105*(6), 1999–2004. https://doi.org/10.1073/pnas.0711799105

Lamb, T. (2012). *Immunity to Parasitic Infection*. John Wiley & Sons. Retrieved from https://books.google.es/books?id=METSVw5k3LwC

Langousis, G. & Hill, K. L. (2014). Motility and more: the flagellum of *Trypanosoma brucei*. *Nature Reviews Microbiologyl,* 12, 505–518. http://doi.org/10.1038/nrmicro3274

Lanteri, C. A., Tidwell, R. R., & Meshnick, S. R. (2008). The Mitochondrion Is a Site of Trypanocidal Action of the Aromatic Diamidine DB75 in Bloodstream Forms of *Trypanosoma brucei*. *Antimicrobial Agents and Chemotherapy*, *52*(3), 875–882. http://doi.org/10.1128/AAC.00642-07

Li, L., Yoder, K., Hansen, M. S. T., Olvera, J., Miller, M. D., & Bushman, F. D. (2000). Retroviral cDNA Integration: Stimulation by HMG I Family Proteins. *Journal of Virology*, 74(23), 10965–10974.

Lim, J.-H., West, K. L., Rubinstein, Y., Bergel, M., Postnikov, Y. V., & Bustin, M. (2005). Chromosomal protein HMGN1 enhances the acetylation of lysine 14 in histone H3. *The EMBO Journal*, 24(17), 3038–3048. http://doi.org/10.1038/sj.emboj.7600768

Lindemose, S., Nielsen, P. E., Hansen, M., & Mollegaard, N. E. (2011). A DNA minor groove electronegative potential genome map based on photo-chemical probing. *Nucleic Acids Research*, 39(14), 6269–6276. https://doi.org/10.1093/nar/gkr204

Lotze, M. T., & Tracey, K. J. (2005). High-mobility group box 1 protein (HMGB1): nuclear weapon in the immune arsenal. *Nature Reviews Immunology*, 5(4), 331–342. https://doi.org/10.1038/nri1594

Lu, X.-J., & Olson, W. K. (2003). 3DNA: a software package for the analysis, rebuilding and visualization of three-dimensional nucleic acid structures. *Nucleic Acids Research*, *31*(17), 5108–5121. https://doi.org/10.1093/nar/gkg680

Luijsterburg, M. S., White, M. F., van Driel, R., & Dame, R. T. (2008). The Major Architects of Chromatin: Architectural Proteins in Bacteria, Archaea and Eukaryotes. *Critical Reviews in Biochemistry and Molecular Biology*, 43(6), 393–418. https://doi.org/10.1080/10409230802528488

Lukes, J., Lys Guilbride, D., Votypka, J., Zikova, A., Benne, R., & Englund, P. T. (2002). Kinetoplast DNA Network: Evolution of an Improbable Structure. *Eukaryotic Cell*, *1*(4), 495–502. https://doi.org/10.1128/EC.1.4.495-502.2002

Macrì, S., Simula, L., Pellarin, I., Pegoraro, S., Onorati, M., Sgarra, R., Manfioletti, G., & Vignali, R. (2016). Hmga2 is required for neural crest cell specification in Xenopus laevis. *Developmental Biology*, 411(1), 25–37. https://doi.org/10.1016/j.ydbio.2016.01.014

Markell, EK, John, DT & Krotoski, WA. (2006). *Markell and Voge's Medical Parasitology*. 9th edition. Saunders Company: USA.

Maroso, M., Balosso, S., Ravizza, T., Liu, J., Aronica, E., Iyer, A. M., … Vezzani, A. (2010). Toll-like receptor 4 and high-mobility group box-1 are involved in ictogenesis and can be targeted to reduce seizures. *Nature Medicine*, *16*(4), 413–419. https://doi.org/10.1038/nm.2127

Martinez de Ilarduya, I., De Luchi, D., Subirana, J. A., Campos, J. L., & Uson, I. (2010). A geometric approach to the crystallographic solution of nonconventional DNA structures: helical superstructures of d(CGATAT). *Angewandte Chemie (International Ed. in English)*, *49*(43), 7920–7922. https://doi.org/10.1002/anie.201003647

Mathis, A. M., Holman, J. L., Sturk, L. M., Ismail, M. A., Boykin, D. W., Tidwell, R. R., & Hall, J. E. (2006). Accumulation and Intracellular Distribution of Antitrypanosomal Diamidine Compounds DB75 and DB820 in African Trypanosomes. *Antimicrobial Agents and Chemotherapy*, *50*(6), 2185–2191. https://doi.org/10.1128/AAC.00192-06

Matovu, E., Stewart, M. L., Geiser, F., Brun, R., Maser, P., Wallace, L. J. M., Burchmore, R. J., Enyaru, J. C. K., Barrett, M. P., Kaminsky, R., Seebeck, T., & de Koning, H. P. (2003). Mechanisms of Arsenical and Diamidine Uptake and Resistance in *Trypanosoma brucei*. *Eukaryotic Cell*, *2*(5), 1003–1008. https://doi.org/10.1128/EC.2.5.1003-1008.2003

Matthews, K. R. (2005). The developmental cell biology of *Trypanosoma brucei*. *Journal of Cell Science*, 118(Pt 2), 283–290. http://doi.org/10.1242/jcs.01649

Mattick, J. S. (2009). The Genetic Signatures of Noncoding RNAs. *PLoS Genetics*, 5(4), e1000459. https://doi.org/10.1371/journal.pgen.1000459

McCoy, A. J., Grosse-Kunstleve, R. W., Adams, P. D., Winn, M. D., Storoni, L. C., & Read, R. J. (2007). *Phaser* crystallographic software. *Journal of Applied Crystallography*, *40*(4), 658–674. https://doi.org/10.1107/S0021889807021206

McKean, P. (2003), Coordination of cell cycle and cytokinesis in *Trypanosoma brucei*. *Current Opinion in Microbiology, 6*, 600-607.

McNicholas, S., Potterton, E., Wilson, K. S., & Noble, M. E. M. (2011). Presenting your structures: the *CCP*4*mg* molecular-graphics software. *Acta Crystallographica Section D: Biological Crystallography*, *67*(Pt 4), 386–394. http://doi.org/10.1107/S0907444911007281

Miao, Y., Cui, T., Leng, F., & Wilson, W. D. (2008). Inhibition of high-mobility-group A2 protein binding to DNA by netropsin: A biosensor-surface plasmon resonance assay. *Analytical Biochemistry*, *374*(1), 7–15. https://doi.org/10.1016/j.ab.2007.10.023

Mitra, S. N., Wahl, M. C., & Sundaralingam, M. (1999). Structure of the side-by-side binding of distamycin to d(GTATATAC)2. *Acta Crystallographica. Section D, Biological Crystallography*, *55*(Pt 3), 602–609.

Montalvo-Quirós, S., Taladriz-Sender, A., Kaiser, M., & Dardonville, C. (2015). Antiprotozoal activity and DNA binding of dicationic acridones. *Journal of Medicinal Chemistry*, *58*(4), 1940–1949. https://doi.org/10.1021/jm5018303

Morávek, Z., Neidle, S., & Schneider, B. (2002). Protein and drug interactions in the minor groove of DNA. *Nucleic Acids Research*, *30*(5), 1182–1191.

Moreno, T., Pous, J., Subirana, J. A., & Campos, J. L. (2010). Coiled-coil conformation of a pentamidine–DNA complex. *Acta Crystallographica Section D Biological Crystallography*, *66*(3), 251–257. https://doi.org/10.1107/S0907444909055693

Murshudov, G. N., Skubák, P., Lebedev, A. A., Pannu, N. S., Steiner, R. A., Nicholls, R. A., Winn, M. D., Long, F. & Vagin, A. A. (2011). *REFMAC* 5 for the refinement of macromolecular crystal structures. *Acta Crystallographica Section D Biological Crystallography*, *67*(4), 355–367. https://doi.org/10.1107/S0907444911001314

Nagle, A. S., Khare, S., Kumar, A. B., Supek, F., Buchynskyy, A., Mathison, C. J. N., … Molteni, V. (2014). Recent Developments in Drug Discovery for Leishmaniasis and Human African Trypanosomiasis. *Chemical Reviews*, 114(22), 11305–11347. http://doi.org/10.1021/cr500365f

Nagle, P. S., Quinn, S. J., Kelly, J. M., O'Donovan, D. H., Khan, A. R., Rodríguez, F., … Rozas, I. (2010). Understanding the DNA binding of novel non-symmetrical guanidinium/2-aminoimidazolinium derivatives. *Organic & Biomolecular Chemistry*, *8*(24), 5558. https://doi.org/10.1039/c0ob00428f

Nagle, P. S., Rodríguez, F., Nguyen, B., Wilson, W. D., & Rozas, I. (2012). High DNA Affinity of a Series of Peptide Linked Diaromatic Guanidinium-like Derivatives. *Journal of Medicinal Chemistry*, *55*(9), 4397–4406. https://doi.org/10.1021/jm300296f

Narlikar, L., & Ovcharenko, I. (2009). Identifying regulatory elements in eukaryotic genomes. *Briefings in Functional Genomics and Proteomics*, 8(4), 215–230. https://doi.org/10.1093/bfgp/elp014

Ndjonka, D., Rapado, L. N., Silber, A. M., Liebau, E., & Wrenger, C. (2013). Natural Products as a Source for Treating Neglected Parasitic Diseases. *International Journal of Molecular Sciences*, 14(2), 3395–3439. http://doi.org/10.3390/ijms14023395

Ngo, H. B., Kaiser, J. T., & Chan, D. C. (2011). Tfam, a mitochondrial transcription and packaging factor, imposes a U-turn on mitochondrial DNA. *Nature Structural & Molecular Biology*, *18*(11), 1290–1296. http://doi.org/10.1038/nsmb.2159

Ngo, H. B., Lovely, G. A., Phillips, R., & Chan, D. C. (2014). Distinct structural features of TFAM drive mitochondrial DNA packaging versus transcriptional activation. *Nature Communications*, 5, 3077. http://doi.org/10.1038/ncomms4077

Nguyen, B., & Wilson, W. D. (2009). The Effects of Hairpin Loops on Ligand−DNA Interactions. *The Journal of Physical Chemistry B*, *113*(43), 14329–14335. https://doi.org/10.1021/jp904830m

Nieto, L., Mascaraque, A., Miller, F., Glacial, F., Ríos Martínez, C., Kaiser, M., Brun, R., & Dardonville, C. (2011). Synthesis and Antiprotozoal Activity of N -Alkoxy Analogues of the Trypanocidal Lead Compound 4,4′-Bis(imidazolinylamino)diphenylamine with Improved Human Blood−Brain Barrier Permeability. *Journal of Medicinal Chemistry*, 54(2), 485–494. https://doi.org/10.1021/jm101335q

Ogbadoyi, E. O., Robinson, D. R., & Gull, K. (2003). A High-Order Trans-Membrane Structural Linkage Is Responsible for Mitochondrial Genome Positioning and Segregation by Flagellar Basal Bodies in Trypanosomes. *Molecular Biology of the Cell, 14*(5), 1769–1779. https://doi.org/10.1091/mbc.E02-08-0525

Oguey, C., Foloppe, N., & Hartmann, B. (2010). Understanding the Sequence-Dependence of DNA Groove Dimensions: Implications for DNA Interactions. PLoS *ONE*, 5(12), e15931. https://doi.org/10.1371/journal.pone.0015931

Oh, D.-B., Kim, Y.-G., & Rich, A. (2002). Z-DNA-binding proteins can act as potent effectors of gene expression *in vivo*. *Proceedings of the National Academy of Sciences*, 99(26), 16666–16671.

Ohe, K., Lalli, E., & Sassone-Corsi, P. (2002). A direct role of SRY and SOX proteins in pre-mRNA splicing. Proceedings of the National Academy of Sciences of the United States of America, 99(3), 1146–1151. http://doi.org/10.1073/pnas.022645899

Ohndorf, U.-M., Rould, M. A., He, Q., Pabo, C. O., & Lippard, S. J. (1999). Basis for recognition of cisplatin-modified DNA by high-mobility-group proteins. *Nature*, 399(6737), 708–712. https://doi.org/10.1038/21460

Ozturk, N., Singh, I., Mehta, A., Braun, T., & Barreto, G. (2014). HMGA proteins as modulators of chromatin structure during transcriptional activation. *Frontiers in Cell and Developmental Biology*, 2, 5. http://doi.org/10.3389/fcell.2014.00005

Paine, M. F., Wang, M. Z., Generaux, C. N., Boykin, D. W., Wilson, W. D., De Koning, H. P., … Tidwell, R. R. (2010). Diamidines for human African trypanosomiasis. *Current Opinion in Investigational Drugs (London, England : 2000)*, *11*(8), 876–883.

Pandit, K. V., Corcoran, D., Yousef, H., Yarlagadda, M., Tzouvelekis, A., Gibson, K. F., … Kaminski, N. (2010). Inhibition and Role of let-7d in Idiopathic Pulmonary Fibrosis. *American Journal of Respiratory and Critical Care Medicine*, 182(2), 220–229. http://doi.org/10.1164/rccm.200911-1698OC

Panyim, S., & Chalkley, R. (1969). High resolution acrylamide gel electrophoresis of histones. *Archives of Biochemistry and Biophysics*, *130*(1), 337–346.

Patterson, A. L. (1934). A fourier series method for the determination of the components of interatomic distances in crystals. *Physical Review*, *46*(5), 372. https://doi.org/10.1103/PhysRev.46.372

Paul, A., & Bhattacharya, S. (2012). Chemistry and biology of DNA-binding small molecules. Current Science, 102(2), 212-231.

Paul, A., Nanjunda, R., Kumar, A., Laughlin, S., Nhili, R., Depauw, S., … Wilson, W. D. (2015). Mixed up minor groove binders: Convincing A·T specific compounds to recognize a G·C base pair. Bioorganic & Medicinal Chemistry Letters, 25(21), 4927–4932. https://doi.org/10.1016/j.bmcl.2015.05.005

Petersen, K., Leah, R., Knudsen, S., & Cameron-Mills, V. (2002). Matrix attachment regions (MARs) enhance transformation frequencies and reduce variance of transgene expression in barley. *Plant Molecular Biology*, 49(1), 45–58.

Pflugrath, J. (2004). Macromolecular cryocrystallography?methods for cooling and mounting protein crystals at cryogenic temperatures. *Methods*, *34*(3), 415–423. https://doi.org/10.1016/j.ymeth.2004.03.032

Pjura, P. E., Grzeskowiak, K., & Dickerson, R. E. (1987). Binding of Hoechst 33258 to the minor groove of B-DNA. *Journal of Molecular Biology*, 197(2), 257–271.

Potaman, V.N., & Sinden, R.R. (2000-2013). DNA: Alternative Conformations and Biology. In: Madame Curie Bioscience Database [Internet]. *Landes Bioscience*. Available from: https://www.ncbi.nlm.nih.gov/books/NBK6545/

Povelones, M. L. (2014). Beyond replication: division and segregation of mitochondrial DNA in kinetoplastids. *Molecular and Biochemical Parasitology*, *196*(1), 53–60. https://doi.org/10.1016/j.molbiopara.2014.03.008

Priotto, G., Kasparian, S., Mutombo, W., Ngouama, D., Ghorashian, S., Arnold, U., Ghabri, S., Baudin, E., Buard, V., Kazadi-Kyanza, S., et al. (2009). Nifurtimox-eflornithine combination therapy for second-stage African *Trypanosoma brucei gambiense* trypanosomiasis: a multicentre, randomised, phase III, non-inferiority trial. *The Lancet*, *374*(9683), 56–64. https://doi.org/10.1016/S0140-6736(09)61117-X

Rabilloud, T., Vuillard, L., Gilly, C., & Lawrence, J. J. (1994). Silver-staining of proteins in polyacrylamide gels: a general overview. *Cellular and Molecular Biology (Noisy-Le-Grand, France)*, *40*(1), 57–75.

Radic, M. Z., Lundgren, K., & Hamkalo, B. A. (1987). Curvature of mouse satellite DNA and condensation of heterochromatin. *Cell*, 50(7), 1101–1108.

Rajewska, M., Wegrzyn, K., & Konieczny, I. (2012). AT-rich region and repeated sequences – the essential elements of replication origins of bacterial replicons. *FEMS*

Microbiology Reviews, 36(2), 408–434. https://doi.org/10.1111/j.1574-6976.2011.00300.x

Ralston, K. S., & Hill, K. L. (2008). The flagellum of *Trypanosoma brucei*: new tricks from an old dog. *International Journal for Parasitology*, 38(8-9), 869–884. http://doi.org/10.1016/j.ijpara.2008.03.003

Ray, D. S. (1989). Conserved sequence blocks in kinetoplast minicircles from diverse species of trypanosomes. *Molecular and Cellular Biology*, *9*(3), 1365–1367.

Reeves, R. (2001). Molecular biology of HMGA proteins: hubs of nuclear function. *Gene*, 277(1), 63–81.

Reeves, R. (2010). HMG Nuclear Proteins: Linking Chromatin Structure to Cellular Phenotype. *Biochimica et Biophysica Acta*, 1799(1-2), 3. http://doi.org/10.1016/j.bbagrm.2009.09.001

Rentzeperis, D., Marky, L. A., Dwyer, T. J., Geierstanger, B. H., Pelton, J. G., & Wemmer, D. E. (1995). Interaction of minor groove ligands to an AAATT/AATTT site: correlation of thermodynamic characterization and solution structure. *Biochemistry*, 34(9), 2937–2945.

Ríos Martínez, C. H., Lagartera, L., Kaiser, M., & Dardonville, C. (2014). Antiprotozoal activity and DNA binding of N-substituted N-phenylbenzamide and 1,3-diphenylurea bisguanidines. *European Journal of Medicinal Chemistry*, 81, 481–491. https://doi.org/10.1016/j.ejmech.2014.04.083

Ríos Martínez, C. H., Lagartera, L., Trujillo, C., & Dardonville, C. (2015a). Bisimidazoline arylamides binding to the DNA minor groove: N1-hydroxylation enhances binding affinity and selectivity to AATT sites. *Med. Chem. Commun.*, *6*(11), 2036–2042. https://doi.org/10.1039/C5MD00292C

Ríos Martínez, C. H., Miller, F., Ganeshamoorthy, K., Glacial, F., Kaiser, M., de Koning, H. P., Eze, A. A., Lagartera, L., Herraiz, Dardonville, C. (2015c). A New Nonpolar *N* -Hydroxy Imidazoline Lead Compound with Improved Activity in a Murine Model of Late-Stage

Trypanosoma brucei brucei Infection Is Not Cross-Resistant with Diamidines. *Antimicrobial Agents and Chemotherapy*, *59*(2), 890–904. https://doi.org/10.1128/AAC.03958-14

Ríos Martínez, C. H., Nué Martínez, J. J., Ebiloma, G. U., de Koning, H. P., Alkorta, I., & Dardonville, C. (2015b). Lowering the pKa of a bisimidazoline lead with halogen atoms results in improved activity and selectivity against *Trypanosoma brucei in vitro*. *European Journal of Medicinal Chemistry*, *101*, 806–817. https://doi.org/10.1016/j.ejmech.2015.07.013

Rodríguez, F., Rozas, I., Kaiser, M., Brun, R., Nguyen, B., Wilson, W. D., … Dardonville, C. (2008). New Bis(2-aminoimidazoline) and Bisguanidine DNA Minor Groove Binders with Potent *in Vivo* Antitrypanosomal and Antiplasmodial Activity. *Journal of Medicinal Chemistry*, 51(4), 909–923. https://doi.org/10.1021/jm7013088

Roeder, R. G. (1996). The role of general initiation factors in transcription by RNA polymerase II. *Trends in Biochemical Sciences*, 21, 327-335.

Rong, H., Li, Y., Shi, X., Zhang, X., Gao, Y., Dai, H., Teng, M.K., Niu, L.W., Liu, Q., Hao, Q. (2007). Structure of human upstream binding factor HMG box 5 and site for binding of the cell-cycle regulatory factor TAF1. *Acta Crystallographica Section D Biological Crystallography*, 63, 730-737. https://doi.org/10.1107/S0907444907017027

Roque, A., Orrego, M., Ponte, I., & Suau, P. (2004). The preferential binding of histone H1 to DNA scaffold-associated regions is determined by its C-terminal domain. *Nucleic Acids Research*, 32(20), 6111–6119. http://doi.org/10.1093/nar/gkh945

Roussel, A., Inisan, A., Knoops-Mouthuy, E. & Cambillau, E. Turbo-Frodo Version OpenGL.1 University of Marseille. *Silicon Graphics, Mountain View, CA* , 1998.

Roy Chowdhury A, Bakshi R, Wang J, Yildirir G, Liu B, Pappas-Brown V, et al. (2010) The Killing of African Trypanosomes by Ethidium Bromide. *PLOS Pathogens* 6(12), e1001226. https://doi.org/10.1371/journal.ppat.1001226

Rubio-Cosials, A., Sidow, J.F., Jimenez-Menendez, N., Fernandez-Millan, P., Montoya, J., Jacobs, H.T., Coll, M., Bernado, P., Sola, M. (2011). Human mitochondrial transcription factor A induces a U-turn structure in the light strand promoter. *Nature Structural & Molecular Biology*. 18: 1281-1289. http://doi.org/10.1038/nsmb.2160

Sánchez-Giraldo, R., Acosta-Reyes, F. J., Malarkey, C. S., Saperas, N., Churchill, M. E. A., & Campos, J. L. (2015). Two high-mobility group box domains act together to underwind and kink DNA. *Acta Crystallographica Section D Biological Crystallography*, 71(7), 1423–1432. https://doi.org/10.1107/S1399004715007452

Sarai, A., Mazur, J., Nussinov, R., & Jernigan, R.L. (1989). Sequence dependence of DNA conformational flexibility. *Biochemistry*, 28(19), 7842–7849. 418. https://doi.org/10.1021/bi00445a046

Scaffidi, P., Misteli, T., & Bianchi, M. E. (2002). Release of chromatin protein HMGB1 by necrotic cells triggers inflammation. *Nature*, 418(6894), 191–195. https://doi.org/10.1038/nature00858

Schnaufer, A., Clark-Walker, G. D., Steinberg, A. G., & Stuart, K. (2005). The F_1-ATP synthase complex in bloodstream stage trypanosomes has an unusual and essential function. *The EMBO Journal*, *24*(23), 4029–4040. http://doi.org/10.1038/sj.emboj.7600862

Schneider, B., Neidle, S., Berman, H.M. (1997). Conformations of the sugar-phosphate backbone in helical DNA crystal structures. *Biopolymers*, 42, 113–124. https://doi.org/10.1002/(SICI)1097-0282(199707)42:1<113::AID-BIP10>3.0.CO;2-0

Schrödinger, LLC. (2015). The PyMOL molecular graphics system, version 1.8.

Scocca, J. R., & Shapiro, T. A. (2008). A mitochondrial topoisomerase IA essential for late theta structure resolution in African trypanosomes. *Molecular Microbiology*, *67*(4), 820–829. https://doi.org/10.1111/j.1365-2958.2007.06087.x

Scott, F. J., Khalaf, A. I., Giordani, F., Wong, P. E., Duffy, S., Barrett, M., ... Suckling, C. J. (2016). An evaluation of Minor Groove Binders as anti-*Trypanosoma brucei brucei*

therapeutics. *European Journal of Medicinal Chemistry*, 116, 116–125. http://doi.org/10.1016/j.ejmech.2016.03.064

Scott, W. G., Finch, J. T., Grenfell, R., Fogg, J., Smith, T., Gait, M. J., & Klug, A. (1995). Rapid crystallization of chemically synthesized hammerhead RNAs using a double screening procedure. *Journal of Molecular Biology*, *250*(3), 327–332. https://doi.org/10.1006/jmbi.1995.0380

Sela, D., Milman, N., Kapeller, I., Zick, A., Bezalel, R., Yaffe, N., & Shlomai, J. (2008). Unique Characteristics of the Kinetoplast DNA Replication Machinery Provide Potential Drug Targets in Trypanosomatids. In H. K. Majumder (Ed.), *Drug Targets in Kinetoplastid Parasites* (pp. 9–21). New York, NY: Springer New York. https://doi.org/10.1007/978-0-387-77570-8_2

Shah, S. N., & Resar, L. M. S. (2012). High mobility group A1 and cancer: Potential biomarker and therapeutic target (review). *Histology and Histopathology*, 27, 567-579.

Shapiro, T. A., & Englund, P. T. (1995). The structure and replication of kinetoplast DNA. *Annual Review of Microbiology*, *49*, 117–143. https://doi.org/10.1146/annurev.mi.49.100195.001001

Sheng, J., Gan, J., & Huang, Z. (2013). Structure-Based DNA-Targeting Strategies with Small Molecule Ligands for Drug Discovery: TARGETING DNAs VIA STRUCTURAL INVESTIGATIONS. *Medicinal Research Reviews*, 33(5), 1119–1173. https://doi.org/10.1002/med.21278

Sicard, F., Destainville, N., & Manghi, M. (2016). DNA denaturation bubbles: Free-energy landscape and nucleation/closure rates. *The Journal of Chemical Physics*, 142, 034903. http://dx.doi.org/10.1063/1.4905668

Slama-Schwok, A., Zakrzewska, K., Leger, G., Leroux, Y., Takahashi, M., Käs, E., & Debey, P. (2000). Structural changes induced by binding of the high-mobility group I protein to a mouse satellite DNA sequence. *Biophysical Journal*, *78*(5), 2543–2559.

Smith, A. E., & Buchmueller, K. L. (2011). Molecular basis for the inhibition of HMGA1 proteins by distamycin A. *Biochemistry*, *50*(38), 8107–8116. https://doi.org/10.1021/bi200822c

Soeiro, M. N. C., Werbovetz, K., Boykin, D. W., Wilson, W. D., Wang, M. Z., & Hemphill, A. (2013). Novel amidines and analogues as promising agents against intracellular parasites: a systematic review. *Parasitology*, *140*(8), 10.1017/S0031182013000292. http://doi.org/10.1017/S0031182013000292

Stott, K., Tang, G. S. F., Lee, K.-B., & Thomas, J. O. (2006). Structure of a Complex of Tandem HMG Boxes and DNA. *Journal of Molecular Biology*, *360*(1), 90–104. https://doi.org/10.1016/j.jmb.2006.04.059

Strekowski, L., & Wilson, B. (2007). Noncovalent interactions with DNA: an overview. *Mutation Research*, 623(1–2), 3–13. https://doi.org/10.1016/j.mrfmmm.2007.03.008

Štros, M. (2010). HMGB proteins: Interactions with DNA and chromatin. *Biochimica et Biophysica Acta (BBA) - Gene Regulatory Mechanisms*, *1799*(1-2), 101–113. https://doi.org/10.1016/j.bbagrm.2009.09.008

Štros, M., Štokrová, J., & Thomas, J. O. (1994). DNA looping by the HMG-box domains of HMG1 and modulation of DNA binding by the acidic C-terminal domain. *Nucleic Acids Research*, *22*(6), 1044–1051.

Szempruch, A. J., Choudhury, R., Wang, Z., & Hajduk, S. L. (2015). *In vivo* analysis of trypanosome mitochondrial RNA function by artificial site-specific RNA endonuclease-mediated knockdown. *RNA*, *21*(10), 1781–1789. http://doi.org/10.1261/rna.052084.115

Tang, D., Kang, R., Zeh III, H. J., & Lotze, M. T. (2010). High-mobility group box 1 and cancer. *Biochimica et Biophysica Acta (BBA) - Gene Regulatory Mechanisms*, 1799(1-2), 131–140. https://doi.org/10.1016/j.bbagrm.2009.11.014

Teo, S. H., Grasser, K. D., & Thomas, J. O. (1995). Differences in the DNA-binding properties of the HMG-box domains of HMG1 and the sex-determining factor SRY. *Eur. J. Biochem. 230*, 943-950. https://doi.org/10.1111/j.1432-1033.1995.0943g.x

Tidwell. R.R, Boykin, D.W. (2003). *DNA and RNA Binders: From Small Molecules to Drugs.* Demeunynck, M., Bailly, C., Wilson, W.D., editors. Vol. 2, 414–460. Weinheim: WILEY-VCH.

Tolstorukov, M. Y., Ivanov, V. I., Malenkov, G. G., Jernigan, R. L., & Zhurkin, V. B. (2001). Sequence-dependent B↔ A transition in DNA evaluated with dimeric and trimeric scales. *Biophysical Journal*, 81(6), 3409–3421.

Tolstorukov, M. Y., Virnik, K. M., Adhya, S., & Zhurkin, V. B. (2005). A-tract clusters may facilitate DNA packaging in bacterial nucleoid. *Nucleic Acids Research*, 33(12), 3907–3918. https://doi.org/10.1093/nar/gki699

Travers, A. A. (2004). The structural basis of DNA flexibility. *Philosophical Transactions Series A Mathematical Physical and Engineering Sciences*, 362:1423–1438. http://dx.doi.org/10.1098/rsta.2004.1390

Vagin, A., & Teplyakov, A. (2010). Molecular replacement with MOLREP. *Acta Crystallographica. Section D, Biological Crystallography*, *66*(Pt 1), 22–25. https://doi.org/10.1107/S0907444909042589

Vaguine, A. A., Richelle, J., & Wodak, S. J. (1999). SFCHECK: a unified set of procedures for evaluating the quality of macromolecular structure-factor data and their agreement with the atomic model. *Acta Crystallographica. Section D, Biological Crystallography*, *55*(Pt 1), 191–205. https://doi.org/10.1107/S0907444998006684

Varani, G., & McClain, W. H. (2000). The G·U wobble base pair: A fundamental building block of RNA structure crucial to RNA function in diverse biological systems. *EMBO Reports*, *1*(1), 18–23. http://doi.org/10.1093/embo-reports/kvd001

Vassella, E., Straesser, K., & Boshart, M. (1997). A mitochondrion-specific dye for multicolour fluorescent imaging of *Trypanosoma brucei*. *Molecular and Biochemical Parasitology*, *90*(1), 381–385.

Vignali, R., Macrì, S., Onorati, M., Basaldella, E., Sgarra, R., Manfioletti, G. (2008). HMGA proteins in *Xenopus laevis*. *Developmental Biology*, 319, 587–598.

Wang, A. H.-J., Quigley, G. J., Kolpak, F. J., Crawford, J. L., van Boom, J. H., van der Marel, G., & Rich, A. (1979). Molecular structure of a left-handed double helical DNA fragment at atomic resolution. Nature, 282(5740), 680–686. https://doi.org/10.1038/282680a0

Wang, J., Pappas-Brown, V., Englund, P. T., & Jensen, R. E. (2014). TbKAP6, a Mitochondrial HMG Box-Containing Protein in *Trypanosoma brucei*, Is the First Trypanosomatid Kinetoplast-Associated Protein Essential for Kinetoplast DNA Replication and Maintenance. *Eukaryotic Cell*, 13(7), 919–932. https://doi.org/10.1128/EC.00260-13

Wang, M., Yu, Y., Liang, C., Lu, A., & Zhang, G. (2016). Recent Advances in Developing Small Molecules Targeting Nucleic Acid. *International Journal of Molecular Sciences*, 17(6), 779. https://doi.org/10.3390/ijms17060779

Wang, Z., & Englund, P. T. (2001). RNA interference of a trypanosome topoisomerase II causes progressive loss of mitochondrial DNA. *The EMBO Journal*, *20*(17), 4674–4683. https://doi.org/10.1093/emboj/20.17.4674

Waring, M. J., Chaires, J. B. and Armitage, B. A. (2005). DNA binders and related subjects. *Springer Science & Business Media*, volume 253.

Watson, J. D., & Crick, F. H. C. (1953). A Structure for Deoxyribose Nucleic Acid. *Nature*, 171, 737-738.

Watson, J. D., Baker, T. A,. Bell, S. P., Gann, A., Levine, M., and Losick, R. (2008). Molecular biology of the gene. 6th edition. San Francisco Cold Spring Harbor, Pearson/Benjamin Cummings; Cold Spring Harbor Laboratory Press, New York.

Weir, H. M., Kraulis, P. J., Hill, C. S., Raine, A. R., Laue, E. D., & Thomas, J. O. (1993). Structure of the HMG box motif in the B-domain of HMG1. *The EMBO Journal*, 12(4), 1311–1319.

Wemmer, D. E., & Dervan, P. B. (1997). Targeting the minor groove of DNA. *Current Opinion in Structural Biology*, 7(3), 355–361.

Whelan, D. R., Hiscox, T. J., Rood, J. I., Bambery, K. R., McNaughton, D., & Wood, B. R. (2014). Detection of an en masse and reversible B- to A-DNA conformational transition in prokaryotes in response to desiccation. *Journal of The Royal Society Interface*, *11*(97), 20140454–20140454. https://doi.org/10.1098/rsif.2014.0454

WHO Media centre (2017). "Fact sheet N°259: Trypanosomiasis, Human African (sleeping sickness)". World Health Organization. Retrieved 17 April 2017.

Wilson, L., Bray, T. & Suddath, F. (1991). Crystallization of proteins by dynamic control of evaporation. *Journal of Crystal Growth* , *110*(1), 142-147. https://doi.org/10.1016/0022-0248(91)90877-8

Wilson, W. D., Tanious, F. A., Mathis, A., Tevis, D., Hall, J. E., & Boykin, D. W. (2008). Antiparasitic compounds that target DNA. *Biochimie*, 90(7), 999–1014. https://doi.org/10.1016/j.biochi.2008.02.017

Winn, M. D., Ballard, C. C., Cowtan, K. D., Dodson, E. J., Emsley, P., Evans, P. R., ... Wilson, K. S. (2011). Overview of the *CCP* 4 suite and current developments. *Acta Crystallographica Section D Biological Crystallography*, *67*(4), 235–242. https://doi.org/10.1107/S0907444910045749

Woodward, R., & Gull, K. (1990). Timing of nuclear and kinetoplast DNA replication and early morphological events in the cell cycle of *Trypanosoma brucei*. Journal of Cell Science, 95(1), 49–57.

World Health Organization and Department of control of neglected tropical diseases. (2016). Report of the second WHO stakeholders meeting on gambiense human African trypanosomiasis elimination, Geneva, 21–23 March 2016. WHO/HTM/NTD/IDM/2016.4

World Health Organization and Department of control of neglected tropical diseases. (2017). Integrating neglected tropical diseases into global health and development: fourth WHO report on neglected tropical diseases. vi, 267. WHO/HTM/NTD/2017.01

World Health Organization. (2015). World health statistics 2015. Geneva: World Health Organization.

Xu, C. W., Hines, J. C., Engel, M. L., Russell, D. G., & Ray, D. S. (1996). Nucleus-encoded histone H1-like proteins are associated with kinetoplast DNA in the trypanosomatid Crithidia fasciculata. *Molecular and Cellular Biology*, *16*(2), 564–576.

Yakovchuk, P., Protozanova, E., & Frank-Kamenetskii, M.D. (2006). Base-stacking and base-pairing contributions into thermal stability of the DNA double helix. *Nucleic Acids Research*, 34(2), 564–574. https://doi.org/10.1093/nar/gkj454

Zhang, Q., & Wang, Y. (2010). HMG Modifications and Nuclear Function. *Biochimica et Biophysica Acta*, 1799(1-2), 28. http://doi.org/10.1016/j.bbagrm.2009.11.009

Zwart, P., Grosse-Kunstleve, R. & Adams, P. (2005). Xtriage and fest: automatic assessment of x-ray data and substructure structure factor estimation. *CCP4 Newsl*, *43*, 27-35.